


Fall 12-2008

Dispersion States and Surface Characteristics of Physically Blended Polyhedral Oligomeric Silsesquioxane/Polymer Hybrid Nanocomposites

Rahul Misra
University of Southern Mississippi

Follow this and additional works at: <https://aquila.usm.edu/dissertations>

 Part of the [Materials Chemistry Commons](#), and the [Polymer Chemistry Commons](#)

Recommended Citation

Misra, Rahul, "Dispersion States and Surface Characteristics of Physically Blended Polyhedral Oligomeric Silsesquioxane/Polymer Hybrid Nanocomposites" (2008). *Dissertations*. 1154.
<https://aquila.usm.edu/dissertations/1154>

This Dissertation is brought to you for free and open access by The Aquila Digital Community. It has been accepted for inclusion in Dissertations by an authorized administrator of The Aquila Digital Community. For more information, please contact aquilastaff@usm.edu.

The University of Southern Mississippi

DISPERSION STATES AND SURFACE CHARACTERISTICS OF PHYSICALLY
BLENDED POLYHEDRAL OLIGOMERIC SILSESQUOXANE/POLYMER HYBRID
NANOCOMPOSITES

by

Rahul Misra

Abstract of a Dissertation
Submitted to the Graduate Studies Office
of The University of Southern Mississippi
in Partial Fulfillment of the Requirements
for the Degree of Doctor of Philosophy

December 2008

COPYRIGHT BY

RAHUL MISRA

2008

The University of Southern Mississippi

DISPERSION STATES AND SURFACE CHARACTERISTICS OF PHYSICALLY
BLENDED POLYHEDRAL OLIGOMERIC SILSESQUIOXANE/POLYMER HYBRID
NANOCOMPOSITES

by

Rahul Misra

A Dissertation

Submitted to the Graduate Studies Office
of The University of Southern Mississippi
in Partial Fulfillment of the Requirements
for the Degree of Doctor of Philosophy

Approved:



December 2008

ABSTRACT

DISPERSION STATES AND SURFACE CHARACTERISTICS OF PHYSICALLY BLENDED POLYHEDRAL OLIGOMERIC SILSESQUIOXANE/POLYMER HYBRID NANOCOMPOSITES

by Rahul Misra

December 2008

Control of dispersion and segregation states of nanostructured additives is one of the biggest challenges in realizing the optimum potential of high performance hybrid polymer nanocomposites. Polyhedral oligomeric silsesquioxane (POSS) nanostructured chemicals, with their hybrid organic-inorganic nature and flexible functionalization with a variety of organic substituents, yield possibilities to control dispersion and tune compatibility in a wide range of polymer systems. The overall goal of this research is to investigate the fundamental parameters that influence the dispersion and segregation states of POSS nanostructured chemicals, and to understand chain dynamics and conformations in physically blended POSS hybrid polymer nanocomposites (HPNC's). Multiple structural and mechanical factors influencing macro to nano scale surface and bulk properties were successfully investigated and correlated. A strategy based on thermodynamic principles for selective control of POSS dispersion states in a given polymer matrix is developed and discussed.

This dissertation consists of eight chapters. Chapter 1 provides a detailed introduction about the development and current research interest in POSS/polymer nanocomposites. This chapter also discusses limitations of current advanced nanoprobe techniques. Chapter 2 establishes the overall goal of this research and specific research

objectives. Chapter 3 establishes the preferential surface migration behavior of physically dispersed, non-reactive, closed cage octaisobutyl POSS (Oib-POSS) in a non-polar polypropylene matrix. Furthermore, influence of POSS surface segregation on the surface properties, especially nano-tribomechanical behavior is also discussed. Chapter 4 expands the studies by melt blending two different types of POSS molecules, a non-reactive, closed cage Oib-POSS and an open cage trisilanolphenyl POSS (Tsp-POSS), in a nylon 6 matrix. This chapter discusses the morphology, nano-dispersion and macro- to nanoscale tribomechanical characteristics in relation to the POSS structures. Chapter 5 probes the molecular miscibility, solution and solid-state chain dynamics in polystyrene solution blended with Oib- and Tsp-POSS based on classical thermodynamic principles. Chapter 6 extends the learnings from chapter 5 to utilize POSS as a dispersion aid to disperse TiO_2 nanoparticles in polypropylene. Chapter 7 explores the surface properties of fluorinated and non-fluorinated POSS coated fabrics. Finally, chapter 8 explores a nature-inspired route to modify polymer surfaces utilizing hydrophobin proteins and their impact on surface morphology and nanotribological characteristics.

DEDICATION

This dissertation is dedicated to my parents, especially my mother who has been a great source of motivation and inspiration from the beginning of my studies. My father always inspires me to follow my dreams and work hard to realize them.

Also, this dissertation is dedicated to my wife who always stood by me and kept my spirit up during my toughest moments.

Finally, this dissertation is also dedicated to my beautiful daughter Ayusha who means a world to me.

ACKNOWLEDGEMENTS

I would like to take this opportunity to thank my research advisor Dr. Sarah E. Morgan for her support, guidance, and encouragement throughout my graduate career. I would also like to thank the members of my graduate committee, Dr. Charles E. Hoyle, Dr. Robert Y. Lochhead, Dr. James Rawlins, Dr. Bruce X. Fu, and Dr. Sergei Magonov, for their guidance and valuable suggestions.

I am thankful to the entire Morgan research group for their friendship and help throughout my studies, in particular, Alp Alidedeoglu, Chris Harris, Paul Jones, Kristin Hamilton, Brandon Drescher, Bobby Cook, and Chris Collins. I would also like to thank Dr. William Jarrett, Dr. Andreas Plagge, and Sara Bayley who helped me during these studies. In addition, I would like to acknowledge Velda Moore, Heatherly Edgar, Kim Wingo, and Erin Prince for their help. I am also thankful to Dr. Joe Lichtenhan for valuable discussions throughout my research.

I am forever grateful to my parents, my wife, and my entire family, all of whom have provided encouragement and support throughout my life.

The author also gratefully acknowledges the financial and material support for this research by National Science Foundation and Hybrid Plastics Inc., MS respectively.

TABLE OF CONTENTS

ABSTRACT.....ii

DEDICATION.....iv

ACKNOWLEDGEMENTS.....v

LIST OF ILLUSTRATIONS.....ix

LIST OF TABLES.....xiv

CHAPTER

I. INTRODUCTION.....1

 Hybrid Polymer Nanocomposites

 Classification of Polymer Composites: Advantages and Challenges

 Polyhedral Oligomeric Silsesquioxane (POSS) Nanostructured Materials

 Developments in POSS/Polymer HPNC's

 Current Research Interests in POSS/Polymer HPNC's

 Thermodynamics of POSS Dispersion

 Tribology: Friction, Wear, and Adhesion Properties

 Friction Measurements for Polymeric Surfaces

 Quasi-static and Dynamic Nanomechanical Properties

 Motivation and Contribution of Current Research

 References

II. OBJECTIVES OF RESEARCH.....38

III. SURFACE ENERGETICS, DISPERSION AND NANOTRIBOMECHANICAL BEHAVIOR OF POSS/PP HYBRID NANOCOMPOSITES.....40

 Abstract

 Introduction

 Experimental

 Results and Discussion

 Conclusions

 Acknowledgements

 References

IV. POSS-NYLON 6 NANOCOMPOSITES: INFLUENCE OF POSS
STRUCTURE ON SURFACE AND BULK PROPERTIES.....80

Abstract
Introduction
Experimental
Results and Discussion
Conclusions
Acknowledgements
References

V. TAILORING MOLECULAR MISCIBILITY AND CHAIN DYNAMICS
OF POSS/POLYSTYRENE BLENDS: CONTROL OF POSS
PREFERENTIAL DISPERSION STATES.....119

Abstract
Introduction
Experimental
Results and Discussion
Conclusions
Acknowledgements
References

VI. POLYHEDRAL OLIGOMERIC SILSESQUIOXANE (POSS)
TRISILANOLS AS DISPERSANTS FOR TITANIUM OXIDE
NANOPOWDER.....158

Abstract
Introduction
Experimental
Results and Discussion
Conclusions
Acknowledgements
References

VII. NON-WETTING, NON-ROLLING, STAIN RESISTANT POLYHEDRAL
OLIGOMERIC SILSESQUIOXANE COATED TEXTILES.....176

Abstract
Introduction
Experimental
Results and Discussion
Conclusions
Acknowledgements
References

VIII. NANOSCALE REDUCTION IS SURFACE FRICTION OF POLYMER SURFACES MODIFIED WITH SC3 HYDROPHOBIN FROM SCHIZOPHYLLUM COMMUNE.....199

Abstract
Introduction
Experimental
Results and Discussion
Conclusions
Acknowledgements
References

CONCLUSIONS AND RECOMMENDED FUTURE WORK.....227

LIST OF ILLUSTRATIONS

| Figure | | |
|---------|---|----|
| I-1. | Schematic representation of various hybrid plastics networks..... | 4 |
| I-2. | Molecular structure of POSS..... | 7 |
| I-3. | Generalized POSS structure: A) open cage, B) closed (condensed) cage..... | 8 |
| I-4. | Various molecular architectures obtained via covalent attachment of POSS.... | 10 |
| III-1. | Schematic structure of Octaisobutyl POSS..... | 45 |
| III-2. | Three dimensional AFM tapping mode height images and surface roughness analysis of melt pressed (A) Neat PP (B) 5% Oib-POSS/PP (C) 10% Oib-POSS/PP (Z Scale: 150 nm, R_q : Root mean square roughness, R_a : Mean roughness, H_{max} : maximum height)..... | 51 |
| III-3. | AFM phase images of melt pressed (A) Neat PP surface (B) 10% Oib-POSS/PP surface, and microtomed (C) Neat PP bulk (D) 10% Oib-POSS/PP bulk..... | 52 |
| III- 4. | SEM/EDAX mapping of melt pressed (A) Neat PP surface (B) 10% Oib-POSS/PP Surface and microtomed (C) 10% Oib-POSS/PP Bulk Nanocomposite..... | 54 |
| III-5. | TEM-EDAX elemental surface mapping of a microtomed 10% Oib-POSS/PP sample (A) Carbon (B) Oxygen (C) Silicon (D) Silicon Overlap..... | 55 |
| III-6. | ATR-FTIR spectra of (A) Oib-POSS (B) Neat PP (C) 5% Oib-POSS/PP (D) 10% Oib-POSS/PP..... | 56 |
| III-7. | Variable angle ATR-FTIR spectra of Oib-POSS/PP HPNC..... | 58 |
| III-8. | Relative concentration as a function of depth in Oib-POSS/PP HPNC..... | 58 |
| III-9. | Friction loops obtained via lateral force microscopy at applied normal force of 28nN for (A) Neat PP (B) 5% Oib-POSS/PP (C) 10% Oib-POSS/PP..... | 59 |
| III-10. | Friction force as a function of applied normal force measured via LFM. COF (μ) is obtained from the slope, adhesive force (F_a) is obtained from the intercept. (A) Neat PP (B) 5% Oib-POSS/PP (C) 10% Oib-POSS/PP..... | 60 |
| III-11. | COF as a function of POSS concentration at different humidity's..... | 62 |
| III-12. | COF as a function of POSS concentration at different loads..... | 63 |

| | | |
|---------|--|-----|
| III-13. | AFM scratch imaging and section analysis (A) Neat PP (B) 10% Oib-POSS/PP..... | 64 |
| III-14. | Nanoindentation force as a function of displacement measured using the Hysitron (A) Neat PP (B) 5% Oib-POSS/PP (C) 10% Oib-POSS/PP..... | 65 |
| III-15. | DMA thermograms of Oib-POSS/PP nanocomposites..... | 70 |
| III-16. | DMA storage modulus of Oib-POSS/PP nanocomposites..... | 70 |
| III-17. | Schematic representation of bulk vs. surface distribution of POSS nanoparticles in Oib-POSS/PP nanocomposite..... | 72 |
| IV-1. | Schematic structures of (A) Oib-POSS (B) Tsp-POSS..... | 85 |
| IV-2. | Tapping Mode AFM phase images of (A) Neat nylon 6 (B) 10% Oib-POSS/nylon 6 (C) 10% Tsp-POSS/nylon 6..... | 94 |
| IV-3. | ATR-FTIR spectra of Oib-POSS/nylon 6 HPC's..... | 96 |
| IV-4. | ATR-FTIR spectra of Tsp-POSS/nylon 6 HPC's..... | 97 |
| IV-5. | SEM micrographs of microtomed bulk (A) Neat nylon 6 (inset image shows lamellar stacks) (B) 10% Oib-POSS/nylon 6 (C) 10% Tsp-POSS/nylon 6..... | 98 |
| IV-6. | EDAX mapping of microtomed bulk neat nylon 6 and POSS/nylon 6 composites..... | 99 |
| IV-7. | TEM/EDAX silicon mapping of (A) 10% Oib-POSS/nylon 6 (B) 10% Tsp-POSS/nylon 6 HPC's microtomed bulk samples..... | 100 |
| IV-8. | Wide angle x-ray diffractograms of (A) Oib-POSS/nylon 6 (B) Tsp-POSS/nylon 6 HPC's..... | 101 |
| IV-9. | Real time AFM friction loops for (A) Neat nylon 6 (B) 5% Tsp-POSS/nylon 6 (C) 10% Tsp-POSS/ nylon 6..... | 105 |
| IV-10. | Pin-on-disc macroscale relative friction coefficients of (A) Oib-POSS/nylon 6 (B) Tsp-POSS/ nylon 6 HPC's at different external loads..... | 106 |
| IV-11. | Quasi-static nanoindentation force-displacement curves for (A) Neat nylon 6 (B) 5% Tsp-POSS/nylon 6 (C) 10% Tsp-POSS/nylon 6..... | 107 |
| IV-12. | Nanoscale dynamic storage modulus as a function of penetration depth for POSS/nylon 6 HPC's..... | 109 |

| | | |
|-------|---|-----|
| V-1. | Schematic structures of (A) Oib-POSS (B) Tsp-POSS..... | 123 |
| V-2. | Schematic representation of $T_{1\rho}(H)$ relaxation experiment pulse sequence... | 127 |
| V-3. | Schematic representation of $T_{1\rho}(C)$ relaxation experiment pulse sequence.... | 128 |
| V-4. | Multi-angle laser light scattering Zimm plots for PS and POSS/PS HPC's.... | 132 |
| V-5. | AFM phase images of (A) Neat PS (B) Tsp-POSS/PS (C) Oib-POSS/PS..... | 134 |
| V-6. | TEM micrographs of (A) Tsp-POSS/PS (B) Oib-POSS/PS HPC's..... | 136 |
| V-7. | ATR-FTIR spectra of POSS/PS HPC's..... | 137 |
| V-8. | ^{13}C CP/MAS spectra of Tsp-POSS (A) before and (B) after TOSS sequence. | 140 |
| V-9. | ^{13}C CP/MAS spectra of (A) Neat Tsp-POSS (B) Neat PS (C) Tsp-POSS/PS HPC..... | 141 |
| V-10. | ^{29}Si spectra of (A) Tsp-POSS (B) Tsp-POSS/PS samples..... | 142 |
| V-11. | ^{29}Si spectra of (A) Oib-POSS (B) Oib-POSS/PS samples..... | 143 |
| V-12. | $^{13}\text{C}\{^1\text{H}\}$ CP/MAS HETCOR 2D contour plot of Tsp-POSS/PS HPC..... | 144 |
| V-13. | $^{29}\text{Si}\{^1\text{H}\}$ CP/MAS HETCOR 2D contour plot of Tsp-POSS/PS HPC..... | 145 |
| V-14. | $^{29}\text{Si}\{^1\text{H}\}$ CP/MAS HETCOR 2D contour plot of Oib-POSS/PS HPC..... | 146 |
| V-15. | $T_{1\rho}(H)$ relaxation decay of neat PS and POSS/PS HPC's..... | 147 |
| V-16. | Change in $T_{1\rho}(C)$ relaxation time of aromatic region of PS, Tsp-POSS/PS, and Oib-POSS/PS HPC's as a function of spin-locking fields..... | 149 |
| V-17. | Change in $T_{1\rho}(C)$ relaxation times of aliphatic region of PS, Tsp-POSS/PS, and Oib-POSS/PS HPC's as a function of spin-locking fields..... | 149 |
| V-18. | Change in ^1H line-widths of Oib-POSS/PS HPC as a function of mixing time..... | 150 |
| VI-1. | Generalized POSS structure A) condensed (closed) cage, B) open cage..... | 160 |
| VI-2. | TGA analysis of (a) untreated TiO_2 , (b) POSS treated TiO_2 after washing, (c) POSS treated TiO_2 before washing..... | 167 |

| | | |
|---------|---|-----|
| VI-3. | TEM images of polypropylene/nano-TiO ₂ blends with different TiO ₂ treatments a) untreated nano-TiO ₂ b) POSS/nano-TiO ₂ blend c) nano-TiO ₂ chemically treated with POSS. Scale bars are indicated on each figure..... | 168 |
| VI-4. | TEM-EDAX images of polypropylene/nano-TiO ₂ blends with different TiO ₂ treatments a) untreated nano-TiO ₂ b) POSS/nano-TiO ₂ blend c) nano-TiO ₂ chemically treated with POSS. Scale bars represent 200 nm. Brightly colored areas indicate titanium..... | 169 |
| VII-1. | Molecular structure of (A) FL-POSS (B) Tsp-POSS..... | 180 |
| VII-2. | AFM Phase image of (A) neat fabric (Z scale:10°) (B) Tsp-POSS coated fabric (Z scale:100°) (C) FL-POSS coated fabric (Z scale:100°) | 184 |
| VII-3. | Three dimensional surface topography of (A) neat fabric (B) Tsp-POSS coated fabric (C) FL-POSS coated fabric(Z scale: 100 nm)..... | 185 |
| VII-4. | SEM micrograph and corresponding EDAX map of (A) neat fabric (B) POSS coated fabric..... | 186 |
| VII-5. | Proton NMR showing presence of POSS on FL-POSS coated fabric..... | 187 |
| VII-6. | Variation in the size of water droplet with time on Teflon film surface..... | 189 |
| VII-7. | Adhesion of water droplet onto POSS coated fabric at varying tilt angles..... | 191 |
| VII-8. | Effect of water and coffee droplet on neat and POSS coated fabric (A) time t=0 (B) t=10 min (C) comparison of stain area after removal of coffee droplets..... | 191 |
| VII-9. | Acid resistance of neat and POSS coated fabric at (A) time t=0 (B) t=20 sec..... | 192 |
| VII-10. | Macroscale relative surface friction of neat and POSS coated fabric..... | 193 |
| VII-11. | TGA analysis of neat and POSS coated fabric..... | 194 |
| VIII-1. | Friction loops for (A) Neat PS (B) Sc3 hydrophobin coated PS..... | 208 |
| VIII-2. | Height and phase image of Sc3 hydrophobin on PS (A) Adsorbed (B) Spin coated..... | 210 |
| VIII-3. | Height and phase image of Sc3 hydrophobin on PBP (A) Adsorbed (B) Spin coated..... | 211 |

| | |
|--|-----|
| VIII-4. Height and phase image of Sc3 hydrophobin rodlet pattern on glass substrate..... | 212 |
| VIII-5. Section analysis of Sc3 hydrophobin on PS (A) Spin coated (B) Adsorbed.... | 214 |
| VIII-6. Section analysis of Sc3 hydrophobin on PBP (A) spin coated (B) adsorbed... | 215 |
| VIII-7. Friction force vs normal force plot for (A) Neat PS (B) Sc3 hydrophobin spin coated on PS (C) Sc3 hydrophobin Adsorbed on PS..... | 216 |
| VIII-8. Friction force vs normal force plot for (A) Neat PBP (B) Sc3 hydrophobin spin coated on PBP (C) Sc3 hydrophobin Adsorbed on PBP..... | 216 |
| VIII-9. Force curves for (A) Neat PS (B) Sc3 hydrophobin coated PS..... | 218 |
| VIII-10. Triboindenter film thickness for (A) Neat PBP (B) Sc3 hydrophobin coated PBP..... | 221 |
| VIII-11. Triboindenter film thickness for (A) Neat PS (B) Sc3 hydrophobin coated PS..... | 221 |

LIST OF TABLES

| Table | | |
|--------|---|-----|
| III-1. | AFM particle size analysis of melt pressed 10wt.% Oib-POSS/PP surface and bulk area..... | 53 |
| III-2. | Maximum penetration depth, reduced modulus and hardness of Oib-POSS/PP HPNC's..... | 66 |
| III-3. | Static contact angle and surface energy of Oib-POSS/PP HPNC's..... | 67 |
| III-4. | Advancing (θ_a), receding water contact Angle (θ_r) and hysteresis (θ_h) of Oib-POSS/PP HPNC's..... | 68 |
| III-5. | DSC crystallization and melting temperatures of Oib-POSS/PP HPNC's..... | 69 |
| IV-1. | Theoretical solubility parameter for Nylon 6, Oib-POSS, and Tsp-POSS..... | 92 |
| IV-2. | Nanoscale surface roughness, relative COF and percentage reduction in COF of POSS/nylon 6 HPC's..... | 95 |
| IV-3. | Static contact angle and surface energy of POSS/nylon 6 HPC's..... | 103 |
| IV-4. | Advancing (θ_a), receding water contact angle (θ_r) and hysteresis (θ_h) of POSS/nylon 6 HPC's..... | 104 |
| IV-5. | Maximum penetration depth, percentage recovery, reduced modulus, and relative hardness of POSS/nylon 6 HPC's obtained <i>via</i> nanoindentation..... | 107 |
| IV-6. | DMA storage modulus, glass transition temperature (DMA and DSC), and melting temperature (DSC) of POSS/nylon 6 HPC's..... | 109 |
| IV-7. | DSC percentage crystallinity of POSS/nylon 6 HPC's..... | 110 |
| V-1. | Theoretical solubility parameter for PS, Oib-POSS, and Tsp-POSS..... | 130 |
| V-2. | Refractive index of PS and POSS/PS HPC solutions..... | 131 |
| V-3. | Dynamic and static light scattering data for PS and POSS/PS HPC's..... | 133 |
| V-4. | AFM particle size analysis POSS/PS HPC's..... | 134 |
| V-5. | AFM surface roughness of PS and POSS/PS HPC's..... | 135 |
| V-6. | Surface Energy of Neat PS, POSS, and POSS/PS HPC's..... | 138 |

| | | |
|---------|--|-----|
| VI-1. | Average particle diameter for nano-TiO ₂ with different surface treatments after dispersion in PP matrix..... | 170 |
| VI-2. | Optical properties of blends with different TiO ₂ treatment..... | 170 |
| VI-3. | Melt flow index of blends with different TiO ₂ treatment..... | 171 |
| VII-1. | AFM roughness analysis on neat and POSS coated fabrics..... | 184 |
| VII-2. | Comparative static water contact angle analysis for POSS coated fabrics and Teflon..... | 187 |
| VII-3. | Contact angle hysteresis for POSS coated fabrics..... | 190 |
| VIII-1. | AFM roughness analysis for neat and Sc3 hydrophobin coated polymer substrates..... | 213 |
| VIII-2. | Relative value of COF and adhesive force for neat and Sc3 hydrophobin coated PS and PBP films..... | 217 |
| VIII-3. | Water contact angle for unmodified and Sc3 hydrophobin coated PS and PBP film surface..... | 219 |
| VIII-4. | Triboindenter thickness data for unmodified and Sc3 hydrophobin spin coated PS and PBP film surface..... | 220 |

CHAPTER I

INTRODUCTION

Hybrid Polymer Nanocomposites

A major challenge in the development of high performance polymeric nanocomposites is the control of nanoparticle dispersion. Typical nanomaterials currently under investigation include layered silicates, nanotubes, nanofibers, inorganic nanoparticles, fullerenes, nanowires, and more recently organic-inorganic hybrid polyhedral oligomeric silsesquioxane (POSS) molecules. The key to realize the optimum potential of hybrid polymer nanocomposites (HPNC's) lies in the ability to control the aggregation and dispersion characteristics of nanomaterials, especially in a physically blended system. The organic-inorganic hybrid nature of nanostructured POSS molecules offers a unique approach to control and tailor their dispersion characteristics. POSS molecules have been dispersed in a variety of polymer matrices as reinforcements to improve their bulk thermo-mechanical properties, primarily through copolymerization of POSS with selected monomers. However, relatively few studies have appeared on physically blended POSS/polymer systems, and, to our knowledge, no studies have focused on utilization of POSS molecules to selectively modify polymeric surfaces to improve their surface characteristics, specifically friction, wear, and adhesion. Although bulk characteristics of POSS based HPNC's have been reported, much work lies ahead to develop a molecular level understanding of chain dynamics and conformations in physically blended POSS/polymer nanocomposite solutions and films. Furthermore, understanding of these molecular level processes will help in correlating POSS chemical composition to its dispersion characteristics. In the current research we have studied the

parameters affecting the dispersion states of nanostructured POSS chemicals in polymer matrices and how dispersion influences the surface and bulk properties of POSS/polymer HPNC's. In addition, significant emphasis is placed on understanding and evaluating fundamental factors controlling the surface friction on the nanoscale and how it translates into macroscopic performance.

Classification of Polymer Composites: Advantages and Challenges

Based on the size of the reinforcing additive(s) polymeric composites are broadly categorized as microcomposites and nanocomposites. In conventional microcomposites the dispersed phase has dimensions on the order of several microns, whereas polymeric nanocomposites are reinforced with a nanostructured additive(s) having at least one dimension in the nanometer range. These nanostructured additives are projected to provide high performance capabilities for engineering polymer applications, imparting the high strength and modulus obtained with traditional fillers without their negative side effects, such as reduced processability and impact strength. Widespread commercialization of polymer nanocomposite materials, however, has been disappointingly slow, and in many cases, observed property enhancements fall far short of expectations, due in large part to the aggregation tendency and difficulty of dispersion of nanoparticles. Additional hurdles include prohibitively high cost of manufacture of nanoparticles and nanocomposites, and potential environmental hazards associated with some nanomaterials. The overall properties of such nanocomposites depend not only on the bulk properties of the individual ingredients, but they are also dependent on the interactions between the different phases as well as the interface. The nature of these interactions is complex in nature and not well understood. As the size of the individual

phases reduces to the atomic scale the role of the interphase becomes more significant and the interactions become increasingly complex in nature.^{1,2}

Figure I-1 shows a schematic view of hybrid plastics networks which includes sol-gel networks, inorganic and organic polymer blends, preceramic polymers, and layered silicate nanocomposites. All these materials have their own advantages and challenges. One of the important classes of hybrid polymer nanocomposites (HPNC's) is based on nanoclays, which are layered silicates with only one dimension in the nanometer range. Layered silicate materials consist of two layers of tetrahedrally-coordinated silicon atoms, bonded to an octahedral sheet of aluminum or magnesium hydroxide.³ Their thickness is around 1 nm, and lateral dimensions vary from 25 nm up to hundreds of nanometers.⁴ These layers stack with a regular van der Waals gap between them, which is termed as interlayer or gallery spacing. Based on their source of origin and structural composition, layered silicate materials are classified as montmorillonite, laponite, hectorite, and saponite etc. In 1990, polymer-clay nanocomposites were first reported by Toyota R&D in Japan.⁵ Since then extensive research has been reported in this class of hybrid polymer nanocomposites. Conventionally, layered silicate/polymer hybrid materials are prepared *via in-situ* polymerization, intercalation of polymer from a solution, direct intercalation of the molten polymer, or sol-gel methods.^{5,6} Unmodified clays are hydrophilic in nature. In order to improve its compatibility with an organic polymer matrix, the surface of the clay is modified with different surfactants and organic modifiers such as n-dodecylamine.⁷ Depending upon the extent of dispersion and aggregation, clay particles exhibit phase-separated, intercalated, or exfoliated morphology. Nanoclay-based HPNC's have been extensively studied and significant

improvements in properties such as thermal,^{8,9,10} mechanical,^{11,12,13} heat resistance,^{14,15} gas barrier properties,^{16,17} and resistance to solvent uptake and flammability^{18,19,20,21} have been reported in the literature. However, these materials suffer from a number of disadvantages including difficult dispersion, costly chemical treatment to improve clay/polymer compatibility, purification of clay, and generally increased melt viscosity even at small clay loadings.^{22,23}

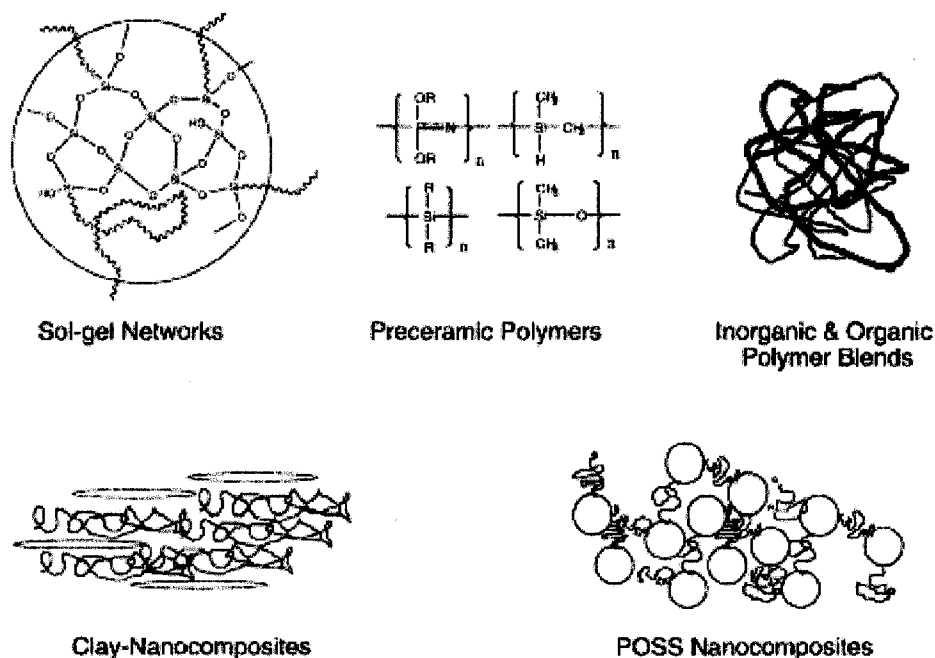


Figure I-1. Schematic representation of various hybrid plastics networks (This figure was drawn following a publication by Lichtenhan, J.D. *Appl. Organometal. Chem.* 1998, 12, 707)²⁴

Another class of HPNC's is based on the use of carbon nanotubes and nanofibers. Carbon nanotubes are graphitic sheets rolled into seamless tubes and have diameters ranging from about a nanometer to tens of nanometers with lengths up to centimeters. Nanotubes were first reported by Iijima and coworkers^{25,26} in 1991. Following this discovery, Gibson *et al.*²⁷ reported exceptionally high Young's modulus for individual

carbon nanotubes. Since then nanotubes have received significant attention due to their high modulus and electrical/thermal conductivity. Nanotubes can be synthesized in two structural forms, single-wall and multiwall. In nanotube based polymer nanocomposites, two dimensions of the dispersed phase are in the nanometer range. Extensive results have been published demonstrating the enhanced electrical, thermal, and mechanical properties of carbon nanotube based HPNC's.^{28,29,30,31,32,33} Utility of these nanocomposites, however, is limited due to high cost and difficulties in dispersion of the nanofillers in the polymer matrix.^{34,35,36} Multiple approaches, including surface modification of nanotubes *via* solution chemistry,³⁷ polymer coating on nanotube surfaces,³⁸ melt blending,³⁹ in-situ polymerization of the nanocomposites,⁴⁰ ultrasonic dispersion in solution,⁴¹ plasma treatment,⁴² and use of surfactants⁴³ have been reported. It is clear from these different approaches that control of aggregation and dispersion of nanotubes still remains the biggest challenge. Lau and Hui⁴⁴ have reported an exhaustive review on the synthesis and properties of nanotubes and polymer nanocomposites based on them.

Another category of polymer nanocomposites is based on inorganic nanoparticles. A variety of inorganic nanoparticles, including metal (Al, Fe, Au, Ag), metal oxide (ZnO, Al₂O₃, CaCO₃, TiO₂), nonmetal oxide (SiO₂) and others (SiC) have been studied.^{45, 46} The choice of nanoparticles depends on the desired properties of the nanocomposites. For example, Al nanoparticles provide high conductivity, calcium carbonate particles are low cost fillers, and silicon carbide (SiC) nanoparticles provide high hardness, corrosion resistance and strength.⁴⁷ Typically, physical blending or the sol-gel route is used to prepare HPNC's based on inorganic nanoparticles.⁴⁸ However, dispersing aids or

coupling agents are needed to improve the dispersion and compatibility of inorganic nanoparticles with the organic polymer matrix.⁴⁹

Over the last ten years, another exciting class of HPNC's based on organic-inorganic hybrid polyhedral oligomeric silsesquioxane (POSS) nanostructured chemicals have emerged. This research work is an effort to develop an ability to control the dispersion states of POSS in a polymer matrix and understand its influence on the surface and bulk characteristics of physically blended POSS/polymer HPNC's.

Polyhedral Oligomeric Silsesquioxane (POSS) Nanostructured Materials

POSS molecules belong to a wide family of silsesquioxane materials and their name is derived from the non-integer (one and one-half or *sesqui*) ratio between silicon and oxygen atoms. In contrast to siloxane, silsesquioxane materials exist as ladder or cage type nanostructures. The first reference to POSS materials dates back to 1946, when the molecules were first isolated *via* the thermolysis of the polymeric products produced from the co-hydrolysis of methyltrichlorosilane with dimethylchlorosilane.⁵⁰ In 1955, Guenther and coworkers⁵¹ explained the mechanism of POSS formation based on the nucleophilic interactions of terminal silanol groups with neighboring siloxane bonds. Another landmark publication related to the characterization of incompletely condensed POSS 'triol' was reported by Brown and Vogt in 1965.⁵² In general, synthesis of POSS is a two-step process; the first step involves formation of Si-O-Si bonds with subsequent formation of the polyhedral network and in the second step structures of the organic substituents are modified. It was twenty years later, in 1989, Feher and coworkers^{53,54} re-initiated research efforts exploring the unique geometry and functionality of silicon-oxygen framework of POSS molecules. In 1991, Air Force office of scientific research

provided funding to Lichtenhan and coworkers for the development of POSS macromers containing polymerizable functional groups and copolymers. In the next five years (1991-1996) publications related to the synthesis of POSS copolymers were reported.^{55,56,57} Finally, in 1998 Hybrid Plastics was started as a spin-off company to commercialize the POSS technology.

Physically, POSS molecules exist either as colorless or white crystalline solids or transparent viscous liquids. POSS compounds are represented by the general molecular formula $(\text{RSiO}_{1.5})_n$ where $n=8, 10$ or 12 . As depicted in Figure I-2, POSS molecules have a nanostructured core of an inorganic silicon-oxygen-silicon (Si-O-Si) network frame, usually known as the skeleton or cage, and a corona of organic moieties (R) attached to the corner silicon atoms. The Si-Si diameter is in the range of 0.54 nm and the average Si-C bond length is in the range of 1.83-2.03 Å. The diameter of these monodisperse particles ranges from one to three nanometers, depending on the composition of the cage. Depending on the molecular weight of substituents, typically the molecular weight of POSS molecules is in the range of 500-1500 atomic mass unit (amu).⁵⁸

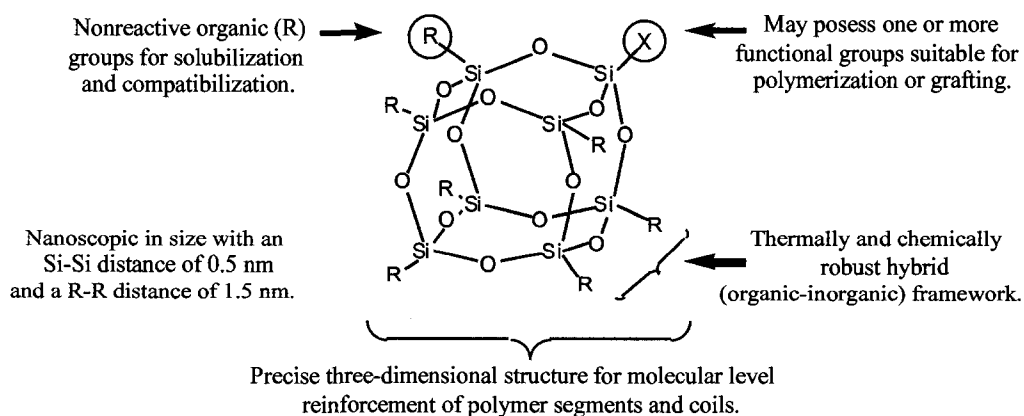


Figure I-2. Molecular structure of POSS.

POSS molecules can be readily modified to provide optimum polymer matrix / nanofiller interaction. Unlike nanoclays or carbon nanotubes, POSS materials offer the advantages of a lightweight nanofiller with tailor-made chemistry that provides immense possibilities to modify the properties of the nanocomposites at the molecular level. The organic substituents (R) can be varied widely to provide a range of different properties, to increase or reduce compatibility with a polymer matrix, or can be made reactive to allow co-polymerization or graft polymerization with a spectrum of monomers. Furthermore, the inorganic cage may be “open” (Figure I-3 A) or “closed” (Figure I-3 B).

Today, over 150 different POSS molecules are produced commercially by Hybrid Plastics Inc. (Hattiesburg, MS). Besides olefins and molecular silicas, a wide variety of POSS molecules with functional groups ranging from halides, epoxies, silanols, and alcohols to acrylates and methacrylates are commercially available.⁵⁹ Several POSS molecules are environmentally benign, non-toxic, and biocompatible, and have been approved by FDA for use in dental composites.^{60,61,62}

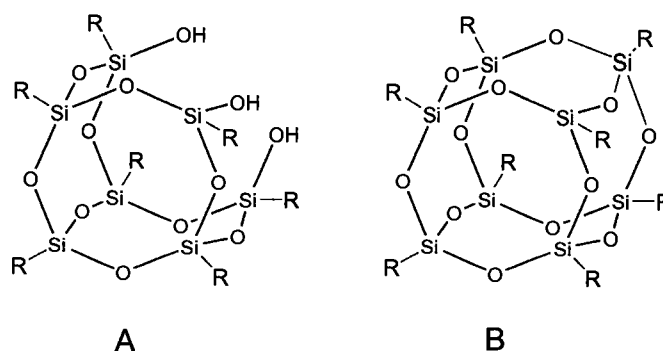


Figure I-3. Generalized POSS structure: A) open cage, B) closed (condensed) cage.

Developments in POSS/Polymer HPNC's

POSS derivatives can be incorporated into a polymer matrix *via* copolymerization, grafting, melt blending or solution blending. Over the last decade POSS has been

copolymerized with multiple monomer systems to produce a wide range of thermoplastics and thermosets with POSS molecules incorporated as an integral part of the polymer chain,^{63,64,65,78-86} with fewer studies on melt blended POSS/ polymer composites.^{66,67,68,69,70} Synthetic approaches include, condensation polymerization, free radical polymerization, ring-opening metathesis polymerization and controlled/living radical polymerization.^{71,72, 73,74,75,76,77} A wide variety of POSS based copolymers have been reported including copolymers of polysiloxane,^{55,78} polynorbornene,⁷² polyurethane,^{79,80} poly(methyl methacrylate),^{56,81} epoxies,⁸² and poly(4-methyl styrene).^{83,84} Various generations of dendrimers based on POSS moieties as the core have also been reported.^{85,86} Figure I-4 shows various molecular architectures including pendant, bead, tri-block, and star obtained *via* covalent attachment of POSS molecules.⁶³ The majority of these research efforts are focused on improving thermomechanical performance of the polymer matrix through uniform POSS dispersion. Haddad *et al.*⁸⁷ studied the random and block copolymers of norbornyl POSS and norbornene. They reported an increase in the glass transition temperature (T_g) of the random copolymers. Additionally, the increase in T_g was found to be dependent on the nature of alkyl substituent groups on the POSS cage. Nanda *et al.*⁸⁸ reported synthesis of well dispersed polyurethane/POSS hybrid materials utilizing a solution polymerization process. Ordered morphologies with homogeneously distributed POSS domains (~100-150 nm) were observed. The authors reported significant increases in physical properties including tensile strength, storage modulus, surface hydrophobicity and glass transition temperature. Coughlin *et al.*⁸⁹ have reported the synthesis of polyethylene-POSS copolymers *via* ring opening metathesis copolymerization. This work was followed by

their studies on the x-ray crystallographic structure,⁹⁰ and control of crystallization and aggregation behavior of polyethylene/POSS copolymers.⁹¹ Nanostructure self assembly, extent of cross-linking during assembly, control of aggregation, spatial distribution of nanoscopic POSS building blocks, molecular dynamics and Monte Carlo simulation studies related to the interchain dynamics of POSS copolymers have also been reported.^{92,93,94,95} Recent developments in nanoscience of POSS-polymers along with advancements in fluorinated POSS and POSS fluoropolymers have been reported.^{96,97} Another major development in POSS copolymers is related to the development of POSS-modified high performance polyimides. Gonzalez and coworkers⁹⁸ copolymerized POSS-dianiline with polyimide *via* condensation polymerization to obtain transparent POSS-polyimide films even at 25 wt.% POSS macromer concentration. These films exhibited significant resistance towards impingement of atomic oxygen.

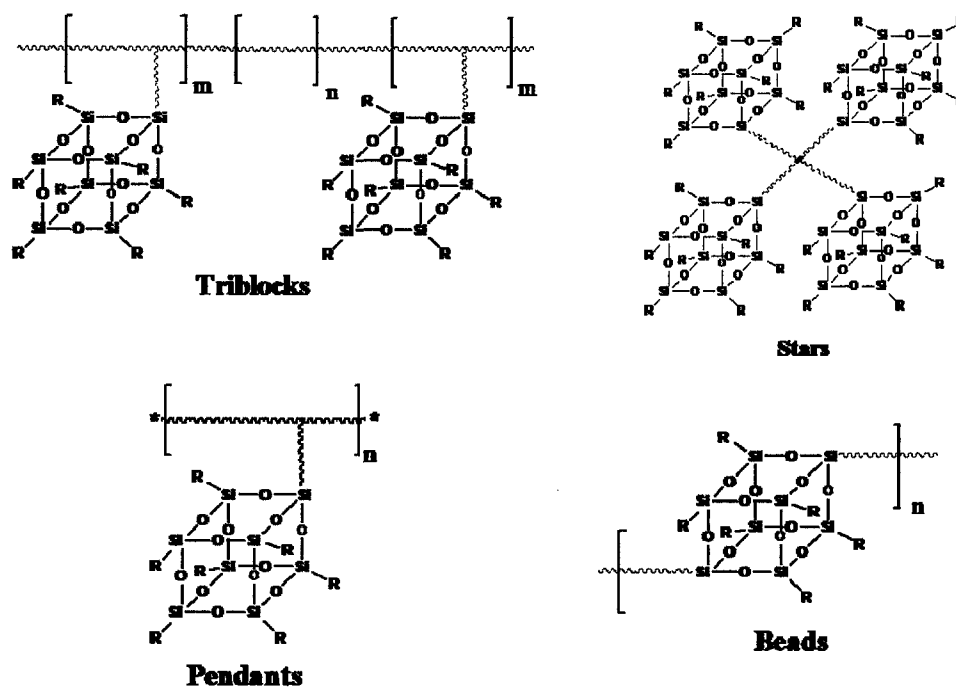


Figure I-4. Various molecular architectures obtained *via* covalent attachment of POSS. (This figure was drawn following a publication by Lichtenhan, J.D. (*Comments Inorg. Chem.* 1995, 17, 115)).

While reactive POSS nanostructured chemicals can be readily dispersed in a polymer matrix at the molecular level through copolymerization, dispersion *via* simple melt mixing is desirable due its wide applicability and cost effectiveness. Morphology studies of hybrid composites prepared *via* melt blending also showed mixed results regarding dispersion of POSS. Most of the studies reveal non-homogenously dispersed POSS crystalline aggregates ranging from a few hundred nanometers to several microns.^{68,99,100} Various research groups have investigated the rheological,⁶⁴ morphological,⁶⁶ viscoelastic,⁶⁷ thermal⁶⁸ and crystallization¹⁰¹ behavior of POSS copolymers and nanocomposites. Fu *et al.*¹⁰² studied the crystallization behavior of octamethyl POSS/isotactic PP under quiescent and shear conditions. They reported an increase in crystallization rate of i-PP on addition of POSS in quiescent conditions, which suggests that POSS molecules act as nucleating agents. At higher POSS content of 30%, the crystallization rate reduced significantly, suggesting a retarded growth mechanism. Schiraldi *et al.*⁶⁷ reported that trisilanolphenyl POSS when blended with polycarbonate yields transparent blends with slightly improved modulus at POSS loading levels up to 5 weight %, while blends of polycarbonate with trisilanolisooctyl POSS at the same loading levels are opaque indicating poor dispersion. Cohen *et al.*¹⁰⁰ studied the effect of three different POSS (cyclohexyl-POSS, methacryl-POSS, and risilanol-phenyl-POSS) on the mechanical behavior of POSS/PMMA films prepared *via* solution bending. Significant increase in the toughening of PMMA was reported, however, the results showed large variability depending upon the nature of POSS composition. Kukaleva *et al.*¹⁰³ reported the rheological and viscoelastic behavior of octamethyl POSS/high density polyethylene (HDPE) nanocomposites prepared *via* melt blending. It was reported that at

low filler content (0.25-0.5 wt %) POSS acts as a lubricant and reduces the viscosity whereas viscosity increases at higher POSS concentrations. Furthermore, X-ray diffraction and DSC studies showed no effect of POSS on the crystallization behavior of HDPE. Fina *et al.*⁶⁸ explored the effect of different alkyl substituents of POSS on the morphology and thermal properties of polypropylene (PP). Improved thermo-oxidative behavior of PP was reported. In addition, it was found that octamethyl POSS acts as nucleating agent, whereas octaisobutyl POSS induces polymorphism in PP at higher POSS loading. Voronkov *et al.*¹⁰⁴ studied the effect of alkyl substituents chain length on the physical and chemical properties of POSS molecules and they have reported that the density and melting point of POSS molecules decreases as the chain length of alkyl substituents increases, whereas volatility and solubility in organic solvents increases. Romo-Uribe *et al.*⁸³ demonstrated that the polymer chain motion is restricted as well as retarded due to the interchain interactions between massive inorganic groups. The POSS molecule acts as an “anchor” point in the polymer matrix, leading to a physical network with individual POSS molecules behaving as weak physical crosslinking sites, thereby retarding the polymer chain motion.⁹² In general, POSS copolymers and nanocomposites exhibit organic/inorganic hybrid properties, demonstrating various degrees of enhanced modulus, stiffness, flame retardancy and thermal stability in comparison to the base polymer.⁶³⁻⁸⁶

The ability to tailor POSS structures in order to achieve desired levels of dispersion in a polymer matrix suggests the possibility of utilizing POSS nanostructured chemicals as dispersing aids for difficult to disperse nanoparticles. The current state-of-the-art uses alkoxy silane coupling agents and various surfactants, such as stearates, to

disperse particles.¹⁰⁵ POSS silanols have several distinct advantages over the traditional approach. POSS silanols are stable in the silanol form, allowing them to be applied directly in one step. Additionally, due to high surface area to volume ratio of POSS, polymer-POSS interaction increases significantly in comparison to coupling agents. Extensive literature reviews on the synthesis and physical properties of various POSS molecules, POSS copolymers, and POSS/polymer blends and nanocomposites have been reported by Pittman *et al.*¹⁰⁶ (2001), Joshi *et al.*¹⁰⁷ (2004), and more recently by Pielichowski and coworkers (2006).¹⁰⁸

Current Research Interests in POSS/Polymers HPNC's

Although multiple studies exploring bulk properties of POSS- polymer HPNC's have appeared over the past 10 years, so far there are very limited published references on surface properties of POSS.^{79,80,96} Limited studies have appeared on the dispersion and bulk thermomechanical characteristics of physically blended POSS/polymer films prepared *via* melt^{66,67,68} and solution^{109,110} blending. Although bulk solution characteristic such as viscosity¹¹¹ have been reported recently, much work lies ahead to develop a molecular level understanding of chain dynamics and conformations in physically blended POSS/polymer nanocomposite solutions and films. There have been studies on the surface properties of other nanocomposite systems,¹⁻⁶ however, systematic study and understanding of the fundamental relationships of POSS structure with surface morphology and nanoscale tribomechanical properties of HPNC's prepared *via* melt mixing have not been explored in detail. Surface properties of POSS based HPNC's reported to date have focused primarily on the hydrophobicity of surfaces with emphasis on utilizing fluorinated POSS. In a recent development, researchers at MIT and AFRL

have reported superhydrophobic and oleophobic poly(methyl methacrylate) surfaces using highly hydrophobic long chain fluorodecyl and fluoroctyl POSS.¹¹² This effect was attributed to the interplay of chemical composition, micro/nano-roughened surface texture, and re-entrant surface curvature. Similarly, Mabry *et al.*¹¹³ have demonstrated that incorporation of fluorinated POSS in fluorinated ethylene-propylene, poly(chlorotrifluoroethylene), and poly(vinylidene fluoride) polymer matrix leads to a significant increase in surface hydrophobicity. Due to their nonpolarizable nature and low surface energy, fluorinated POSS compounds act as a processing aid in the processing of fluoropolymers.^{96,113} The Morgan research group and others have reported surface segregation behavior of POSS in selected POSS/polymer combinations.^{70,114,115} Surface segregation is defined as the preferential enrichment of one component of a multi-component system at the air-surface interface and has attracted significant attention. In the literature, surface enrichment, self-stratification, and surface migration are used synonymously with surface segregation. The concept of self-stratification was introduced in 1976 by Funke *et al.*,¹¹⁶ and is well documented for polymer blends,^{117,118} block copolymers,^{119,120} and polymer solutions.¹²¹ For example, Andrea *et al.*¹²² reported the migration of low molecular weight solid lubricants (zinc-stearate and oleamide) in polyethylene. Due to their low surface energy, fluorinated polymers and additives are commonly used as surface modifying agents. Block copolymers containing fluorinated blocks are reported to form surface segregated domains.¹²³ Similarly, Desmazes *et al.*¹²⁴ reported the migration of low surface energy fluorinated additives in vinylidene chloride based polymer coatings. Toselli and coworkers¹²⁵ reported significant changes in the surface hydrophobicity and friction of alkoxysilane containing perfluoropolyether due to

the preferential segregation of the fluorinated segments. Multiple factors, including competing enthalpic and entropic interactions, surface energy, molecular weight and architecture, relative wettability, degree of phase separation, composite morphology and sample preparation influence the surface migration behavior. Depending upon the conditions, one or several of these factors predominate over the others. Esker and coworkers^{114,115} studied the phase separation behavior and morphological evolution in dewetting thin films of POSS/poly(tert-butyl acrylate) blends as a function of annealing temperature and time. Takahara and coworkers^{110,126} evaluated the surface dewetting characteristics of polystyrene-POSS hybrid films prepared *via* solution blending. They reported a strong influence of the dispersion state of POSS on the surface dewetting characteristics. Fukuda *et al.*¹²⁷ also reported a higher concentration of POSS moieties on the film surface for a poly(methylmethacrylate) (PMMA)/POSS system. The authors synthesized a tadpole shaped hybrid polymer with an inorganic head of fluorinated POSS and an organic tail of PMMA, blended the hybrid polymer with PMMA in solution, and prepared a film *via* spin coating. Recently, Gupta *et al.*¹²⁸ have reported the entropy driven segregation of surface modified cadmium selenide/zinc sulfide core-shell nanoparticles in multilayered composite structures. Similarly, Mackey and coworkers^{129,130} investigated the self-assembly and miscibility behavior of crosslinked polystyrene nanoparticles and dendritic polyethylene blended with high molecular weight polystyrene. These studies underscore the importance of the ratio of the radius of gyration (R_g) of polymer chains to nanoparticle radius on the compatibility, diffusion, and segregation process.

Thermodynamics of POSS Dispersion

Understanding the thermodynamics of nanoparticle filled polymer systems is important for predicting the influence of size, volume fraction, and chemical nature of the solid additive on the overall performance of the material. The assembly of nanoparticles in thin polymer films is driven by the complex interplay of entropic and enthalpic factors.^{131,132} Vaia and coworkers^{133,134,135,136} have reported thermodynamics and kinetics of melt intercalation of layered silicate polymer nanocomposites. Balazs *et al.*¹³⁷ have reported modeling studies on the thermodynamic behavior of nanoparticle filled binary polymer blend systems. Recently, the Morgan research group has reported the thermodynamics of POSS dispersion.¹³⁸ Thermodynamic driving forces for dispersion and segregation behavior of the POSS/Polymer blends can be examined using the Gibbs free energy of mixing (ΔG_m) equation (1), written in equation 2 for mixtures in terms of solubility parameters and volume fraction of each component.

$$\Delta G_m = \Delta H_m - T\Delta S_m \quad (1)$$

$$\Delta G_m = V_1(\delta_1 - \delta_2)^2 \Phi_1\Phi_2 + RT(n_1 \ln \Phi_1 + n_2 \ln \Phi_2) \quad (2)$$

V = molar volume, δ = solubility parameter, Φ = volume fraction, n = mole fraction

R = gas constant, T = absolute temperature

Minimization of the positive enthalpy term (ΔH_m) and minimal decreases in entropy (ΔS_m) are necessary to achieve good mixing. If enthalpic interactions are substantially greater in magnitude than entropic interactions, the dispersion state is decided primarily by the difference in the solubility parameters. Correct choice of nonreactive organic and reactive functional groups can lead to favorable enthalpy of mixing by improved interaction of the POSS cages with the polymer matrix. Nanoscopic

cage size of the POSS molecules contributes significantly towards the favorable entropic term. The entropic term is mainly dominated by the ratio of radius of gyration of polymer chains to the size of POSS aggregates. If the size of POSS aggregates is small compared to the radius of gyration (R_g) of the polymer chains, the entropic penalty for incorporating POSS into the polymer matrix should be small due to the minimal constraints placed on the conformation of the chains. In contrast, if the POSS aggregate size is large relative to R_g , the entropic penalty will be high due to the retardation of segmental motion of the polymer chains. In order to offset this high entropic penalty, individual polymer chains will extend and stretch away from POSS aggregates, driving surface segregation. Kinetic dispersion is favored by high shear mixing process such as twin screw extrusion. Hence selection of a suitable POSS cage for a given polymer system is extremely critical and by proper selection thermodynamics and kinetics of dispersion can be significantly controlled.

Tribology: Friction, Wear, and Adhesion Properties

High performance polymer nanocomposites have significant potential applications ranging from lightweight structural components, to micro- and nano-electromechanical (MEMS/NEMS) devices, to protective films and coatings. For these diverse applications, however, it is critical to understand not only the bulk mechanical properties, but also surface tribological and nanomechanical characteristics, their correlation, and translation of properties from nano to macroscale. Since the term “tribology” will be used frequently in this dissertation, it is pertinent to define it at this stage. The word tribology is derived from the Greek word “tribo” which means rubbing. The American Heritage dictionary defines the term tribology as: “The science of the

mechanisms of friction, lubrication, and wear of interacting surfaces that are in relative motion.” Depending upon the scales of study, tribology studies are further classified as macrotribology and nanotribology. In macrotribology, heavy loads (Newton’s) are applied on test components with relatively large mass over a large contact area and wear is unavoidable. Nanotribology, on the other hand, is related to the friction, wear, and adhesion on a molecular scale (single to few surface asperities contact) under small loads (nano- to micro Newton’s). In this load regime, tribological performance is dominated by surface properties and limited wear is observed. While macroscale friction behavior reflects the performance of materials, nanoscale measurements are important for developing an understanding of complex atomic scale interactions that govern macroscopic properties. Although significant literature is available on the macroscopic friction behavior of materials, much work lies ahead to develop mechanistic insights on the molecular level.

The first formal written description of the classical laws related to macroscopic friction was published in 1699 by the French physicist Guillaume Amonton, in which he proposed two laws for the macroscopic friction phenomenon. The first law of friction states that the friction force, which resists the sliding motion between two surfaces in contact, is proportional to the force that acts in the direction perpendicular to the direction of relative motion of the two surfaces. The second law of friction states that frictional force is independent of the apparent area of contact. Later, a third law of macroscopic friction was added to these two laws by Charles Augustin de Coulomb, which states that frictional force is not a function of velocity at ordinary sliding speeds.¹³⁹

Owens has reported some of the earliest pioneering work on the macroscopic friction, lubrication, and adhesion behavior of vinylidene chloride-acrylonitrile copolymer polymer thin films lubricated by several long chain fatty acid lubricants.^{140,141,142} Lubrication behavior of these fatty acids was explained on the basis of their low surface energy. Effective lubrication was reported for a solid fatty amide of 22 carbons chain length and lubrication efficiency decreased with reduction in chain length of the lubricant. Migration of low molecular weight lubricants, for example oleamide, was observed. In their pioneering work on friction and molecular structure, Pooley and Tabor¹⁴³ demonstrated that during the sliding process the strength of adhesion at the interface and the bulk shear strength of the sliding bodies can be linked to the frictional characteristics of the surfaces in contact. Bulk transfer of material generally leads to higher friction.¹⁴⁴ In semi-crystalline polymers, reduced friction may result from orientation of crystalline chains in the direction of shear. In the case of Teflon, the extremely low friction is attributed to the formation of a transfer film combined with orientation of crystalline chains in the sliding direction.¹⁴⁵ In amorphous polymers, where little orientation is expected, the friction is related to hardness of the surface and the ability to resist formation of wear particles that can increase friction.

Over the last decade, multiple studies exploring the nanotribological behavior of polymers^{146,147,148,149,150} have appeared in the literature. Some studies on the lubrication behavior of various nanoparticles such as molybdenum disulphide (MoS_2)¹⁵¹, silica¹⁵², diamond nanoparticles,¹⁵³ and fullerene-like inorganic nanoparticles¹⁵⁴ have been reported. The Morgan research group has an interest in understanding molecular scale lubricity and friction processes in POSS/polymer nanocomposites,⁷⁰ self-reinforced

polymers,¹⁴⁷ hydrophobin protein modified polymer surfaces,¹⁵⁵ and block copolymers.¹⁵⁶ In the literature, three dominant friction mechanisms are reported, including adhesive, adhesive and roughness, and plowing mechanisms.^{157,158,159,160} Recently, Laine and coworkers¹⁶¹ suggested a self-lubricating “nano ball bearing” mechanism for low friction POSS nanomaterials. The absolute value of the measured friction differs for macro and nanoscale testing, with lower values measured *via* AFM. It has been suggested that these differences in magnitude are related to effects of contact stress which controls the plastic deformation, plowing, adhesion forces and differences in surface damage (wear) at macro vs. nanoscale.^{162,163} Nanoscale adhesive forces measured by atomic force microscopy (AFM) methods are related to the van der Waals attraction and meniscus formation between the surface and the AFM probe.^{164,165} Relative magnitude of the two forces depends upon multiple factors, including surface roughness, hydrophobicity, distance between probe and surface and relative humidity.¹⁶⁶ On the nanoscale, wear is limited, so contribution to friction *via* plowing is expected to be small. However, on macroscale friction testing, the area of contact as well as the surface asperities in contact between the sliding surfaces is orders of magnitude higher than at the nanoscale. Thus, a substantially higher number of wear particles are produced, causing greater bulk deformation and plowing of the polymer surface, resulting in a substantially higher measured COF at macroscale. Additionally, increased shear force is required due to the greater number of asperities at the surface, contributing to the higher COF at macroscale.

Friction Measurements for Polymeric Surfaces

Atomic force microscopy in lateral force mode (LFM) has emerged as a reliable tool for investigating nanotribological characteristics, whereas macroscale friction is

generally measured by Pin-on-disc type tribometers. Analytically Amonton's law describes the friction at the macro scale (Equation 2). According to this law the friction coefficient (μ) is the ratio of the friction force (F_f) to the total normal force (F_n).^{167,168}

$$\mu = F_f / F_n \quad (2)$$

Polymeric materials deviate from this law because surface friction is influenced by multiple structural and mechanical factors including adhesion, roughness, plowing, capillary forces, heterogeneity on the surface, shear stress, surface hardness and true area of contact.^{169,170,171} Nanoscale friction characteristics are significantly influenced by the magnitude of the adhesive force between the AFM probe and the surface. Taking into account these adhesive forces, the relative coefficient of friction (COF) for polymer materials can be best described by Equation 3.

$$\mu = F_f / (F_1 + F_a) \quad (3)$$

Where total normal force $F_n = F_1 + F_a$, F_1 = applied load, and F_a = adhesion between tip and surface. Hence friction force can be expressed as by Equation 4:

$$F_f = \mu F_1 + \mu F_a \quad (4)$$

The relative value of coefficient of friction is obtained from the slope of the linear plot of friction force as a function of applied normal load. At the molecular level, these forces can be determined using AFM. The sample undergoes forward and backward motion under the tip and real time extending and retracting images are obtained from the scope. Qualitatively, the gap between the extending and retracting line is a measure of the friction force at a given normal load. In order to measure the friction force quantitatively the mean value of the separation distance between scope extending and

retracting voltage signals is taken.¹⁷² The adhesive force (F_a) between the AFM tip and the substrate is estimated by two methods, from the measured force curve and from the intercept of the friction force vs. applied load plots.^{173,174}

Quasi-static and Dynamic Nanomechanical Properties

Friction behavior depends not only on the chemical nature and the adhesion between the surfaces in contact, but also on the mechanical properties, such as the relative hardness and modulus of the materials. To develop a more comprehensive understanding of tribology of filled polymer composites at the nanoscale surface regime, studies exploring nanoscale surface friction in conjunction with quasi-static and dynamic nanomechanical behavior are needed. According to contact mechanics theories, surface friction is directly proportional to the shear stress and the true area of contact.^{171,172} Surface hardness, which influences relative surface friction, is commonly measured using macroscale indentation techniques.¹⁷⁵ With advances in nanoscale characterization techniques, nanoindentation is now utilized frequently to evaluate localized surface hardness and elastic modulus based on the method developed by Oliver and Pharr.¹⁷⁶ Measurements are based on a force curve generated as a stiff probe penetrates the material surface. A force curve plots the applied load to the probe with respect to displacement into the specimen, and information about modulus, hardness, elastic recovery, and plastic deformation is obtained.¹⁷⁷ Property measurements are based on the contact mechanics of an axisymmetric indenter with an elastically isotropic half space developed by Oliver and Pharr.¹⁷⁶ Hardness values (H) are calculated using Equation 5:

$$H = P_{\max} / A \quad (5)$$

Where P_{\max} = maximum applied load, and A = contact area between the probe and the specimen. Reduced modulus (E_r) values are taken from the slope (dh/dP) of the unloading portion of the force curve and are dependant upon the contact area (Equation 6)

$$E_r^{-1} = (dh/dP)(2A^{1/2} / \pi^{1/2}) \quad (6)$$

Here h = depth of penetration, and P = applied load

Quasi-static nanomechanical properties of clay and silica filled polymer nanocomposites have been reported.^{178,179,180,181} Recently, dynamic nanoindentation techniques have been utilized to investigate the nanoscale viscoelastic properties of neat polymers as well as composites.^{182,183,184} Mohanty and coworkers¹⁸⁵ reported the dynamic elastic modulus for clay-based polymer nanocomposites. Improved elastic modulus of the composite material was attributed to the reinforcing nature of clay platelets.

Although AFM and nanoindentation tools provide vital information about nanoscale material properties, these techniques have their own limitations and challenges. Among these, the absolute quantitative measurement of friction forces is a significant challenge because of the variability in the different calibration approaches. Different calibration methods have been proposed^{186,187,188} however, no universally applicable method has emerged yet that provides a precise calibration of various AFM cantilever probes independent of lever geometry and tip radius. Additionally, overall tip geometry and cantilever elastic constant are commonly taken from suppliers data which in certain cases may vary from the actual value. Although Oliver and Pharr method is commonly used for nanoindentation measurements, some authors have pointed out its limitations for polymeric materials, especially when measurements are conducted at low loading rate

and holding time.^{189, 190} The viscoelastic nature of polymers causes the indenter to penetrate even in the unloading cycle. Corrections to the Oliver and Pharr method have also been reported.¹⁹¹ However, comparative evaluations of nanotribomechanical properties of materials can be made using these simplified methods. While absolute values of nanomechanical properties may be suspect, comparative evaluations of materials performed under identical experimental conditions are generally considered valid.

Motivation and Contribution of Current Research

The primary motivation for this research was to analyze the ability to control and tailor the segregation and dispersion states of nanostructured POSS molecules in a polymer matrix, through control of the POSS cage structure and organic substituents. In addition, it was of interest to develop a fundamental understanding of how these dispersion states affects the nano- to macro scale properties of POSS/polymer HPNC's at the surface and in the bulk. When this research was initiated, multiple studies concerning the use of POSS as a nanofiller to improve bulk thermal and mechanical properties were reported, primarily through incorporation of POSS monomers in copolymers. However, nanoscale tribomechanical characteristics and fundamental factors controlling the surface tribological and nanomechanical behavior of POSS HPNC's in physical blends were not reported. Furthermore, lack of in-depth molecular level understanding of chain dynamics and conformations in physically blended POSS HPNC solutions and films provided an additional motivation for these studies. To the best of our knowledge, this dissertation reports the first comprehensive work on how POSS dispersion states, surface morphology and properties at the macro to molecular level can be controlled by the

physical blending of specifically tailored POSS molecules in the polymer matrix. In addition, this study contributes towards expanding the current understanding of structure-property relationships of POSS HPNC's by correlating the surface behavior with material (structure, functionalities, stratification and aggregation) and mechanical (roughness, hardness, and modulus) characteristics.

This dissertation is composed of eight chapters. Chapter 2 outlines the overall research goal and specific objectives of this research. Chapter 3 establishes the preferential surface migration behavior of physically dispersed, non-reactive, closed cage octaisobutyl POSS (Oib-POSS) in a non-polar polypropylene matrix. Furthermore, influence of POSS surface segregation on the surface properties, especially nano-tribomechanical behavior, is also discussed. Chapter 4 expands the studies by melt blending two different types of POSS molecules, a non-reactive, closed cage Oib-POSS and an open cage trisilanolphenyl POSS (Tsp-POSS), in a nylon 6 matrix. This chapter discusses the influence of POSS cage structure and functionality on the surface and bulk properties of nanocomposites. Chapter 5 probes the molecular miscibility, solution and solid state chain dynamics of POSS/polystyrene solution blends to tailor preferential dispersion state of POSS. Chapter 6 extends the learning from chapter 5 to utilize POSS as a dispersion aid to disperse other nanoparticles in a polymer matrix. Chapter 7 explores the unique surface characteristics provided by POSS molecules to modify fabric surfaces to obtain non-wetting, non-rolling, stain and acid resistant, low friction fabric surfaces. Finally, chapter 8 explores a nature-inspired route to modify polymer surfaces utilizing hydrophobin proteins and their impact on surface morphology and nanotribological characteristics.

References

-
- ¹ Alexandre, M.; Dubois, P. *Mater. Sci. Eng. R.:Reports* **2000**, *28*, 1.
 - ² Chow, W. S.; Ishak, Z. A. Mohd, K.; Kocsis, J. *Journal of Polymer Science, Part B: Polymer Physics* **2005**, *43*, 1198.
 - ³ Ray, S.; Okamoto, M. *Prog. Polym. Sci.* **2003**, *28*, 1539.
 - ⁴ Saunders, J.; Goodwin, J.; Richardson, R.; Vincent, B. *J. Phys. Chem. B* **1999**, *103*, 9211.
 - ⁵ Okada, A.; Kawasumi, M.; Usuki, A.; Kojima, Y.; Kurauchi, T.; Kamigaito, O. *Mater Res Symp Proc* **1990**, *171*, 45.
 - ⁶ Giannelis, E.P.; Krishnamoorti, R.; Manias, E. *Adv. Polym. Sci.* **1999**, *138*, 107.
 - ⁷ Kojima, Y.; Usuki, A.; Kawasumi, M.; Okada, A.; Kurauchi, T.; Kamigaito, O. *J. Polym. Sci. Part A: Polym. Chem.* **1993**, *31*, 983.
 - ⁸ Wang, D.; Wilkie, C. A. *Polym Degrad Stab* **2003**, *80*, 171.
 - ⁹ Wang, S.; Hu, Y.; Wang, Z.; Yong, T.; Chen, Z.; Fan, W. *Polym Degrad Stab* **2003**, *80*, 157.
 - ¹⁰ Xu, M.; Choi, Y. S.; Kim, Y. K.; Wang, K. H.; Chung, I. *J Polym* **2003**, *44*, 6387.
 - ¹¹ Giannelis, E. P. *Adv Mater* **1996**, *8*, 29.
 - ¹² Maity, P.; Yamada, K.; Okamoto, M.; Ueda, K.; Okamoto, K. *Chem Mater* **2002**, *14*, 4656.
 - ¹³ Chen, G. X.; Hao, G. J.; Guo, T. Y.; Song, M. D.; Zhang, B. H. *J Mater Sci Lett* **2002**, *21*, 1587.
 - ¹⁴ Liu, T.; Lim, K. P.; Tjiu, W. C.; Pramoda, K. P.; Chen, Z. K. *Polymer* **2003**, *44*, 3529.
 - ¹⁵ Priya, L.; Jog, J. P. *J Polym Sci Part B: Polym Phys* **2003**, *41*, 31.

-
- ¹⁶ Pramanik, M.; Srivastava, S. K.; Biswas, K. S.; Bhowmick, A. K. *J Appl Polym Sci* **2003**, *87*, 2216.
- ¹⁷ Chang, J. H.; Park, D. K. *Polym Bull* **2001**, *47*, 191.
- ¹⁸ Hadal, R.; Nathani, H.; Tanniru, M.; Misra, R. D. K. . 'Annual Technical Conference-Society of Plastics Engineers **2005**, *63*, 1444.
- ¹⁹ Okada, A.; Usuki, A. *Mater. Sci. Eng., C: Biomim. Mater., Sensors Syst.* **1995**, *C3*, 109.
- ²⁰ Usuki, A.; Kojima, Y.; Kawasumi, M.; Okada, A.; Fukushima, T.; Kurauchi, T.; Kamigaito, O. *J Mater Res* **1993**, *8*, 1179.
- ²¹ Yano, K.; Usuki, A.; Okada, A.; Kurauchi, T.; Kamigaito, O. *J Polym Sci Part A: Polym Chem* **1993**, *31*, 2493.
- ²² Lan, T.; Pinnavaia, T. *J Chem Mater* **1994**, *6*, 2216.
- ²³ Wang, Z.; Pinnavaia, T. *J Chem. Mater* **1998**, *10*, 1820.
- ²⁴ Joseph, J. S.; Lichtenhan, J. D. *Appl. Organometal. Chem.* **1998**, *12*, 707.
- ²⁵ Iijima, S. *Nature* **1991**, *354*, 56.
- ²⁶ Iijima, S.; Ichihashi, T. *Nature* **1993**, *363*, 603.
- ²⁷ Treacy, M. M.; Ebbesen, T.W.; Gibson, J.M. *Nature* **1996**, *381*, 678.
- ²⁸ Lu, J. P. *Journal of Physics and Chemistry of Solids* **1997**, *58*, 1649.
- ²⁹ Robertson, D. H.; Brenner, D.W.; Mintmire, J.W. *Physical Review B* **1992**, *45*, 12592.
- ³⁰ Ebbesen, T. W.; Lezec, H. J.; Hiura, H.; Bennett, J. W.; Ghaemi, H. F.; Thio, T. *Nature* **1996**, *382*, 54.
- ³¹ Berber, S.; Kwon, Y. K.; Tomanek, D. *Physical Review Letters* **2000**, *84*, 4613.
- ³² Yakobson, B. I.; Brabec, C. J.; Bernholc, J. *Physical Review Letters* **1996**, *76*, 2511.

-
- ³³ Benedict, L. X.; Crespi, V. H.; Louie, S.G.; Cohen, M. L. *Physical Review B* **1995**, *52*, 14935.
- ³⁴ Calvert, P. Potential applications of carbon nanotubes, CRC Press: Boca Raton, USA, **1997**, 277.
- ³⁵ Favier, V.; Canova, G.R.; Shrivastava, S.C.; Cavaille, J.Y. *Polym. Eng. Sci.* **1997**, *37*, 1732.
- ³⁶ Chazeau, L.; Cavaille, J.Y.; Canova, G.; Dendievel, R.; Boutherein, B. *J. Appl. Polym. Sci.* **1999**, *71*, 1797.
- ³⁷ Chen, J.; Hamon, M. A.; Hu, H.; Chen, Y.; Rao, A. M.; Eklund, P. C.; Haddon, R.C. *Science* **1998**, *282*, 95.
- ³⁸ Star, A.; Stoddart, J. F.; Steurman, D.; Diehl, M.; Boukai, A.; Wong, E.W.; Yang, X.; Chung, S. W.; Choi, H.; Heath, J. R. *Angew Chem Int Ed* **2001**, *40*, 1721.
- ³⁹ Siochi, E.J.; Working, D.C.; Park, C.; Lillehei, P.T.; Rouse, J. H.; Topping, C. C.; Bhattacharyya, A. R.; Kumar, S. *Composites Part B-Engineering* **2004**, *35*, 439.
- ⁴⁰ Jia, Z.; Wang, Z.; Xu, C.; Liang, J.; We, B.; Wu, D.; Zhu, S. *Mater Sci. Eng.* **1999**, *395*, 400.
- ⁴¹ Qian, D.; Dickey, E.C.; Andrews, R.; Rantell, T. *Appl. Phys. Lett.* **2000**, *76*, 2868.
- ⁴² Jang, J.; Bae, J.; Yoon, S.H. *Journal of Materials Chemistry* **2003**, *13*, 676.
- ⁴³ Gong, X.; Liu, J.; Baskaran, S.; Voise, R.D.; Young, S. *Chem. Mater.* **2000**, *12*, 1049.
- ⁴⁴ Lau, K.T.; Hui, D. *Composites Part B* **2002**, *33*, 263.
- ⁴⁵ Tang, J.; Wang, Y.; Liu, H.; Xia, Y.; Schneider, B. *J. of Applied Polymer Science* **2003**, *90*, 1053.
- ⁴⁶ Zheng, Y.P.; Zheng Y.; Ning, R.C. *Materials Letters* **2003**, *57*, 2940.

-
- ⁴⁷ Ma, D.; Hugener, T. A.; Siegel, R.W.; Christerson, A.; Martensson, E.; Onneby, C.; Schadler, L. *Nanotechnology* **2005**, *16*, 724.
- ⁴⁸ Chen, Y.C.; Zhou, S. X.; Yang, H. H.; Wu, L.M. *Journal of Applied Polymer Science* **2005**, *95*, 1032.
- ⁴⁹ Yong, V.; Hahn, H.T. *Nanotechnology* **2004**, *15*, 1338.
- ⁵⁰ Scott, D.W. *J. Am. Chem. Soc.* **1946**, *68*, 356.
- ⁵¹ Sprung, M. M.; Guenther, F. O. *J. Am. Chem. Soc.* **1955**, *77*, 6045.
- ⁵² Brown, J. F.; Vogt, L. H.; *J. Am. Chem. Soc.* **1965**, *87*, 4313.
- ⁵³ Feher, F. J.; Newman, D. A.; Walzer, J. F. *J. Am. Chem. Soc.* **1989**, *111*, 1741.
- ⁵⁴ Feher, F. J.; Newman, D. A. *J. Am. Chem. Soc.* **1989**, *112*, 1931.
- ⁵⁵ Lichtenhan, J. D.; Feher, F. J.; Gilman, J. W. *Macromolecules* **1993**, *26*, 2141.
- ⁵⁶ Lichtenhan, J. D.; Otonari, Y.; Carr M. J. *Macromolecules* **1995**, *28*, 8435.
- ⁵⁷ Laine, R. M.; Sellinger, A. *Macromolecules* **1996**, *29*, 2327.
- ⁵⁸ Lichtenhan, J.D.; Noel, C.J.; Bolf, A.G.; Ruth P.N. *Mat. Res. Soc. Symp. Proc.* **1996**, *435*, 3.
- ⁵⁹ <http://www.hybridplastics.com> (accessed September 06, 2008).
- ⁶⁰ Fong, H.; Dickens, S.H.; Flaim, G. M. *Dental Materials* **2005**, *21*, 520.
- ⁶¹ Dodiuk-Kenig, H.; Maoz, Y.; Lizenboim, K.; Eppelbaum, I.; Zalsman, B.; Kenig, S. *J. Adhesion Science and Technology* **2006**, *20*, 1401.
- ⁶² Klapdohr, S.; Moszner, N. *Chemical Monthly* **2005**, *136*, 21.
- ⁶³ Lichtenhan, J.D. *Comments Inorg. Chem.* **1995**, *17*, 115.
- ⁶⁴ Shockey, E. G.; Bolf, A. G.; Jones, P. F.; Schwab, J. J.; Chaffee, K. P.; Haddad, T. S.; Lichtenhan, J. D. *Appl. Organomet. Chem.* **1999**, *13*, 311.

-
- ⁶⁵ Lee, A.; Lichtenhan, J. D. *J. Appl. Polym. Sci.* **1999**, *73*, 1993.
- ⁶⁶ Fu, B. X.; Hsiao, B. S.; Pagola, S.; Stephens, P.; White, H.; Rafailovich, M.; Sokolov, J.; Mather, P. T.; Jeon, H. G.; Phillips, S.; Lichtenhan, J.; Schwab, J. *Polymer* **2001**, *42*, 599.
- ⁶⁷ Zhao, Y.; Schiraldi, D. A. *Polymer* **2005**, *46*, 11640.
- ⁶⁸ Fina, A.; Tabuani, D.; Frache, A.; Camino, G., *Polymer* **2005**, *46*, 7855.
- ⁶⁹ Chen, J. H.; Chiou, Y. D. *J. Polym. Sci., Part B: Polym. Phys.* **2006**, *44*, 2122.
- ⁷⁰ Misra, R.; Fu, B. X.; Morgan, S. E. *J. Polym. Sci., Part B: Polym. Phys.* **2007**, *45*, 2441.
- ⁷¹ Zheng, L.; Farris, R. J.; Coughlin, E. B. *Macromolecules* **2001**, *34*, 8034.
- ⁷² Mather, P. T.; Jeon, H. G.; Romo-Uribe, A.; Haddad, T. S.; Lichtenhan, J. D. *Macromolecules* **1999**, *32*, 1194
- ⁷³ Devaux, E.; Rochery, M.; Bourbigot, S. *Fire Mater* **2002**, *26*, 149.
- ⁷⁴ Constable, G. S.; Lesser, A. J.; Coughlin, E. B. *Macromolecules* **2004**, *37*, 1276.
- ⁷⁵ Matyjaszewski, K. Controlled Radical Polymerization. Proceedings of a Symposium at the 213th ACS National Meeting **1998**, *685*, 483.
- ⁷⁶ Matyjaszewski, K. Controlled/Living Radical Polymerization. Progress in ATRP, NMP, and RAFT. Proceedings of a Symposium on Controlled Radical Polymerization **2000**, *768*, 484.
- ⁷⁷ Jeon, H. G.; Mather, P. T.; Haddad, T. S. *Polym Int* **2000**, *49*, 453.
- ⁷⁸ Mantz, R. A.; Jones, P. F.; Chaffee, K. P.; Lichtenhan, J. D.; Gilman, J. W.; Ismail, I. M. K.; Burmeister, J. *Chem Mater* **1996**, *8*, 1250.
- ⁷⁹ Turri, S.; Levi, M. *Macromolecules* **2005**, *38*, 5569.

-
- ⁸⁰ Turri, S.; Levi, M. *Macromolecular Rapid Communications* **2005**, *26*, 1233.
- ⁸¹ Patel, R.R.; Mohanraj, R.; Pittman, C.U. *J. Polym. Sci., Part B: Polym. Phys.* **2005**, *44*, 234.
- ⁸² Lee, A.; Lichtenhan, J.D. *Macromolecules* **1998**, *31*, 4970.
- ⁸³ Romo-Uribe, A.; Mather, P.T.; Haddad, T.S.; Lichtenhan, J.D. *J. Polym. Sci., Part B: Polym. Phys.* **1998**, *36*, 1857.
- ⁸⁴ Haddad, T.S.; Lichtenhan, J.D. *Macromolecules* **1996**, *29*, 7302.
- ⁸⁵ Zhang, X.; Haxton, K. J.; Ropartz, L.; Cole-Hamilton, D. J.; Morris, R. E. *Dalton Trans* **2001**, 326,1.
- ⁸⁶ Hong, B.; Thoms, T.P.S.; Murfee, H. J.; Lebrun, M. J. *Inorg. Chem.* **1997**, *36*, 6146.
- ⁸⁷ Haddad, T. S.; Mather, P. T.; Jeon, H. G.; Chun, S. B.; Phillips, S. H. *Mat. Res. Soc. Symp. Proc.* **2000**, *628*, 2.
- ⁸⁸ Nanda, A. K.; Wicks, D. A.; Madbouly, S. A.; Otaigbe, J. U. *Macromolecules* **2006**, *39*, 7037.
- ⁸⁹ Coughlin E. B.; Farris, R. J.; Zheng, L. *J. Polym. Sci. Part A: Polym. Chem.* **2001**, *39*, 2920.
- ⁹⁰ Coughlin E. B.; Farris, R. J.; Zheng, L.; Waddon, A. J. *Macromolecules* **2002**, *35*, 2375.
- ⁹¹ Coughlin E. B.; Waddon, A. J.; Zheng, L.; Farris, R. J. *Nano Lett* **2002**, *2*, 1149.
- ⁹² Bharadwaj, R.K., Berry, R.J., Farmer, B.L. *Polymer* **2000**, *41*, 7209.
- ⁹³ Patel, R.R., Mohanraj, R., Pittman, C.U., *J. Polym. Sci., Part B: Polym. Phys.* **2006**, *44*, 234.
- ⁹⁴ Waddon, A. J.; Zheng, L.; Farris, R. J.; Coughlin, E. B. *Nanoletters* **2002**, *2*, 1149.

-
- ⁹⁵ Lamm, M. H.; Chen, T.; Glotzer, S. C. *Nanoletters* **2003**, *3*, 989.
- ⁹⁶ Phillips, S.H.; Haddad, T.S.; Tomczak, S.J. *Current Opinion in Solid State and Materials Science* **2004**, *8*, 21.
- ⁹⁷ Mabry, J. M.; Vij, A.; Iacono, S. T.; Viers, B. D. *Angew. Chem. Int. Ed.* **2008**, *47*, 4137.
- ⁹⁸ Gonzalez, R. I.; Phillips, S. H.; Hoflund, G. B. J. *Spacecraft rockets* **2000**, *37*, 463.
- ⁹⁹ Lee, Y. J.; Kuo, S. W.; Huang, W. J.; Lee, H. Y.; Chang, F. C. *J. Polym. Sci., Part B: Polym. Phys.* **2004**, *42*, 1127.
- ¹⁰⁰ Kopesky, E.T.; McKinley, G.H.; Cohen, R.E. *Polymer* **2006**, *47*, 299.
- ¹⁰¹ Joshi, M., Butola, B.S. *Polymer* **2004**, *45*, 4953.
- ¹⁰² Fu, B.X.; Yang, L.; Somani, R.H.; Zong, S.X.; Hsiao, B.S.; Phillips, S.; Blanski, R.; Ruth, P. J. *J. Polym. Sci., Part B: Polym. Phys.* **2001**, *39*, 2727.
- ¹⁰³ Joshi, M.; Butola, B. S.; Simon, G.; Kukaleva, N. *Macromolecules* **2006**, *39*, 1839.
- ¹⁰⁴ Voronkow, M.G.; Lavrentyev, V. I. *Top. Curr. Chem.* **1982**, *102*, 199.
- ¹⁰⁵ DeArmitt, C.; Rotheron, R. *Plastics, Additives, and Compounding* **2002**, *4*, 12.
- ¹⁰⁶ Pittman, C. U.; Ni, H.; Wang, L. ; Li, G. *J Inorg Organomet Polym* **2001**, *11*, 123.
- ¹⁰⁷ Joshi, M.; Butola, B. S. *Journal of macromolecular science Part C—Polymer Reviews* **2004**, *44*, 389.
- ¹⁰⁸ Pielichowski, K.; Njuguna, J.; Janowski, B.; Pielichowski, J. *Adv. Polym Sci* **2006**, *201*, 225.
- ¹⁰⁹ Ning, H.; Martin, B.; Andreas, S. *Macromolecules* **2007**, *40*, 9672.
- ¹¹⁰ Hosaka, N.; Torikai, N.; Otsuka, H.; Takahara, A. *Langmuir* **2007**, *23*, 902.
- ¹¹¹ Kidane, A. G.; Edirisinghe, M. J.; Bonhoeffer, P.; Seifalian, A. M. *Biorheology* **2007**,

-
- 44, 265.
- ¹¹² Tuteja, A.; Choi, W.; Ma, M.; Mabry, J.; Mazzella, S.; Rutledge, G.; Mckinley, G.; Cohen, R. E. *Science* **2007**, *318*, 1618.
- ¹¹³ Mabry, J. M.; Vij, A.; Iacono, S.T.; Grabow, W.W. *ACS Polymer Preprints* **2005**, *46*, 630.
- ¹¹⁴ Paul, R.; Karabiyik, U.; Swift, M. C.; Esker, A. R. *Langmuir* **2008**, *24*, 5079.
- ¹¹⁵ Paul, R.; Karabiyik, U.; Swift, M. C.; Hottle, J. R.; Esker, A. R. *Langmuir* **2008**, *24*, 4676.
- ¹¹⁶ Funke, W. *J Oil Colour Chem Assoc* **1976**, *59*, 398.
- ¹¹⁷ Eisenriegler, E.; Kremer, K.; Binder, K. *J Chem Phys* **1982**, *77*, 6296.
- ¹¹⁸ Ober, R.; Paz, L.; Taupin, C.; Pincus, P.; Boileau, S. *Macromolecules* **1983**, *16*, 50.
- ¹¹⁹ Shull, K. R.; Kramer, E.J.; Hadziioannou, G.; Tang, W. *Macromolecules* **1990**, *23*, 4780.
- ¹²⁰ Liebler, L. *Makromol Chem Macromol Symp* **1988**, *16*, 1.
- ¹²¹ Gaines, G. L. *J Chem Phys* **1969**, *73*, 3143.
- ¹²² Foldes, E.; Andrea, S. E. *Journal of vinyl and additive technology* **1997**, *3*, 220.
- ¹²³ Sivaniah, E.; Genzer, J. *Langmuir* **2001**, *17*, 4342.
- ¹²⁴ Rixens, B.; Severac, R.; Boutevin, B.; Desmazes, P. L. *Polymer* **2005**, *46*, 3579.
- ¹²⁵ Fabbri, P.; Messori, M.; Montecchi, M.; Pilati, F.; Taurino, R.; Tonelli, C.; Toselli, M. *J. Appl. Polym. Sci.* **2006**, *102*, 1483.
- ¹²⁶ Hosaka, N.; Otsuka, H.; Hino, M.; Takahara, A. *Langmuir* **2008**, *24*, 5766.
- ¹²⁷ Koh, K.; Sugiyam, S.; Morinaga, T.; Ohno, K.; Tsuji, Y.; Fukuda, T.; Yamahiro, M.; Iijima, T.; Oikawa, H.; Watanabe, K.; Miyashita, T. *Macromolecules* **2005**, *38*, 1264.

-
- ¹²⁸ Gupta, S.; Zhang, Q.; Emrick, T.; Balazs A. C.; Russell T. P. *Nature Materials* **2006**, *5*, 229.
- ¹²⁹ Mackay, M. E.; Tuteja, A.; Duxbury, P. M.; Hawker, C. J.; Horn, B. V.; Guan, Z.; Chen, G.; Krishnan, R. S. *Science* **2006**, *311*, 1740.
- ¹³⁰ Krishnan, R. S.; Mackay, M. E.; Duxbury, P. M.; Pastor, A.; Hawker, C. J.; Horn, B. V.; Asokan, S.; Wong, M. *Nano Lett.* **2007**, *7*, 484.
- ¹³¹ Stamm, M.; Sommer, J. U. *Nature Materials* **2007**, *6*, 260.
- ¹³² Schadler, L. *Nature Materials* **2007**, *6*, 257.
- ¹³³ Vaia, R.A.; Ishii, H.; Giannelis, E.P. *Chem Mater* **1993**, *5*, 1694.
- ¹³⁴ Vaia, R.A.; Jandt, K.D.; Kramer, E.J.; Giannelis, E.P. *Macromolecules* **1995**, *28*, 8080.
- ¹³⁵ Vaia, R.A.; Giannelis, E.P. *Macromolecules* **1997**, *30*, 7990.
- ¹³⁶ Vaia, R.A.; Giannelis, E.P. *Macromolecules* **1997**, *30*, 8000.
- ¹³⁷ He, G.; Ginzburg, V. V.; Balazs, A. C. *J. Polym. Sci, Part B: Polym Phys* **2006**, *44*, 2389-2403.
- ¹³⁸ Misra, R.; Bruce, X. Fu.; Morgan, S. E. Manuscript submitted.
- ¹³⁹ Abdelmaksoud, M.; Bender, J.; Krim, J. *Phys. Rev. Lett.* **2004**, *92*, 176101.
- ¹⁴⁰ Owens, D. K. *J. App. Polym. Sci.* **1964**, *8*, 1465.
- ¹⁴¹ Owens, D. K. *J. App. Polym. Sci.* **1964**, *8*, 1477.
- ¹⁴² Owens, D. K. *J. App. Polym. Sci.* **1970**, *14*, 185.
- ¹⁴³ Pooley, C. M.; Tabor, D. *Proc. R Soc. Lond. A.* **1972**, *329*, 251.
- ¹⁴⁴ Biswas, S. K.; Vijayan, K. *Wear* **1992**, *158*, 193.
- ¹⁴⁵ Podesta, A.; Fantoni, G.; Milani, P.; Guida, C.; Volponi, S. *Thin Solid Films* **2002**,

-
- 419, 154.
- ¹⁴⁶ Song, C., Chen, Y., Gan, D., Wang, Z. *High Performance Polymers* **2002**, *14*, 183.
- ¹⁴⁷ Morgan, S. E., Misra, R., Jones, P. J. *Polymer* **2006**, *47*, 2865.
- ¹⁴⁸ Podesta, A.; Fantoni, G.; Milani, P.; Guida, C.; Volponi, S. *Thin Solid Films* **2002**, *419*, 154.
- ¹⁴⁹ Michel, D.; Kopp-Marsaudon, K.; Aime, J. *Tribology Letters* **1998**, *4*, 75.
- ¹⁵⁰ Komura, M.; Qiu, Z.; Ikehara, T.; Nakajima, K.; Nishi, T. *Polymer Journal* **2006**, *38*, 31.
- ¹⁵¹ Rapoport. L.; Fleischer, N.; Tenne, R. *J. Mater. Chem.* **2005**, *15*, 1782.
- ¹⁵² Garcia, M.; Rooij, M. D.; Winnubst, L.; Verweij, H. *J. Appl. Polym. Sci.* **2004**, *92*, 1855.
- ¹⁵³ Tao, X.; Jiazheng, Z.; Kang, X. *J. Phys. D: Appl. Phys.* **1996**, *29*, 2932.
- ¹⁵⁴ Rapoport. L.; Tenne, R. *Industrial lubrication and tribology* **2002**, *54*, 171.
- ¹⁵⁵ Misra, R., Li, J., Cannon, G. C., Morgan, S.E. *Biomacromolecules* **2006**, *7*, 1463.
- ¹⁵⁶ Phillips, J.P., Deng, X., Stephen, R., Fortenberry, E., Todd, M., Stevenson, S., Misra, R., Morgan, S.E., Long, T. *Polymer* **2007**, *48*, 6773.
- ¹⁵⁷ Bhushan, B.; Israelachvili, J. N.; Landman, U. *Nature* **1995**, *374*, 607.
- ¹⁵⁸ Mate, C. M.; McClelland, G. M.; Erlandsson, R.; Chiang, S. *Phys. Rev. Lett.* **1987**, *59*, 1942.
- ¹⁵⁹ Bhushan, B.; Ruan, J. *J. Apply. Phys.* **1994**, *76*, 5022.
- ¹⁶⁰ Bhushan, B.; Koinkar, V. N. *Wear* **1996**, *202*, 110.

-
- ¹⁶¹ Brick, C.M.; Chan, E.R.; Glotzer, S.C.; Marchal, J.C.; Martin, D.C.; Laine, R.M. *Adv. Mater.* **2007**, *19*, 82.
- ¹⁶² Koinkar, V. N.; Bhushan, B. *J. Vac.Sci.Technol.* **1996**, *14*, 2378.
- ¹⁶³ McClelland, G. M. *Adhesion and Friction*; Springer, Berlin, 1989; p.1.
- ¹⁶⁴ Sunderajan, S.; Bhusan, B. *J. Appl. Phys.* **2000**, *88*, 4825.
- ¹⁶⁵ Bhusan, B. *Tribol. Int.* **1995**, *28*, 85.
- ¹⁶⁶ Stifter, T.; Marti, O.; Bhusan, B. *Phys. Rev. B.* **2000**, *62*, 13667.
- ¹⁶⁷ Howell, H.G.; Mazur, J. *J Text Inst* **1953**, *44*, 59.
- ¹⁶⁸ Adamson, A.W. *Physical Chemistry of Surfaces*; Wiley: New York, **1990**, 460.
- ¹⁶⁹ Pooley, C.M.; Tabor, D. *Proc. R. Soc. Lond. A.* **1972**, *329*, 251.
- ¹⁷⁰ Bhushan, B. *Wear* **2001**, *251*, 1105.
- ¹⁷¹ Helt, J. M.; Batteas, J. D. *Langmuir* **2006**, *22*, 6130.
- ¹⁷² Bhushan, B. *Handbook of Micro/Nano Technology*, 2nd ed.; CRC Press: Boca Raton, FL, **1999**, 41.
- ¹⁷³ Baselt, D. R.; Baldeshwieler, J. D. *J Vac Sci Tech B* **1992**, *10*, 2316.
- ¹⁷⁴ Magonov, S.N., *Encyclopedia of Analytical Chemistry*, R.A. Meyers (Ed.); John Wiley & Sons: Chichester, **2000**, 7432.
- ¹⁷⁵ Tabor, D. *The Hardness of Metals*; Oxford University Press: London, 1951.
- ¹⁷⁶ Oliver, W. C., Pharr, G.M., *J.Mat.Res.* **1992**, *7*, 1564.
- ¹⁷⁷ VanLandingham, M.R.; McKnight, S.H.; Palmese, G.R.; Elings, J.R.; Huang, X.; Bogetti, T.A.; Eduljee, R.F.; Gillespie, J.W. *J. Adhesion*, **1997**, *64*, 31.
- ¹⁷⁸ Shen, L.; Phang, I. Y.; Liu, T.; Zeng, K. *Polymer* **2004**, *45*, 3341.
- ¹⁷⁹ Beake, B. D.; Chen, S.; Hull, J. B.; Gao, F. *J Nanosci Nanotechnol* **2002**, *2*, 73-79.

-
- ¹⁸⁰ Hu, Y.; Shen, L.; Yang, H.; Wang, M.; Liu, T.; Liang, T. *Polym Test* **2006**, *25*, 492.
- ¹⁸¹ Xu, G. C.; Li, A. Y.; Zhang, L. D. ; Wu, G. H. *Journal of reinforced plastics and composites* **2005**, *23*, 1365.
- ¹⁸² Park, K.; Mishra, S.; Lewis, G.; Losby, J.; Fan, Z.; Park, J. B. *Biomaterials* **2004**, *25*, 2427.
- ¹⁸³ Asif, S. A.; Wahl, K. J.; Colton, R. J.; Warren, O. L. *J Appl Phys* **2001**, *90*, 1192.
- ¹⁸⁴ Mohanty, B.; Katti, K. S.; Katti, D. R.; Verma, D. *J Mater Res* **2006**, *21* 2045.
- ¹⁸⁵ Sikdar, D.; Katti, D.; Katti, K.; Mohanty, B. *J. App. Polym. Sci.* **2007**, *105*, 790.
- ¹⁸⁶ Bogdanovic, G.; Meurk, A.; Rutland, M. W. *Colloid Surf. B-Biointerfaces* **2000**, *19*, 397.
- ¹⁸⁷ Feiler, A.; Attard, P.; Larson, I. *ReV. Sci. Instrum.* **2000**, *71*, 2746.
- ¹⁸⁸ Sader, J. E. *ReV. Sci. Instrum.* **2003**, *74*, 2438.
- ¹⁸⁹ Hochstetter, G.; Jimenez, A.; Loubet, J. L. *J. Macromol. Sci., B: Phys.* **1999**, *38*, 681.
- ¹⁹⁰ Loubet, J. L.; Georges, J. M.; Meille, J. *Nanoindentation Techniques in Materials Science and Engineering*; ASTM: Philadelphia, PA, 1986.
- ¹⁹¹ Field, J. S.; Swain, M. V. *J. Mater. Res.* **1993**, *8*, 297

CHAPTER II

OBJECTIVES OF RESEARCH

The overall goal of this research is to investigate the fundamental parameters that influence the dispersion and segregation states of POSS nanostructured chemicals in polymer matrices, and to understand chain dynamics and conformations in physically blended POSS HPNC's. The specific objective is to develop a molecular level understanding of the effects of POSS segregation and dispersion states on nano- to macro scale properties at the surface and in the bulk. Of primary interest is to study surface tribomechanical characteristics and the fundamental factors controlling these properties.

The main objectives of this research include:

1. Identify suitable POSS-Polymer matrix combinations using theoretical solubility calculations.
2. Prepare HPNC's at varying POSS concentrations using melt and solution blending methods.
3. Investigate chain dynamics and conformations in solution using refractive index measurements, dynamic light scattering (DLS), and multi-angle laser light scattering (MALLS).
4. Prepare smooth film samples for surface analysis by carefully pressing melt extrudate between clean silicon wafers.
5. Investigate POSS dispersion and segregation characteristics and morphology of HPNC's utilizing atomic force microscopy (AFM), transmission electron microscopy (TEM), scanning electron microscopy (SEM), energy dispersive x-ray analysis (EDX), fixed and variable angle attenuated total reflectance fourier

transform infrared (ATR-FTIR) spectroscopy, solid-state NMR spectroscopy, X-ray diffraction (WAXD), static and dynamic contact angle, and surface energy measurements.

6. Investigate nanoscale tribomechanical properties using AFM and Hysitron nanoindenter along with macroscale friction using Pin-on disc tribometer.
7. Characterize bulk thermomechanical properties utilizing differential scanning calorimetry (DSC), thermogravimetric analysis (TGA), and dynamic mechanical analysis (DMA).
8. Develop a fundamental understanding of structure-property relationships for POSS HPNC's based on thermodynamic principles.

CHAPTER III
SURFACE ENERGETICS, DISPERSION AND NANOTRIBOMECHANICAL
BEHAVIOR OF POSS/PP HYBRID NANOCOMPOSITES

Abstract

Hybrid organic-inorganic polymer nanocomposites incorporating polyhedral oligomeric silsesquioxane (POSS) nanoparticles are of increasing interest for high performance materials applications. Octaisobutyl POSS/polypropylene nanocomposites were prepared at varying POSS concentrations *via* melt blending. The interplay of POSS molecular geometry, composition and concentration in relation to the tribological, nanomechanical, surface energy and bulk properties of the nanocomposites was investigated. Ultra-low friction and enhanced hardness, modulus and hydrophobicity were observed for the nanocomposite surfaces, with minimal changes in the bulk thermomechanical properties. Parallel AFM, SEM, TEM and spectroscopic analyses demonstrated significant differences in POSS distribution and aggregation in the surface and the bulk, with preferential segregation of POSS to the surface. Additionally, contact angle studies reveal significant reduction in surface energy and increase in hysteresis with incorporation of POSS nanoparticles. The differences in bulk and surface properties are largely explained by the gradient concentration of POSS in the polymer matrix, driven by POSS/POSS and POSS/polymer interactions.

Introduction

High performance hybrid polymer nanocomposites (HPNC's) with improved surface properties, specifically improved tribological performance such as reduced friction and wear, have significant potential applications ranging from microelectronic devices and aeronautic applications to low friction fibers for bandages and other prosthetic applications.¹ Conventionally, fluorinated materials such as polytetrafluoroethylene (PTFE) are used for low friction applications; however, these materials are immiscible with most polymers, difficult to process, costly and subject to environmental concerns. These practical challenges motivate the development of novel strategies for developing cost effective, processable and non-halogenated low friction surfaces. In an attempt to address these challenges, we have studied HPNC's of polyhedral oligomeric silsesquioxane (POSS) nanoparticles in a polymeric matrix prepared via melt blending techniques and evaluated their surface and bulk properties.

A fully condensed POSS molecule has a nanostructured core of an inorganic silicon-oxygen-silicon (Si-O-Si) network frame surrounded by a corona of organic moieties (R) attached to the corner silicon atoms. The diameter of a fully extended POSS molecule varies from one to several nanometers, depending on the composition of the substituents.^{2,3} POSS based HPNC's inherit their merits from the robust inorganic POSS cages combined with processable organic polymers. Over the last decade POSS has been copolymerized with multiple monomer systems to produce a wide range of thermoplastics and thermosets with POSS molecules incorporated as an integral part of the polymer chain.^{1,2,3,4,5,6,7,8,9} The majority of these research efforts are focused on improving thermomechanical performance of the polymer matrix through uniform

molecular level POSS nanoparticle dispersion achieved by directly incorporating POSS moieties into the polymer chain.^{9,10} Thermomechanical properties are reported to be strongly influenced by the structure and concentration of the POSS moieties, POSS-POSS interactions and POSS-polymer interactions. In general, hybridization of an organic polymer matrix with inorganic POSS results in improved thermal and mechanical properties along with increase in oxidative and flame resistance.^{3-8,11} Recently Nanda et al.¹² synthesized well dispersed polyurethane/POSS hybrid materials utilizing a solution polymerization process. Ordered morphologies with homogeneously distributed POSS domains (~100-150 nm) were observed. The authors reported significant increases in physical properties, including tensile strength, storage modulus, complex viscosity, surface hydrophobicity and glass transition temperature. Nanostructure self assembly, extent of crosslinking during assembly, control of aggregation, spatial distribution of nanoscopic POSS building blocks, molecular dynamics and Monte Carlo simulation studies related to the interchain dynamics of POSS copolymers have also been reported.^{6,13,14,15}

Fewer studies have been reported in which POSS nanoparticles are physically dispersed in the polymer matrix utilizing high shear melt mixing processes.^{16,17,18,19} As in the case of hybrid materials prepared via chemical incorporation of POSS, improvements in thermomechanical properties are reported for melt-blended systems. Again, the changes in the properties are highly dependent on the POSS structure and its interactions with the polymer matrix. In most of the studies, it was reported that POSS incorporation does not affect the crystallization behavior of the polymer matrix.²⁰ However, in some studies it was reported that incorporation of certain types of POSS molecules induce

polymorphism in selected polymer systems.¹⁸ Morphology studies of hybrid composites prepared via melt blending also showed mixed results regarding dispersion of POSS. Most of the studies reveal non-homogeneously dispersed POSS crystalline aggregates ranging from a few hundred nanometers to several microns.^{6,18}

Recently, studies on surface properties of POSS HPNC's have appeared in the literature, and these are focused mainly on the surface hydrophobicity of POSS based copolymers,^{21,22} fluorinated POSS,²³ and fluorinated POSS/fluorinated polymer composites.²⁴ All of these studies report increased hydrophobicity on incorporation of POSS nanoparticles. Takahara et al.²⁵ evaluated surface dewetting characteristics of polystyrene-POSS hybrid films prepared via solution dispersion of POSS and PS in a common solvent. They report segregation of POSS to the film surface. Fukuda *et al.*²⁶ also reported a higher concentration of POSS moieties on the film surface for a poly(methylmethacrylate) (PMMA)/POSS system. The authors synthesized a tadpole shaped hybrid polymer with an inorganic head of fluorinated POSS and an organic tail of PMMA, blended the hybrid polymer with PMMA in solution, and prepared a film via spin coating. While surface property investigations reported to date have focused primarily on hydrophobicity of POSS HPNC surfaces, the tribological and nanomechanical properties of POSS/polymer nanocomposite surfaces have not been explored in detail. Additionally, little has been reported for surface properties of melt-blended systems, and most studies have focused on solution-blended systems.

As the size of engineering devices moves towards miniaturization, understanding of surface properties is critical, and control of tribological performance such as friction and wear is of particular importance for devices containing moving parts. Friction is an

aggregate effect arising from physical phenomena such as adhesion, viscosity, capillary forces, surface chemistry, and electrostatic interactions; and any one of these properties can dominate friction performance depending upon the operating conditions. Friction behavior of a multicomponent system is influenced by complex interactions between the components, their geometry and their relative contribution to surface roughness. To develop a model of friction for thin films and systems containing nanoparticles, friction measurements at nanoscale are invaluable in developing a fundamental understanding of these complex interactions. In this study we have utilized nanoprobe lateral force microscopy (LFM) and nanoindentation to investigate the nanoscale surface tribological and mechanical behavior of Octaisobutyl (Oib)-POSS/ Polypropylene (PP) HPNC's.

In the present investigation, nanocomposites of octaisobutyl-POSS (Oib-POSS) with polypropylene were prepared at varying concentrations via melt blending. Complimentary microscopy and spectroscopy techniques were employed to evaluate nanoscale dispersion of POSS particles in thin polymer films. Surface and bulk properties of the HPNC's were analyzed with specific focus on nanotribological behavior. The interplay of POSS molecular geometry, composition and concentration in relation to the nanotribomechanical properties and surface energy was investigated to develop an understanding of the nanotribological behavior of these HPNC's, with the ultimate goal of developing non-halogenated low friction surfaces with controlled POSS dispersion and maintained performance properties in the bulk.

Experimental

Materials

Isotactic Polypropylene (Hival[®] 2420) (PP) was purchased from General Polymers (Cincinnati, OH) and Octaisobutyl POSS (MSO825) (Oib-POSS) was provided by Hybrid Plastics Inc. (Hattiesburg, MS). Oib-POSS was received as a crystalline white powder. All materials were used as received unless mentioned specifically. The chemical structure of the Oib-POSS molecule is shown in Figure III-1.

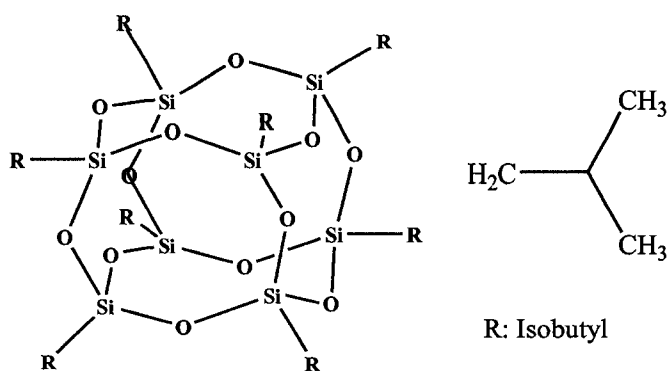


Figure III-1. Schematic structure of Octaisobutyl POSS.

Sample Preparation

Melt blends of Oib-POSS with PP were prepared utilizing a CT-25 co-rotating twin screw extruder (B&P Processing, screw diameter = 25 mm and L:D ratio of 44:1). Blends were prepared at 0, 5 and 10 weight % Oib-POSS in PP. Samples were extruded at 225°C and 300 rpm. To obtain smooth films for evaluation of the surface, samples were prepared by melt pressing the extrudate between two clean silicon wafers. For evaluations of the bulk, samples were prepared by cryomicrotoming pellets at -90°C using a diamond knife.

Atomic Force Microscopy Surface Topography, Friction, and Wear

Atomic force microscopy (AFM) surface topography and relative friction studies were conducted on a MultiMode™ scanning probe microscope from Veeco Instruments, Inc. (Santa Barbara, CA). Probes were purchased from Veeco Probes, (Santa Barbara, CA). A silicon probe with 125µm long silicon cantilever, nominal force constant of 40 N/m and resonance frequency of 275 KHz was used for tapping mode surface topography studies. A triangular silicon nitride (Si₃N₄) probe, with a nominal cantilever spring constant of 0.58 N/m, was used for relative surface friction studies. AFM studies were conducted under ambient conditions in a temperature (27°C) and humidity (40-45%) controlled room. All samples were stored in a humidity controlled chamber and measurements were conducted in the same day to minimize environmental effects. Surface topographies of the melt pressed surfaces and the cryomicrotomed bulk regions were studied on 5µm x 5µm scan areas with an image resolution of 512 x 512 pixels at a scan rate of 1Hz. Multiple areas were imaged and figures show representative morphology. Nanoscale relative surface friction studies were performed via AFM in lateral force mode on 5 µm x 5 µm scan areas. Force-distance curves and friction loops were obtained at different set points to obtain statistical data for analysis. Surface roughness analysis was performed using Nanoscope version 5.30 r2 image analysis software. To verify the reproducibility, two sets of readings were taken for each sample and an average value is reported. The differences between the two readings were less than one percent.

AFM wear testing was performed on melt pressed HPNC's samples on a Multimode AFM in contact mode. The probe used was a steel cantilever mounted with a

diamond tip, having a force constant of 182 N/m and resonant frequency 53 kHz. Deflection sensitivity of the cantilever was 267 nm/V based on its calibration on a sapphire surface. Free air cantilever deflection was set to zero. A $2\mu\text{m} \times 2\mu\text{m}$ wear pattern was created on each sample at a deflection setpoint of 0.5 V and a constant external force of 24 μN . After one complete scan, AFM was switched from contact to tapping mode to image the worn surface. A $10\mu\text{m} \times 10\mu\text{m}$ scan area was selected for imaging wear debris followed by section analysis to compare the depth profiles of samples.

Scanning Electron Microscopy-Energy Dispersive X-Ray (SEM-EDAX)

To qualitatively confirm the presence of POSS molecules on the surface and in the bulk of HPNC's samples, scanning electron microscopy and elemental mapping was performed using an FEI Quanta 200 Scanning Electron Microscope (SEM) in environmental scanning mode, coupled with a Thermo-Noran Vantage light element energy dispersive x-ray detector. Characterization of all the elements except hydrogen was obtained by X-ray spectroscopy under electron flux. The SEM images were obtained at a voltage 20 kV and pressure of 1 torr.

Transmission Electron Microscopy-Energy Dispersive X-Ray (TEM-EDAX)

Bulk morphology of Oib-POSS/PP nanocomposites was investigated using a JOEL-2100 ultra high resolution transmission electron microscope (Joel Ltd., Tokyo, Japan) at an accelerating voltage of 200kV. Ultrathin sections, about 90 nm thick, were prepared by cryoultramicrotoming the samples with a diamond knife using a Leica EM UC6 cryomicrotome at -90°C . Subsequently, the ultrathin sections were collected on a 600 mesh copper grid. Elemental composition of the ultrathin sections was analyzed by

mapping the carbon, oxygen and silicon elements using energy dispersive X-ray analysis. Elemental maps were acquired using EDAX Genesis software.

Attenuated Total Reflectance Fourier Transform Infrared (ATR-FTIR) Spectroscopy

To analyze surface composition of the nanocomposites, Micro ATR-FTIR spectroscopy measurements were conducted on the melt-pressed surfaces using a Bio-Rad FTS-6000 FTIR single-beam spectrometer with 4 cm^{-1} resolution. The surfaces of each specimen were analyzed using a 2 mm germanium (Ge) crystal with a 45° angle maintaining constant contact pressure between the crystal and the specimens. To obtain quantitative surface depth profile, variable angle ATR (VATR) with a Ge and KRS-5 crystal ($52.5 \times 20 \times 3$ mm parallelogram with a face cut angle of 45°) was used. Ratio of relative intensities of polymer and POSS absorbances were taken as measure of relative concentration profile.

Macroscale Friction

Dynamic coefficient of friction (COF) measurements were performed according to ASTM G 99, using a pin-on-disk tribometer (Micro Photonics Inc., PA). Two sets of readings were taken for each film sample ($1'' \times 1''$) inside a controlled humidity chamber at 27°C . Film samples were mounted firmly on a flat metal disc, which was rotated (path radius 3 mm) against a steel ball (3 mm diameter, Small Parts Inc., Miami Lakes, FL) at 20 rpm for 20 min. Relative friction measurements were conducted as a function of relative humidity (15%, 60%, and 90% RH at 3N external load) and external load (3N, 4N, and 5N at 60% RH). In order to verify the transfer of POSS material to the counter surface, steel ball was dipped in CDCl_3 to extract POSS from its surface. Silica NMR was conducted to probe the presence of POSS in the extract.

Nanoindentation Studies

Nanoindentation was performed on the melt pressed film surfaces to determine the nanoscale relative hardness and reduced modulus of the Oib-POSS/PP HPNC's. The Triboindenter (Hysitron, Inc., Minneapolis, MN) was operated with a three-sided diamond (Berkovich type) tip, calibrated on fused silica. Nanoindentation was performed under closed loop with load control using a compliance method in which the force-displacement curves were obtained during loading and unloading cycles. As the indenter presses into the surface, the displacement is recorded continuously as a function of the applied load. A single indent was made on every surface by applying a normal load with a loading rate of $50\mu\text{N}/\text{sec}$. Unloading rate was maintained similar to loading rate and a 5 sec. hold time was provided at the maximum force of $2000\mu\text{N}$. Total cycle time for the load control indentation was 85 sec. Indentation tests were conducted at different regions across the surface to confirm the homogeneity of POSS distribution on the sample surface.

Contact Angle and Surface Energy

Static and dynamic contact angle measurements were conducted using the sessile drop technique by a ramè-hart goniometer coupled with DROPimage[®] data analysis software. Small drops of water ($10\mu\text{l}$) were dropped onto a flat surface and the image of the drop was captured. Contact angle hysteresis was calculated by measuring advancing and receding contact angles using the tilting plate technique. Five measurements were taken and averaged. Surface energy was calculated by measuring the contact angle between the sample surface, deionized water, and diiodomethane (CH_2I_2) as a second test fluid, utilizing the Fowkes²⁷ and Owens-Wendt method.²⁸

Dynamic Mechanical Analysis (DMA)

DMA was used to investigate the thermal transitions, relaxation behavior and dynamic storage modulus of Oib-POSS/PP nanocomposites. Thermal transitions were recorded using a TA Q800 dynamic mechanical analyzer over a temperature range of -50 to 175°C at a heating rate of 2°C/min and an oscillation frequency of 1Hz.

Modulated Differential Scanning Calorimetry (M-DSC)

Modulated DSC, in which a modulation of $\pm 1^\circ\text{C}$ was performed every 60 seconds, was utilized to obtain precise thermal data. A TA Instruments Q Series DSC Q100 was used to determine the melting (T_m) and crystallization temperature (T_c) of the samples. Each sample, approximately 10 mg weight, was analyzed under a nitrogen blanket. Samples were heated initially from -50°C to 250°C at a rate of 10°C per minute in order to erase their thermal history. This heating cycle was followed by cooling the samples from 250°C to -50°C at the rate of 5°C per minute to study their crystallization behavior. Finally, melting behavior was studied by further reheating the samples from -50°C to 250°C at a programmed rate of 10°C per minute.

Results and Discussion

AFM images of the Oib-POSS/PP nanocomposites are shown in Figures III-2 and III-3. Incorporation of POSS in the PP matrix leads to dramatic modification of the polymer surface, as revealed by tapping mode AFM images of the Oib-POSS/PP blends (Figure III). While the surface of the neat PP sample, shown in Fig. III-2A, is smooth with no apparent surface features (root mean square roughness, RMS, of 1.1 nm), the Oib-POSS/PP blends exhibit raised features with increased surface roughness (Fig. III-2B: 5% Oib-POSS blend, RMS = 7.2 nm, Fig. III-2C: 10% Oib-POSS blend, RMS = 12.1 nm). These raised features are attributed to the presence of POSS aggregates, whose presence is further substantiated by EDAX and ATR-FTIR analyses presented later in this section.

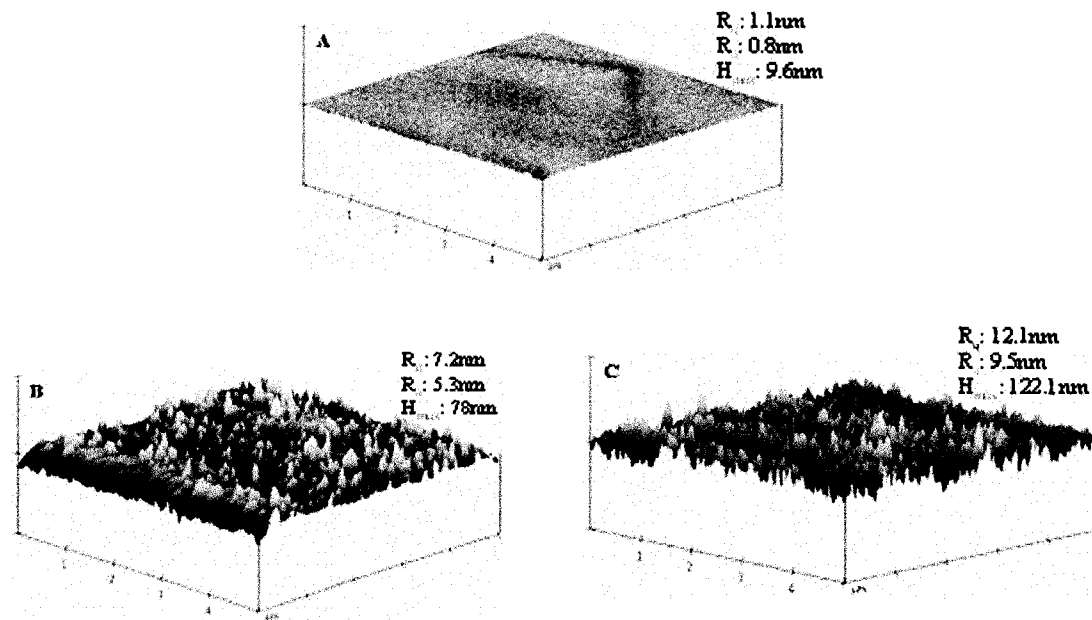


Figure III-2. Three dimensional AFM tapping mode height images and surface roughness analysis of melt pressed (A) Neat PP (B) 5% Oib-POSS/PP (C) 10% Oib-POSS/PP (Z Scale: 150 nm, R_q : Root mean square roughness, R_a : Mean roughness, H_{max} : maximum height).

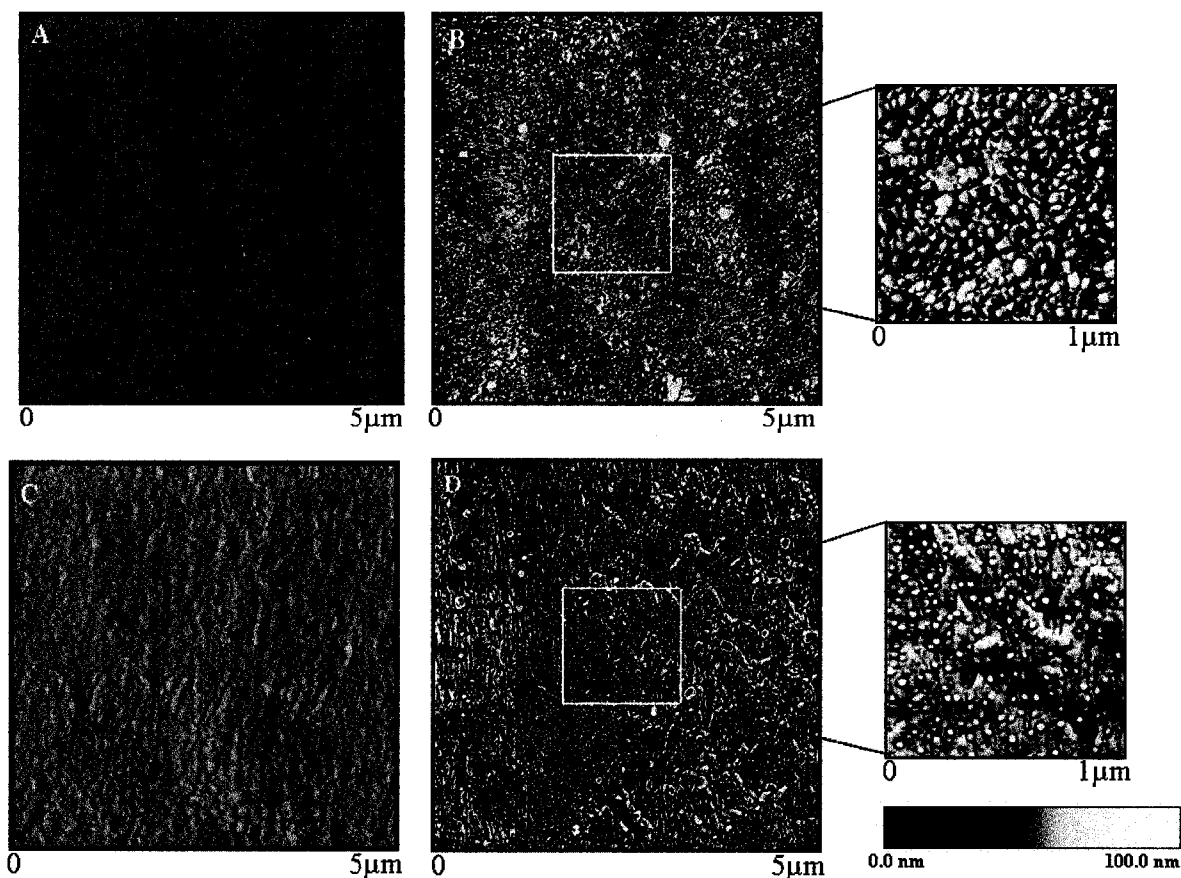


Figure III-3. AFM phase images of melt pressed (A) Neat PP surface (B) 10% Oib-POSS/PP surface, and microtomed (C) Neat PP bulk (D) 10% Oib-POSS/PP bulk.

Similar features are observed in bulk Oib-POSS/PP, which are absent in neat PP samples (Figure III-3). Furthermore, analysis of the morphology of the surface in comparison to that of the bulk indicates that there is preferential segregation of the POSS aggregates to the surface. AFM phase imaging provides insight about the distribution of nanostructured POSS domains based on the differences in localized stiffness and modulus. In Figure III-3 AFM phase images of melt pressed surfaces of neat PP (Fig. III-3A) and the 10% Oib-POSS/PP blend (Fig. III-3B) are presented in comparison to phase images of bulk samples prepared via cryomicrotoming (neat PP bulk in Fig. III-3C, 10% Oib-POSS/PP bulk in Fig. III-3D). The neat PP surfaces are featureless, while the POSS

blends show raised spherical/oblong features that are presumed to arise from the presence of POSS aggregates. Image analysis (Table III-1) indicates that the features have a mean length of 38 nm and mean width of 21 nm on the surface, while the features in the bulk show a mean length of 61 nm and mean width of 23 nm. The greater elongation and the greater variability of particle size in the bulk may be a result of microtoming effects.

While these oblong features are present both on the surface and in the bulk of the melt-pressed sample, the features are more widely distributed and lower in concentration in the bulk microtomed sample, indicating preferential segregation to the surface of the composite. As the POSS aggregates are of the size of several to less than one hundred nanometers, we will refer to the systems as nanocomposites in the remainder of the discussion.

Table III-1. AFM Particle Size Analysis of Melt Pressed 10wt.% Oib-POSS/PP Surface and Bulk Area.

| Dimension | Mean | Minimum | Maximum | Sigma |
|----------------|------|---------|---------|-------|
| <u>Surface</u> | | | | |
| Length (nm) | 37.9 | 13.8 | 162.0 | 22.8 |
| Width (nm) | 20.8 | 13.8 | 86.5 | 9.3 |
| <u>Bulk</u> | | | | |
| Length (nm) | 60.9 | 13.8 | 774.0 | 70.8 |
| Width (nm) | 22.8 | 13.8 | 210.0 | 19.5 |

Similar oblong features are observed in SEM images of Oib-POSS/PP nanocomposites, and SEM/EDAX analysis provides further evidence of POSS enrichment at the surface in the nanocomposites. SEM images with EDAX evaluation of melt-pressed surfaces and microtomed samples of the bulk are shown in Figure III-4. As observed in the AFM analysis, the PP melt-pressed surface appears smooth in the SEM image (Figure III-4A), while the 10% Oib-POSS/PP nanocomposite exhibits raised

spherical features covering the surface. The POSS molecules appear to form a network assembly with interconnected spherical beads on the surface. We attribute this network morphology to the POSS intermolecular attractions.

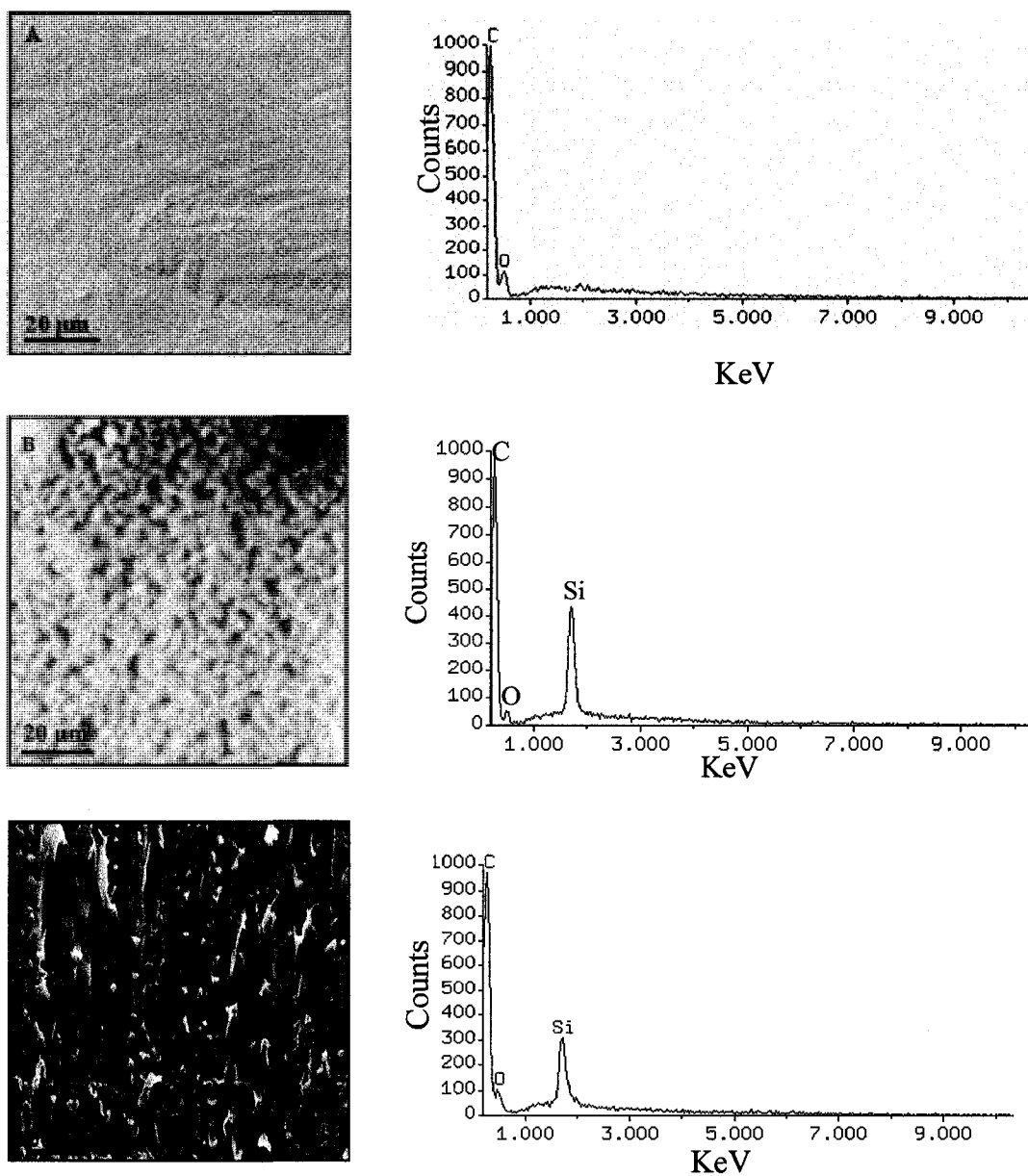


Figure III- 4. SEM/EDAX mapping of melt pressed (A) Neat PP surface (B) 10% Oib-POSS/PP Surface and microtomed (C) 10% Oib-POSS/PP Bulk Nanocomposite.

Elemental mapping via EDAX provides further insight into the chemical identity of these spherical features present on the surface and in the bulk. This analysis reveals a strong signal attributed to silicon for the POSS-containing samples that is absent in the neat PP sample. For the microtomed bulk sample, the spherical features are more widely distributed and at lower concentration, with concomitant reduction in the silicon signal in the EDAX analysis. Consistent with the information obtained from AFM phase imaging, SEM micrographs and differences in the silicon peak intensity observed in the EDAX analysis indicate that POSS molecules have an affinity for the surface. In recognition of the fact that EDAX probes the sample from the surface to several microns depth, complimentary tools such as ATR-FTIR were utilized to validate these findings.

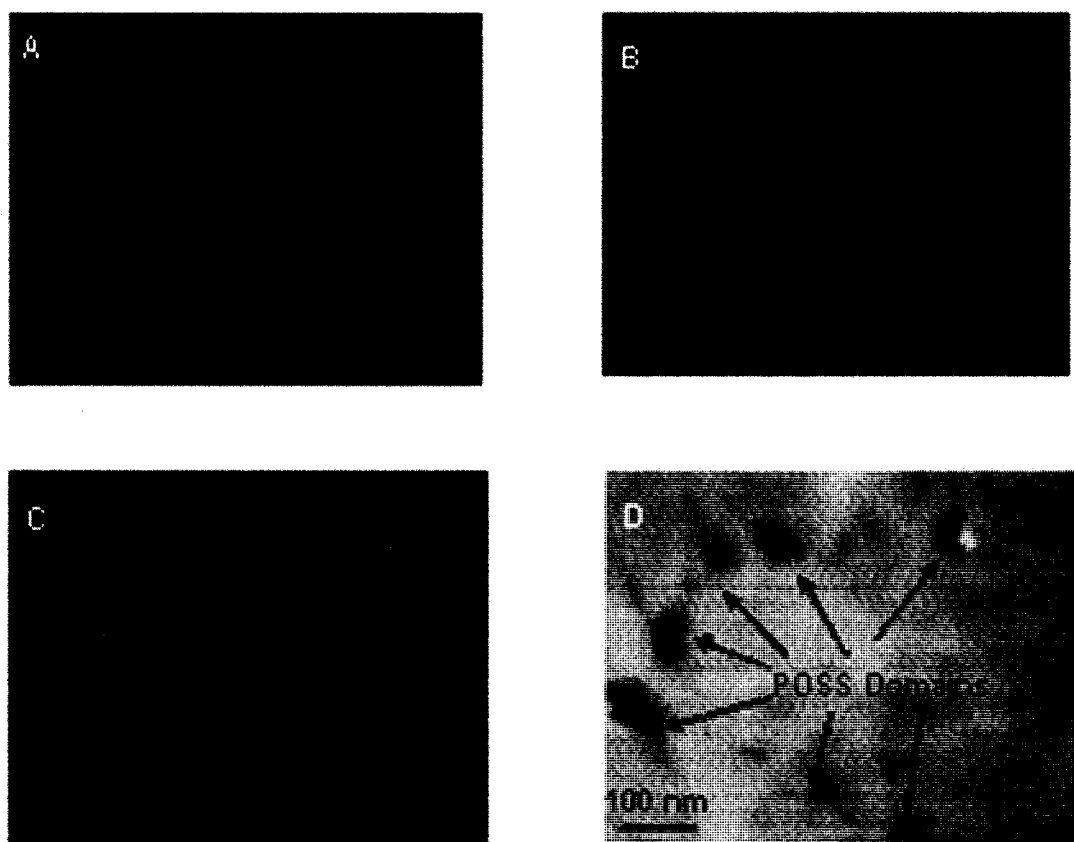


Figure III-5. TEM-EDAX elemental surface mapping of a microtomed 10% Oib-POSS/PP sample (A) Carbon (B) Oxygen (C) Silicon (D) Silicon Overlap.

TEM imaging coupled with EDAX analysis of the POSS nanocomposites reveals further information about the POSS dispersion in the nanocomposite. Widely dispersed oblong particles ranging from 10 to 100 nm in length are observed in a microtomed sample of the 10% Oib-POSS/PP nanocomposite (Figure III-5). Elemental mapping reveals that the areas where the particles appear are rich in silicon and oxygen, and poor in carbon. Areas away from the particles exhibit high carbon concentration with low silicon and oxygen concentrations. These findings provide further confirmation that the observed particles are indeed POSS aggregates.

ATR-FTIR analysis provides further evidence of POSS surface enrichment (Figure III-6). For reference purposes, IR spectra of Oib-POSS and neat PP are shown in traces A and B respectively.

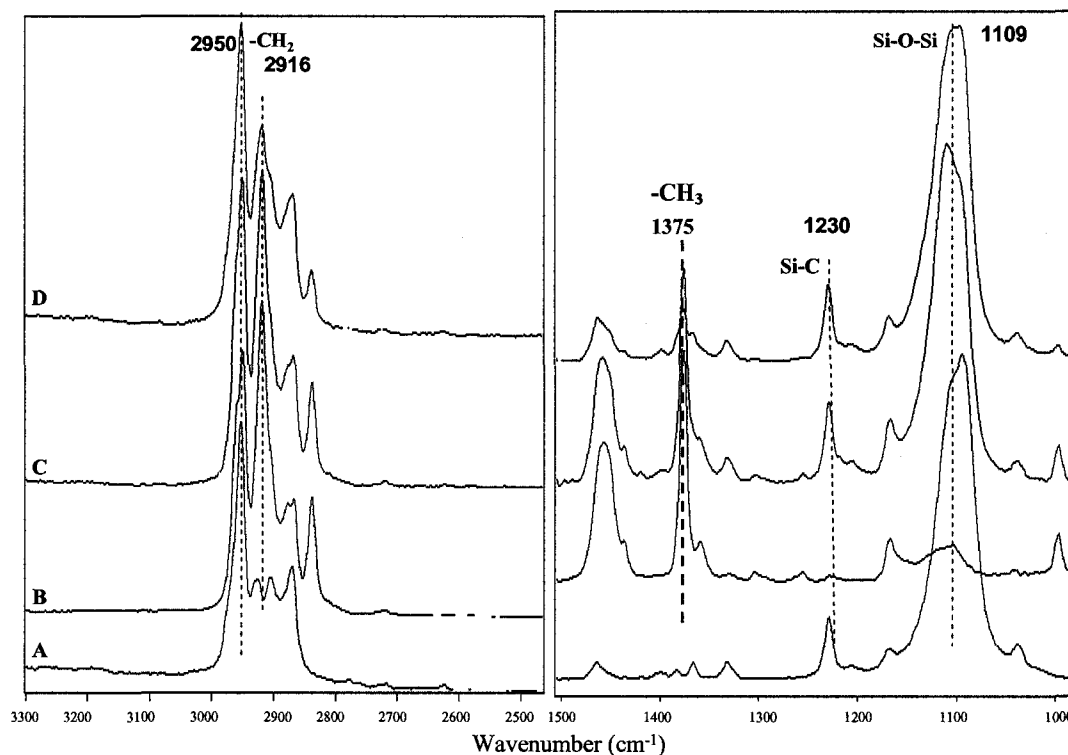


Figure III-6. ATR-FTIR spectra of (A) Oib-POSS (B) Neat PP (C) 5% Oib-POSS/PP (D) 10% Oib-POSS/PP.

Characteristic absorbances are observed in the pure Oib-POSS trace at 1109 cm^{-1} , attributed to Si-O-Si stretching vibrations, and at 1230 cm^{-1} , corresponding to $-\text{CH}_2$ symmetric stretching vibrations and Si-C symmetric vibrations. These absorbances are absent in the neat PP spectrum. The characteristic 1109 cm^{-1} and 1230 cm^{-1} absorbances are observed in the 5% Oib-POSS/PP (Trace C) and 10% Oib-POSS/PP composites, with strong intensity signals indicating the presence of POSS on the surface. Absorbance at 1375 cm^{-1} is attributed to $-\text{CH}_3$ vibrations in PP. Absorbances at 2916 cm^{-1} to 2950 cm^{-1} corresponding to $-\text{CH}_2$ asymmetric stretching vibrations are observed in all samples, as would be expected based on the structure of the materials.^{29,30}

Preferential surface migration of Oib-POSS in PP matrix was further confirmed with variable angle ATR depth profile analysis. As discussed earlier, absorbance at 1375 cm^{-1} (A) corresponds to PP whereas absorbance at 1109 cm^{-1} (B) is attributed to POSS. Depth of penetration (D) of the IR radiation at different angles was calculated using equation 1.^{29,31}

$$D = \lambda / 2\pi n_1 [\sin^2\theta - (n_2/n_1)^2]^{1/2} \quad (1)$$

Where λ is the wavelength of the radiation in microns; n_1 and n_2 are the refractive indices of the ATR crystal and polymer film respectively, and θ is the angle of incidence of the IR beam on the ATR crystal. Figure III-7 shows the VATR spectra for HPNC at different penetration depths. This spectrum clearly shows that the ratio of intensity of POSS (I_B) and PP (I_A) absorbances decrease with increase in penetration depth indicating preferential surface migration of Oib-POSS in PP. Figure III-8 shows a plot of I_B/I_A as a function of penetration depth. This figure shows that relative POSS concentration is higher in the region 500 nm from the surface after which it shows a sharp decline indicating lower amount of POSS at higher penetration depths.

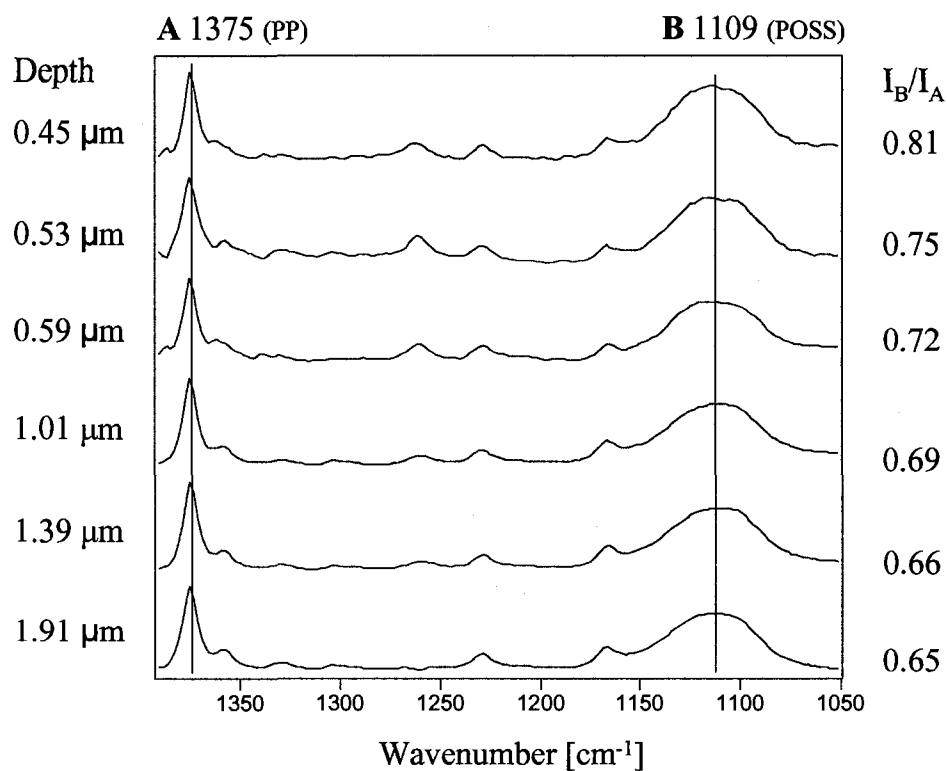


Figure III-7. Variable angle ATR-FTIR spectra of Oib-POSS/PP HPNC.

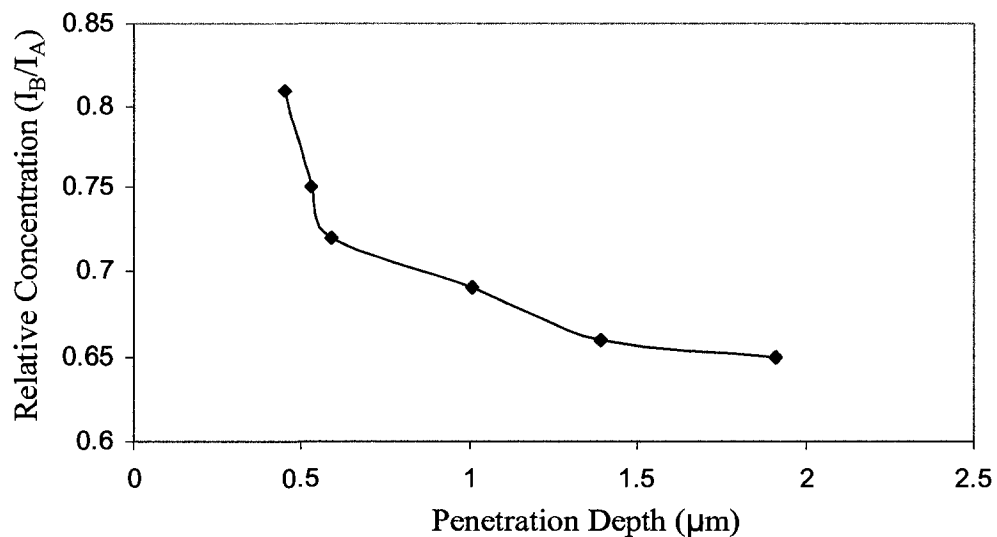


Figure III-8. Relative concentration as a function of depth in Oib-POSS/PP HPNC.

In parallel to the morphological and compositional changes observed for the POSS/polymer nanocomposites, dramatic changes in surface mechanical and physical

properties were observed. Lateral force microscopy (LFM) was employed to evaluate nanoscale relative friction and adhesion of the nanocomposite materials. As described in detail in the introduction section, the probe is scanned across the surface and the frictional force it experiences in contact with the surface is measured in LFM. By evaluating the frictional force as a function of the applied normal force, a relative coefficient of friction is obtained. Real time friction loops for neat PP and Oib-POSS/PP nanocomposites at equivalent loading force are shown in Figure III-9. The distance between the extending and retracting friction curves is a qualitative measure of the friction between the probe and the surface.³² Surface friction measurements were conducted at a fixed scan rate of 1 Hz, consistent with methods commonly reported in the literature for polymer samples.^{30,36} POSS nanocomposites exhibit reduced relative friction in comparison to the neat polymer, with friction decreasing as a function of increasing POSS concentration.

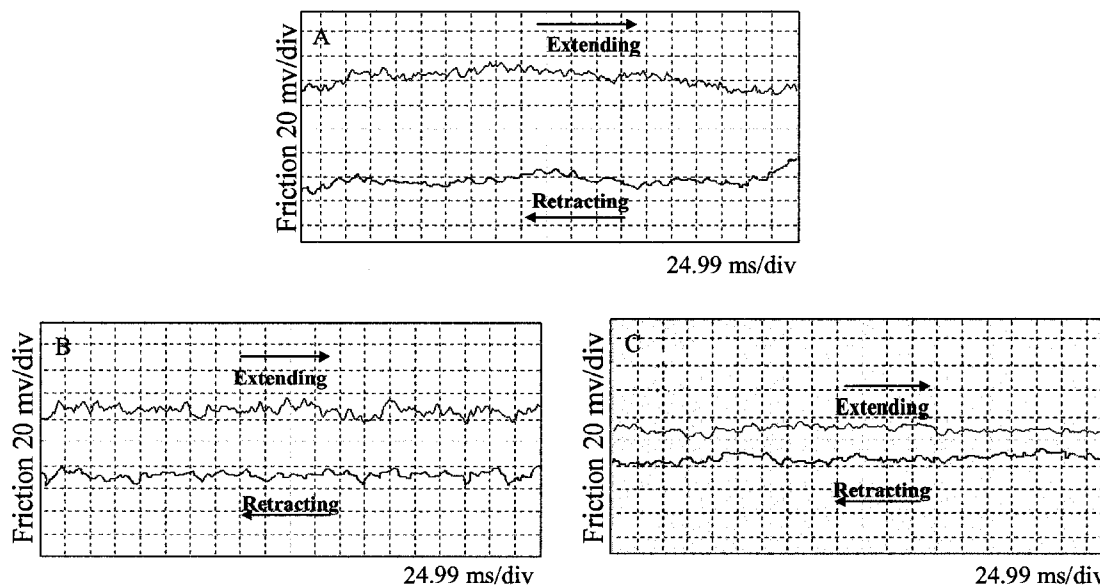


Figure III-9. Friction loops obtained via lateral force microscopy at applied normal force of 28nN for (A) Neat PP (B) 5% Oib-POSS/PP (C) 10% Oib-POSS/PP.

In Figure III-10 plots of friction force as a function of applied normal force are shown, and high correlation coefficients are achieved for all systems. Relative coefficient of friction decreases with increasing POSS concentration, from a value of 0.17 for neat PP to 0.07 for the 10% Oib-POSS/PP nanocomposite (The LFM COF of Teflon is reported as 0.03.³³). Note that relative values of COF are reported, using the nominal force constant for the probe as described in the experimental section. Although this will not provide absolute values of force of adhesion and friction force, comparison of the relative values is valid as the same cantilever is employed to obtain the measurements.³⁴ The samples were imaged in tapping mode after LFM measurements to ensure that surfaces were not damaged during the friction studies, and no artifacts were observed on the images. Additionally, AFM probes were imaged via SEM after surface friction measurements to ensure that there were no visible changes to the geometry of the probe during scanning.

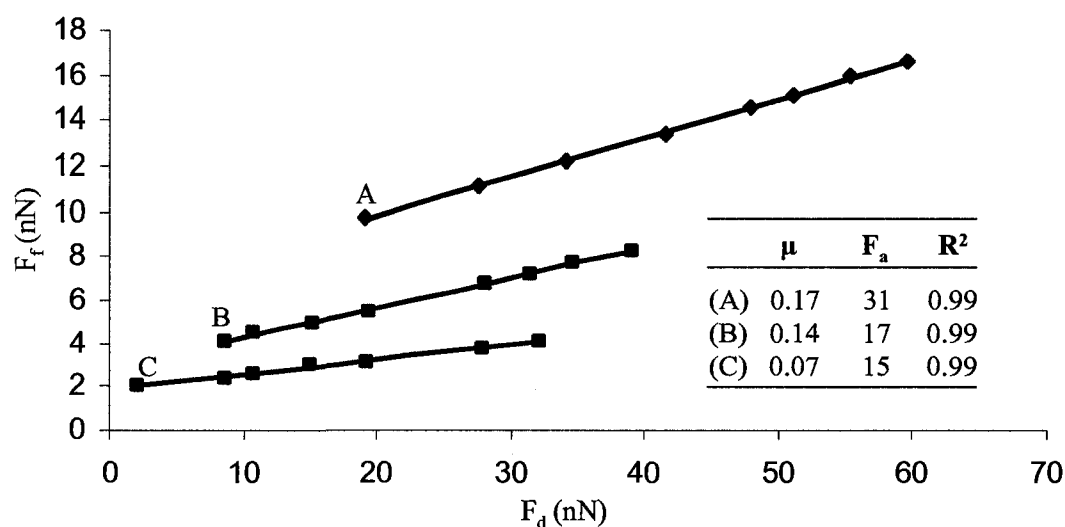


Figure III-10. Friction force as a function of applied normal force measured via LFM. COF (μ) is obtained from the slope, adhesive force (F_a) is obtained from the intercept. (A) Neat PP (B) 5% Oib-POSS/PP (C) 10% Oib-POSS/PP.

Sliding friction is determined by multiple structural and mechanical factors, including adhesion, roughness, plowing, capillary forces, heterogeneity on the surface, shear stress, surface hardness and true area of contact.^{35,36,37} We attribute the observed reduction in nanoscale surface friction for the POSS nanocomposites to the interplay of a number of these factors, particularly increase in surface hardness and modulus, discussed in later sections. Another important parameter is the observed increase in surface roughness for the nanocomposite surfaces. Increase in the surface roughness reduces the real area of contact between the AFM probe and the surface, thereby reducing the observed friction. Some authors have suggested a self-lubricating “nano ball bearing” mechanism for low friction nano-materials including POSS,³⁸ diamond nanoparticles³⁹ and fullerene-like inorganic nanoparticles.⁴⁰

Nanoscale friction characteristics are also significantly influenced by the magnitude of the adhesive force between the AFM probe and the surface. The relative force of adhesion (F_a) between the probe and the surface decreases for the POSS-containing nanocomposites in comparison to the neat PP (Figure III-8). This reduced adhesion may in part explain the reduced friction for the POSS nanocomposites. The adhesive force between the hydrophobic PP and the relatively hydrophilic AFM probe is small. Incorporation of the hydrophobic Oib-POSS nanoparticles increases the surface hydrophobicity and further reduces the adhesive interaction between the surface and the AFM probe, with a 50% reduction in measured relative F_a for the 10% Oib-POSS/PP nanocomposite. The reduction in relative adhesive force is indicative of reduced sticking and sliding friction between the surface and the AFM probe.

Similar trends were observed in macroscale friction measurements. Variation in the relative surface friction of HPNC's as a function of POSS concentration at 15%, 60%, and 90% relative humidity's and an external load of 3 N is shown in Figure III-11. HPNC's exhibit lower relative friction compared to neat PP at all three humidity levels (dry to highly humid). An average 21%-71% reduction in relative surface friction was observed by the incorporation of 5% and 10% Oib-POSS in PP respectively. This effect is attributed to the uniform presence of spherical nanoscopic POSS molecules on the film surface which exhibit lower friction levels than PP. Additionally, lower friction values were obtained with increasing humidity. For example, the 10% Oib-POSS/PP sample shows increase in surface friction reduction from 65% to 77% as humidity changes from 15% to 90%. This effect can be explained in part due to the presence of a thin moisture layer on the film surface, which acts as a lubricant, thereby reducing relative surface friction.

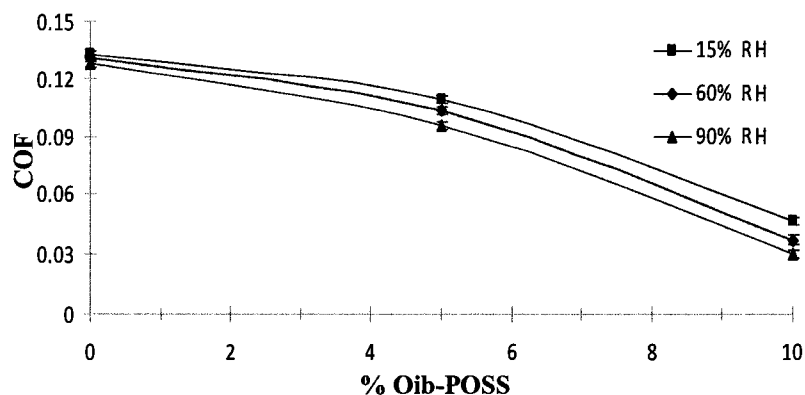


Figure III-11. COF as a function of POSS concentration at different humidity's.

Variation in the relative surface friction of HPNC's in relation to the POSS concentration at different external loads of 3N, 4N, and 5N at 60% relative humidity is shown in Figure III-12. All samples show increase in surface friction with increase in

external applied load. However, Oib-POSS/PP HPNC's exhibit lower relative friction compared to neat PP at all the three loads. This result is attributed, in part, to improved wear or scratch resistance of HPNC's surface compared to neat PP which was further confirmed by AFM wear tests. Additionally, silicon NMR conducted on the CDCl_3 extract from steel ball used in friction test does not show any characteristic silicon peaks indicating no transfer of POSS from HPNC surface to counter steel ball surface (at least within the NMR detection levels).

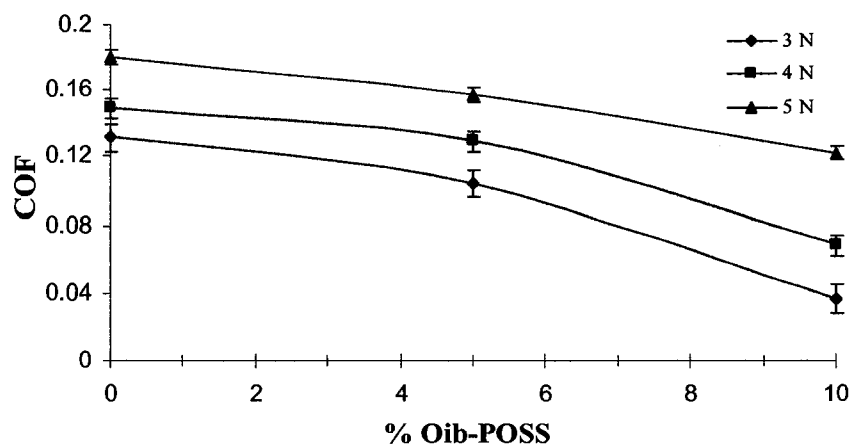


Figure III-12. COF as a function of POSS concentration at different loads.

Besides surface friction, POSS/PP HPNC's exhibit significantly improved wear resistance. Figure III-13 (A) and (B) shows the scratched PP and Oib-POSS/PP surfaces with wear debris on it along with their section analysis. Under similar external load and scan parameters neat PP surface shows more wear debris on the surface compared to HPNC surface indicating higher scratch resistance of HPNC surface. Less debris on the HPNC surface also contributes towards low surface friction by minimizing damage to the surface by wear particles. In addition, section analysis of both samples clearly shows the difference between the scratch depths of two samples. HPNC surface exhibit 65% less

scratch depth compared to neat PP. This result is attributed, in part, to the presence of rigid inorganic POSS cages on the surface which was earlier confirmed via multiple microscopic and spectroscopic techniques.

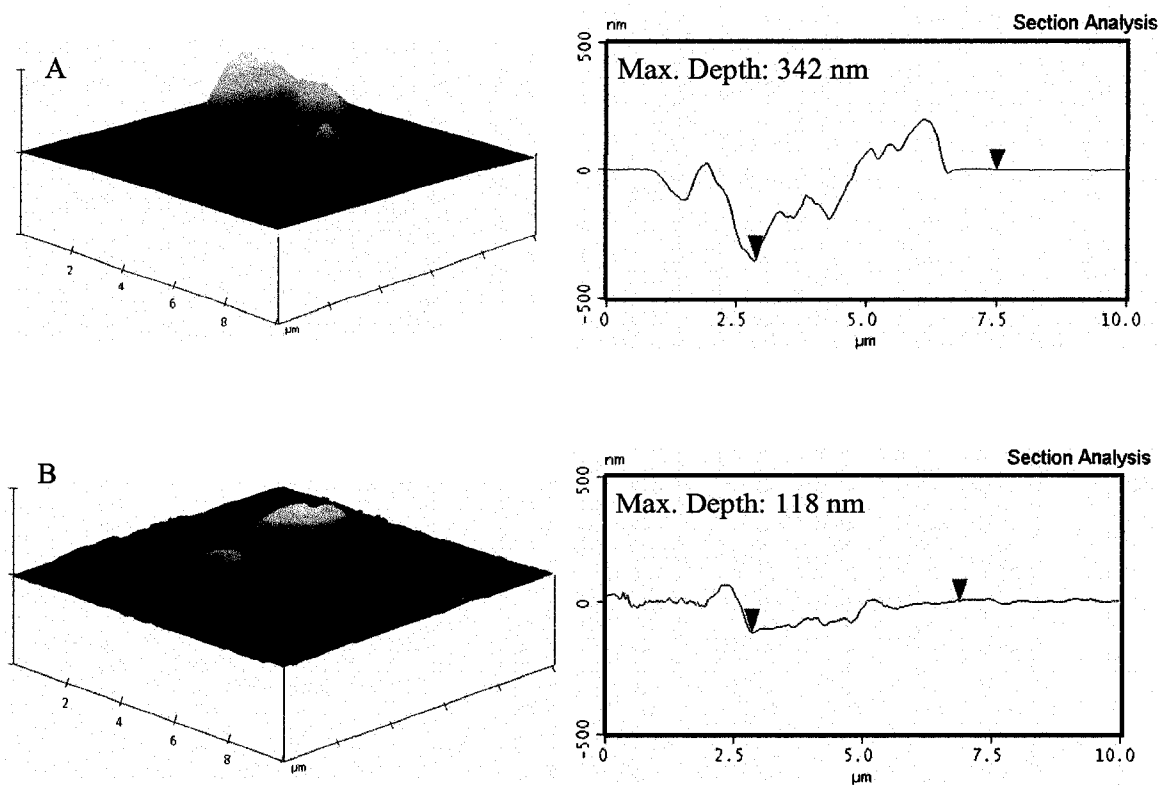


Figure III-13. AFM scratch imaging and section analysis (A) Neat PP (B) 10% Oib-POSS/PP.

Surface wear and friction behavior depends not only on the chemical nature and the adhesion between the surfaces in contact, but also on the mechanical properties, such as the relative hardness and modulus of the materials. According to contact mechanics theories, surface friction is directly proportional to the shear stress and the true area of contact.^{35,36} Study of the surface nanomechanical properties of the Oib-POSS/PP

nanocomposites provides mechanistic insights for the improved friction properties of these HPNC's.

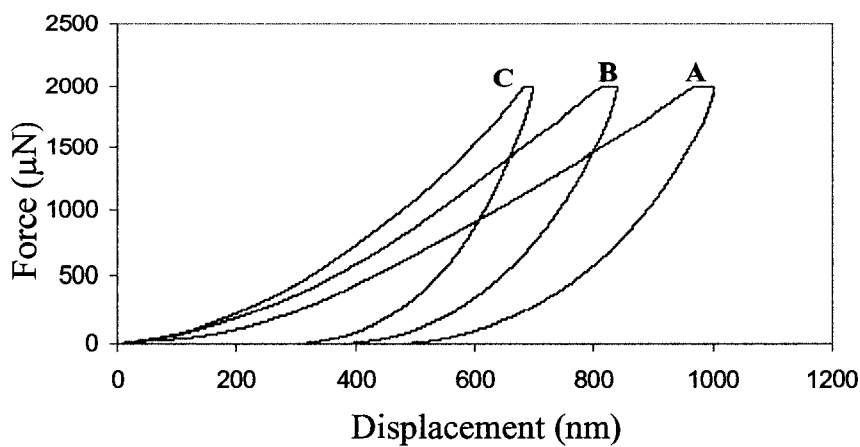


Figure III-14. Nanoindentation force as a function of displacement measured using the Hysitron. (A) Neat PP (B) 5% Oib-POSS/PP (C) 10% Oib-POSS/PP.

Nanoindentation evaluation revealed increased surface hardness and modulus for the POSS nanocomposites. Force/displacement curves for the materials are shown in Figure III-14, while maximum penetration, reduced modulus and hardness values are given in Table III-2. Surface hardness and reduced modulus increase as a function of increasing POSS concentration, while maximum penetration depth decreases. At 5 wt.% POSS concentration, surface hardness and modulus increase by 40%, and further increase by 100% at 10 wt.% POSS concentration. Thus, incorporation of low percentages of Oib-POSS results in dramatic surface hardening of the PP nanocomposite. POSS nanoparticles, due to their robust inorganic silicon oxygen structure, provide nanoscale reinforcement to the PP matrix. These findings can be further correlated to the reduced surface friction exhibited by the POSS HPNC's in LFM studies. Surface friction is related to the hardness of the surface and the ability to resist formation of wear particles. Due to their high surface hardness and modulus, these HPNC's exhibit greater resistance

to plastic deformation, scratching, and wear compared to the neat PP matrix. These combined mechanical property factors help to explain the observed low friction coefficients for the POSS nanocomposites.

Table III-2. Maximum Penetration Depth, Reduced Modulus and Hardness of Oib-POSS/PP HPNC's.

| Sample | Max. Penetration (nm) | Reduced modulus (GPa) | Hardness (MPa) |
|------------------|--------------------------|--------------------------|-------------------|
| Neat PP | 1000 | 1.9 | 109 |
| PP+ 5% Oib-POSS | 840 | 2.7 | 157 |
| PP+ 10% Oib-POSS | 699 | 3.9 | 225 |

Surface modification as a function of POSS nanoparticle concentration was also observed in contact angle studies. Contact angle measurement provides insight into the hydrophobicity as well as the surface energy of the film. Surfaces with water contact angle less than 90° are considered wetting whereas those with water contact angle greater than 90° are considered nonwetting.⁴¹ When a liquid drop is placed on a flat and smooth surface, it spreads over the surface until the mechanical and thermodynamic forces are balanced. Work of adhesion (W_A) is expressed by Young's equation (2).

$$W_A = \gamma_{LV} (1 + \cos\theta) \quad (2)$$

Where γ_{LV} , γ_{SV} are liquid-vapor, solid-vapor interfacial tension respectively and θ is contact angle. Work of adhesion is used to calculate the polar (γ_{SV}^p) and dispersive components (γ_{SV}^d) of surface energy using Fowkes²⁷ and Owens-Wendt²⁸ geometric mean formula (Equation 3).

$$W_A = 2 [\{\gamma_{LV}^d * \gamma_{SV}^d\}^{1/2} + \{\gamma_{LV}^p * \gamma_{SV}^p\}^{1/2}] \quad (3)$$

Static contact angles obtained with water and diiodomethane, along with surface energies and polar and dispersive components calculated by the Owens-Wendt method,²⁸ are given in Table III-3. Surface hydrophobicity increases and surface energy decreases with increasing POSS concentration. Incorporation of 10% Oib-POSS yields a 43% reduction in the surface energy, to a value of 24 mN/m, and a 27% increase in the water contact angle, to 99°, approaching reported values of 16 mN/m surface energy and 120° contact angle for Teflon.⁴²

Table III-3. Static Contact Angle and Surface Energy of Oib-POSS/PP HPNC's.

| Sample | Contact angle (°) | | Surface Energy (γ) (mN/m) | Polar (γ^p) (mN/m) | Dispersive (γ^d) (mN/m) |
|------------------|-------------------|---------------|---------------------------------------|--------------------------------|-------------------------------------|
| | Water | Diiodomethane | | | |
| Neat PP | 78.1 | 43.3 | 42.2 | 4.1 | 38.1 |
| PP+ 5% Oib-POSS | 89.0 | 51.6 | 35.1 | 2.0 | 33.1 |
| PP+ 10% Oib-POSS | 99.0 | 69.7 | 24.2 | 1.4 | 22.8 |

Increase in the water contact angle demonstrates the hydrophobic nature of the Oib-POSS/PP nanocomposite surface. This can be explained in part by the cumulative effect of the eight hydrophobic isobutyl groups attached to the corner silicon atoms of the POSS cage. The effect is pronounced due to the higher concentration of Oib-POSS moieties on the film surface. Increments in surface hydrophobicity may also be related to the surface roughness,^{43, 44} which was observed by AFM roughness analysis to increase with increasing POSS concentration. The ultra low friction coefficients observed for these materials may also be related to their low surface energy. Low surface energy of POSS nanoparticles causes them to preferentially migrate towards the surface. This factor coupled with weak interactions between the Oib-POSS and the PP matrix partly explains the observed gradient in POSS distribution from bulk to the surface. These findings are

consistent with previously reported studies showing increased surface hydrophobicity for other POSS/polymer systems and POSS molecules with fluorinated alkyl chains attached to the POSS cage.^{12, 21-24}

Surface dynamics were further studied via dynamic water contact angle analysis. The advancing (θ_a) and receding (θ_r) water contact angles were measured and their difference, the contact angle hysteresis (θ_h), was calculated (Table III-4). Contact angle hysteresis increases with increasing POSS incorporation. Hysteresis is influenced by many factors, including the surface roughness, chemical heterogeneity of the surface, presence of low molecular weight species, and molecular orientation.⁴⁵ In a multiphase system advancing contact angle is more sensitive to the low surface energy or hydrophobic domains whereas receding contact angle is more sensitive to the high surface energy or hydrophilic domains.⁴⁶ We attribute the increased hysteresis in the POSS containing systems to the surface roughness as well as the chemical heterogeneity imparted by the enrichment of Oib-POSS nanoparticles on the PP surface. These factors coupled with the low surface energy characteristic of Oib-POSS, which promotes its migration towards the surface, explains the hysteresis behavior exhibited by Oib-POSS/PP nanocomposites.

Table III-4. Advancing (θ_a), Receding Water Contact Angle (θ_r) and Hysteresis (θ_h) of Oib-POSS/PP HPNC's.

| Sample | θ_a (°) | θ_r (°) | θ_h (°) |
|------------------|----------------|----------------|----------------|
| Neat PP | 77.3 | 72.9 | 4.4 |
| PP+ 5% Oib-POSS | 86.3 | 78.2 | 8.1 |
| PP+ 10% Oib-POSS | 96.7 | 86.1 | 10.6 |

While microscopy, spectroscopy, nanotribology, nanomechanical and contact angle analyses all indicate dramatic modification of surface properties for these nanocomposites, bulk properties are only minimally affected by incorporation of POSS in the PP matrix. DSC analysis showed only minimal changes in T_c and T_m for POSS nanocomposites in comparison to neat PP, with a two degree reduction in the thermal transition temperatures for 10% incorporation of Oib-POSS (Table III-5).

Table III-5. DSC Crystallization and Melting Temperatures of Oib-POSS/PP HPNC's.

| Sample | T_c ($^{\circ}\text{C}$) | T_m ($^{\circ}\text{C}$) |
|------------------|------------------------------|------------------------------|
| Neat PP | 115 | 167 |
| PP+ 5% Oib-POSS | 114 | 166 |
| PP+ 10% Oib-POSS | 113 | 165 |

Similarly, DMA evaluation showed minimal changes in thermomechanical behavior. Loss factor ($\tan\delta$) is shown in Figure III-15. Two relaxation processes are observed, the β -transition at low temperature (-10°C to 35°C) and the α -transition at higher temperature (50°C to 140°C). The β -transition is generally attributed to the glass transition temperature, while the α -relaxation process is associated with the relaxation of restricted amorphous chains in the crystalline phase of the polymer.⁴⁷ Incorporation of POSS leads to a broadening of the β -transition peak and a small reduction in the calculated transition temperature from 15°C for neat PP to 12°C for 10% Oib-POSS/PP. The α -transition peak, on the other hand, is sharper for the POSS-containing nanocomposites and the transition temperature increases slightly from 81°C for the neat PP to 85°C for 10% Oib-POSS/PP.

Storage modulus obtained via DMA is shown in Figure III-16. A slight increase in the storage modulus of the nanocomposites is observed in comparison to that of the neat PP. An approximate 10% increase in storage modulus is observed in the glassy regime for the 10% Oib-POSS/PP composite, while the observed increase in reduced modulus of the surface measured by nanoindentation was 100% for the same HPNC (Table III-2).

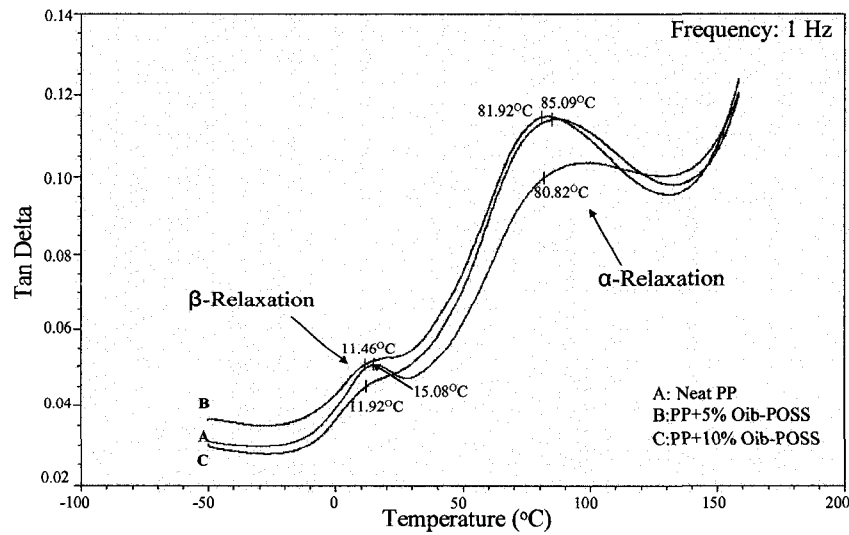


Figure III-15. DMA thermograms of Oib-POSS/PP nanocomposites.

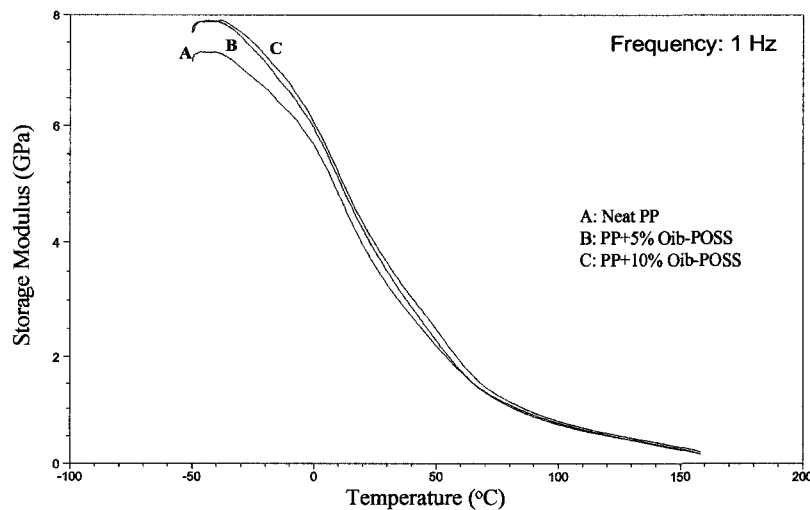


Figure III-16. DMA storage modulus of Oib-POSS/PP nanocomposites.

These findings again illustrate the dramatic effect of surface segregation of the Oib-POSS in the PP matrix. Similar preferential migration is reported for incompatible polymer blends.^{48,49,50,51} The mechanism of self-stratification for incompatible blends can be explained on the basis of the degree of incompatibility between the two phases and surface energy.^{52,53,54} In principle, a similar mechanism of surface segregation is expected for the Oib-POSS/PP blend. POSS moieties preferentially segregate towards the film-air surface as a consequence of the strong thermodynamic driving force to minimize the surface energy. The nanoscale size of the POSS molecules, as well as the degree of control and opportunity to tune the interactions through substituents on the POSS cage, differentiate these materials from conventional additives.

In the present study, melt mixing of a commercial POSS molecule in a commercial PP matrix resulted in nanocomposites displaying dramatic increase in surface hardness and modulus, with parallel increase in hydrophobicity, decrease in surface energy and decrease in measured coefficient of friction. In fact, measured friction, hydrophobicity and surface energy levels approach that of Teflon, in a completely non-halogen system. Bulk properties, on the other hand, were minimally affected. Thus findings indicate that the incorporation of a small amount of POSS of the correct composition allows desired modification of surface properties, without dramatic alteration of bulk polymer performance. Conversely, altering the chemical composition of the POSS substituents and adjusting processing parameters will provide further modification of bulk properties of the nanocomposite.

Overall dispersion and domain size of POSS in the polymer matrix is a function of various inter- and intramolecular forces acting between POSS-POSS moieties as well

as between POSS and the polymer matrix. Dispersion and compatibility of POSS in the polymer matrix can be controlled by the proper selection of organic (R) groups attached to the corner silicon atom. Furthermore, various processing parameters including shear forces and temperature profile during the melt extrusion process also play crucial roles in improving dispersion of POSS particles in the polymer matrix. In the present system, octaisobutyl substituted POSS demonstrates intermolecular forces that result in small aggregates, while providing enough compatibility with the PP matrix to generate well-dispersed nanoparticle aggregates in the range of 10 – 100 nm, schematically illustrated in Figure III-17.

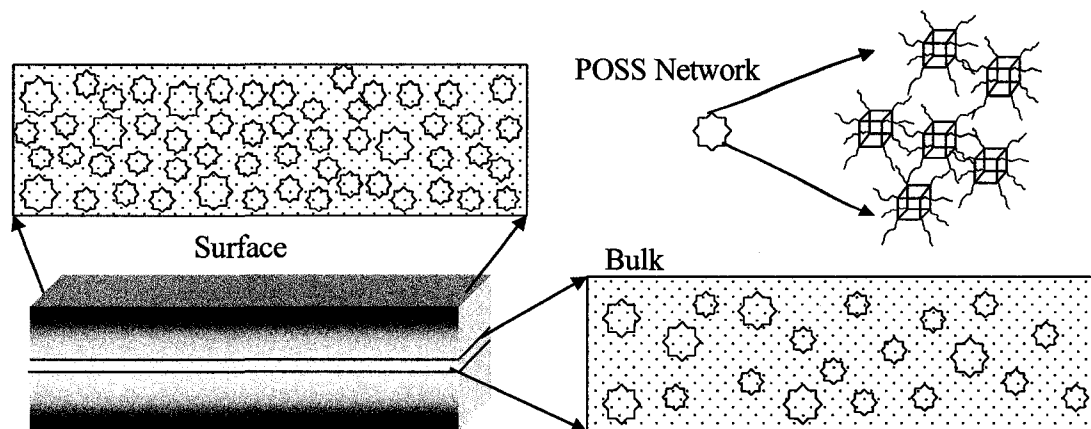


Figure III-17. Schematic representation of bulk vs. surface distribution of POSS nanoparticles in Oib-POSS/PP nanocomposite.

As observed from the microscopic studies, this schematic represents the differences in the POSS distribution and aggregation in bulk vs. surface, thereby manifesting POSS concentration gradient between the bulk and surface. Additionally, the hydrophobicity and low surface energy characteristics of the POSS aggregates drive their segregation towards the surface of the nanocomposite. This research work

contributes to the existing understanding of surface properties of POSS/polymer HPNC's through correlation of tribological and nanomechanical behavior with POSS structure, composition and dispersion behavior. These findings to date indicate that POSS gradient concentration can be precisely controlled through correct control of the POSS chemical structure, polymer matrix and melt processing conditions, to produce nanocomposites in a cost effective process with desired surface and bulk properties for a wide range of important technical applications.

Conclusions

POSS/polypropylene hybrid polymer nanocomposites were successfully prepared via high shear melt mixing and their bulk and surface properties investigated. POSS aggregates ranging in size from 10 to 100 nm were observed dispersed in the PP matrix via AFM, SEM/EDAX and TEM/EDAX analysis. Dramatic modification of surface properties was demonstrated. Incorporation of 10% Oib-POSS yielded a 60% reduction in relative coefficient of friction, from 0.17 to 0.07, a doubling of hardness (109 MPa to 225 MPa) and reduced modulus (1.9 GPa to 3.9 GPa) measured by nanoindentation, and an increase in water contact angle from 78° to 99°. In addition, HPNC surfaces also exhibit significantly improved scratch and wear resistance. Bulk property evaluations, on the other hand, showed only minimal changes on incorporation of POSS, with a 10% increase in modulus measured by DMA for 10% POSS/PP nanocomposites. Combined microscopy and spectroscopy analysis demonstrated preferential segregation of the POSS aggregates to the surface in comparison to the bulk region. The POSS concentration gradient helps explain observed differences in surface and bulk properties of the nanocomposites.

The ultra low nanoscale friction demonstrated by the POSS nanocomposites is a function of both the structural features of the Oib-POSS nanoparticles and the surface nanomechanical properties. The low friction is attributed to the interplay of a number of factors, with the enhanced surface hardness and modulus reducing surface friction by providing resistance to plastic deformation, surface damage and production of wear particles. Further, the increased surface roughness, resulting in reduced contact area between the AFM probe and the surface, in combination with the demonstrated high

hydrophobicity and reduced adhesion contribute significantly towards reducing surface friction. The enhanced tribological performance of these materials, combined with their high surface hardness and hydrophobicity indicate their potential utility for applications such as micro/nanoelectronic devices requiring ultra low friction and wear performance. Precise control of surface properties is indicated through optimization of POSS structure and POSS/polymer interactions.

Acknowledgements

This work was supported primarily by the STTR program of the National Science Foundation under Award Number OII-0539295. This work was also supported by the major research instrumentation program of the National Science Foundation under Award Numbers MRI0421406, DMR0421403 and DMR0215873.

References

-
- ¹ Lichtenhan, J. D. *Comments Inorg Chem* **1995**, *17*, 115.
- ² Shockey, E. G.; Bolf, A. G.; Jones, P. F.; Schwab, J. J.; Chaffee, K. P.; Haddad, T. S.; Lichtenhan, J. D. *Appl Organomet Chem* **1999**, *13*, 311.
- ³ Zheng, L.; Farris, R. J.; Coughlin, E. B. *Macromolecules* **2001**, *34*, 8034.
- ⁴ Romo-Urbe, A.; Mather, P. T.; Haddad, T. S.; Lichtenhan, J. D. *J Polym Sci Part B: Polym Phys* **1998**, *36*, 1857.
- ⁵ Patel, R. R.; Mohanraj, R.; Pittman, C. U. *J Polym Sci Part B: Polym Phys* **2006**, *44*, 234.
- ⁶ Lee, Y. J.; Kuo, S. W.; Huang, W. J.; Lee, H. Y.; Chang, F. C. *J Polym Sci Part B: Polym Phys* **2004**, *42*, 1127.
- ⁷ Kuo, S. W.; Lin, H. C.; Huang, W. J.; Huang, C. F.; Chang, F. C. *J Polym Sci Part B: Polym Phys* **2006**, *44*, 673.
- ⁸ Kim, G. M.; Qin, H.; Fang, X.; Sun, F. C.; Mather, P. T. *J Polym Sci Part B: Polym Phys* **2003**, *41*, 3299.
- ⁹ Lee, W.; Ni, S.; Deng, J.; Kim, B. S.; Satija, S.K.; Mather, P. T.; Esker, A.R. *Macromolecules* **2007**, *40*, 682.
- ¹⁰ Schwab, J. J.; Lichtenhan, J. D. *Appl Organometal Chem* **1998**, *12*, 707.
- ¹¹ Lee, A.; Lichtenhan, J. D. *J Appl Polym Sci* **1999**, *73*, 1993.
- ¹² Nanda, A. K.; Wicks, D. A.; Madbouly, S. A.; Otaigbe, J. U. *Macromolecules* **2006**, *39*, 7037.
- ¹³ Waddon, A. J.; Zheng, L.; Farris, R. J.; Coughlin, E. B. *Nanoletters* **2002**, *2*, 1149.
- ¹⁴ Bharadwaj, R. K.; Berry, R. J.; Farmer, B. L. *Polymer* **2000**, *41*, 7209.

-
- ¹⁵ Lamm, M. H.; Chen, T.; Glotzer, S. C. *Nanoletters* **2003**, *3*, 989.
- ¹⁶ Fu, B. X.; Hsiao, B. S.; Pagola, S.; Stephens, P.; White, H.; Rafailovich, M.; Sokolov, J.; Mather, P. T.; Jeon, H. G.; Phillips, S.; Lichtenhan, J.; Schwab, J. *Polymer* **2001**, *42*, 599.
- ¹⁷ Zhao, Y.; Schiraldi, D. A. *Polymer* **2005**, *46*, 11640.
- ¹⁸ Fina, A.; Tabuani, D.; Frache, A.; Camino, G. *Polymer* **2005**, *46*, 7855.
- ¹⁹ Chen, J. H.; Chiou, Y. D. *J Polym Sci Part B: Polym Phys* **2006**, *44*, 2122.
- ²⁰ Joshi, M.; Butola, B. S.; Simon, G.; Kukaleva, N. *Macromolecules* **2006**, *39*, 1839.
- ²¹ Turri, S.; Levi, M. *Macromolecules* **2005**, *38*, 5569.
- ²² Turri, S.; Levi, M. *Macromolecular Rapid Communications* **2005**, *26*, 1233.
- ²³ Mabry, J. M.; Vij, A.; Iacono, S. T.; Grabow, W. W. *Polymer Preprints, American Chemical Society, Division of Polymer Chemistry* **2005**, *46*, 630.
- ²⁴ Iacono, S. T.; Ligon, S. C. Jr.; Mabry, J. M.; Vij, A.; Smith, D. W. Jr. *Polymer Preprints, American Chemical Society, Division of Polymer Chemistry* **2005**, *46*, 635.
- ²⁵ Hosaka, N.; Torikai, N.; Otsuka, H.; Takahara, A. *Langmuir* **2007**, *23*, 902.
- ²⁶ Koh, K.; Sugiyam, S.; Morinaga, T.; Ohno, K.; Tsuji, Y.; Fukuda, T.; Yamahiro, M.; Iijima, T.; Oikawa, H.; Watanabe, K.; Miyashita, T. *Macromolecules* **2005**, *38*, 1264.
- ²⁷ Fowkes, F. M.; Kaczinski, M. B.; Dwight, D. W. *Langmuir* **1991**, *7*, 2464.
- ²⁸ Owens, D. K.; Wendt, R. C. *J Appl Polym Sci* **1969**, *13*, 174.
- ²⁹ Urban, M. W. *Vibrational Spectroscopy of Molecules and Macromolecules on Surfaces*; John Wiley & Sons: New York, 1993.
- ³⁰ Enlow, E. M.; Kennedy, J. L.; Nieuwland, A. A.; Hendrix, J. E.; Morgan, S. L. *Applied Spectroscopy* **2005**, *59*, 986.

-
- ³¹ Harrick, N. J. *Internal Reflectance Spectroscopy*, Wiley-Interscience, New York 1967.
- ³² Magonov, S. N. *Encyclopedia of Analytical Chemistry*; John Wiley & Sons: Chichester, 2000.
- ³³ Podesta, A.; Fantoni, G.; Milani, P.; Guida, C.; Volponi, S. *Thin Solid Films* **2002**, *419*, 154.
- ³⁴ Paige, M. F. *Polymer* **2003**, *44*, 6345.
- ³⁵ Bowden, F.P.; Tabor, D.F. *The Friction and Lubrication of Solids-Part 2*, Clarendon Press, Oxford, U.K. 1964.
- ³⁶ Bhushan, B. *Principles and Applications of Tribology*, Wiley, NY, 1999.
- ³⁷ Helt, J. M.; Batteas, J. D. *Langmuir* **2006**, *22*, 6130.
- ³⁸ Brick, C.M.; Chan, E.R.; Glotzer, S.C.; Marchal, J.C.; Martin, D.C.; Laine, R.M. *Adv. Mater.* **2007**, *19*, 82.
- ³⁹ Tao, X.; Jiazheng, Z.; Kang, X. *J.Phys.D: Appl. Phys.* **1996**, *29*, 2932.
- ⁴⁰ Rapoport, L.; Fleischer, N.; Tenne, R. *J. Mater. Chem.* **2005**, *15*, 1782.
- ⁴¹ Wapner, P. G.; Hoffman, W. P. Report from Air Force Research Lab Edwards AFB Ca Space And Missile Propulsion Div.
- ⁴² <http://www.amcx.com/pdfs/siteamc148-18vsprlyne060103.pdf>, accessed 11/15/06
- ⁴³ Zhang, X. T.; Sato, O.; Taguchi, M.; Einaga, Y.; Murakami, T.; Fujishima, A. *Chem Mater* **2005**, *17*, 696.
- ⁴⁴ Gao, L.; McCarthy, T. J. *Langmuir* **2006**, *22*, 2966.
- ⁴⁵ Muller, B.; Riedel, M.; Michel, R.; Hofer, R.; Heger, D.; Grutzmacher, D. *J Vac Sci & Tech B: Microelectronics and Nanometer Structures* **2001**, *19*, 1715.
- ⁴⁶ Schwartz, L. W.; Garoff, L. *Langmuir* **1985**, *1*, 219.

-
- ⁴⁷ McCrum, G.; Read, B. E.; Williams, G. *Anelastic and Dielectric Effects in Polymer Solids*; John Wiley & Sons: London 1967.
- ⁴⁸ Funke, W. *J Oil Colour Chem Assoc* **1976**, 59, 398.
- ⁴⁹ Toussaint, A. *Prog Org Coat* **1996**, 28, 183.
- ⁵⁰ Messori, M.; Toselli, M.; Pilati, F.; Fabbri, P.; Tonelli, C. *Surf Coat Int Part B: Coat Trans* **2002**, 85, 197.
- ⁵¹ Messori, M.; Toselli, M.; Pilati, F.; Tonelli, C. *Polymer* **2001**, 42, 9877.
- ⁵² Walbridge, D.J. *Prog Org Coat* **1996**, 28, 155.
- ⁵³ Carr, C.; Wallstoem, E. *Prog Org Coat* **1996**, 28, 161.
- ⁵⁴ Benjamin, S.; Carr, C.; Walbridge, D.J. *Prog Org Coat* **1996**, 28, 197.

CHAPTER IV

POSS-NYLON 6 NANOCOMPOSITES: INFLUENCE OF POSS STRUCTURE ON
SURFACE AND BULK PROPERTIES

Abstract

Hybrid organic/inorganic nanocomposites based on polyhedral oligomeric silsesquioxane (POSS) nanostructured chemicals and nylon 6 were prepared *via* melt mixing. Two structurally and chemically different POSS molecules, a closed cage, non-polar octaisobutyl POSS (Oib-POSS) and an open cage, polar trisilanolphenyl POSS (Tsp-POSS) with differing predicted solubility parameters were evaluated in the nylon matrix. Surface analysis, including quasi-static and dynamic nanoindentation and nanotribological techniques, revealed exceptional improvements in modulus and hardness along with significant reductions in friction. Additionally, surface wetting characteristics of the nylon were reversed, with POSS incorporation yielding low surface energy, highly hydrophobic surfaces. AFM, TEM, SEM, spectroscopic techniques and thermomechanical analysis were employed to evaluate nanoscale dispersion and bulk properties of the composites. Tsp-POSS, with its higher predicted solubility in nylon, exhibited enhanced dispersion and tribomechanical properties at both nano and bulk scale.

Introduction

Polyhedral oligomeric silsesquioxane (POSS) nanostructured chemicals, with their organic-inorganic hybrid nature, well defined three-dimensional nanoscopic architecture, and monodisperse particle size, are the subject of intense research interest. The POSS cage consists of eight, ten or twelve Si atoms, with Si:O ratio of 2:3, Si-Si diameter of 0.54 nm and Si-C bond length in the range of 1.83-2.03 Å.¹ The cage can be functionalized with a wide range of organic substituents.^{1,2} While the organic groups on the POSS molecule provide an opportunity to tune the compatibility with a target polymer matrix, the inorganic Si-O-Si cage facilitates reinforcing action. Over the past decade, much of the POSS research effort has centered on synthesis of homo- and block copolymers with POSS as an integral part of the polymer chain,^{1,2,3,4,10-18} with fewer studies of POSS/melt blended composites.^{5,6,7,8,9} A wide variety of POSS based copolymers, including polysiloxane,^{10,11} polynorbornene,¹² polyurethane,^{13,14} poly(methyl methacrylate),^{15,16} epoxies,¹⁷ and poly(4-methyl styrene)¹⁸ have been reported.

The crystallization kinetics,¹⁹ rheological,² morphological,⁵ and viscoelastic⁶ characteristics of POSS copolymers and nanocomposites have been investigated by a number of groups. Monte Carlo simulation studies related to the interchain dynamics of POSS copolymers have also been reported.^{20,21} In general, changes in the properties are highly dependent on the POSS structure and its interactions with the polymer matrix. Recently, reports on surface modification of polymers through incorporation of POSS^{9,22} and fluorinated POSS^{23,24} have appeared. Previously we reported the preferential surface segregation of non-reactive octaisobutyl POSS in POSS/polypropylene nanocomposites prepared by melt blending.⁹ The resulting nanocomposites displayed high

hydrophobicity, increased surface hardness, and low friction attributed to the presence of nanostructured POSS domains on the surface. Esker and coworkers^{25,26} studied the phase separation behavior and morphological evolution in dewetting thin films of POSS/poly(tert-butyl acrylate) blends as a function of annealing temperature and time. Similarly, Takahara et al.²⁷ reported the use of POSS nanofillers to control the surface dewetting characteristics of polystyrene. Fukuda et al.²⁸ reported a higher concentration of POSS on the film surface for PMMA/POSS blends, resulting in increased hydrophobicity. Mabry et al.²⁴ reported superhydrophobic and superoleophobic poly(methyl methacrylate) surfaces using highly hydrophobic long chain fluorodecyl and fluorooctyl POSS. Superoleophobicity was attributed to the interplay of POSS chemical composition, nano/micro-roughened surface texture, and re-entrant surface curvature. Commonly, low friction and non-wetting characteristics are achieved by using fluoropolymers or low molecular weight fluorinated additives or their combination. However, high cost, extreme processing conditions, and environmental concerns limit their applicability. It is of interest to develop low friction hydrophobic surfaces using non-fluorinated systems.

As the size of engineering devices moves towards miniaturization, understanding of surface properties is critical, and control of tribological performance such as friction and wear is of particular importance for devices containing moving parts. Nanotribological behavior of polymers^{29,30} and polymer blend systems³¹ has been reported. However, to develop a more comprehensive understanding of tribology of filled polymer composites at the nanoscale surface regime, studies exploring nanoscale surface friction in conjunction with quasi-static and dynamic nanomechanical behavior

are needed. Surface hardness, which influences relative surface friction, is commonly measured using macroscale indentation techniques.³² With advances in nanoscale characterization techniques, nanoindentation is now utilized frequently to evaluate localized surface hardness and elastic modulus based on the method developed by Oliver and Pharr.³³ Quasi-static nanomechanical properties of polymer-clay nanocomposites have been reported.^{34,35,36} Recently, dynamic nanoindentation techniques have been utilized to investigate the nanoscale viscoelastic properties of neat polymers as well as composites.^{37,38,39} Mohanty and coworkers⁴⁰ reported the dynamic elastic modulus for clay-based polymer nanocomposites. Improved elastic modulus of the composite material was attributed to the reinforcing nature of clay platelets.

The current study examines the effects of POSS structure and polymer compatibility on composite morphology, surface and bulk properties. Nylon 6, an important engineering polymer used in applications requiring low surface friction and improved mechanical properties, was selected as the matrix polymer. Two POSS structures, a fully condensed, non-polar, octa-substituted octaisobutyl-POSS cage and an open cage, hepta-substituted, polar trisilanophenyl-POSS, were dispersed in the nylon matrix at varying concentrations *via* melt mixing. Selection of POSS molecules was based on the structure and nature of the POSS cages and their expected compatibility with nylon 6. Significant differences in dispersion, morphology, surface characteristics (roughness, static and dynamic nanomechanical properties, friction and wetting) and bulk (crystallization and thermomechanical) properties were observed, related to the POSS structure and predicted solubility in the polymer matrix. Results indicate the potential to

specifically design POSS nanocomposites with desired surface enhancement capabilities through control of POSS chemical structure.

Experimental

Materials

An unfilled and non-lubricated grade of nylon 6 homopolymer (Capron[®] 8202 NL, $M_w=71000$ D, density 1.13 gm/cc) was purchased from BASF. Two different types of POSS, a closed cage octaisobutyl POSS (MSO825) (Oib-POSS) and an open cage trisilanophenyl POSS (SO1458) (Tsp-POSS), were provided by Hybrid Plastics Inc. (Hattiesburg, MS). Oib-POSS and Tsp-POSS were received as crystalline white powders at room temperature. All materials were used as received unless otherwise mentioned. The chemical structures of Oib-POSS and Tsp-POSS are shown in Figure IV-1.

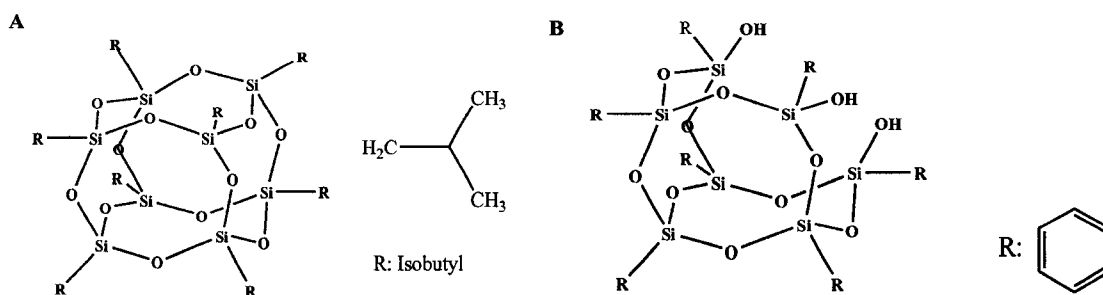


Figure IV-1. Schematic structures of (A) Oib-POSS (B) Tsp-POSS

Sample Preparation

POSS/nylon 6 hybrid polymer composites (HPC's) were prepared at concentrations of 0, 5 and 10 weight % of POSS in nylon 6. HPC's were prepared by melt blending at 250°C utilizing a CT-25 co-rotating twin screw extruder (B&P Processing, screw diameter = 25mm and L:D ratio of 44:1). Smooth films for surface morphology and tribomechanical analysis were prepared by melt pressing the extrudate between two clean silicon wafers.

POSS Specific Gravity Measurements

Specific gravity of POSS powders was measured using a standard specific gravity bottle (10 ml) with a conical neck and a round glass stopper with a fine bore along the length. Excess fluid was released through the bore keeping volume constant. Methanol ($\rho = 0.791$ gm/cc) was used as the test fluid and specific gravity was calculated using equation 1.

$$\text{Specific Gravity} = [(W_2 - W_1) \cdot \rho_f] / [(W_4 - W_1) - (W_3 - W_2)] \quad (1)$$

Where, ρ_f = density of test fluid, W_1 = weight of the empty bottle, W_2 = weight of bottle + powder, W_3 = weight of (bottle+powder) + fluid used to fill the rest of the bottle, and W_4 = weight of the bottle + fluid.

Atomic Force Microscopy (AFM) Surface Topography and Nanoscale Relative Surface Friction

Surface topography studies were conducted on a MultiMode™ scanning probe microscope from Veeco Instruments, Inc. (Santa Barbara, CA). Probes were purchased from Veeco Probes, (Santa Barbara, CA). A silicon probe with a 125 μ m long silicon cantilever, nominal force constant of 40 N/m, and resonance frequency of 275 KHz was used for tapping mode surface topography studies. 5 μ m x 5 μ m scan size areas were evaluated with an image resolution of 512 x 512 pixels at a scan rate of 1Hz. Multiple areas were imaged and figures show representative morphology.

Nanoscale relative surface friction studies were performed *via* AFM in lateral force mode (LFM) using a triangular silicon nitride (Si₃N₄) probe with a nominal cantilever spring constant of 0.58 N/m on a 1 μ m x 1 μ m scan area. Samples were stored in a humidity controlled chamber and measurements were conducted on the same day to

minimize environmental effects. AFM studies were performed under ambient conditions in a temperature (27°C) and humidity controlled (40-45%) room. Force- distance curves as well as friction loops were obtained at different set points to obtain statistical data for analysis. In AFM nanoscale friction measurements, total normal force is the sum of an adhesive force (F_a), which acts between the surface and probe, and the normal loading force (F_l) which is applied on the cantilever.⁴¹ Friction force (F_f) was calculated by the average distance between the extending and retracting friction loops. Thus, relative coefficient of friction (COF, μ) can be best described by the following equation (2).

$$\mu = F_f / (F_l + F_a) \quad (2)$$

Relative COF was calculated based on the nominal force constant of the AFM cantilever, which provides the relative values of surface friction rather than the absolute value. This approach is valid to compare the relative surface friction between unmodified and modified surfaces as the same cantilever was used for all measurements. To verify reproducibility, two sets of readings were taken for each sample and an average value is reported. Additionally, to ensure that tips and surfaces were not damaged during LFM measurements, probes and surfaces were imaged *via* SEM and tapping mode AFM respectively.

Attenuated Total Reflectance Fourier Transform Infrared (ATR-FTIR) Spectroscopy

Micro ATR-FTIR spectroscopy measurements were conducted using a Bio-Rad FTS-6000 FT-IR single-beam spectrometer with 4 cm⁻¹ resolution. Samples were analyzed using a 2 mm germanium crystal with a 45° angle maintaining constant contact pressure between the crystal and the specimens.

Scanning Electron Microscopy-Energy Dispersive X-Ray (SEM-EDAX)

Samples were microtomed with a diamond knife using a Leica EM UC6 cryomicrotome at -20°C. Morphology of the microtomed samples was investigated using an FEI Quanta 200 Scanning Electron Microscope (SEM) in environmental scanning mode, equipped with a Thermo-Noran Vantage light element energy dispersive x-ray detector providing elemental composition. Characterization of all the elements except hydrogen was obtained by X-ray spectroscopy under electron flux. Micrographs were obtained at a voltage of 25 kV and a pressure of 1 torr.

Transmission Electron Microscopy-Energy Dispersive X-Ray (TEM-EDAX)

Ultra high resolution transmission electron microscope (JEOL-2100, Jeol Ltd., Tokyo, Japan), at an accelerating voltage of 200 kV, was utilized to investigate the dispersion of POSS nanoparticles in the bulk. Ultrathin sections of POSS/nylon 6 HPC's, with an average thickness of 100 nm, were prepared by cryoultramicrotoming the samples with a diamond knife using a Leica EM UC6 cryomicrotome at -20°C. These ultrathin sections were collected on a 600 mesh copper grid. To observe the POSS rich domains, elemental maps of these sections were acquired using energy dispersive X-ray in conjunction with TEM using EDAX Genesis software.

Wide-Angle X-ray Diffraction (WAXD)

X -ray diffraction studies of POSS/nylon 6 HPC's were conducted on the melt pressed samples, and neat POSS samples were tested in powder form. Samples were quenched in an ice/water mixture. Diffraction patterns were obtained using a Rigaku D/MAX-Ultima-III Diffractometer in transmission mode at room temperature using Cu

K α radiation at a tube current of 44 mA and an acceleration voltage of 40 kV. Scan range was 3°- 60° at a step interval of 0.01° and a scanning rate of 2°/min.

Water Contact Angle and Surface Energy

Static and dynamic contact angles were measured using the sessile drop technique by a ramè-hart goniometer coupled with DROPimage[®] data analysis software. Ten μ l of water was dropped onto a flat film surface and an image of the drop was captured. Contact angle hysteresis was calculated by measuring advancing and receding contact angles using the tilting plate technique. Five measurements were taken across the film surface and an average value is reported. Surface energy was calculated utilizing the Fowkes⁴² and Owens-Wendt method⁴³ by measuring the contact angles with deionized water and diiodomethane (CH₂I₂).

Friction Evaluation

Macroscale dynamic coefficient of friction (COF) measurements were performed according to ASTM G 99, using a pin-on-disk tribometer (Micro Photonics Inc., PA). Two sets of readings were taken for each film sample (1" x 1") inside a controlled humidity chamber (10% relative humidity) at 27°C. Film samples were mounted firmly on a flat metal disc, which was rotated (path radius 3 mm) against a steel ball (3 mm diameter, Small Parts Inc., Miami Lakes, FL) at 20 rpm for 20 min. Relative surface friction measurements were conducted at external loads of 3N, 4N, and 5N. All measurements were conducted at low relative humidity to minimize the influence of the moisture layer, which acts as a lubricant.

Quasi-Static and Dynamic Nanoindentation (Nano-DMA)

Quasi-static and dynamic nanomechanical properties were evaluated at room temperature using a Triboindenter (Hysitron, Inc., Minneapolis, MN) operated with a three-sided diamond (Berkovich type) tip calibrated on fused silica. Closed loop load control quasi-static nanoindentation was performed using a compliance method, in which real time force-displacement curves were obtained during loading and unloading cycles. As the indenter presses into the surface, the displacement is recorded as a function of the applied load. A single indent was made on every surface by applying a normal load with a loading rate of $50\mu\text{N}/\text{sec}$. Unloading rate was identical to loading rate and a 5 sec. hold time was provided at the maximum force of $2000\mu\text{N}$. Total cycle time for load control indentation was 85 sec. Indentation tests were performed at multiple regions across the surface to determine the variation, and an average value is reported. Modulus, elastic recovery, plastic deformation and hardness data are extracted from plots of force as a function of displacement based on the procedures developed by Oliver and Pharr.²⁹

Dynamic storage modulus was measured as a function of penetration depth. To isolate the response of indenter and material, air calibration was performed prior to indentation. Samples were subjected to a variable dynamic load ($100\text{-}1000\mu\text{N}$) at a loading rate of $10\mu\text{N}/\text{s}$ and a constant frequency of 75 Hz. Total cycle time for this test was 143 sec.

Dynamic Mechanical Analysis (DMA)

Bulk thermo-mechanical behavior was investigated using a TA Q800 dynamic mechanical analyzer in tensile mode. Samples were analyzed from 0 to 200°C at a heating rate of $2^\circ\text{C}/\text{min}$ and an oscillation frequency of 1Hz.

Modulated Differential Scanning Calorimetry (M-DSC)

Modulated DSC, in which a modulation of $\pm 1^\circ\text{C}$ was performed every 60 seconds, was utilized to obtain precise thermal data. Glass transition (T_g) and melting temperatures (T_m) were obtained utilizing a TA Instruments Q Series DSC Q100. Samples, ~ 10 mg in weight, were analyzed under a nitrogen blanket. To erase the thermal history, samples were heated initially from 25°C to 250°C at a rate of 10°C per minute. This cycle was followed by cooling the samples from 250°C to 25°C at a rate of 10°C per minute, and finally reheating the samples from 25°C to 250°C at a rate of 10°C per minute. Percentage crystallinity of all samples was calculated using equation 3.

$$X_c = \{ \Delta H_f / (1-f) \Delta H_f^0 \} \quad (3)$$

Where ΔH_f and ΔH_f^0 are the enthalpy of fusion of the polymer in the blend and in 100% crystalline nylon 6, respectively and f represents the weight fraction of POSS in the composite. Value of ΔH_f^0 used in these calculations was 188 J/g .⁴⁴

Results and Discussion

To understand and predict the compatibility and dispersion characteristics of POSS in a nylon 6 matrix, theoretical solubility parameters (δ) were estimated following Hoy's method.⁴⁵ Materials with close solubility parameters are expected to exhibit greater compatibility and better dispersion characteristics. Recently, Mark *et al.*⁴⁶ investigated the dispersion characteristics of POSS in a polysiloxane melt and elastomer. They reported good agreement between the theoretical solubility parameters and observed microscopic dispersion of POSS particles. In this study, solubility parameters based on the group molar-attraction constant (G) were calculated by the structural formula and density (ρ) of the material using equation 4.

$$\delta = (\rho \Sigma G_i) / M_o \quad (4)$$

Where ΣG_i is the sum of molar attraction constants for the groups in the molecule and M_o is the molecular weight of the material. G_i values were estimated from Hoy's table of group molar-attraction constants.⁴⁷ The G value for Si-O ($278 \text{ (cal.cm}^3/\text{mol)}^{1/2}$) was calculated using poly(dimethylsiloxane) ($\rho=0.98 \text{ gm/cm}^3$ and $M_o= 74 \text{ gm/mol}$) with a literature reported solubility parameter of $7.58 \text{ (cal/cm}^3)^{1/2}$.⁴⁸ Measured densities, ΣG_i values, and calculated solubility parameters for the materials are shown in Table IV-1.

Table IV-1. Theoretical Solubility Parameter for Nylon 6, Oib-POSS, and Tsp-POSS.

| Sample | $\rho \text{ (gm/cm}^3)$ | $M_o \text{ (gm/mol)}$ | $\Sigma G_i \text{ (kcal.cm}^3/\text{mol)}^{1/2}$ | $\delta \text{ (cal/cm}^3)^{1/2}$ |
|----------|--------------------------|------------------------|---|-----------------------------------|
| Nylon 6 | 1.13 | 113 | 1.10 | 11.0 |
| Oib-POSS | 0.92 | 872 | 7.43 | 7.8 |
| Tsp-POSS | 1.16 | 930 | 7.93 | 9.8 |

As expected based on the chemical structures of the POSS, the calculated solubility parameter for Tsp-POSS is close to that of nylon 6 (difference in the solubility parameter $\Delta\delta_{\text{Tsp-POSS/nylon 6}} = 1.2 \text{ (cal/cm}^3)^{1/2}$) while that of Oib-POSS differs by more than three units ($\Delta\delta_{\text{Oib-POSS/nylon 6}} = 3.2 \text{ (cal/cm}^3)^{1/2}$). More importantly, close values of solubility parameters provide favorable enthalpy of mixing for Tsp-POSS compared to Oib-POSS in nylon 6, and thus greater compatibility and better dispersion is expected for Tsp-POSS/nylon samples.

Tapping mode AFM phase images of neat nylon 6 and POSS/nylon 6 HPC's are shown in Figure IV-2(A)-(C). Neat nylon 6 exhibits regular crystalline features on the surface. Figure IV-2(A) insert (scan area: 300 nm x 300 nm) shows the uniform small crystals, 30-60 nm wide, with no preferential orientation. It is well supported in the literature that multiple factors, including processing method, quenching time and method, film thickness and nucleating agents influence the crystal growth and spherulitic morphology in nylon 6.^{49,50,51} In this study, limited crystal formation on the surface is attributed to the rapid quenching, absence of nucleating agents, and molding process. The nylon 6 surface exhibits root mean square (RMS) roughness of 2.1 nm (Table IV-2), attributed to the presence of small crystals and the melt pressing process. Incorporation of POSS results in increase in roughness and changes in the surface topography, with the appearance of larger raised features on the surface. These features were identified as POSS aggregates through multiple tools, including ATR-FTIR, nanoindentation, surface energy, and hysteresis measurements, as discussed in later sections. Additionally, nylon 6 crystals are not directly observed in the phase images of HPC's, but they may be present in the layer beneath the larger POSS aggregates. Overall dispersion and domain

size of POSS moieties in a polymer matrix is a function of inter- and intramolecular forces acting between POSS and the polymer matrix as well as between POSS molecules themselves.

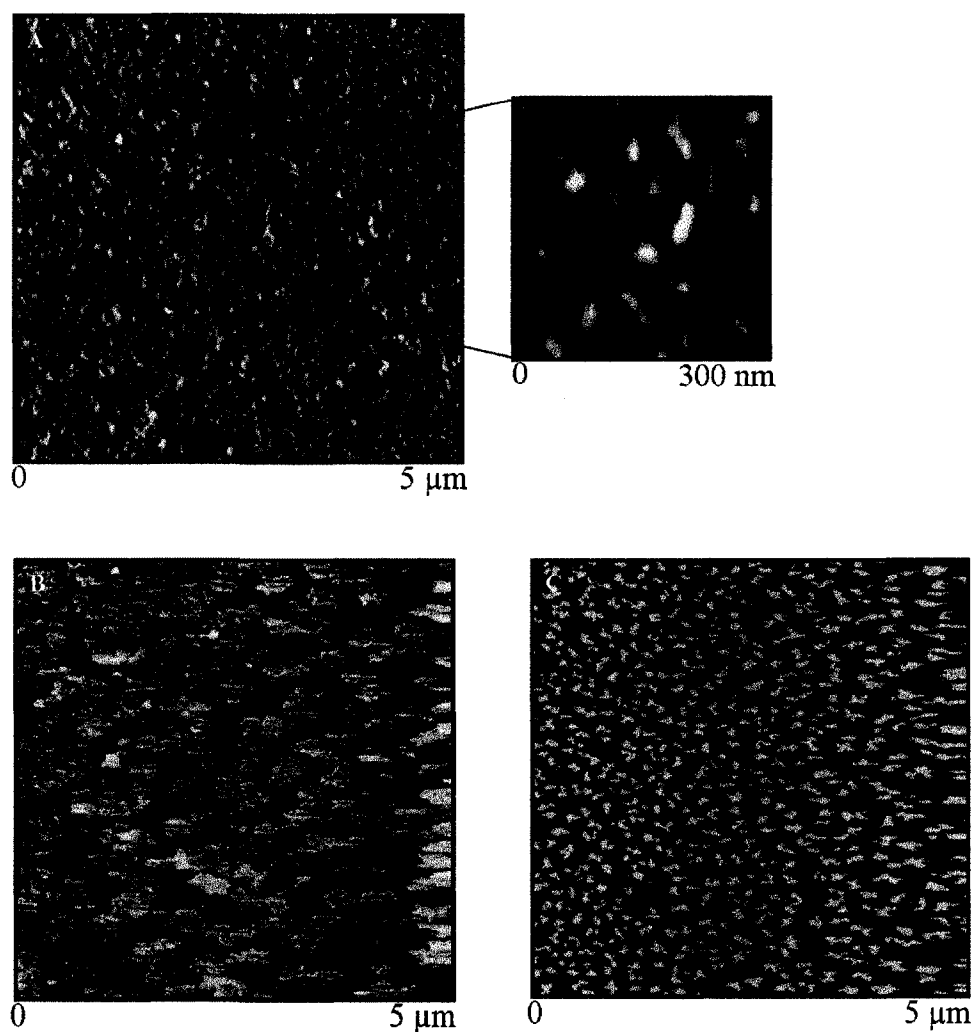


Figure IV-2. Tapping Mode AFM phase images of (A) Neat nylon 6 (Inset figure shows crystalline lamellae) (B) 10% Oib-POSS/nylon 6 (C) 10% Tsp-POSS/nylon 6.

The AFM phase images provide information about the distribution of POSS domains based on the differences in localized stiffness and modulus. Bright regions in the phase images (Fig. IV-2 B and C) are attributed to the harder POSS domains whereas

dark regions represent the relatively soft nylon 6 matrix. Tsp-POSS, owing to its better compatibility and dispersion, exhibits smaller, regularly dispersed POSS domains (100-150 nm) and lower roughness (RMS roughness= 2.4-2.6 nm) compared to the large, irregular POSS domains (200-500 nm) and higher surface roughness (RMS roughness= 3.5-3.9 nm) in the Oib-POSS HPC's. The enhanced dispersion in the Tsp-POSS blends is related to the open-cage, polar structure of the molecule, which allows hydrogen bonding between the nylon 6 amide linkages and -OH group in the Tsp-POSS and results in small, uniform POSS clusters. Large aggregates in the Oib-POSS HPC's, on the other hand, most likely arise from greater POSS-POSS attractions compared to POSS-nylon 6 interactions.

Table IV-2. Nanoscale Surface Roughness, Relative COF and Percentage Reduction in COF of POSS/nylon 6 HPC's.

| Sample | Roughness (nm) | | COF | % Reduction in COF |
|-----------------------|----------------|------|------|--------------------|
| | RMS | Mean | | |
| Neat Nylon 6 | 2.1 | 1.6 | 0.20 | -- |
| Nylon 6+ 5% Oib-POSS | 3.5 | 2.4 | 0.15 | 25 |
| Nylon 6+ 10% Oib-POSS | 3.9 | 2.8 | 0.14 | 30 |
| Nylon 6+ 5% Tsp-POSS | 2.4 | 1.8 | 0.12 | 40 |
| Nylon 6+ 10% Tsp-POSS | 2.6 | 2.0 | 0.11 | 45 |

ATR-FTIR evaluations were performed to evaluate the chemical composition of the surfaces. IR spectra of Oib-POSS/nylon 6 blends, neat POSS and nylon 6 are shown in Figure IV-3. Pure Oib-POSS shows characteristic absorbances at 1100 cm^{-1} , attributed to Si-O-Si stretching vibration, 1220 cm^{-1} corresponding to $-\text{CH}_2$ symmetric stretching vibrations and Si-C symmetric vibration, and 2870 cm^{-1} as well as 2950 cm^{-1}

corresponding to CH_2 symmetric and asymmetric stretching vibrations. Neat nylon 6 shows characteristic absorption bands at 1640 cm^{-1} , attributed to the amide I band, which results from the $\text{C}=\text{O}$ stretching vibration of the amide group coupled to the bending of the N-H bond and the stretching of the C-N bond, 1545 cm^{-1} due to N-H bending and C-N stretching vibrations, and 2855 and 2930 cm^{-1} bands corresponding to the CH_2 symmetric and asymmetric stretching vibrations.^{52,53} IR spectra of Oib-POSS/nylon 6 show absorption bands corresponding to both nylon 6 and Oib-POSS, indicating the presence of Oib-POSS on the surface. A slight shift in the Si-O-Si stretching vibration peak from 1100 to 1108 cm^{-1} , observed in both HPC's, is attributed to interactions between POSS and the polymer matrix.

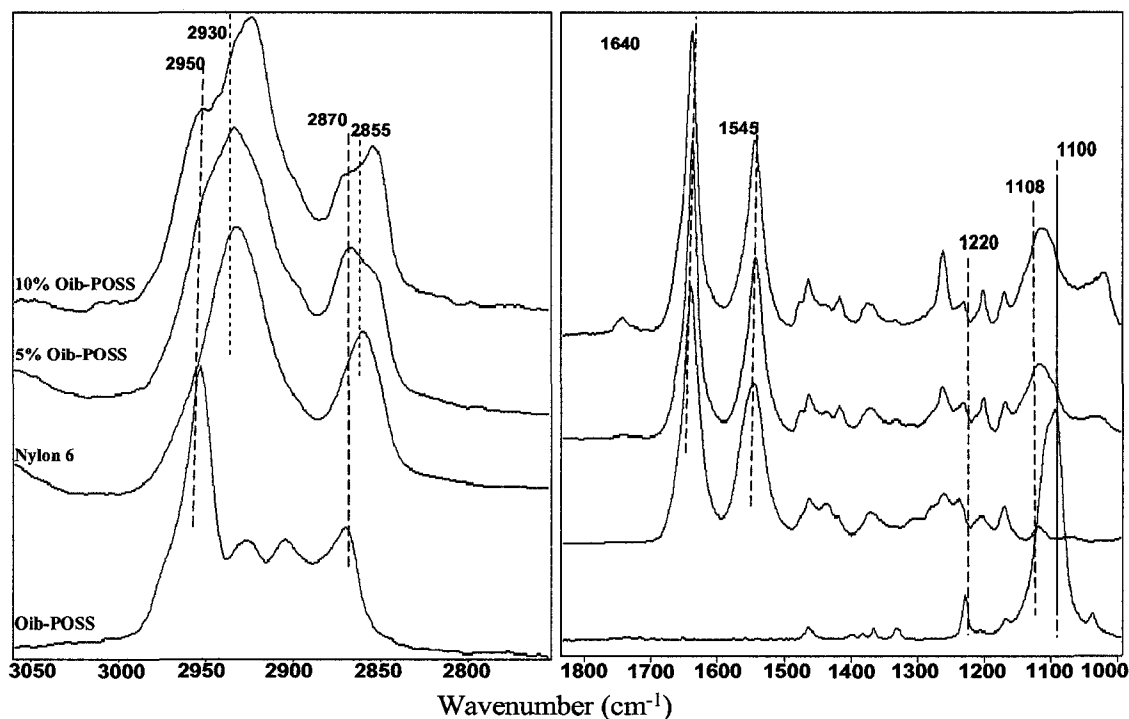


Figure IV-3. ATR-FTIR spectra of Oib-POSS/nylon 6 HPC's.

ATR-FTIR spectra of Tsp-POSS samples are shown in Figure IV-4. Tsp-POSS shows characteristic Si-O-Si stretching vibration absorbances at 1100 cm^{-1} and 1134 cm^{-1} . Additionally, an Si-OH deformation absorbance at 1030 cm^{-1} is observed along with a phenyl ring deformation absorbance at 1000 cm^{-1} and an absorbance at 1430 cm^{-1} corresponding to phenyl ring vibration. IR spectra of Tsp-POSS/nylon 6 blends show a strong Si-O-Si stretching absorption at 1134 cm^{-1} and a shoulder at 1100 cm^{-1} . As the siloxane chain lengthens the Si-O-Si band splits into two bands and broadens, which is attributed to the open cage structure of Tsp-POSS. Presence of absorption bands corresponding to nylon 6 as well as Tsp-POSS in the IR spectra of Tsp-POSS/nylon 6 HPC's indicates the presence of Tsp-POSS on the composite surface.

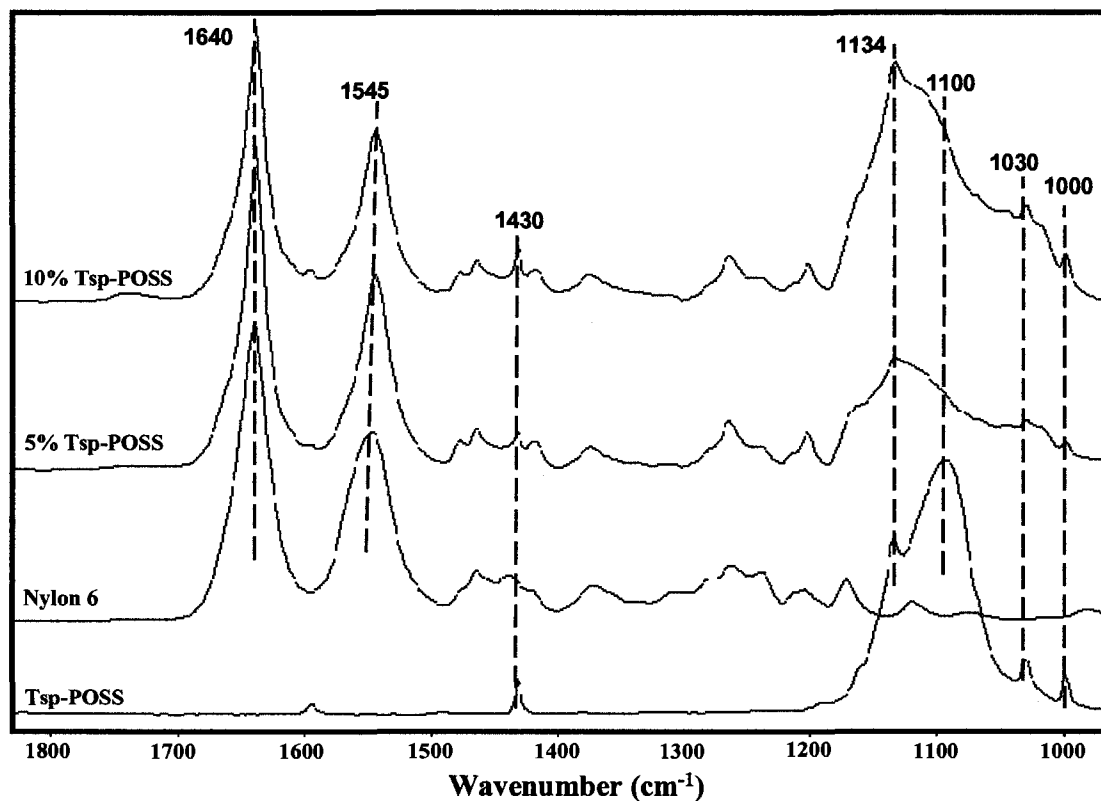


Figure IV-4. ATR-FTIR spectra of Tsp-POSS/nylon 6 HPC's.

SEM images of bulk morphology of microtomed samples are shown in Figure IV-5(A)-(C). Neat nylon 6 exhibits a smooth surface with limited crystal formation (Fig. IV-5A). A high magnification image (Fig. IV-5A*) shows 100-200 nm wide bundles, along with 20-50 nm wide lamellar stacks and a few individual lamellae (5-10 nm wide). These lamellar stacks and bundles appear anisotropic in orientation. Galeski *et al.*⁵⁴ reported similar multi-scale spherulitic morphology for compression and injection molded bulk nylon 6 samples. POSS/nylon 6 HPC's exhibit spherical aggregates, of large size and broad particle distribution (100 nm to 10 μm) for Oib-POSS, with smaller, evenly dispersed particles for Tsp-POSS (50 – 150 nm).

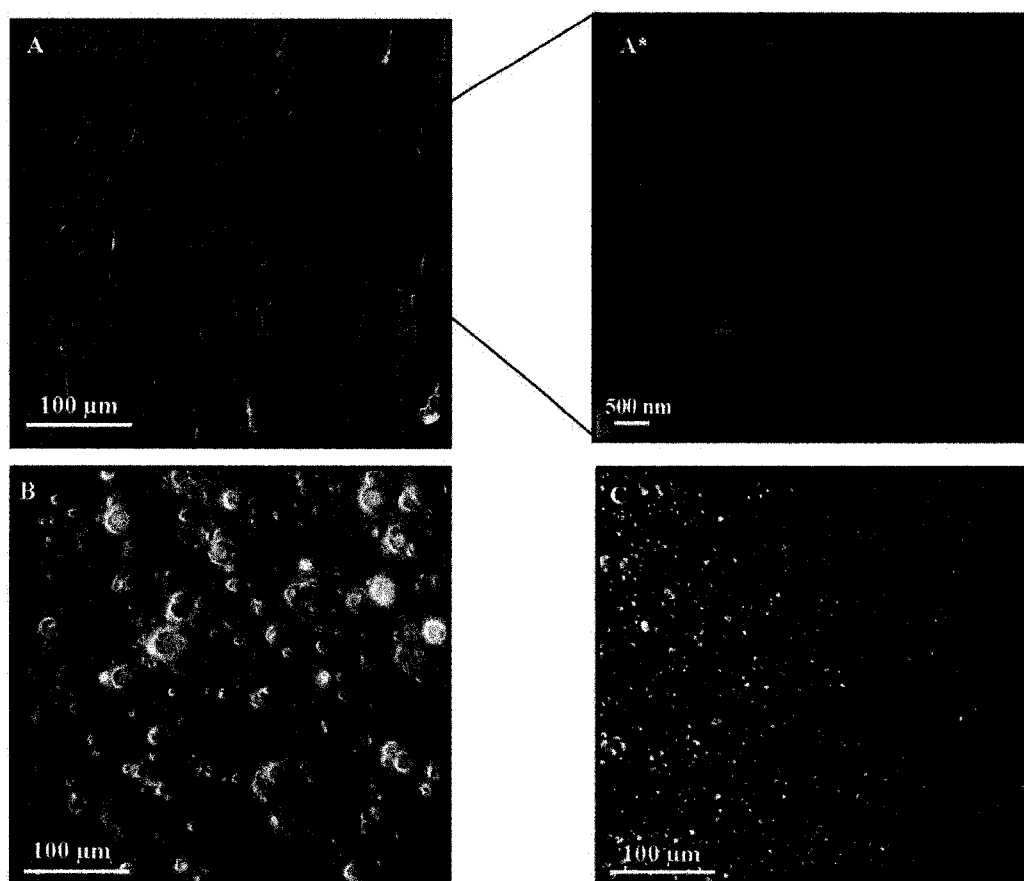


Figure IV-5. SEM micrographs of microtomed bulk (A) Neat nylon 6 (inset image shows lamellar stacks) (B) 10% Oib-POSS/nylon 6 (C) 10% Tsp-POSS/nylon 6.

EDAX elemental analysis (Figure IV-6 (A)-(C)) of the spherical features indicates that they are POSS aggregates with the appearance of the signature peak of silicon at 1.7 KeV. Consistent with the information obtained from AFM surface morphology studies, Tsp-POSS shows enhanced dispersion due to its greater compatibility with the nylon matrix.

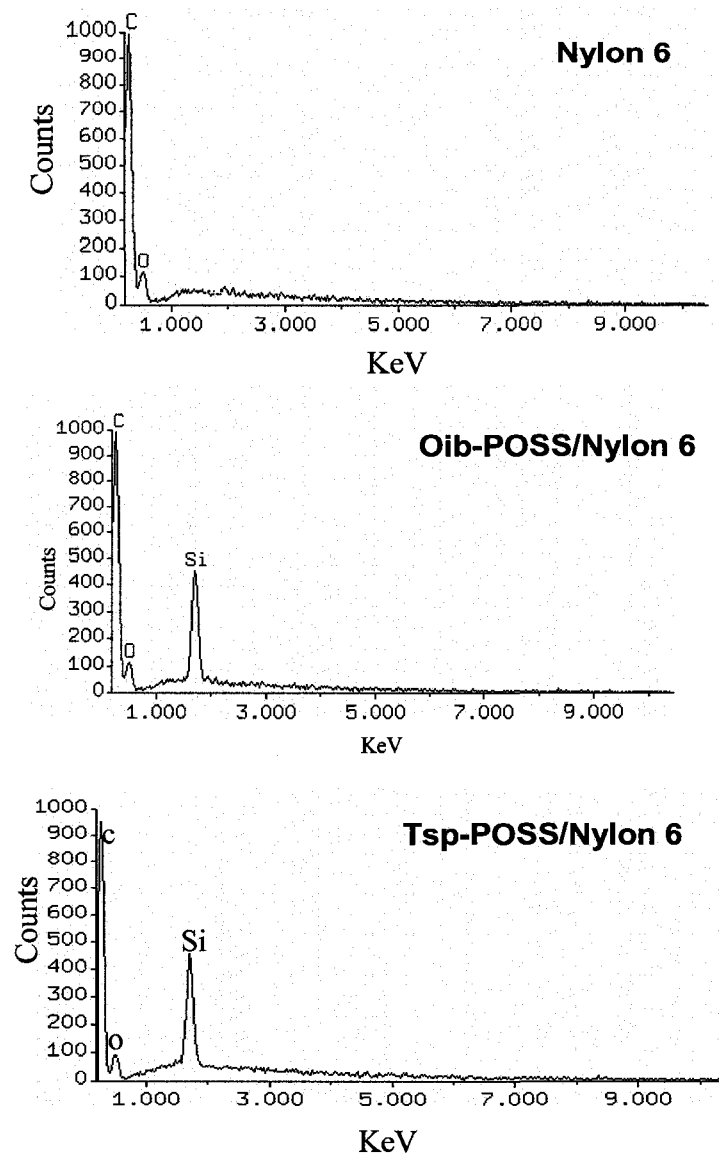


Figure IV-6. EDAX mapping of microtomed bulk neat nylon 6 and POSS/nylon 6 composites.

Recognizing the fact that SEM/EDAX probes the surface a few microns deep (3-4 μm) and has limited lateral resolution (1-2 μm), ultra-high resolution TEM with lateral resolution in the range of 15-20 nm was utilized to probe the dispersion of POSS in the bulk. EDAX elemental mapping coupled with TEM analysis further indicates improved compatibility and dispersability of Tsp-POSS in comparison to Oib-POSS in nylon 6. Figures IV-7(A) and (B) show representative TEM-EDAX silicon overlap maps (100K magnification) of ultrathin sections of 10 wt.% Oib-POSS/nylon 6 and Tsp-POSS/nylon 6 samples respectively. The Tsp-POSS composite shows uniform, highly dispersed small POSS aggregates (10-50 nm) in the nylon 6 matrix, while the Oib-POSS blends show large aggregates (>100 nm) that are more widely dispersed. The observed dispersion behavior is in agreement with the theoretical solubility predictions discussed earlier. However, the particles observed on the surface via AFM imaging are larger in size than those observed in the bulk, particularly for the Tsp-POSS composites. This indicates that preferential segregation of POSS to the surface, with simultaneous increase in POSS aggregation size near the surface appears to occur in both systems.

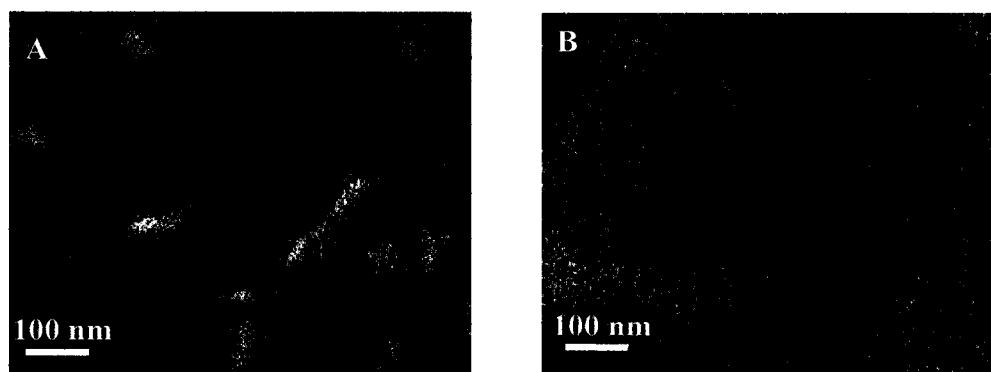


Figure IV-7. TEM/EDAX silicon mapping of (A) 10% Oib-POSS/nylon 6 (B) 10% Tsp-POSS/nylon 6 HPC's microtomed bulk samples.

WAXD studies were performed to evaluate the influence of POSS on the microstructure and crystallization behavior of nylon 6. X-ray diffractograms of POSS/nylon 6 HPC's are shown in Figures IV-8 (A) and (B). For comparison purposes, diffractograms of neat nylon 6, Oib-POSS and Tsp-POSS are also shown. Neat Oib-POSS exhibits characteristic crystalline peaks at $2\theta = 8.0^\circ$ ($d = 11.0 \text{ \AA}$), 8.9° ($d = 9.9 \text{ \AA}$), and 10.9° ($d = 8.1 \text{ \AA}$), whereas Tsp-POSS exhibits its characteristic crystalline peaks at $2\theta = 7.2^\circ$ ($d = 12.3 \text{ \AA}$), 8.7° ($d = 10.2 \text{ \AA}$), and 27.4° ($d = 3.3 \text{ \AA}$). The presence of sharp peaks in the WAXD patterns of neat POSS samples indicates their highly crystalline nature.

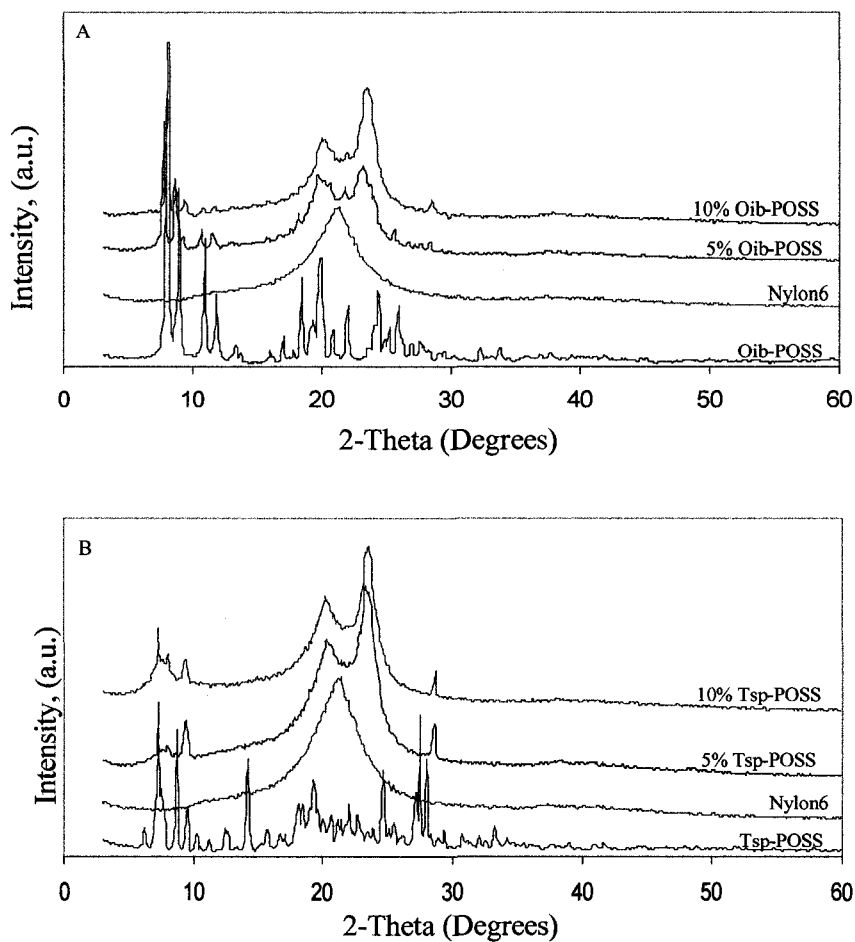


Figure IV-8. Wide angle x-ray diffractograms of (A) Oib-POSS/nylon 6 (B) Tsp-POSS/nylon 6 HPC's.

X-ray diffractograms reveal significant differences in the crystallization behavior of nylon 6 and POSS/nylon 6 HPC's. Three different crystalline structures (monoclinic α , pseudo-hexagonal γ , and metastable pseudo-hexagonal β) can co-exist in nylon 6. Paul et al.⁵⁵ reported significant differences in the surface vs. bulk crystallization behavior of nylon 6 prepared by melt processing. They observed the formation of only γ -crystals on the surface with co-existence of both α - and γ -crystals in the bulk region. Multiple factors including thermal history, additives, moisture, applied stress and crystallization time influence the crystallization behavior of nylon 6.⁵⁶ It is well supported in the literature that external conditions such as rapid quenching, which forces crystallization to occur at low temperature, restricts polymer chain mobility and thereby favors the formation of the γ form.^{57,58} Neat nylon 6, which was rapidly quenched, shows a broad peak at $2\theta=21.3^\circ$ ($d=4.2 \text{ \AA}$), attributed to the γ form of nylon 6.⁵⁹ In contrast, POSS/nylon 6 HPC's samples show two sharp peaks at $2\theta=20.3^\circ$ ($d=4.4 \text{ \AA}$) and 23.3° ($d=3.8 \text{ \AA}$), attributed to the more thermodynamically stable α -form of nylon 6.⁶⁰ Formation of α -crystals in HPC's is attributed to increased polymer chain mobility, which is further supported by molecular dynamics studies,^{23,24} that indicate that incorporation of POSS enhances chain mobility by reducing the inter-chain contacts in the matrix polymer. In addition to the predominant α -crystals, Oib-POSS/nylon 6 samples show a small peak at $2\theta=21.3^\circ$ indicating the presence of a small amount of co-existing γ -crystals which may arise from the limited restriction in polymer chain mobility imposed by large POSS aggregates. Thus, the effect of POSS on nylon 6 crystallization depends on the POSS structure, its aggregation state, and the interactions between POSS and nylon phase.

In view of these significant changes in morphology, it is of interest to see how these changes translate into surface and bulk properties. Table IV-3 shows the static contact angles and surface energies with their polar and dispersive components. Neat nylon 6 is hygroscopic in nature which is evident from its low water contact angle value (61°). Incorporation of POSS renders the composite surface hydrophobic (water contact angle > 90°). Additionally, surface hydrophobicity increases with increase in POSS concentration. At 10 wt.% POSS concentration, Tsp-POSS HPC's show water contact angle of 100° (63% increase) and Oib-POSS HPC's exhibit 105° (71% increase), approaching the hydrophobicity of a Teflon surface (water contact angle 110±2°). Higher surface hydrophobicity and the non-wetting nature of these HPC's is linked, in part, to their nanoscale surface roughness caused by the presence of POSS aggregates on the surface. Furthermore, incorporation of POSS leads to a dramatic reduction in total surface energy, with specific reduction in the polar component. Tsp-POSS HPC's exhibit higher polar components than Oib-POSS HPC's, as is expected based on the higher polarity of the silanol-containing Tsp-POSS. The low surface energy of POSS drives POSS molecules to the surface to minimize the total surface energy.⁹

Table IV-3. Static Contact Angle and Surface Energy of POSS/nylon 6 HPC's.

| Sample | Contact angle (°) | | Surface Energy (γ) (mN/m) | Polar (γ^p) (mN/m) | Dispersive (γ^d) (mN/m) |
|-----------------------|-------------------|--------------------------------|---------------------------------------|--------------------------------|-------------------------------------|
| | H ₂ O | CH ₂ I ₂ | | | |
| Neat Nylon 6 | 61 | 41 | 51.0 | 12.0 | 39.0 |
| Nylon 6+ 5% Oib-POSS | 97 | 53 | 33.0 | 0.5 | 32.5 |
| Nylon 6+ 10% Oib-POSS | 105 | 63 | 26.9 | 0.2 | 26.7 |
| Nylon 6+ 5%Tsp-POSS | 94 | 52 | 34.0 | 1.1 | 32.9 |
| Nylon 6+ 10%Tsp-POSS | 100 | 61 | 28.5 | 0.6 | 27.9 |

Surface dynamics were further studied *via* dynamic water contact angle analysis (Table IV-4). Hysteresis values are influenced by multiple factors, including surface roughness, chemical heterogeneity of the surface, presence of low molecular weight species, and molecular orientation.¹³ Oib-POSS HPC's exhibit significantly higher hysteresis compared to Tsp-POSS HPC's, which show hysteresis levels similar to those of neat nylon 6. This behavior is in large part explained by the greater roughness and more irregular aggregate size for the Oib-POSS HPC's as observed via AFM and SEM. Surface roughness and chemical heterogeneity on the surface, coupled with the low surface energy of POSS molecules, explains the hysteresis behavior of these HPC's. Complimentary to ATR-FTIR findings, surface energy and hysteresis measurements further indicate the presence of POSS on the surface.

Table IV-4. Advancing (θ_a), Receding Water Contact Angle (θ_r) and Hysteresis (θ_h) of POSS/nylon 6 HPC's.

| Sample | θ_a (°) | θ_r (°) | θ_h (°) |
|-----------------------|----------------|----------------|----------------|
| Neat Nylon 6 | 66 | 58 | 8.0 |
| Nylon 6+ 5% Oib-POSS | 103 | 89 | 14.0 |
| Nylon 6+ 10% Oib-POSS | 108 | 90 | 18.0 |
| Nylon 6+ 5%Tsp-POSS | 98 | 89 | 9.0 |
| Nylon 6+ 10%Tsp-POSS | 104 | 94 | 10.0 |

Nanoscale relative surface friction was evaluated by AFM in lateral force mode (LFM). Figure IV-9 (A)-(C) exhibits real time friction loops for all samples. Qualitatively, the average distance between the extending and retracting lines indicate relative friction between the surface and the probe.⁶¹ Reduced average distance between extending and retracting traces for the POSS HPC's demonstrate reduction in friction.

Table IV-2 shows the relative COF, with Oib-POSS HPC's showing a 25-30% reduction and the Tsp-POSS HPC's showing a 40-45% reduction in relative surface friction.

Friction reduction is explained by the greater surface hardness in the POSS-containing composites and the increase in surface roughness, which reduces the true area of contact between the probe and the surface. The lower friction exhibited by the Tsp-POSS blends is attributed to the more regular dispersion and reduced surface heterogeneity in this composite.

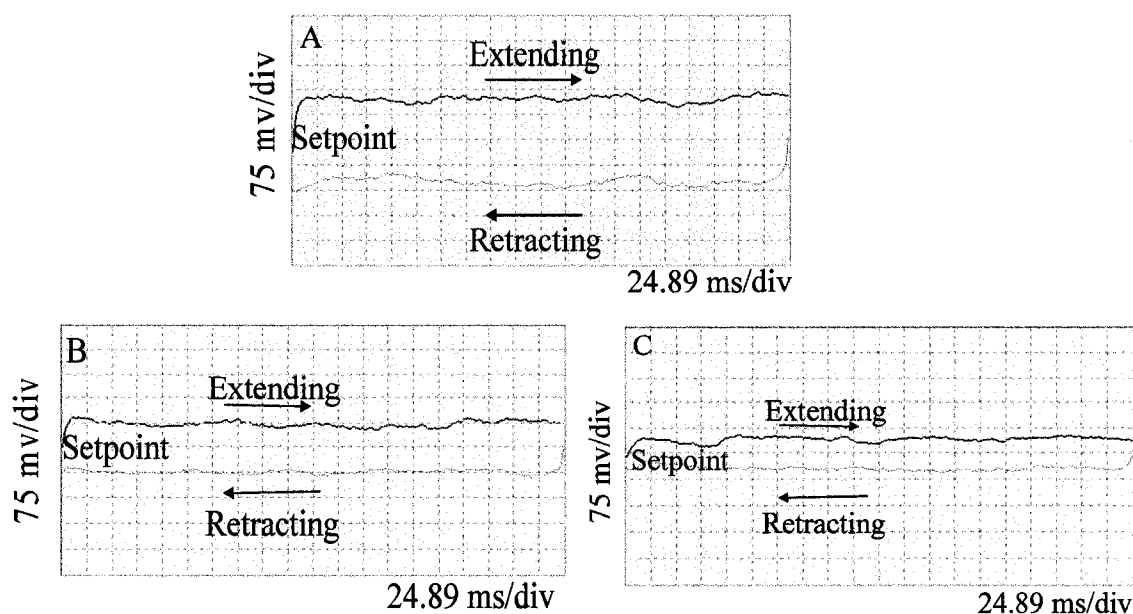


Figure IV-9. Real time AFM friction loops for (A) Neat nylon 6 (B) 5% Tsp-POSS/nylon 6 (C) 10% Tsp-POSS/ nylon 6.

Similar trends were observed in the macroscale relative surface friction measurements. Figure IV-10 (A) and (B) show the macroscale surface friction of HPC's in relation to the POSS type and concentration at external loads of 3N, 4N, and 5N at 10% relative humidity. POSS/nylon HPC's exhibit lower relative surface friction than neat nylon 6 at all loads, with open cage Tsp-POSS/nylon 6 exhibiting lower friction than closed cage Oib-POSS/nylon 6. Reduction in relative surface friction is attributed to the

uniform presence of POSS moieties on the film surface. Additionally, lower friction coefficients for Tsp-POSS HPC's is attributed to its lower surface heterogeneity and better miscibility with nylon 6 compared to Oib-POSS.

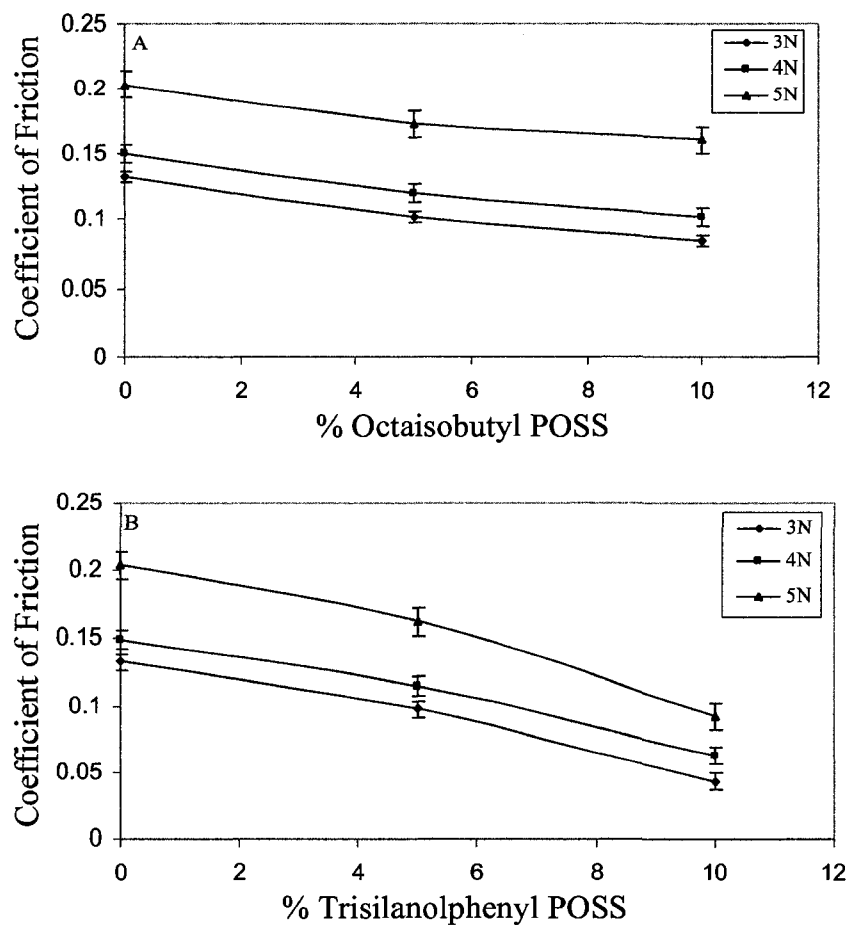


Figure IV-10. Pin-on-disc macroscale relative friction coefficients of (A) Oib-POSS/nylon 6 (B) Tsp-POSS/ nylon 6 HPC's at different external loads.

Nanoindentation force-displacement plots for neat nylon 6 and Tsp-POSS/nylon 6 HPC's are shown in Figure IV-11. For a given applied load maximum penetration depth (Table IV-5) reduces significantly after incorporation of POSS, indicating surface hardening of HPC's. This is attributed mainly to the presence of robust POSS cages on the surface, as established in surface energy and IR studies. Resistance to penetration

increases with increasing POSS concentration, with a 50% reduction in maximum penetration depth for HPC's containing 5 wt.% POSS and a 70% reduction for the 10 wt.% POSS HPC's.

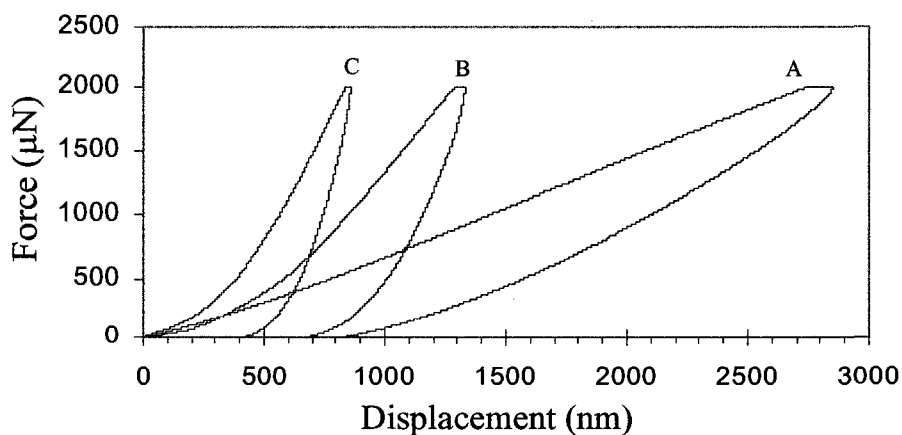


Figure IV-11. Quasi-static nanoindentation force-displacement curves for (A) Neat nylon 6 (B) 5% Tsp-POSS/nylon 6 (C) 10% Tsp-POSS/nylon 6.

Dramatic increase in nanoscale reduced modulus and hardness are observed for all of the HPC's, with increasing hardness and modulus observed with increasing POSS concentration (Table IV-5). Incorporation of 5 wt.% POSS yields a 6-fold increase in the reduced modulus, while 16-fold increases are observed at 10% POSS incorporation.

Table IV-5. Maximum Penetration Depth, Percentage Recovery, Reduced Modulus, and Relative Hardness of POSS/nylon 6 HPC's Obtained *via* Nanoindentation

| Sample | Max. Penetration Depth (μm) | %Recovery | Reduced Modulus (MPa) | Hardness (MPa) |
|-----------------------|--|-----------|-----------------------|----------------|
| Neat Nylon 6 | 2.85 | 71 | 137 | 24 |
| Nylon 6+ 5% Oib-POSS | 1.35 | 59 | 776 | 75 |
| Nylon 6+ 10% Oib-POSS | 0.85 | 55 | 2230 | 166 |
| Nylon 6+ 5% Tsp-POSS | 1.33 | 47 | 987 | 66 |
| Nylon 6+ 10% Tsp-POSS | 0.86 | 48 | 2380 | 157 |

At similar loadings, no significant differences in the nanomechanical properties were observed between Oib- and Tsp-POSS composites, indicating that the preferential segregation of the inorganic POSS cages to the surface is the primary driving force for the observed surface hardening.

In addition to the quasi-static nanomechanical properties, dynamic viscoelastic behavior of POSS/nylon 6 HPC's was studied *via* nano-DMA. Variation of nanoscale dynamic storage modulus as a function of penetration depth is shown in Figure IV-12. All surfaces exhibit higher modulus at low penetration depth (surface) compared to that at higher penetration depth (bulk). This is attributed, in part, to the difference in the time scale of cooling for surface and bulk in the melt blending process. On a molecular level, rapid cooling of the surface restricts chain mobility at the surface compared to the bulk, leading to higher surface modulus. POSS/nylon HPC's exhibit higher modulus at all penetration depths than neat nylon, and appear to reach a stable modulus value at lower penetration depth (~ 325 nm). This result indicates that POSS provides nanoscale reinforcement to the nylon 6 matrix, attributed, in part, to higher restrictions in chain mobility due to the presence of the relatively large POSS domains. While it might be expected that the better dispersed Tsp-POSS molecules with greater interaction with the nylon matrix would yield higher dynamic modulus values, no significant differences were observed for the two systems. As observed in the quasi-static nanoindentation experiments, concentration of inorganic POSS cages at the surface has the greatest effect on the modulus, regardless of the POSS structure (at least within the concentration regime evaluated). The increased surface hardness and modulus explain, in part, the low coefficients of friction observed for the POSS/nylon 6 HPC's.

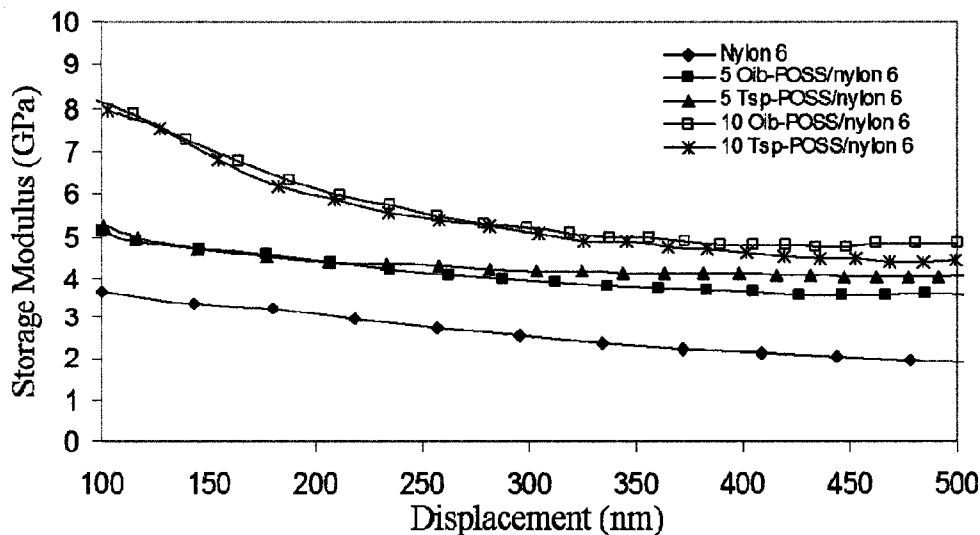


Figure IV-12. Nanoscale dynamic storage modulus as a function of penetration depth for POSS/nylon 6 HPC's.

While dramatic changes were observed in nanomechanical properties of these HPC's, smaller changes were observed in bulk analysis. DMA studies show a small increase in the glass transition temperature (4-5 degrees) and 30 – 46% increases in storage modulus with the incorporation of POSS (Table IV-6). For comparison purposes, glass transition behavior was also analyzed through DSC (Table IV-6), and only marginal increases (2-4 °C) were observed.

Table IV-6. DMA Storage Modulus, Glass Transition Temperature (DMA and DSC), and Melting Temperature (DSC) of POSS/nylon 6 HPC's.

| Sample | Storage Modulus @ 30°C (GPa) | % Increase in Modulus | T _g (°C) (DMA) | T _g (DSC) (°C) | T _m |
|-----------------------|---------------------------------|--------------------------|------------------------------|------------------------------|----------------|
| Neat Nylon 6 | 1.34 | -- | 46 | 49 | 218 |
| Nylon 6+ 5% Oib-POSS | 1.77 | 32 | 51 | 52 | 217 |
| Nylon 6+ 10% Oib-POSS | 1.81 | 35 | 51 | 53 | 217 |
| Nylon 6+ 5% Tsp-POSS | 1.91 | 43 | 50 | 51 | 217 |
| Nylon 6+ 10% Tsp-POSS | 1.96 | 46 | 51 | 52 | 217 |

Minimal improvement in the glass transition behavior can be explained on the basis of two counteracting processes. Formation of POSS aggregates provides an inertial effect by restricting the segmental mobility of polymers, resulting in increase in the T_g .⁶² However, the formation of α -crystals (WAXD studies) is associated with higher chain mobility, causing an increase in the T_g . Balance of these opposing forces is reflected in the marginal change in the T_g of these HPC's. In addition, melting temperatures (Table IV-6), measured via DSC, remains virtually the same for all the samples. These results are consistent with other findings where POSS/polymer physical blends do not show appreciable changes in the bulk thermal behavior.^{6,7,9} While significant increases in storage modulus are observed *via* DMA evaluation, these improvements are minor in comparison to the order-of-magnitude surface modulus improvements observed *via* nanoindentation. Table IV-7 shows the effect of POSS on percentage crystallinity of nylon. These results show that incorporation of POSS leads to an increase in percentage crystallinity indicating that POSS molecules acts a nucleating agent. This result compliments WAXD data in which crystalline POSS peaks were observed. Tsp-POSS owing to its better compatibility and dispersion exhibit less crystallinity compared to more incompatible Oib-POSS.

Table IV-7. DSC Percentage Crystallinity of POSS/nylon 6 HPC's.

| Sample | ΔH_f (J/g) | % X_c |
|-----------------------|--------------------|---------|
| Neat Nylon 6 | 45.9 | 24.4 |
| Nylon 6+ 5% Oib-POSS | 52.2 | 29.2 |
| Nylon 6+ 10% Oib-POSS | 59.7 | 35.3 |
| Nylon 6+ 5% Tsp-POSS | 48.9 | 27.4 |
| Nylon 6+ 10% Tsp-POSS | 49.7 | 29.4 |

In contrast to the nanoindentation experiments, where no significant difference was observed in the nanomechanical properties with the two types of POSS, Tsp-POSS yielded 10% greater improvements in the bulk modulus than the Oib-POSS, presumably due to its increased dispersion and compatibility. The differences in POSS effects on surface and bulk modulus can be explained in part by the relative difference in POSS concentration, which is much higher at the surface. The Tsp-POSS also appears to form larger aggregates at the surface, which may inhibit interaction with the nylon chains, masking any difference in performance between the Tsp-POSS and Oib-POSS composites. In the bulk, the Tsp-POSS is dispersed at the nano-level, allowing greater interaction with the nylon chain. Thus, differences in performance of Tsp-POSS and Oib-POSS composite properties are more apparent in the bulk than at the surface.

Conclusions

As an extension of our previous work on polypropylene/octaisobutyl POSS composites, we have evaluated the effects of POSS structure and theoretical solubility parameter on the morphology and properties of melt blended POSS/nylon 6 composites. This study demonstrates that the morphology and mechanical properties of the composites are dictated by the predicted solubility of the POSS molecule in the nylon 6 matrix. Surface and bulk morphology were evaluated using multiple microscopic (AFM, SEM/EDAX, TEM/EDAX, and WAXD) and spectroscopic (ATR-FTIR) techniques. As predicted by its solubility parameter, Tsp-POSS exhibits greater compatibility, smaller POSS domains and enhanced dispersion in nylon 6 in comparison to Oib-POSS. However, while Tsp-POSS shows nanoscale dispersion in the nylon matrix, both POSS molecules show preferential segregation to the surface, driven by their low surface energy, and formation of larger aggregates at the surface than in the bulk.

Measured nanomechanical and bulk thermomechanical properties are related to the observed composite morphology. Quasi-static nanoindentation studies reveal significantly increased nanoscale surface modulus and hardness for POSS-containing composites. Dynamic nanoindentation (nano-DMA) studies show that HPC's exhibit higher modulus than neat nylon at all penetration depths evaluated. While nano-DMA measurements show a doubling of surface modulus on incorporation of POSS (3.8 MPa for neat nylon vs 8 MPa for 10% POSS-filled composites), only 30% - 40% increases are observed in bulk modulus determined from standard DMA. Greater improvements in bulk modulus were observed for the more compatible Tsp-POSS molecule. Although both types of POSS molecules exhibit preferential segregation to the surface, the Tsp-

POSS shows better miscibility and dispersion due to greater interaction with the nylon matrix, and therefore improved mechanical properties.

Relative surface friction studies using AFM/LFM on nanoscale and pin-on-disc tribometry on macroscale reveal significant friction reduction on incorporation of POSS at both scales. Reduction in relative surface friction is attributed to the presence of POSS aggregates on the surface, increased surface roughness, increased surface hardness and improved nanomechanical properties. The level of friction reduction depends on the molecular structure and concentration of POSS, with Tsp-POSS showing greater effectiveness and a 43% friction reduction on 10% POSS incorporation. Surface wetting characteristics are also altered on incorporation of POSS, with measured water contact angles approaching that of Teflon for 10% filled nylon blends. Dynamic contact angle surface hysteresis measurements indicate the stability of the POSS composite performance, with Oib-POSS exhibiting greater hysteresis due to higher surface roughness and reduced compatibility.

Ultra-low friction, surface hardened, hydrophobic nylon 6/POSS nanocomposites were prepared successfully *via* melt blending. More importantly, friction reduction and non-wetting characteristics were achieved using a non-fluorinated POSS/polymer combination. Combined performance properties of these composites indicate their potential utility for applications such as low friction microelectronics or fabrics. For the blends evaluated, performance is related to the predicted solubility of the POSS in the polymer matrix, indicating the potential to develop POSS nanocomposite systems with desired properties through specific design of the POSS molecular structure.

Acknowledgements

This work was supported by the STTR Program of the National Science Foundation under Award Number OII-0539295 and RET Program of the National Science Foundation under EEC-0602032. This work was also supported by the major research instrumentation program of the National Science Foundation under Award Numbers MRI0421406, DMR0421403 and DMR0215873.

References

-
- ¹ Lichtenhan, J. D. *Comments Inorg. Chem.* **1995**, *17*, 115.
- ² Shockey, E. G.; Bolf, A. G.; Jones, P. F.; Schwab, J. J.; Chaffee, K. P.; Haddad, T. S.; Lichtenhan, J. D. *Appl. Organomet. Chem.* **1999**, *13*, 311.
- ³ Lee, A.; Lichtenhan, J. D. *J. Appl. Polym. Sci.* **1999**, *73*, 1993.
- ⁴ Romo-Uribe, A.; Mather, P. T.; Haddad, T. S.; Lichtenhan, J. D. *J. Polym. Sci., Part B: Polym. Phys.* **1998**, *36*, 1857.
- ⁵ Fu, B. X.; Hsiao, B. S.; Pagola, S.; Stephens, P.; White, H.; Rafailovich, M.; Sokolov, J.; Mather, P. T.; Jeon, H. G.; Phillips, S.; Lichtenhan, J. D.; Schwab, J. *Polymer* **2001**, *42*, 599.
- ⁶ Zhao, Y.; Schiraldi, D. A. *Polymer* **2005**, *46*, 11640.
- ⁷ Fina, A.; Tabuani, D.; Frache, A.; Camino, G. *Polymer* **2005**, *46*, 7855.
- ⁸ Chen, J. H.; Chiou, Y. D. *J. Polym. Sci., Part B: Polym. Phys.* **2006**, *44*, 2122.
- ⁹ Misra, R.; Fu, B. X.; Morgan, S. E. *J. Polym. Sci., Part B: Polym. Phys.* **2007**, *45*, 2441.
- ¹⁰ Lichtenhan, J. D.; Vu, N.Q.; Carter, J.A.; Gilman, J.W.; Feher, F.J. *Macromolecules* **1993**, *26*, 2141.
- ¹¹ Mantz, R.A.; Jones, P.F.; Chaffee, K.P.; Lichtenhan, J.D.; Gilman, J.W.; Ismail, I.M.K.; Burmeister, J. *Chem Mater* **1996**, *8*, 1250.
- ¹² Mather, P.T.; Jeon, H.G.; Romo-Uribe, A.; Haddad, T.S.; Lichtenhan, J. D. *Macromolecules* **1999**, *32*, 1194.
- ¹³ Turri, S.; Levi, M. *Macromolecules* **2005**, *38*, 5569.
- ¹⁴ Turri, S.; Levi, M. *Macromolecular Rapid Communications* **2005**, *26*, 1233.

-
- ¹⁵ Patel, R.R.; Mohanraj, R.; Pittman, C.U. *J Polym Sci Part B: Polym Phys* **2006**, *44*, 234.
- ¹⁶ Lichtenhan, J. D.; Otonari, Y. A.; Carr, M. J. *Macromolecules* **1995**, *28*, 8435.
- ¹⁷ Lee, A.; Lichtenhan, J. D. *Macromolecules* **1998**, *31*, 4970.
- ¹⁸ Haddad, T.S.; Lichtenhan, J. D. *Macromolecules* **1996**, *29*, 7302.
- ¹⁹ Joshi, M.; Butola, B. S. *Polymer* **2004**, *45*, 4953.
- ²⁰ Bharadwaj, R. K.; Berry, R. J.; Farmer, B. L. *Polymer* **2000**, *41*, 7209.
- ²¹ Patel, R. R.; Mohanraj, R.; Pittman, C. U. *J. Polym. Sci., Part B: Polym. Phys.* **2006**, *44*, 234.
- ²² Phillips, S. H.; Haddad, T. S.; Tomczak, S. J. *Current Opinion in Solid State and Materials Science* **2004**, *8*, 21.
- ²³ Mabry, J. M.; Vij, A.; Iacono, S.T.; Grabow, W. W. *ACS Polymer Preprints* **2005**, *46*, 630.
- ²⁴ Tuteja, A.; Choi, W.; Ma, M.; Mabry, J.; Mazzella, S.; Rutledge, G.; Mckinley, G.; Cohen, R. E. *Science* **2007**, *318*, 1618.
- ²⁵ Paul, R.; Karabiyik, U.; Swift, M. C.; Esker, A. R. *Langmuir* **2008**, *24*, 5079.
- ²⁶ Paul, R.; Karabiyik, U.; Swift, M. C.; Hottle, J. R.; Esker, A. R. *Langmuir* **2008**, *24*, 4676.
- ²⁷ Hosaka, N.; Otsuka, H.; Hino, M.; Takahara, A. *Langmuir* **2008**, *24*, 5766.
- ²⁸ Koh, K.; Sugiyam, S.; Morinaga, T.; Ohno, K.; Tsuji, Y.; Fukuda, T.; Yamahiro, M.; Iijima, T.; Oikawa, H.; Watanabe, K.; Miyashita, T. *Macromolecules* **2005**, *38*, 1264.
- ²⁹ Song, C.; Chen, Y.; Gan, D.; Wang, Z. *High Performance Polymers* **2002**, *14*, 183.
- ³⁰ Morgan, S. E.; Misra, R.; Jones, P. J. *Polymer* **2006**, *47*, 2865.

-
- ³¹ Komura, M.; Qiu, Z.; Ikehara, T.; Nakajima, K.; Nishi, T. *Polymer Journal* **2006**, *38*, 31.
- ³² Tabor, D. *The Hardness of Metals*; Oxford University Press: London, 1951.
- ³³ Oliver, W.C.; Pharr, G. M. *J. Mat. Res.* **1992**, *7*, 1564.
- ³⁴ Shen, L.; Phang, I. Y.; Liu, T.; Zeng, K. *Polymer* **2004**, *45*, 3341.
- ³⁵ Beake, B. D.; Chen, S.; Hull, J. B.; Gao, F. *J Nanosci Nanotechnol* **2002**, *2*, 73.
- ³⁶ Hu, Y.; Shen, L.; Yang, H.; Wang, M.; Liu, T.; Liang, T. *Polym Test* **2006**, *25*, 492.
- ³⁷ Park, K.; Mishra, S.; Lewis, G.; Losby, J.; Fan, Z.; Park, J. B. *Biomaterials* **2004**, *25*, 2427.
- ³⁸ Asif, S. A.; Wahl, K. J.; Colton, R. J.; Warren, O. L. *J Appl Phys* **2001**, *90*, 1192.
- ³⁹ Mohanty, B.; Katti, K. S.; Katti, D. R.; Verma, D. *J Mater Res* **2006**, *21* 2045.
- ⁴⁰ Sikdar, D.; Katti, D.; Katti, K.; Mohanty, B. *J. App. Polym. Sci.* **2007**, *105*, 790.
- ⁴¹ Bhushan, B. *Handbook of Micro/Nano Technology*, 2nd ed.; CRC Press: Boca Raton, FL, 1999, 41.
- ⁴² Fowkes, F. M.; Kaczinski, M. B.; Dwight, D. W. *Langmuir* **1991**, *7*, 2464.
- ⁴³ Owens, D. K.; Wendt, R. C. *J Appl Polym Sci.* **1969**, *13*, 1741.
- ⁴⁴ Aharoni, S. M. *n-Nylons*. New York: John Wiley & Sons; 1997.
- ⁴⁵ Hoy, K. L. *J. Paint Technology* **1970**, *42*, 76.
- ⁴⁶ Liu, L.; Ming, T.; Liang, G.; Chen, W.; Zhang, L.; Mark, J. E. *Journal of Macromolecular Science, Part A: Pure and Applied Chemistry* **2007**, *44*, 659.
- ⁴⁷ Hoy, K. L. Group molar-attraction constants. In *Polymer Handbook*, 2nd Edn.; Bradrup, J., Immergut, E.H. (eds.); IV-339. Wiley & Sons: New York, 1975.

-
- ⁴⁸ Grulke, E. A. Solubility parameter values. In *Polymer Handbook*, 4th Edn.; Brandrup, J., Immergut, E. H. and Grulke, E. A (eds.); VII/675ff. Wiley & Sons: New York 1999.
- ⁴⁹ Ferreiro, V.; Coulon, G.; *J Polym Sci, Part B: Polym Phys* **2004**, *42*, 687.
- ⁵⁰ Ferreiro, V.; Pennec, Y.; Seguela, R.; Laureyns, J.; Coulon, G.; *Polymer* **2000**, *41*, 1561.
- ⁵¹ Ferreiro, V.; Depecker, C.; Laureyns, J.; Coulon, G.; *Polymer* **2004**, *45*, 6013.
- ⁵² Urban, M.W. *Vibrational spectroscopy of molecules and macromolecules on surfaces*, John Wiley & Sons, Inc. 1993.
- ⁵³ Enlow, E.M.; Kennedy, J. L.; Nieuwland, A. A.; Hendrix, J. E.; Morgan, S. L. *Applied Spectroscopy* **2005**, *59*, 986.
- ⁵⁴ Galeski, A.; Argon, A. S.; Cohen, R. E. *Makromol Chem* **1986**, *188*, 1195.
- ⁵⁵ Paul, D. R.; Fornes, T. D. *Polymer* **2003**, *44*, 3945.
- ⁵⁶ Illers, K.H.; Haberkorn, H. *Makromol Chem* **1971**, *142*, 31.
- ⁵⁷ Murthy, N. S.; Aharoni, S. M.; Szollosi, A. B. *J Polym Sci, Part B: Polym Phys* **1984**, *23*, 2549.
- ⁵⁸ Salem, D. R.; Moore, R. A. F.; Weigmann, H. D. *J Polym Sci, Part B: Polym Phys* **1987**, *25*, 567.
- ⁵⁹ Holmes, R.; Bunn, D. W.; Smith, D. J. *J. Polym. Sci.* **1955**, *17*, 159.
- ⁶⁰ Brill, R. Z. *Phys. Chem. B* **1943**, *53*, 61.
- ⁶¹ Ruan, J. A.; Bhushan, B. *J. Tribol.* **1994**, *116*, 378.
- ⁶² Wu, J.; Haddad, T. S.; Kim, G. M.; Mather, P. T. *Macromolecules* **2007**, *40*, 544.

CHAPTER V

TAILORING MOLECULAR MISCIBILITY AND CHAIN DYNAMICS OF POSS/
POLYSTYRENE BLENDS: CONTROL OF POSS PREFERENTIAL DISPERSION
STATES

Abstract

Hybrid polyhedral oligomeric silsesquioxane (POSS)/polystyrene nanocomposites with two different POSS molecules, octaisobutyl POSS (Oib-POSS) and trisilanolphenyl POSS (Tsp-POSS), were prepared *via* solution blending in toluene. Molecular miscibility and chain dynamics of the blends in solution and films were investigated in relation to the POSS structure and predicted solubility. Solution dynamics analysis indicates random coil conformation of neat PS and POSS/PS blends, with larger variability in the results for blend solutions. Surface and bulk morphology analysis (AFM/TEM) revealed significant differences in the preferential dispersion states of Tsp- and Oib-POSS molecules. Tsp-POSS, with its greater predicted solubility in PS, exhibited nanoscale dispersion throughout the bulk leading to transparent films. Oib-POSS on the other hand, with its reduced predicted solubility in PS, exhibited preferential surface segregation, aggregation of POSS particles and hazy films. Surface energy measurements showed 78 and 15% fractional surface coverage for Oib-POSS and Tsp-POSS, respectively. Solid-state NMR relaxation studies suggest aggregation of Oib-POSS molecules. Additional NMR studies, including silicon CP/MAS, 2D HETCOR, and WISE, indicate close spatial proximity and interaction between Tsp-POSS molecules and PS chains, contrasting with poor interaction and immiscibility of Oib-POSS with PS.

Introduction

A major challenge in the development of high performance polymeric nanocomposites is the control of nanoparticle dispersion. Polyhedral oligomeric silsesquioxane (POSS) nanostructured chemicals, with their hybrid organic-inorganic nature and flexible functionalization with a variety of organic substituents, yield possibilities to control dispersion and tune compatibility in a wide range of polymer systems.^{1,2} POSS molecules are cage-like structures described by the general chemical structure $R(\text{SiO}_{1.5})_n$, where $n=8, 10$ or 12 . This cage is surrounded by a corona of organic groups and it may be a fully condensed “closed” or an “open” structure. Depending on the nature of the substituents, the size of POSS nanoparticles ranges from 1-3 nm.³ POSS molecules can be incorporated into a polymer matrix by co-polymerization or physical blending routes. The majority of the studies reported to date have focused on the synthesis of POSS copolymers.^{4,5,6,7,8,9,10,11} Limited studies have appeared on the dispersion and bulk thermomechanical characteristics of physically blended POSS/polymer films prepared via melt^{12,13,14} and solution^{15,16} blending. Although bulk solution characteristic such as viscosity¹⁷ have been reported recently, much work lies ahead to develop a molecular level understanding of chain dynamics and conformations in physically blended POSS/polymer nanocomposite solutions and films. Furthermore, understanding of these molecular level processes will help in correlating chemical composition with the segregation and dispersion characteristics of POSS nanoparticles.

Surface segregation, defined as the preferential enrichment of one component of a multi-component system at the air-surface interface, has attracted significant attention. The concept of self-stratification was introduced in 1976 by Funke et al.¹⁸ and is well

documented for polymer blends,^{19,20} block copolymers,^{21,22} and polymer solutions.²³ Our laboratories and others have recently reported surface segregation in POSS/polymer blends. Our studies demonstrated that surface segregation of selected POSS nanoparticles leads to improved surface hydrophobicity and tribomechanical characteristics of melt blended POSS/polymer nanocomposites.^{24,25} Takahara and coworkers²⁶ reported a strong influence of POSS nanofillers on the surface dewetting characteristics of POSS-filled thin polystyrene films. Similarly, Esker and coworkers^{27,28} studied the phase separation behavior and morphological evolution in dewetting thin films of POSS/poly(tert-butyl acrylate) blends as a function of annealing temperature and time. Fukuda et al.²⁹ reported a higher concentration of POSS on the film surface for PMMA/POSS blends, resulting in increased hydrophobicity. Recently, Gupta et al.³⁰ have reported the entropy driven segregation of surface modified cadmium selenide/zinc sulfide core-shell nanoparticles in multilayered composite structures. Similarly, Mackey and coworkers^{31,32} investigated the self-assembly and miscibility behavior of cross-linked polystyrene nanoparticles and dendritic polyethylene blended with high molecular weight polystyrene. These studies underscore the importance of the ratio of the radius of gyration (R_g) of polymer chains to nanoparticle radius on the compatibility, diffusion, and segregation process.

Solid-state nuclear magnetic resonance (NMR) spectroscopy has emerged as a valuable tool to probe the molecular miscibility, interactions and chain dynamics in multi-component hybrid polymer systems.^{33,34,35} Recently, Strachota et al.³⁶ utilized solid-state NMR to study the domain selective relaxation behavior in a variety of POSS reinforced epoxy networks and reported marked motional heterogeneities.

The current study is an attempt to understand the ability to control and tailor the dispersion states of POSS in polymeric films prepared from solution. The effects of POSS structure, molecular miscibility, and chain dynamics on the dispersion and segregation behavior of POSS nanoparticles in solution blended POSS/polystyrene (PS) nanocomposites are examined. Two POSS molecules, a closed cage octaisobutyl POSS (Oib-POSS) and an open cage trisilanolphenyl POSS (Tsp-POSS), with differing solubility parameters and expected compatibility with PS were chosen for evaluation. Solution dynamics were probed *via* static and dynamic light scattering. Molecular miscibility, chain dynamics and dispersion properties in films were investigated utilizing multiple solid-state NMR techniques, including ^{13}C CP/MAS, 2D ^1H - ^{13}C and ^1H - ^{29}Si HETCOR, and wide-line separation (WISE) spectroscopy, as well as AFM, TEM and contact angle studies.

Experimental

Materials

Polystyrene (M_w 280,000 Dalton) and HPLC grade toluene were purchased from Sigma-Aldrich Company (St. Louis, MO). A closed cage octaisobutyl POSS (MSO825) (Oib-POSS) and an open cage trisilanolphenyl POSS (SO1458) (Tsp-POSS) were provided by Hybrid Plastics Inc. (Hattiesburg, MS) as crystalline white powders. All materials were used as received unless otherwise specified. The chemical structures of Oib-POSS and Tsp-POSS are shown in Figure V-1 (A) and (B) respectively.

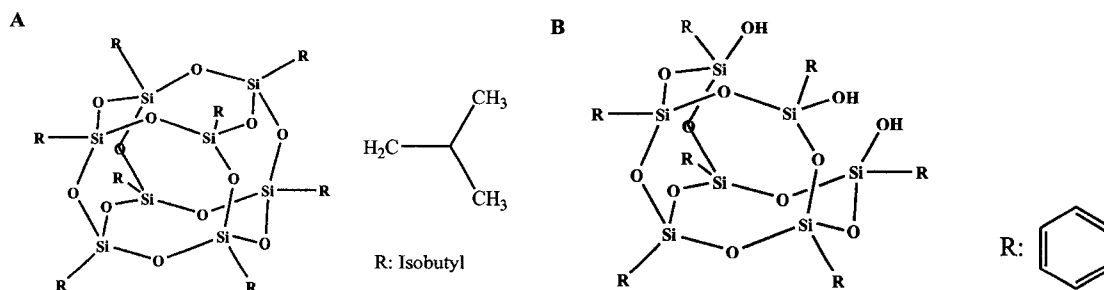


Figure V-1. Schematic structures of (A) Oib-POSS (B) Tsp-POSS.

Composite Preparation

POSS/PS hybrid polymer composites (HPC's) were prepared at concentrations of 0, 5, and 10 weight % of POSS in PS. Both POSS and PS were solution blended in toluene by stirring blend solutions (concentration 10 wt. %) for 12 hrs. Films were prepared using a draw-down bar on a clean glass slide. The films were dried at room temperature for 2 days followed by additional drying under vacuum at 110°C (above the glass transition temperature of PS) for another 12 hrs to remove any residual solvent.

Refractive Index Measurements

Refractive index of neat PS and HPC solutions was measured using a Bausch & Lomb Abbe-3L refractometer. The Prism surface was covered uniformly by placing 2-3 drops of sample using a glass pipette. To avoid scratching of the prism surface, the tip of glass pipette should not touch the prism while placing the sample. Refractive index was measured by placing a crisp demarcation line between the dark and the bright region at the center of the crosshair. In addition, the prism surface was gently cleaned using ethanol and a soft tissue paper after each measurement.

Multiangle Laser-Light Scattering (MALLS)

Multiangle laser-light scattering experiments were performed using a DAWN-DSP (Wyatt Technology Corp., Santa Barbara, CA) in batch mode at 27°C. Vertically polarized He-Ne laser light ($\lambda = 690$ nm) was utilized as an incident beam. Scintillation vials were cleaned thoroughly with filtered DI water and dried before use. POSS/PS blend solutions with concentrations ranging from 1-5 mg/ml were prepared using filtered HPLC grade toluene (Sigma-Aldrich). Blend solutions were filtered using 0.45 μm PTFE filters. The refractive index increment (dn/dc) for each blend solution was measured using a Bausch & Lomb Abbe-3L refractometer. Baseline was established with filtered toluene. Detectors were normalized using a polystyrene standard ($M_w = 44000$ gm/mol) solution. Samples were analyzed in batch mode for 5 minutes. Radius of gyration (R_g), molecular weight (M_w), and second virial coefficient (A_2) were obtained by analyzing Zimm plots using ASTRA for Windows software (version 4.90.07).

Dynamic Light Scattering (DLS)

Dynamic light scattering studies were conducted to evaluate the aggregation behavior of POSS nanoparticles in blend solutions by measuring hydrodynamic radius (R_h). DLS measurements were performed using a Malvern Zetasizer Nanoseries (Worcestershire, UK) with a 4 mW He-Ne laser operating at $\lambda = 632.8$ nm, an avalanche photodiode detector with high quantum efficiency, and an ALV/LSE-5003 multiple tau digital correlator electronics system.

Atomic Force Microscopy (AFM) Surface Morphology

Surface morphology studies were conducted on a MultiModeTM scanning probe microscope from Veeco Instruments, Inc. (Santa Barbara, CA). A silicon probe with a 125 μm long silicon cantilever, nominal force constant of 40 N/m, and resonance frequency of 275 kHz was used for tapping mode surface topography studies. Surface topographies of film samples were studied on 1 μm x 1 μm scan size areas at an image resolution of 512 x 512 pixels and a scan rate of 1Hz. Multiple areas were imaged and figures show representative morphology.

Transmission Electron Microscopy (TEM) Bulk Morphology

Ultra-high resolution transmission electron microscope (JOEL-2100, Joel Ltd., Tokyo, Japan), at an accelerating voltage of 200 kV, was utilized to investigate the dispersion of POSS as well as the resulting microstructure of POSS/PS HPC's. TEM samples were prepared by putting a drop of diluted HPC solution on a 600 mesh copper grid and allowing the solvent to evaporate.

Attenuated Total Reflectance Fourier Transform Infrared (ATR-FTIR) Spectroscopy

To analyze the surface composition of nanocomposite films, Micro ATR-FTIR spectroscopy measurements were conducted on the film surfaces using a Bio-Rad FTS-6000 FTIR single-beam spectrometer with 4 cm^{-1} resolution. The surfaces of each specimen were analyzed using a 2 mm germanium (Ge) crystal with a 45° angle maintaining constant contact pressure between the crystal and the specimens.

Surface Energy Measurements

Surface energy of neat POSS powders was measured according to the Washburn method³⁷ utilizing two probe liquids – benzyl alcohol and diiodomethane (CH_2I_2). The packed cell method was used on a Kruss K100 Tensiometer. The cell, a standard Kruss FL12 cell, was packed with 0.50 grams of powder for each experiment. Hexane was used as the perfect wetting liquid for the material constant experiments. Additionally, the surface energy of HPC film surfaces were calculated utilizing the Fowkes³⁸ and Owens-Wendt method³⁹ by measuring the contact angles with deionized water and glycerol. Static contact angles were measured using the sessile drop technique by a Ramè-Hart goniometer coupled with DROPimage[®] data analysis software.

Solid-State ^{13}C Cross-Polarization/Magic Angle Spinning NMR Spectroscopy

Solid-state NMR spectra were obtained utilizing a Varian^{UNITY} INOVA 400 NMR spectrometer (Varian Inc., Palo Alto, CA) equipped with a standard Chemagnetics 7.5 mm PENCIL[™] style probe. Samples were placed into zirconia rotor sleeves, sealed with Teflon[™] caps, and spun at a rate of 4.0 kHz. Carbon spectra were obtained using the standard cross-polarization/magic angle spinning (CP/MAS) technique. High-power proton decoupling was applied during data acquisition to remove ^1H - ^{13}C dipolar coupling

and yield high-resolution spectra.⁴⁰ Additionally, Total Suppression of Spinning Side bands (TOSS) technique was implemented to remove spinning side bands.⁴¹ The ^1H 90° pulse width was $4.0\ \mu\text{s}$, and the cross-polarization contact time was 1 ms. The dead time delay was $6.4\ \mu\text{s}$ between cross-polarization and proton dipolar coupling. The data acquisition time was 45 ms, with a recycle delay of 7.5 s between scans.

Proton rotating-frame spin-lattice relaxation ($T_{1\rho}$) experiments were performed using a Chemagnetics 4.0 mm probe. Spectra were acquired by applying a ^1H RF spin-locking field prior to cross-polarization. Figure V-2 shows the $T_{1\rho}(\text{H})$ pulse sequence; here the ^1H 90° pulse width was $3.5\ \mu\text{s}$, the cross-polarization contact time was $500\ \mu\text{s}$, and the dead time delay was $6.4\ \mu\text{s}$. The data acquisition period was $30\ \mu\text{s}$, with a ^1H decoupling field of 71.4 kHz applied to remove ^1H - ^{13}C dipolar coupling. The spin rate was 6 kHz, and the recycle delay between scans was 7 seconds. Carbon rotating frame spin-lattice relaxation ($T_{1\rho}(\text{C})$) experiments (Figure V-3) were performed using the 7.5 mm CP/MAS probe. Spectra were obtained by applying a ^{13}C RF spin-locking field immediately after the cross-polarization pulse. The length of spin-locking pulse was varied from 0.25 to 10 ms, and RF fields of 42.8, 45.5, 50, 55.6, and 63.6 kHz were used.

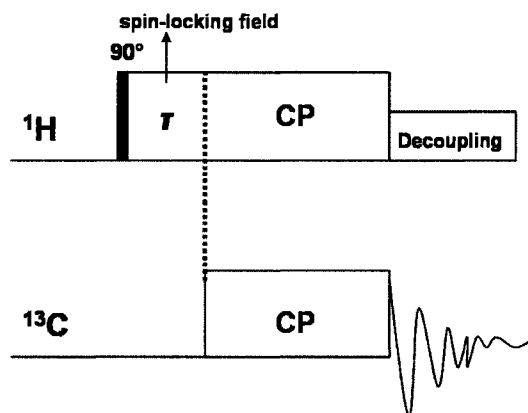


Figure V-2. Schematic representation of $T_{1\rho}(\text{H})$ relaxation experiment pulse sequence.

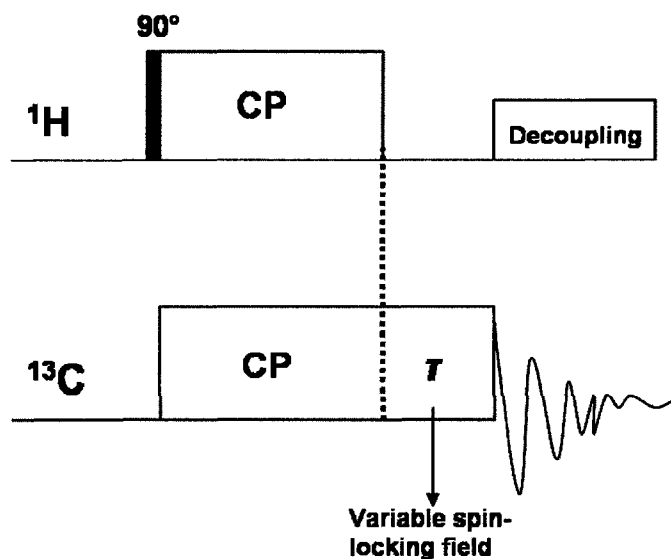


Figure V-3. Schematic representation of $T_{1\rho}(C)$ relaxation experiment pulse sequence.

Solid-State ^{29}Si NMR Spectroscopy

Solid-state ^{29}Si NMR spectra were obtained using a 7.5 mm Chemagnetics standard CP/MAS probe. The standard CP/MAS technique with high-power proton decoupling applied during data acquisition was used.¹ For ^{29}Si spectra, the ^1H 90° pulse width was 4.0 μs , the cross-polarization contact time was 5 ms, and the dead time delay was 6.4 μs . The data acquisition time was 45 ms, with a recycle delay of 4.5 s utilized between consecutive scans. Approximately 1500 scans were accumulated per spectrum. For each spectrum, the free induction decay (FID) was zero-filled to 32k points and a Gaussian filter was applied prior to Fourier transformation.

Solid state ^1H - ^{13}C and ^1H - ^{29}Si HETCOR 2D NMR Spectroscopy

Solid-state ^1H - ^{13}C HETCOR spectra were obtained using sample spinning rate of 3.0 kHz. Homonuclear proton decoupling during t_1 evolution was achieved *via* frequency-switched Lee-Goldburg (FSLG) method.⁴² The number of scans accumulated

for each t_1 point was 192 with t_1 phase cycling achieved using the time proportional phase incrementation (TPPI) method. Selective ^1H - ^{13}C and t_2 acquisition times were 500 μs and 20 ms, respectively. In addition, the TOSS pulse sequence was utilized to suppress the side-bands in the F_2 dimension.² ^1H - ^{29}Si HETCOR spectra were obtained using a spin rate of 2.5 kHz with a cross-polarization and t_2 acquisition time of 1 ms and 20 ms, respectively. The number of scans accumulated for each t_1 point using TPPI phase cycling was 128 with a 4.5 s recycle delay between them. Both dimensions were zero-filled to 2k points and a forward linear prediction was applied to t_1 prior to 2-D Fourier transformation. Data processing was performed using Varian 6.1C software.

Wide-line Separation (WISE) NMR Spectroscopy

Solid-state wide-line separation (WISE) NMR spectroscopy was performed using a standard Chemagnetics 7.5 mm PENCILTM style probe and sample spinning rate of 3.0 kHz.^{43,44} Side bands due to the aromatic ring carbons were suppressed using TOSS. The ^1H 90° pulse width was 4.0 μs , the cross-polarization contact time was 500 μs , and the dead time delay was 6.4 μs . The data acquisition time was 45 ms, with a recycle delay of 4 s utilized between the scans. Sweepwidths in ^1H and ^{13}C spectra were 1250 and 301 ppm, respectively. The number of t_1 increments was 128 with 128 scans per increment. TPPI phase cycling was used to obtain phase-sensitive data, with an additional 192 points added to the F_1 dimension *via* linear prediction. Both dimensions were zero-filled to 2048 points with Lorentzian and Gaussian apodization applied to t_1 and t_2 prior to Fourier transformation.

Results and Discussion

To understand and predict the compatibility and dispersion characteristics of POSS molecules in a PS matrix, theoretical solubility parameters (δ) were estimated via Hoy's method.^{45,46} Materials with similar solubility parameters exhibit greater compatibility and better dispersion characteristics than those with widely differing solubility parameters. In recent studies of POSS/nylon²⁵ and POSS/polysiloxane⁴⁷ melt blends, good agreement between the theoretical solubility parameters and observed microscopic dispersion of POSS particles was reported. Solubility parameters and group molar-attraction constants (ΣG_i) values for the materials used in this study are shown in Table V-1. As expected based on the chemical structures, calculated solubility parameter for Tsp-POSS is closer to that of PS (difference in solubility parameter $\Delta\delta_{\text{Tsp-POSS/PS}} = 0.6$ (cal/cm³)^{1/2}), than δ for Oib-POSS ($\Delta\delta_{\text{Oib-POSS/PS}} = 1.4$ (cal/cm³)^{1/2}). Thus better compatibility and dispersion characteristics are expected for Tsp-POSS in PS.

Table V-1. Theoretical Solubility Parameter Values for PS, Oib-POSS, and Tsp-POSS

| Sample | ρ (gm/cm ³) | M_o (gm/mol) | ΣG_i (kcal.cm ³ /mol) ^{1/2} | δ (cal/cm ³) ^{1/2} |
|----------|------------------------------|----------------|---|--|
| PS | 1.00 | 104 | 0.89 | 9.2 |
| Oib-POSS | 0.92 | 872 | 7.43 | 7.8 |
| Tsp-POSS | 1.16 | 930 | 7.93 | 9.8 |

Refractive index of neat PS and POSS/PS HPC solutions are shown in Table V-2. At 10 wt.% POSS concentration, all solutions exhibit optical transparency with virtually no change in the refractive index, indicating the solubility of POSS molecules and PS chains at the concentrations evaluated. Films formed from Tsp-POSS/PS solutions were transparent, but the Oib-POSS/PS films were hazy, attributed to aggregation and segregation of the Oib-POSS molecules.

Table V-2. Refractive Index of PS and POSS/PS HPC Solutions

| Sample | RI |
|-------------|--------|
| PS | 1.5083 |
| Tsp-POSS/PS | 1.5054 |
| Oib-POSS/PS | 1.5041 |

Multi-angle laser light scattering (MALLS) and dynamic light scattering studies were performed to study PS/POSS interactions in solution. Figure V-4 shows the Zimm plots for neat PS and POSS/PS blends. Table V-3 shows the hydrodynamic radius (R_h), radius of gyration (R_g), weight average molecular weight (M_w), and second virial coefficient (A_2) for neat polymer and POSS blends in toluene. The A_2 value and R_g/R_h ratio determined for PS agree with literature reports for PS in toluene⁴⁸ and the measured molecular weight matches the supplier reported value. In general, measured values for the PS-POSS blends show greater variability than the PS homopolymer parameters, indicating that there may be associations of varying sizes in the POSS/PS solutions. These aggregates act as an independent scattering source and influence intra- and inter-particle interference of light waves, contributing to higher variability. In addition to aggregation, factors including solution concentration, nature of solvent, mixed solvent systems, and aggregate distribution have also been reported to contribute to variability in light scattering experiments.^{49,50,51} In our studies, average values determined for A_2 , R_h and R_g are higher for Oib-POSS/PS blends than those measured for neat PS, indicating more expanded PS chains in the presence of Oib-POSS. The Tsp-POSS/PS blends, on

the other hand, exhibit values within one standard deviation of those measured for neat PS.

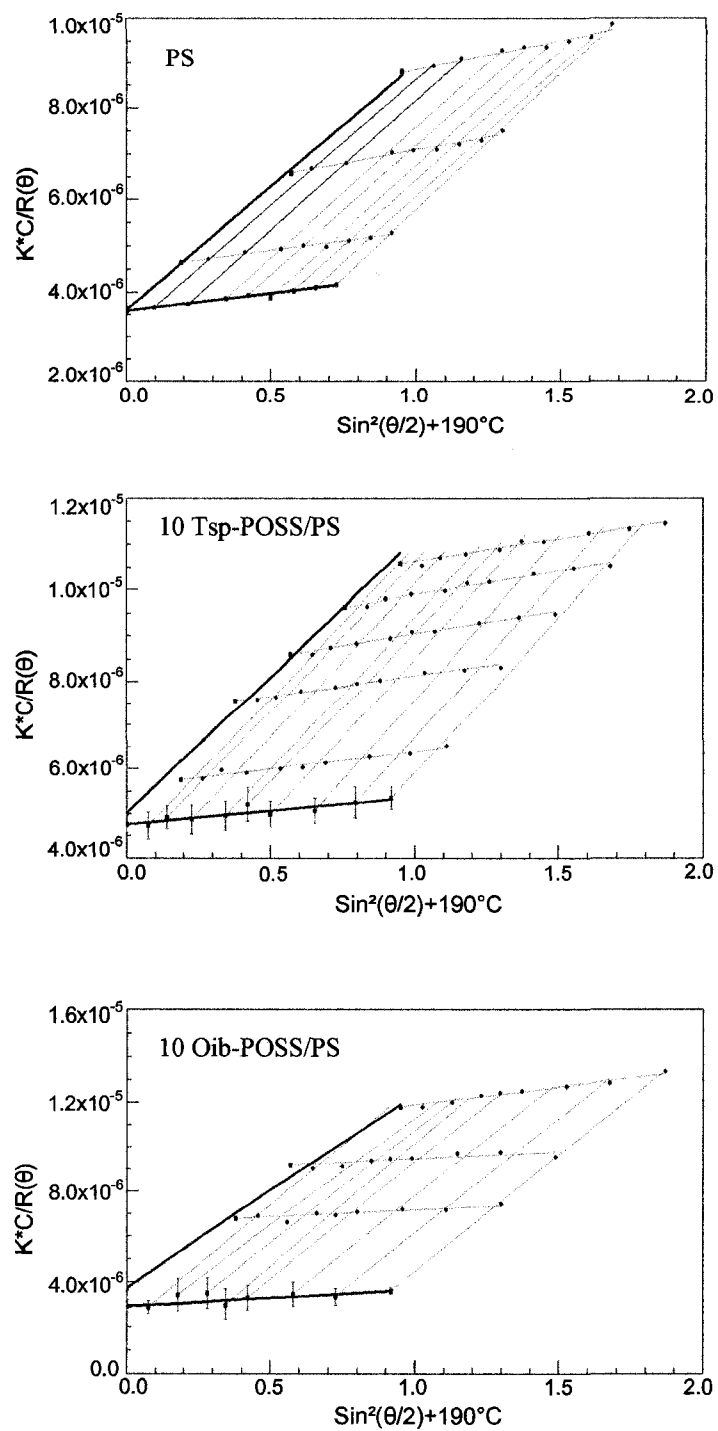


Figure V-4. Multi-angle laser light scattering Zimm plots for PS and POSS/PS HPC's.

Differences in the light scattering behavior can be explained by the differing solubility parameters. Tsp-POSS is predicted to show greater interaction with the PS chain, and thus a smaller radius is expected. Oib-POSS, on the other hand, owing to its larger difference in solubility parameter and structural incompatibility with PS acts as a defect in the PS chain conformation. This increases the mass weighted average distance from the center of mass and results in a higher radius value. Calculated R_g/R_h ratios indicate that all three solutions exhibit random coil conformation in toluene solution, as they fall in the range of values generally considered to represent random coils (R_g/R_h of 1.27-2.05).^{52,53}

Table V-3. Dynamic and Static Light Scattering Data for PS and POSS/PS HPC's (\pm Values indicate One Standard Deviation)

| Sample | R_h (nm) | R_g (nm) | $x=(R_g/R_h)$ | $M_w * e^{-5}$ (gm/mol) | $A_2 * e^{-5}$ (mol ml/gm ²) |
|-------------|----------------|----------------|----------------|----------------------------|---|
| PS | 19.8 \pm 1.1 | 27.0 \pm 2.0 | 1.36 \pm 0.2 | 2.8 \pm 0.1 | 5.1 \pm 0.2 |
| Tsp-POSS/PS | 16.8 \pm 1.5 | 23.5 \pm 6.5 | 1.39 \pm 1.1 | 2.9 \pm 0.2 | 5.8 \pm 0.5 |
| Oib-POSS/PS | 22.5 \pm 2.1 | 33.0 \pm 7.5 | 1.47 \pm 2.2 | 2.9 \pm 0.5 | 8.2 \pm 0.7 |

Tapping mode AFM phase images of the samples are shown in Figure V-5 (A)-(C). Neat PS exhibits a smooth featureless surface (root mean square roughness, RMS, of 0.17 nm), while the POSS samples show raised features attributed to POSS aggregates and crystallites. Oib-POSS/PS samples exhibit relatively large raised and elongated surface features (avg. diameter \sim 50 nm) with broad particle size distribution, while Tsp-

POSS/PS samples exhibit surface features an order of magnitude smaller in size (avg. diameter ~5 nm) with narrow size distribution (Table V-4).

Table V-4. AFM Particle Size Analysis of POSS/PS HPC's

| Dimension | Mean | Minimum | Maximum | Sigma |
|--------------------|------|---------|---------|-------|
| <u>Tsp-POSS/PS</u> | | | | |
| Diameter (nm) | 5.7 | 2.2 | 38.9 | 5.1 |
| Length (nm) | 12.4 | 2.8 | 87.9 | 14.8 |
| <u>Oib-POSS/PS</u> | | | | |
| Diameter (nm) | 48.9 | 11.0 | 436 | 67.8 |
| Length (nm) | 81.8 | 13.8 | 851 | 128 |

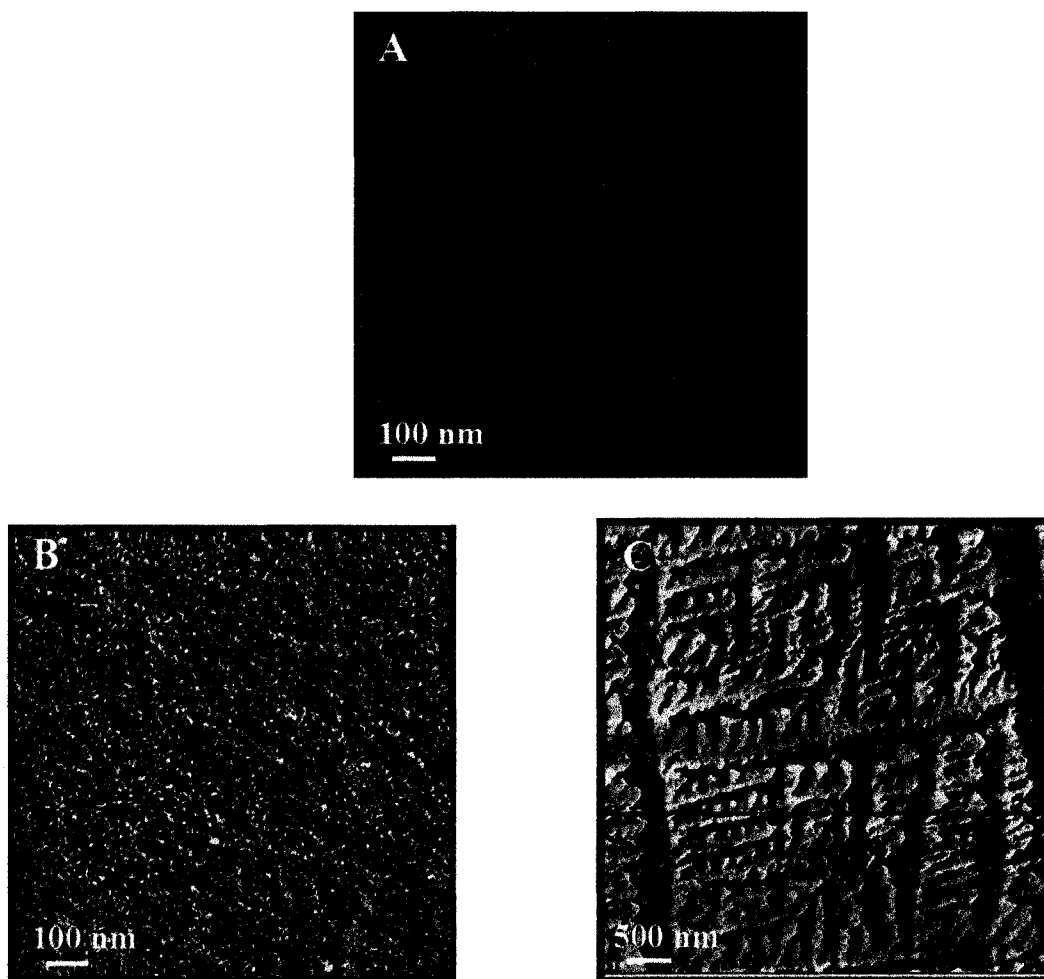


Figure V-5. AFM phase images of (A) Neat PS (B) Tsp-POSS/PS (C) Oib-POSS/PS.

In addition, Oib-POSS samples exhibit significantly higher roughness values (RMS roughness= 4.6 nm), while Tsp-POSS blends yield roughness values similar to those of the neat PS surface (RMS roughness= 0.19 nm) (Table V-5). Surface morphology analysis indicates preferential segregation of Oib-POSS aggregates to the surface, which is further indicated by surface energy and bulk morphology analyses discussed in later sections. Differences in the dispersion and migration behavior are linked to the structural differences in the two types of POSS. The greater solubility of Tsp-POSS in PS, due to its phenyl substituents, allows greater POSS-PS intermolecular attractions and results in smaller and more uniform POSS domains. In Oib-POSS samples, on the other hand, POSS-PS interactions are weaker while POSS-POSS interactions are stronger, resulting in larger POSS aggregates.

Table V-5. AFM Surface Roughness of PS and POSS/PS HPC's.

| Sample | RMS Roughness (nm) | Mean Roughness (nm) | Max. Height (nm) |
|-------------|--------------------|---------------------|------------------|
| PS | 0.17 | 0.13 | 1.8 |
| Tsp-POSS/PS | 0.19 | 0.16 | 2.3 |
| Oib-POSS/PS | 4.64 | 3.88 | 24.5 |

TEM micrographs of Tsp-POSS and Oib-POSS/PS blends are shown in Figures V-6 (A) and (B), respectively. In the Tsp-POSS sample, small aggregates (5-10 nm) are observed distributed evenly through the bulk. The Oib-POSS sample shows large (> 100 nm), widely dispersed aggregates. This behavior is consistent with the theoretical solubility predictions, and the enhanced Tsp-POSS dispersion is attributed to its higher

compatibility with PS. The TEM studies also indicate that Oib-POSS preferentially migrates to the surface, while Tsp-POSS remains dispersed throughout the bulk.

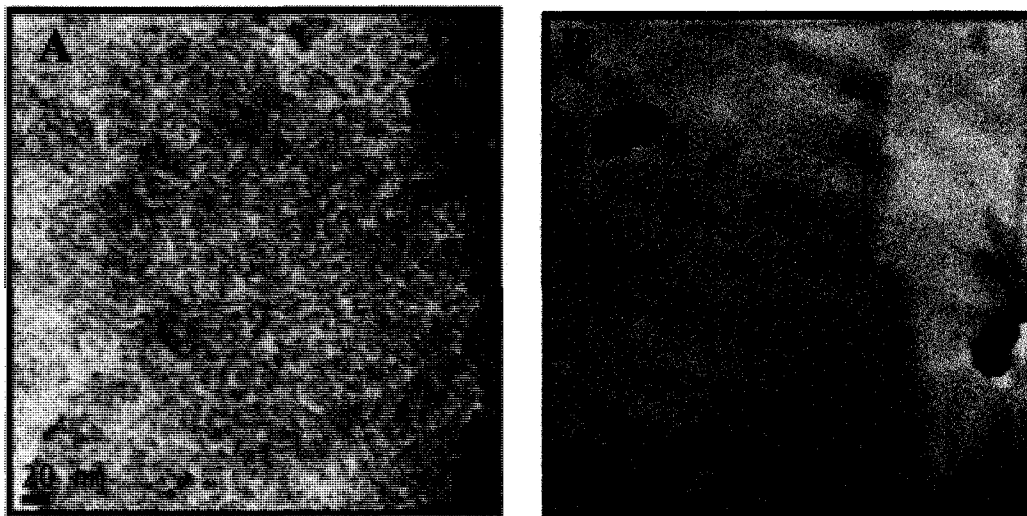


Figure V-6. TEM micrographs of (A) Tsp-POSS/PS (B) Oib-POSS/PS HPC's.

ATR-FTIR analyses (Figure V-7) further provide support for the differences in the dispersion states of Oib- and Tsp-POSS in PS matrix. For reference purposes, IR spectra of neat POSS and PS are shown along with the POSS/PS spectra. Characteristic absorbances are observed in the pure POSS trace at 1100 cm^{-1} , attributed to Si-O-Si stretching vibrations, at 1134 cm^{-1} related to Si-OH stretching vibration, and at 1230 cm^{-1} corresponding to $-\text{CH}_2$ symmetric stretching vibrations and Si-C symmetric vibrations. These absorbances are absent in the neat PS spectrum which shows characteristic absorbances at 1030 cm^{-1} corresponding to C-H bending vibration of phenyl ring, at 1451 cm^{-1} corresponding to C-H deformation vibration of PS backbone, and at 1492 cm^{-1} corresponding to C-H stretching vibration of phenyl ring in PS. Spectra of POSS/PS HPC's exhibit absorbances corresponding to both neat POSS and PS indicating composite nature of the surface. However, Oib-POSS/PS exhibits a sharp and

high intensity absorbance at 1100 cm^{-1} whereas Tsp-POSS shows a broad and low intensity absorbance at 1134 cm^{-1} . Comparison of absorbance pattern for both HPC's suggests that Oib-POSS prefers surface compared to Tsp-POSS. Microscopic (TEM/AFM) and spectroscopic analyses coupled with roughness measurements, and theoretical solubility predictions, support the observed differences in the dispersion states of Oib- and Tsp-POSS.

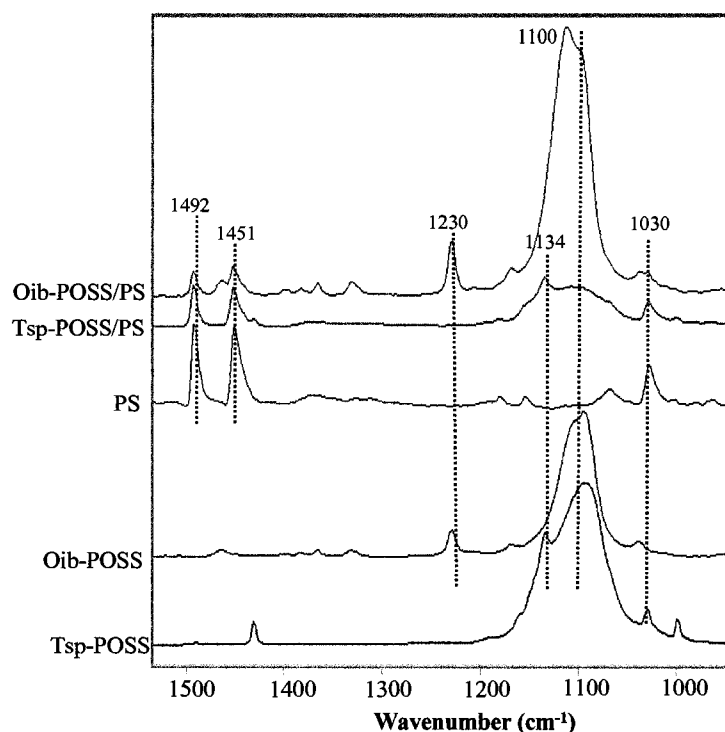


Figure V-7. ATR-FTIR spectra of POSS/PS HPC's.

Surface energy measurements provide further indication of Oib-POSS surface segregation. Table V-6 shows the surface energy of neat PS, POSS, and POSS/PS HPC's. Surface segregation of additives is often attributed to the drive to minimize overall surface energy. Oib-POSS/PS films exhibit a surface energy value of 24 mN/m , similar to that of neat Oib-POSS, indicating significant surface segregation. Tsp-

POSS/PS films, on the other hand, yield surface energy measurement of 35 mN/m, similar to that of neat PS (34 mN/m), indicating minimal surface segregation.

Table V-6. Surface Energy of Neat PS, POSS, and POSS/PS HPC's

| Sample | Surface Energy (mN/m) |
|---------------|-----------------------|
| Neat PS | 34.0 |
| Neat Oib-POSS | 21.3 |
| Neat Tsp-POSS | 23.7 |
| Tsp-POSS/PS | 35.0 |
| Oib-POSS/PS | 24.0 |

Assuming the surface energy of the composite is proportional to the fractional surface coverage of POSS (f_{POSS}), equation 1 can be used to estimate f_{POSS} .

$$f_{\text{POSS}} = (\gamma_{\text{composite}} - \gamma_{\text{PS}}) / (\gamma_{\text{POSS}} - \gamma_{\text{PS}}) \quad (1)$$

For Oib-POSS/PS composites, f_{POSS} is estimated at 78%, while Tsp-POSS/PS composites yield an estimate of 15% f_{POSS} .

Thermodynamic driving forces for dispersion and segregation behavior of the POSS/PS blends can be examined using the Gibbs free energy (ΔG) equation (2), written in equation 3 for mixtures in terms of solubility parameters and volume fraction of each component.

$$\Delta G_m = \Delta H_m - T\Delta S_m \quad (2)$$

$$\Delta G_m = V_1(\delta_1 - \delta_2)^2 \Phi_1\Phi_2 + RT(n_1 \ln \Phi_1 + n_2 \ln \Phi_2) \quad (3)$$

V = molar volume, δ = solubility parameter, Φ = volume fraction, n = mole fraction

R = gas constant, T = absolute temperature

Minimization of the positive enthalpy term and minimal decreases in entropy are necessary to achieve good mixing. If enthalpic interactions are substantially greater in magnitude than entropic interactions, the dispersion state is decided primarily by the difference in the solubility parameters. For Oib-POSS/PS blends, the relatively large difference in solubility parameters ($\Delta\delta_{\text{Oib-POSS/PS}} = 1.4 \text{ (cal/cm}^3)^{1/2}$) results in non-favorable enthalpic interactions that promote surface segregation of the POSS. In the Tsp-POSS case, the more favorable enthalpic interactions indicated by the similar solubility parameters ($\Delta\delta_{\text{Tsp-POSS/PS}} = 0.6 \text{ (cal/cm}^3)^{1/2}$) allow dispersion of Tsp-POSS throughout the bulk PS matrix.

If entropic forces dominate, the entropic penalty imposed by the presence of POSS particles on the mobility of the polymer chain becomes important. The size of POSS aggregates relative to the size of the polymer chains is critical. Theoretically, if the size of POSS aggregates is small compared to the radius of gyration (R_g) of the polymer chains, the entropic penalty for incorporating POSS into the polymer matrix should be small due to the minimal constraints placed on the conformation of the chains. In contrast, if the POSS aggregate size is large relative to R_g , the entropic penalty will be high due to the retardation of segmental motion of the polymer chains. In order to offset this high entropic penalty, individual polymer chains will extend and stretch away from POSS aggregates, driving surface segregation. Based on combined enthalpic and entropic considerations, it is therefore expected that in a PS matrix Tsp-POSS should disperse throughout the bulk, while Oib-POSS should segregate to the surface. Our TEM, AFM and surface energy results support this hypothesis.

Molecular miscibility and chain dynamics of the composites were analyzed through a series of solid state NMR studies. Carbon CP/MAS spectra of open cage Tsp-POSS acquired with and without TOSS sequence are shown in Figures V-8(A) and (B), respectively. Sharp peaks are observed due to the crystalline nature of modified POSS. The four different NMR signals correspond to the phenyl carbons at the para- (**a**, 132 ppm), meta- (**b**, 128 ppm), and ortho- (**c**, 136 ppm) positions. The phenyl carbon attached to silicon oxide moiety on the POSS cage is labeled **d** (130 ppm).

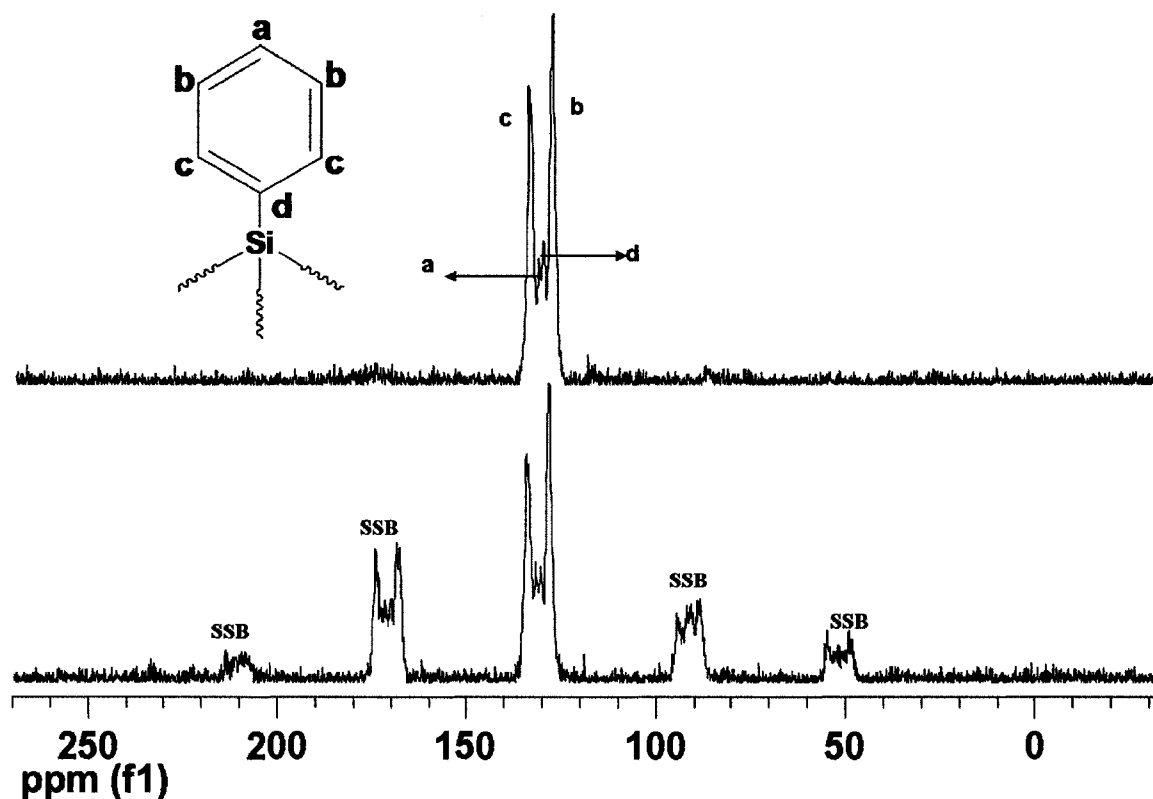


Figure V-8. ^{13}C CP/MAS spectra of Tsp-POSS (A) before and (B) after TOSS sequence.

Carbon CP/MAS spectra of all samples are shown in Figures V-9 (A)-(C). The PS spectrum exhibits resonances corresponding to the backbone methylene carbon **a** (39 ppm), the methine carbon **b** (42 ppm) attached to the phenyl ring, the quaternary aromatic carbon **c** (~145 ppm) and the aromatic carbons of phenyl ring at ortho-, meta-,

and para-positions **d**, **e**, and **f** (120–137 ppm), respectively. The POSS/PS HPC spectrum shows signals corresponding to the aliphatic backbone carbon of the PS matrix as well as overlapping aromatic carbon peaks due to the presence of phenyl groups in both Tsp-POSS and PS. The small shoulders observed in the HPC spectra are probably due to the Tsp-POSS material. Although the low signal-to-noise ratio prevents any extensive analysis, the broadness of the resonances suggest the modified POSS material is not in its original form, which in turn supports earlier data indicating its dispersion throughout the PS matrix.

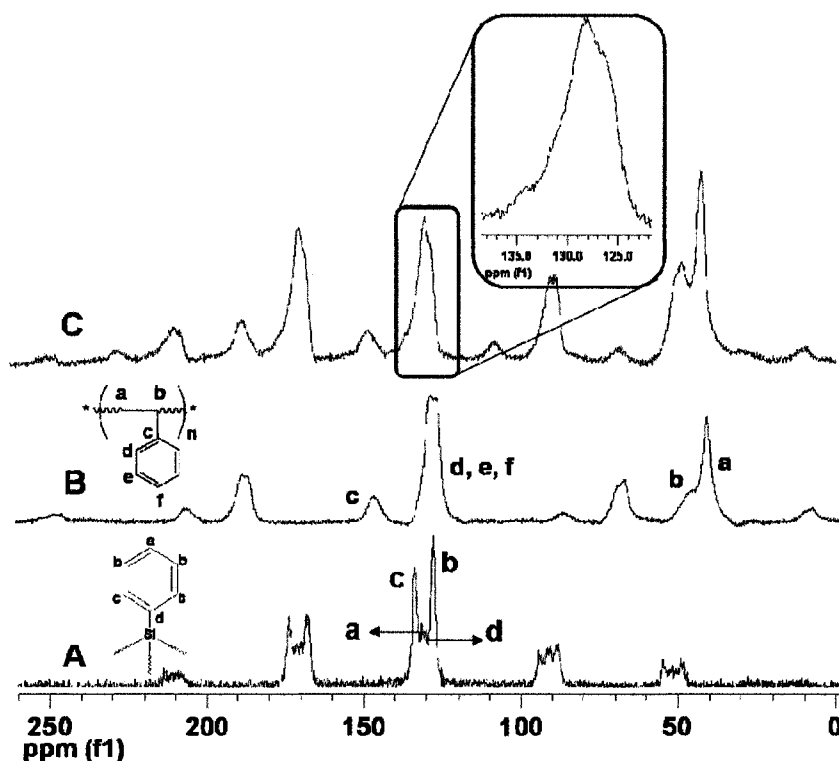


Figure V-9. ^{13}C CP/MAS spectra of (A) Neat Tsp-POSS (B) Neat PS (C) Tsp-POSS/PS HPC.

Silicon CP/MAS NMR studies were implemented to obtain additional structural information regarding the interaction between Tsp-POSS and the PS matrix. The neat Tsp-POSS spectrum has sharp, narrow peaks between -64 and -72 ppm and -76 and -

82 ppm, corresponding to T₂ and T₃ sites, respectively (Figure V-10 (A)). Unmodified closed cage POSS, a T₈ structure, has resonances between -65 to -67 ppm; thus, the chemical shift values observed for Tsp-POSS, a T₇ structure, are consistent.^{54,55,56} However, upon blending Tsp-POSS with the PS matrix the ²⁹Si spectra broadens considerably (Figure V-10 (B)). This is attributed to Tsp-POSS losing its crystalline nature and instead becoming dispersed on a molecular scale via π - π interactions. This is confirmed by comparing the ²⁹Si spectra of Oib-POSS and its HPC (Figures V-11 (A) and (B)). Both samples show only a single, sharp resonance at -66 ppm. This indicates that the crystalline nature of Oib-POSS remains unchanged when blended into the PS matrix, and thus the POSS is not dispersed at the nanoscopic level. This hypothesis was further verified by two dimensional heteronuclear correlation experiments (¹H-¹³C and ¹H-²⁹Si 2D HETCOR).

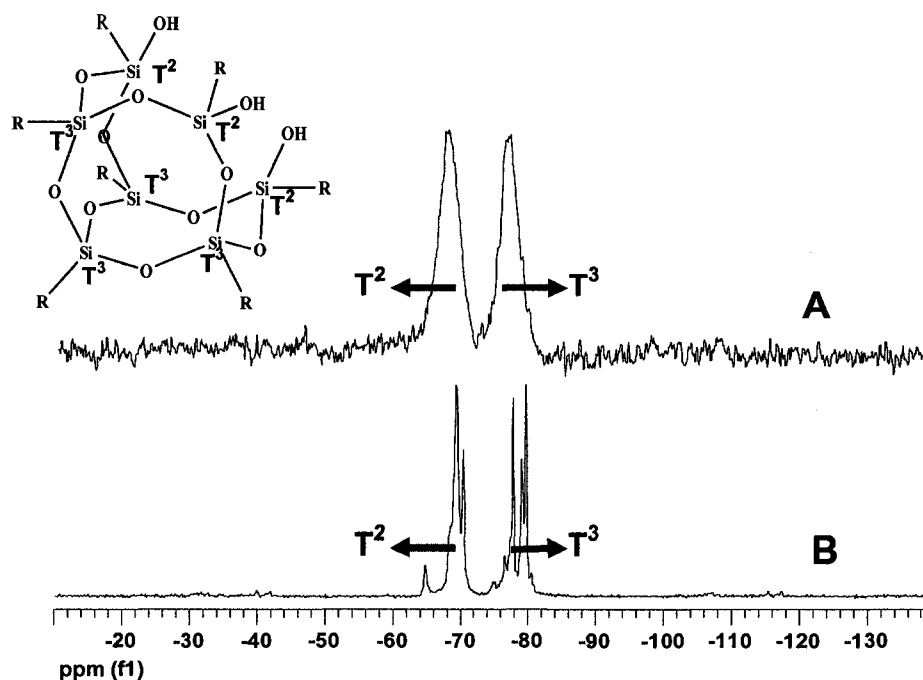


Figure V-10. ²⁹Si spectra of (A) Tsp-POSS (B) Tsp-POSS/PS samples.

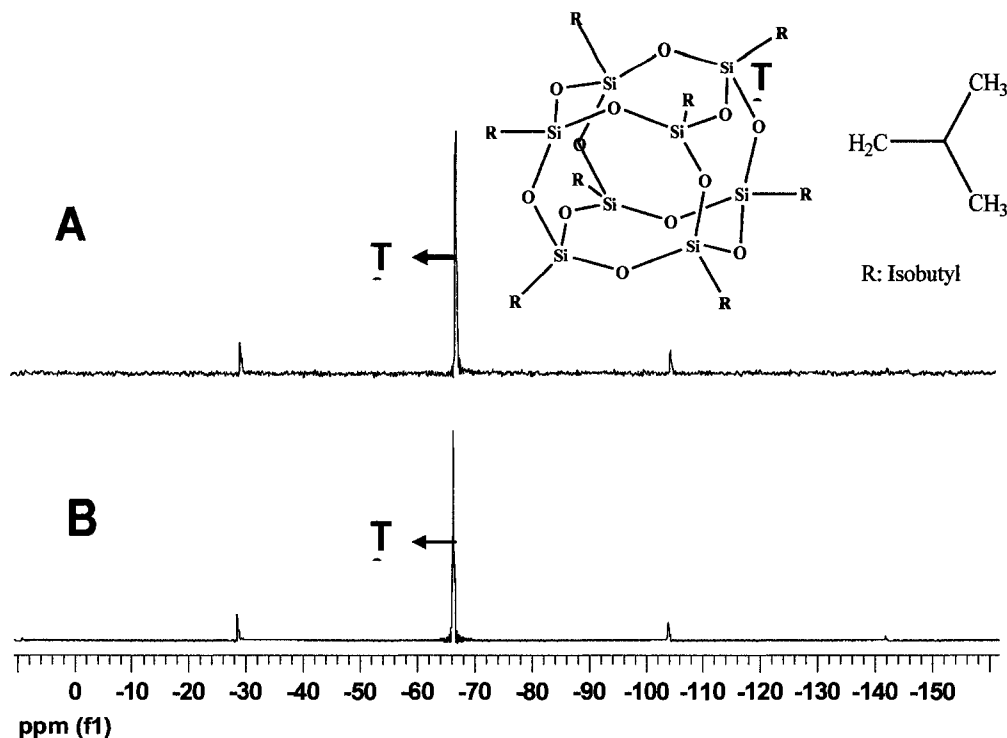


Figure V-11. ^{29}Si spectra of (A) Oib-POSS (B) Oib-POSS/PS samples

In 2D heteronuclear correlation NMR experiments chemical shifts from dipole coupled species are separated into different frequency dimensions. Recent studies have successfully utilized this technique in elucidating phase structure and chemical interactions in polymer blends.^{57, 58} Figure V-12 shows the 2D contour plot of the ^{13}C $\{^1\text{H}\}$ HETCOR spectrum of Tsp-POSS/PS, with the ^1H projection and a separately acquired ^{13}C CP/MAS spectra plotted along the horizontal and vertical axis, respectively. The ^1H projection shows two broad proton resonances attributed to aromatic protons (downfield) and aliphatic protons (upfield). The aromatic and aliphatic carbons for PS are strongly correlated to both proton analogs. This is expected, since all the carbon and proton sites are in close proximity. In addition, however, there is a small but observable

correlation between the downfield shoulder of the aromatic ring carbon, due to the phenyl groups of Tsp-POSS.

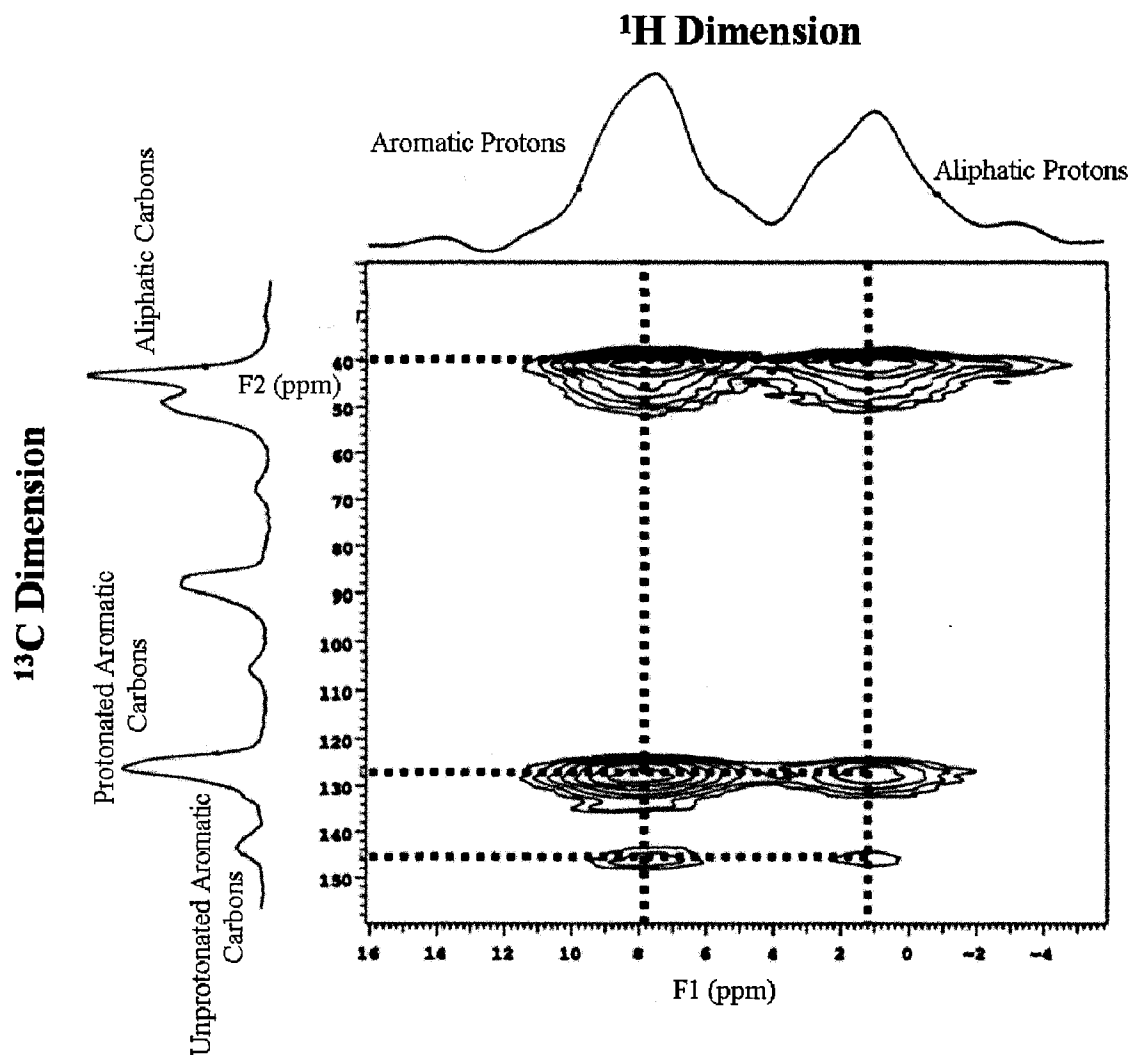


Figure V-12. $^{13}\text{C}\{^1\text{H}\}$ CP/MAS HETCOR 2D contour plot of Tsp-POSS/PS HPC.

The $^{29}\text{Si}\{^1\text{H}\}$ CP/MAS HETCOR 2D contour plot is shown in Figure V-13, with a separate ^{29}Si CP/MAS spectrum and the ^1H projection shown along the vertical and horizontal axis, respectively. The contour plot clearly shows the two ^{29}Si peaks (T_2 and T_3) correlate only to the aromatic ^1H moiety. This supports Tsp-POSS being in close spatial proximity with nearby PS chains. Similar spectra were also acquired for

Oib-POSS/PS HPC's (Figure V-14). The plot shows only a weak correlation between the isobutyl aliphatic protons (assignment based on the small width of the ^1H projection) and the with T_3 silicon site. This indicates that Oib-POSS molecules are located spatially far from PS chains, and is in line with the light scattering observations discussed earlier.

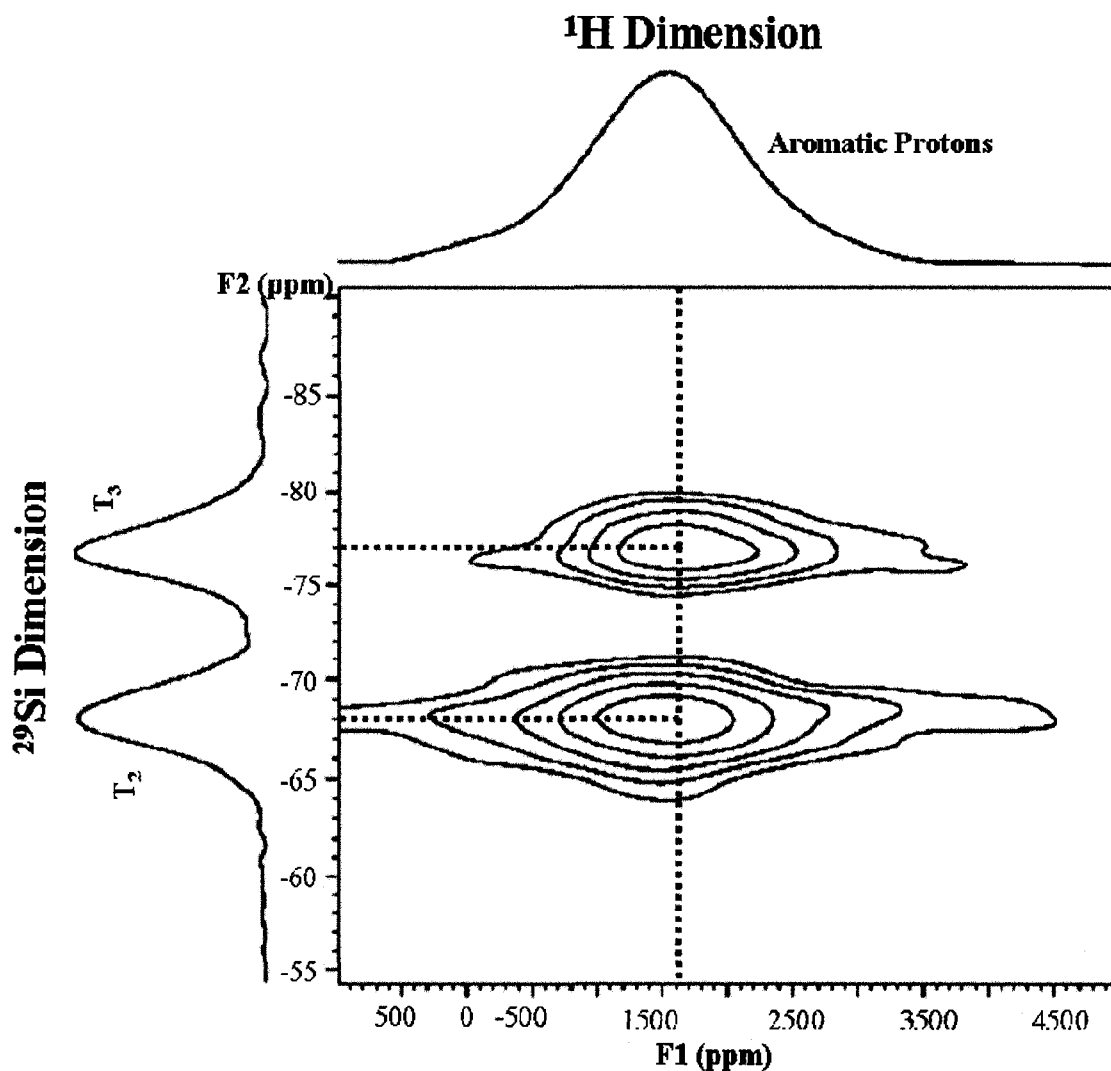


Figure V-13. $^{29}\text{Si}\{^1\text{H}\}$ CP/MAS HETCOR 2D contour plot of Tsp-POSS/PS HPC.

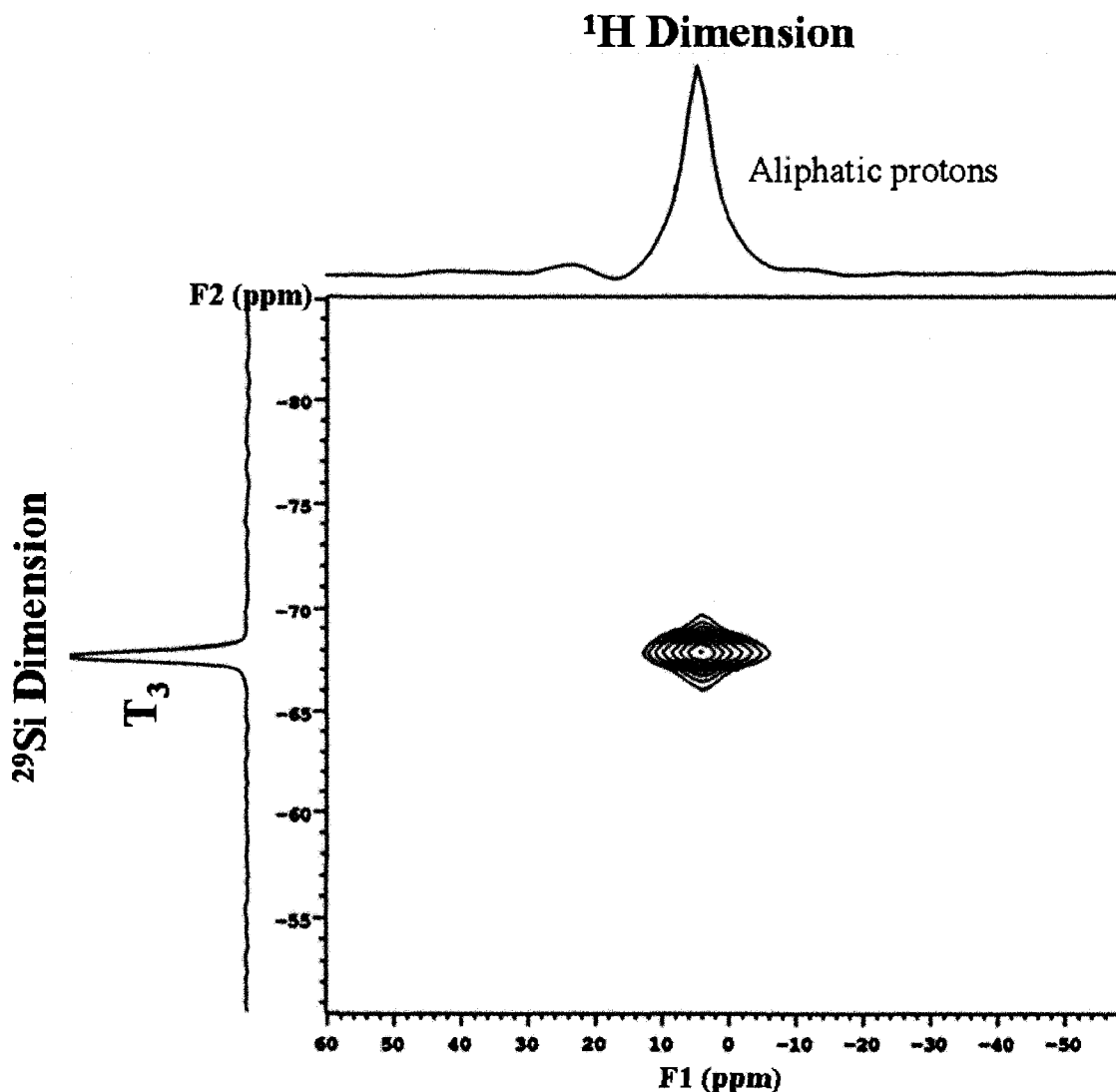


Figure V-14. $^{29}\text{Si}\{^1\text{H}\}$ CP/MAS HETCOR 2D contour plot of Oib-POSS/PS HPC.

Furthermore, solid-state rotating frame proton spin-lattice relaxation ($T_1(\text{H})$) experiments, which are sensitive to the molecular motions occurring in the 10-100 kHz range, were performed to gain additional insight about the miscibility and homogeneity of POSS/PS HPC's. The numerical values of relaxation time constant are associated with the number of phases in a mixture, which in turn provides information about the miscibility and homogeneity in a multi-component polymer system at the nanometer

scale. Figure V-15 shows the plot of ^{13}C resonance intensity versus delay time for the selected aromatic carbon of all samples. Within the experimental error, T_1 (H) relaxation decay of Tsp-POSS/PS HPC's follows a mono-exponential trend which overlaps with the relaxation decay of neat PS, indicating a homogeneous distribution of Tsp-POSS in the polystyrene matrix. However, the relaxation decay for the aromatic signal of Oib-POSS/PS HPC's shows a deviation from mono-exponential behavior and exhibits a different decay rate. This observation indicates inhomogeneity in the Oib-POSS/PS samples due to the favorable aggregation of Oib-POSS.

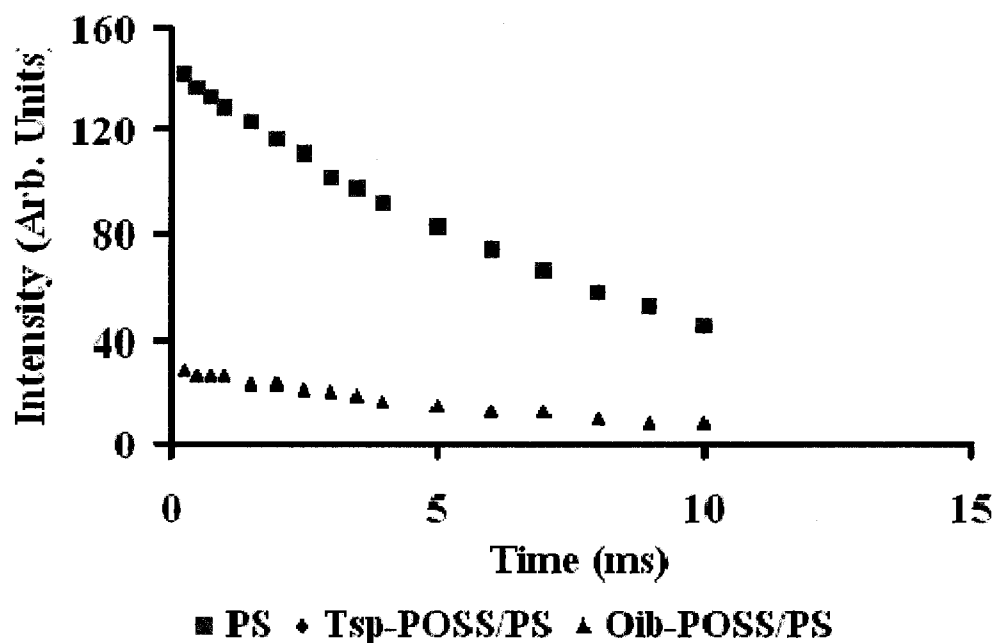


Figure V-15. $T_{1\rho}$ (H) relaxation decay of neat PS and POSS/PS HPC's.

It should be noted that T_1 (H) measurements are dominated by spin diffusion and provide information about the relaxation of the whole system rather than the dynamics of chain segments. In order to understand factors favoring the better miscibility in the Tsp-POSS/PS system, carbon rotating frame spin-lattice relaxation times (T_1 (C)) were measured. Carbon T_1 relaxation is not influenced by spin diffusion, due to small ^{13}C - ^{13}C

dipolar coupling arising from the low natural abundance and large separation of the nuclei. It should be noted that the decay of ^{13}C magnetization under spin-locking conditions is the sum of ^{13}C T_1 and cross relaxation between carbons and protons ($T_{1\text{CH}}^{\text{D}}$). For carbons in semi-crystalline polymers, the $T_{1\text{CH}}^{\text{D}}$ term dominates, whereas for carbons in glassy polymers the main term is ^{13}C T_1 spin-lattice relaxation.

To understand the relaxation processes contributing to $T_1(\text{C})$ and to probe the effect of POSS molecules on the chain dynamics of the PS matrix, $T_1(\text{C})$ relaxation times of the aromatic region for the Tsp-POSS cage, aromatic region of the PS chain and backbone aliphatic region of PS were measured at various spin locking fields. Here an exponential dependence on the RF spin-locking field indicates the domination of the cross-relaxation mechanism, while a quadratic dependence means molecular motion is dominant. Figures V-16 and V-17 show the RF-dependence of the $T_1(\text{C})$ relaxation times for the aromatic and aliphatic sites, respectively. There is no clear trend observed for the aromatic carbons for PS and Tsp-POSS, and the Oib-POSS/PS material shows little variation with RF spin-locking strength. The complexity in the relaxation behavior for the phenyl rings is probably due to the large chemical shift anisotropy of these moieties, which provides an additional relaxation mechanism. Figure V-17, however, clearly shows the presence of Tsp-POSS affects $T_1(\text{C})$ relaxation times for the aliphatic carbon positions. This is expected, since the motional behavior of the polymer backbone would be affected by Tsp-POSS segregating close to the PS chains (via π - π interactions between phenyl rings). The presence of Oib-POSS, while slightly increasing $T_1(\text{C})$ relaxation times, does not perturb the overall RF-field dependence. This behavior is consistent with Oib-POSS acting simply as a filler material.

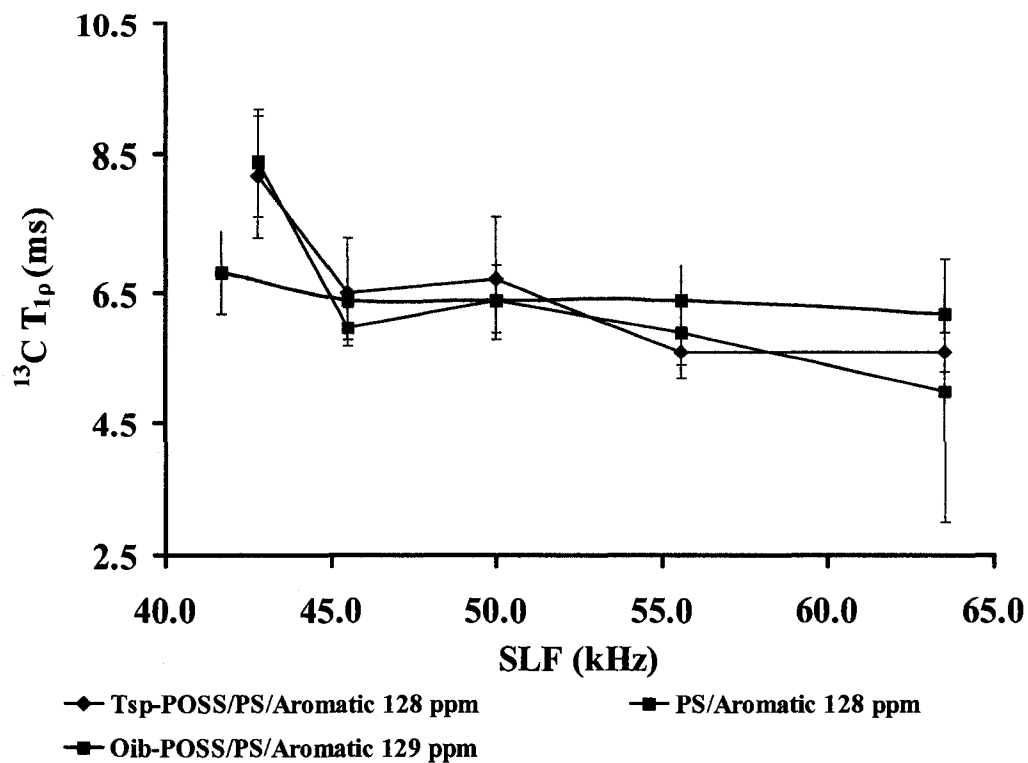


Figure V-16. Change in $T_{1\rho}(C)$ relaxation time of aromatic region of PS, Tsp-POSS/PS, and Oib-POSS/PS HPC's as a function of spin-locking fields.

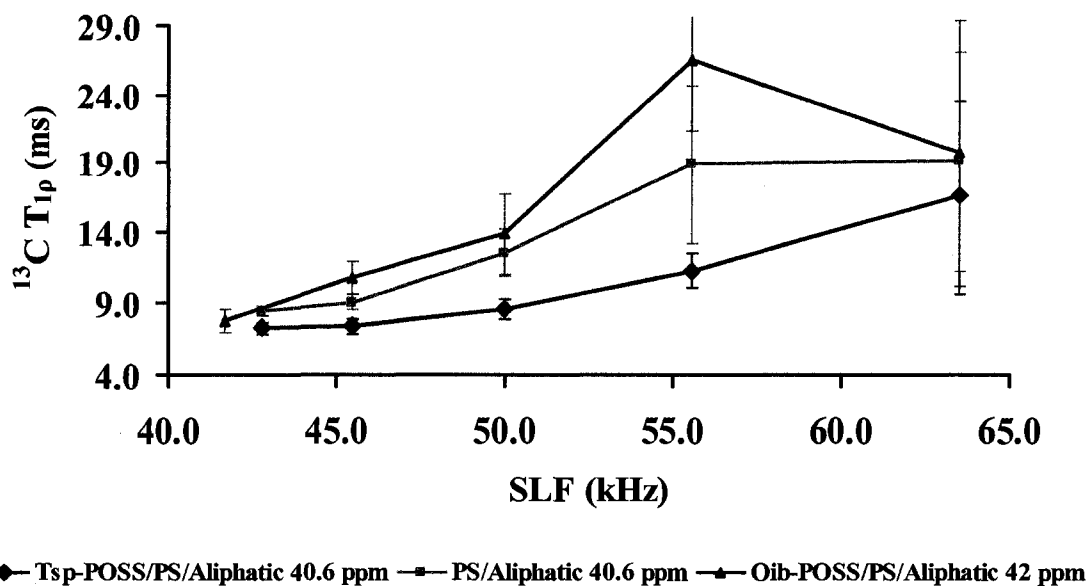


Figure V-17. Change in $T_{1\rho}(C)$ relaxation times of aliphatic region of PS, Tsp-POSS/PS, and Oib-POSS/PS HPC's as a function of spin-locking fields.

The ^1H line-shape can also be used to investigate the molecular dynamics of polymers. However, line-widths are difficult to measure directly from the spectrum due to the low ^1H resolution as compared to the chemical shift. The WISE experiment is a pertinent tool to measure the dipolar line-widths in which carbon chemical shifts appear in the detected (F_2) dimension and its corresponding proton line-width appears in the indirect (F_1) dimension. Information about the molecular dynamics and miscibility of polymer blends is obtained from this method. For miscible polymer blends, the ^1H line-width will become equal for all carbon sites as the mixing time is increased via spin diffusion, while in immiscible systems this will not occur. Figure V-18 shows the change of proton line-widths versus various mixing times for the aromatic and aliphatic regions of Oib-POSS/PS. No significant change in proton line-widths was observed with increasing mixing time, indicating lack of interaction and immiscibility between Oib-POSS and PS matrix in all regions.

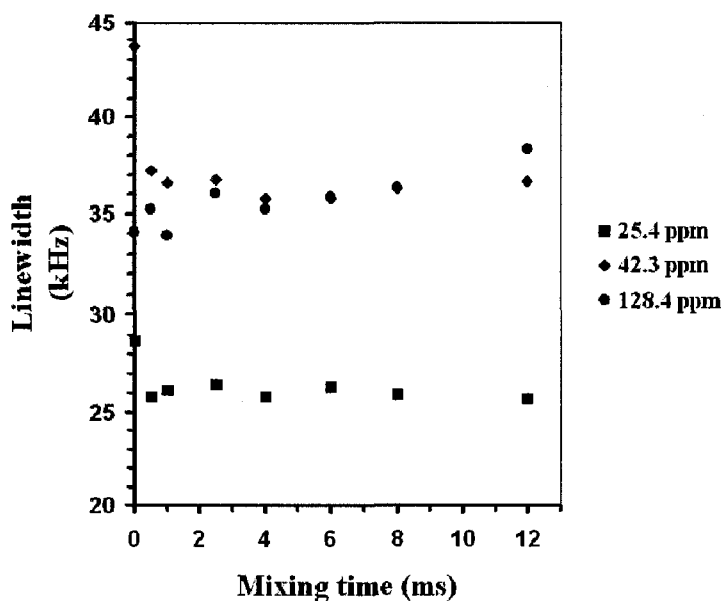


Figure V-18. Change in ^1H line-widths of Oib-POSS/PS HPC as a function of mixing time.

Conclusions

This study demonstrates that POSS solubility and dispersion in a polystyrene matrix can be tailored by varying the substituent organic groups, and that calculated solubility parameters provide a good indication of ultimate dispersion in films cast from solution. Morphology, molecular miscibility, and solution and solid-state chain dynamics of solution blended POSS/PS HPC's were evaluated and explained on the basis of classical thermodynamic principles. Solution dynamics, investigated via dynamic and multi-angle laser light scattering, indicate the random coil conformation of neat PS and POSS/PS blends in toluene solution. Larger variability in the results obtained for the blends compared to neat PS is attributed to the presence of varying size aggregates in the solution which act as independent light scattering sources and influence the intra-particle interference of light waves. Surface and bulk morphology (AFM/TEM) studies of films prepared from the solutions revealed significant differences in the preferential dispersion characteristics of Oib- and Tsp-POSS in PS. Tsp-POSS, with its higher solubility in PS, yielded transparent films with roughness close to that of neat PS films and nano-level dispersion of POSS molecules throughout the bulk. Oib-POSS, with its reduced solubility in PS, yielded hazy films, high surface roughness, large POSS aggregates and preferential segregation of POSS to the surface. Fractional surface coverage, estimated from surface energy measurements, was 15% for Tsp-POSS and 78% for Oib-POSS. Surface segregation of Oib-POSS was attributed to the non-favorable enthalpic interactions and high entropic penalty imposed on PS chains through incorporation of large POSS aggregates.

Solid-state NMR experiments were performed to investigate the molecular miscibility and dynamics in films. Silicon CP/MAS NMR spectra of neat Tsp-POSS exhibit sharp peaks attributed to the crystalline nature of POSS. Similar spectra of Tsp-POSS/PS blends show two broad peaks, indicating reduction in crystallinity and suggesting that Tsp-POSS disperses on a molecular level when blended with PS. Furthermore, 2D HETCOR studies show strong correlation between the two Si peaks of Tsp-POSS (T_2 and T_3) with the aromatic proton from PS. This is attributed to the close spatial proximity of Tsp-POSS molecules and PS chains driven by π - π attractions between the phenyl rings. In contrast, Oib-POSS/PS samples exhibit weak resonance correlation between the silicon peak from POSS and the aliphatic protons from PS. Significant differences in the relaxation behavior for the blends were observed in proton spin-lattice relaxation studies. Neat PS and Tsp-POSS/PS blends exhibit overlapping mono-exponential decay behavior, indicating molecular level dispersion of Tsp-POSS. Entirely different decay curves were obtained for Oib-POSS/PS blends, indicating inhomogeneity in Oib-POSS dispersion. Furthermore, proton line-widths measurements at various mixing times (WISE studies), indicate lack of interaction and immiscibility of Oib-POSS with PS.

The results from these studies help to explain surface modification behavior observed in these and previous studies of POSS/polymer composites prepared *via* melt and solution processes. Calculated solubility parameters proved to be a useful tool for predicting dispersion and segregation of POSS molecules in the polystyrene matrix, and should be applicable to other POSS/polymer systems. These findings further suggest

possibilities of tailoring surface and bulk properties of POSS/polymer nanocomposites through control of the POSS structure.

Acknowledgements

This work was supported primarily by the Office of Naval Research, Award No. N00014-07-1-1057. The authors would like to acknowledge Hybrid Plastics Inc., MS for providing POSS materials. The authors would also like to thank Dr. Christopher Rulison (Augustine Scientific Inc., OH) and Adam Smith (McCormick research group, USM) for their help in surface energy and light scattering measurements, respectively.

References

-
- ¹ Chen, G. X.; Shimizu, H. *Polymer* **2008**, *49*, 943.
- ² Wheeler, P. A.; Misra, R.; Cook, B.; Morgan, S. E., Lichtenhan, J. D. *J. Appl. Polym. Sci.* **2008**, *108*, 2503.
- ³ Lichtenhan, J. D.; Schwab, J. J.; Reinerth, W. A. *Chemical Innovation* **2001**, *31*, 3.
- ⁴ Lichtenhan, J. D. *Comments Inorg. Chem.* **1995**, *17*, 115.
- ⁵ Shockey, E. G.; Bolf, A. G.; Jones, P. F.; Schwab, J. J.; Chaffee, K. P.; Haddad, T. S.; Lichtenhan, J. D. *Appl. Organomet. Chem.* **1999**, *13*, 311.
- ⁶ Lee, A.; Lichtenhan, J. D. *J. Appl. Polym. Sci.* **1999**, *73*, 1993.
- ⁷ Romo-Uribe, A.; Mather, P. T.; Haddad, T. S.; Lichtenhan, J. D. *J. Polym. Sci., Part B: Polym. Phys.* **1998**, *36*, 1857.
- ⁸ Patel, R. R.; Mohanraj, R.; Pittman, C. U. *J Polym Sci Part B: Polym Phys* **2006**, *44*, 234.
- ⁹ Lee, A.; Lichtenhan, J. D. *Macromolecules* **1998**, *31*, 4970.
- ¹⁰ Turri, S.; Levi, M. *Macromolecules* **2005**, *38*, 5569.
- ¹¹ Mather, P. T.; Jeon, H. G.; Romo-Uribe, A.; Haddad, T. S.; Lichtenhan, J. D. *Macromolecules* **1999**, *32*, 1194.
- ¹² Fu, B. X.; Hsiao, B. S.; Pagola, S.; Stephens, P.; White, H.; Rafailovich, M.; Sokolov, J.; Mather, P. T.; Jeon, H. G.; Phillips, S.; Lichtenhan, J.; Schwab, J. *Polymer* **2001**, *42*, 599.
- ¹³ Zhao, Y.; Schiraldi, D. A. *Polymer* **2005**, *46*, 11640.
- ¹⁴ Fina, A.; Tabuani, D.; Frache, A.; Camino, G. *Polymer* **2005**, *46*, 7855.
- ¹⁵ Ning, H.; Martin, B.; Andreas, S. *Macromolecules* **2007**, *40*, 9672.

-
- ¹⁶ Hosaka, N.; Torikai, N.; Otsuka, H.; Takahara, A. *Langmuir* **2007**, *23*, 902.
- ¹⁷ Kidane, A. G.; Edirisinghe, M. J.; Bonhoeffer, P.; Seifalian, A. M. *Biorheology* **2007**, *44*, 265.
- ¹⁸ Funke, W., *J Oil Colour Chem Assoc* **1976**, *59*, 398.
- ¹⁹ Eisenriegler, E.; Kremer, K.; Binder, K. *J Chem Phys* **1982**, *77*, 6296.
- ²⁰ Ober, R.; Paz, L.; Taupin, C.; Pincus, P.; Boileau, S. *Macromolecules* **1983**, *16*, 50.
- ²¹ Shull, K. R.; Kramer, E. J.; Hadziioannou, G.; Tang, W. *Macromolecules* **1990**, *23*, 4780.
- ²² Liebler, L. *Makromol Chem Macromol Symp* **1988**, *16*, 1.
- ²³ Gaines, G. L. *J Chem Phys* **1969**, *73*, 3143.
- ²⁴ Misra, R.; Fu, B. X.; Morgan, S. E. *J. Polym. Sci., Part B: Polym. Phys.* **2007**, *45*, 2441.
- ²⁵ Misra, R.; Fu, B. X.; Morgan, S. E. Manuscript submitted.
- ²⁶ Hosaka, N.; Otsuka, H.; Hino, M.; Takahara, A. *Langmuir* **2008**, *24*, 5766.
- ²⁷ Paul, R.; Karabiyik, U.; Swift, M. C.; Esker, A. R. *Langmuir* **2008**, *24*, 5079.
- ²⁸ Paul, R.; Karabiyik, U.; Swift, M. C.; Hottle, J. R.; Esker, A. R. *Langmuir* **2008**, *24*, 4676.
- ²⁹ Koh, K.; Sugiyam, S.; Morinaga, T.; Ohno, K.; Tsuji, Y.; Fukuda, T.; Yamahiro, M.; Iijima, T.; Oikawa, H.; Watanabe, K.; Miyashita, T. *Macromolecules* **2005**, *38*, 1264.
- ³⁰ Gupta, S.; Zhang, Q.; Emrick, T.; Balazs, A. C.; Russell, T. P. *Nature Materials* **2006**, *5*, 229.
- ³¹ Mackay, M.E.; Tuteja, A.; Duxbury, P.M.; Hawker, C.J.; Horn, B.V.; Guan, Z.; Chen, G.; Krishnan, R.S. *Science* **2006**, *311*, 1740.

-
- ³² Krishnan, R.S. ; Mackay, M.E.; Duxbury, P.M.; Pastor, A.; Hawker, C.J.; Horn, B.V.; Asokan, S.; Wong, M. *Nano Lett.* **2007**, *7*, 484.
- ³³ Stejskal, E.O.; Schaefer, J.; Sefcik, M.D.; McKay, R.A. *Macromolecules* **1981**, *14*, 275.
- ³⁴ Clauss, J.; Schmidt-Rohr, K.; adam, A.; Boeffel, C.; Spiess, H. W. *Macromolecules* **1992**, *25*, 5208.
- ³⁵ Hou, S. S.; Bonagamba, T. J.; Beyer, F. L.; Madison, P. H.; Schmidt-Rohr, K. *Macromolecules* **2003**, *36*, 2769.
- ³⁶ Brus, J.; Urbanova, M.; Strachota, A. *Macromolecules* **2008**, *41*, 372.
- ³⁷ Washburn, E. W., *Phys. Rev.* **1921**, *17*, 374.
- ³⁸ Fowkes, F. M.; Kaczinski, M. B.; Dwight, D. W. *Langmuir* **1991**, *7*, 2464.
- ³⁹ Owens, D. K.; Wendt, R. C. *J Appl Polym Sci.* **1969**, *13*, 1741.
- ⁴⁰ Schaefer, J.; Stejskal, E. O.; Buchdahl, R. *Macromolecules* **1977**, *10*, 384.
- ⁴¹ Dixon, W. T. *J. Chem. Phys.* **1982**, *77*, 1800.
- ⁴² Bielecki, A; Kolbert, A. C.; Levitt, M. H., *Chem. Phys. Lett.* **1989**, *155*, 341.
- ⁴³ Clauss, J.; Schmidt-Rohr, K.; Spiess, H. W. *Acta Polymer* **1993**, *44*, 1.
- ⁴⁴ Schmidt-Rohr, K.; Clauss, J. *Macromolecules* **1992**, *25*, 3273.
- ⁴⁵ Hoy, K. L. *J. Paint Technology* **1970**, *42*, 76.
- ⁴⁶ Hoy, K. L. Group molar-attraction constants. In *Polymer Handbook*, 2nd Edn.; Bradrup, J., Immergut, E.H. (eds.);IV-339. Wiley & Sons: New York, 1975.
- ⁴⁷ Liu. L., Ming, T., Liang, G., Chen, W., Zhang, L., Mark, J. E. *Journal of Macromolecular Science, Part A: Pure and Applied Chemistry* **2007**, *44*, 659.

-
- ⁴⁸ Pusey, P. N.; Vaughan, J. M.; Williams, V. G. *J. Chem. Soc., Faraday Trans.* **1974**, *70*, 1696.
- ⁴⁹ Braun, B.; Dorgan, J. R.; Chandler, J. P. *Biomacromolecules* **2008**, *9*, 1255.
- ⁵⁰ Mays, J. M.; Terao, K. *European Polymer Journal* **2004**, *40*, 1623.
- ⁵¹ Negadi, A.; Duval, M.; Benmouna, M. *Polymer Bulletin* **1999**, *43*, 261.
- ⁵² Burchard, W.; Schmidt, M.; Stockmayer, W.H. *Macromolecules* **1980**, *13*, 580.
- ⁵³ Akcasu, Z.A.; Benmouna M. *Macromolecules* **1978**, *11*, 1193.
- ⁵⁴ Unno, M.; Alias, S. B.; Saito, H.; Matsumoto, H. *Organometallics* **1996**, *15*, 2413.
- ⁵⁵ Feher, F. J.; Souvilong, D.; Lewis, G. T. *J. Am. Chem. Soc.* **1997**, *119*, 11323.
- ⁵⁶ Rikowski, E.; Marsmann, H. C. *Polyhedron* **1997**, *16*, 3357.
- ⁵⁷ Li, S.; Rice, D. M.; Karasz, F. E. *Macromolecules* **1994**, *27*, 2211.
- ⁵⁸ White, J. L.; Mirau, P. A. *Macromolecules* **1994**, *27*, 1648.

CHAPTER VI

POLYHEDRAL OLIGOMERIC SILSESQUIOXANE (POSS) TRISILANOLS AS
DISPERSANTS FOR TITANIUM OXIDE NANOPOWDER

Abstract

Trisilanol isobutyl polyhedral oligomeric silsesquioxane (POSS) was used to disperse nano-sized titanium dioxide (TiO_2) particles in polypropylene (PP). The silanol groups of the POSS cage bind to the surface of the TiO_2 particles, creating a layer of isobutyl POSS that improves compatibility with the PP matrix. POSS was an effective dispersant both when applied in a chemical pretreatment of TiO_2 and when simply added to the blend during melt compounding. Average particle size of the TiO_2 was reduced from 70 nm for neat TiO_2 to 50 nm for the POSS/ TiO_2 blend to 33 nm for the TiO_2 chemically treated with POSS. Additionally, the POSS coating improved the color of the material and reduced the catalytic effect of TiO_2 on thermo-oxidative degradation.

Introduction

Polymeric nanocomposites have been the subject of intense research interest over the past fifteen years, spawned by advances such as the discovery of spherical fullerenes and carbon nanotubes and Toyota's initial commercialization of nylon/clay nanocomposite materials.^{1,2} Nanofillers are projected to provide advanced performance capabilities for engineering polymer applications, imparting the high strength and modulus obtained with traditional fillers without their negative side effects, such as reduced processability and impact strength. Widespread commercialization of polymer nanocomposite materials, however, has been disappointingly slow, and, in many cases, observed property enhancements fall far short of expectations, due in large part to the aggregation tendency and difficulty of dispersion of nanoparticles. Additional hurdles include prohibitively high cost of manufacture of nanoparticles and nanocomposites, and potential environmental hazards associated with some nanomaterials.^{3,4,5,6,7,8,9,10,11,12,13}

Polyhedral oligomeric silsesquioxane (POSS) nanostructured chemicals (Figure 1) provide a unique approach for the development of polymeric nanoengineered materials. POSS molecules are cage-like organic-inorganic structures described by the general chemical structure $\text{RSiO}_{1.5}$. As illustrated in Figure VI-1, POSS molecules consist of a Si-O-Si inorganic cage, surrounded by an organic corona, represented by substituents "R". The inorganic cage, with structure $(\text{SiO}_{1.5})_n$ where $n=8, 10$ or 12 , may be a fully condensed "closed" (Fig.VI-1 A) or "open" (Fig.VI-1B) structure. The diameter of these monodisperse particles ranges from one to three nanometers, depending on the composition of the cage. The substituents can be varied widely to provide a range of different properties, to increase or reduce compatibility with a polymer matrix, or can

be made reactive to allow co-polymerization or graft polymerization with a spectrum of monomers.

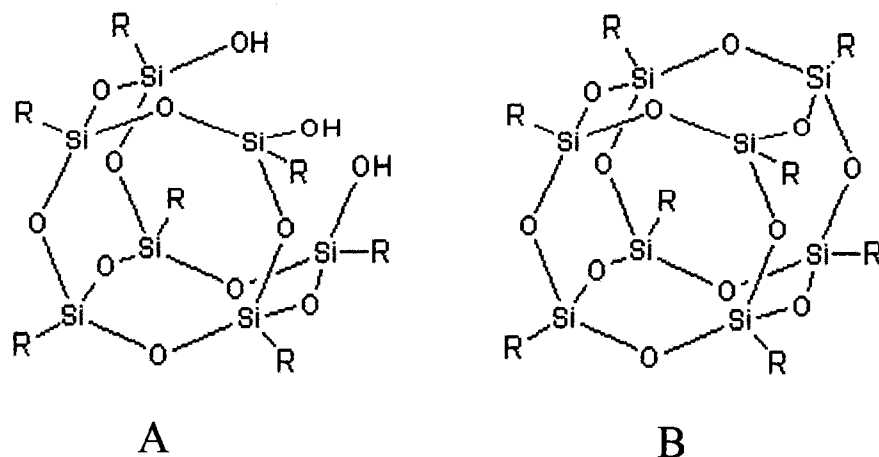


Figure VI-1. Generalized POSS structure A) condensed (closed) cage, B) open cage.

The first reference to POSS materials dates to 1946, when the molecules were first isolated via the thermolysis of the polymeric products produced from the co-hydrolysis of methyltrichlorosilane with dimethylchlorosilane.¹⁴ Extensive POSS research was performed at the Air Force Research Laboratory in subsequent years,^{15,16} and in 1998 Hybrid Plastics was formed as a spin-off company to commercialize the technology. Today, over 150 different POSS molecules are produced commercially.¹⁷ Besides olefins and molecular silicas, a wide variety of POSS molecules with functional groups ranging from halides, epoxies, silanols, and alcohols to acrylates and, methacrylates are commercially available.¹⁷ A large number of studies have been devoted to the chemical incorporation of POSS derivatives into polymer matrices via copolymerization or grafting.^{18,19,20} Various POSS based monomers and macromers have been synthesized and a wide variety of POSS based copolymers have been reported, including copolymers of polysiloxane,^{21,22} polynorbornene,²³ polyurethane,^{24,25}

poly(methyl methacrylate),^{26,27} epoxies,²⁸ and poly(4-methyl styrene).^{29,30} In general, these copolymers exhibit organic/inorganic hybrid properties, demonstrating to various degrees enhanced modulus, stiffness, flame retardancy and thermal stability in comparison to the base polymer.^{31,32,33,34}

While reactive POSS nanostructured chemicals can be readily dispersed in a polymer matrix at the molecular level through copolymerization, dispersion via simple melt mixing is desirable due its wide applicability and low cost of manufacturing. This approach has been less studied, and fewer reports of melt mixing non-reactive POSS in polymer matrices have appeared.^{32,33,34,35,36,37} It is clear from these limited studies that the choice of organic substituent is critical for compatibility and dispersion of POSS in the polymer. For example, Schiraldi *et al.*³³ reported that trisilanolphényl POSS when blended with polycarbonate yields transparent blends with slightly improved modulus at POSS loading levels up to 5 weight %, while blends of polycarbonate with trisilanolisooctyl POSS at the same loading levels are opaque, indicating poor dispersion.³³

The ability to tailor POSS structures in order to achieve desired levels of dispersion in a polymer matrix suggests the possibility of utilizing POSS nanostructured chemicals as dispersing aids for difficult to disperse nanoparticles. The current state-of-the-art uses alkoxy silane coupling agents and various surfactants, such as stearates, to disperse particles.³⁸ POSS silanols possess several distinct advantages over the traditional approach. POSS silanols are stable in the silanol form, allowing them to be applied directly in one step. Additionally, since POSS silanols do not readily react with each other, only a monolayer of POSS will be deposited on the filler's surface with little

possibility of oligomer and condensed particle formation. Three silanol groups per cage produce stronger, more robust bonds than typical coupling agents. Because of POSS's enormous surface area to volume ratio, polymer-POSS interaction increases dramatically in comparison to coupling agents.

In the current study, polypropylene blends with POSS and nanosized titanium dioxide (nano-TiO₂) particles were prepared via two methods; first, simple melt mixing of the individual materials, and secondly by first chemically treating the nano-TiO₂ particles with reactive POSS molecules and then melt blending with polypropylene. TiO₂ was chosen as a model particle to test the theory of using POSS as a dispersant and surface treatment for metal oxides. Blend properties were evaluated *via* transmission electron microscopy (TEM), colorimetry, thermal gravimetric analysis (TGA) and melt flow indexing.

Experimental

Materials

Nano-TiO₂ (with nominal particle size of 21 nm) was obtained from Degussa (Aeroxide Titanium Dioxide P 25). Polypropylene (PP) was purchased from Ashland Distribution (Hival 5250). Trisilanol isobutyl POSS (TSI-POSS) was manufactured by Hybrid Plastics and is a free flowing white powder.

Sample Preparation

Three types of nano-TiO₂ blends were prepared. The first type, uncoated nano-TiO₂, was prepared by melt-blending as-received nano-TiO₂ particles into PP. The second type, nano-TiO₂/POSS blend, was prepared by melt blending nano-TiO₂ and TSI-POSS with PP at desired compositions. In the third type, POSS-treated nano-TiO₂ blend, the nano-TiO₂ was first chemically treated with TSI-POSS and then melt blended into PP. For the POSS chemical treatment, nano-TiO₂ (162 g), TSI-POSS (16.5 g), and hexanes (1350 g) were added to a 3 liter round bottom flask. The flask was attached to a Buchi rotovap and rotated for 1 hr under atmospheric temperature and pressure. Vacuum was then applied to remove the hexanes. The solid white powder was processed through a jet mill, resulting in a low density white powder (110 g).

The melt blends were prepared using a B&P Process twin screw extruder with 25 mm screws and an L/D ratio of 40:1 at a temperature of 225 °C. PP and nano-TiO₂ were added by separate feeders at a rate of 9 kg/hr and 0.09 kg/hr, respectively. The nano-TiO₂/POSS blend was prepared by first blending TSI-POSS with PP at a 5 wt-% loading, followed by a second extrusion step in which the nano-TiO₂ was added. Films for optical tests were prepared on a Carver hydraulic melt press at 200 °C.

Transmission Electron Microscopy-Energy Dispersive X-Ray (TEM-EDAX)

For TEM-EDAX analysis, a JOEL-2100 ultra high resolution transmission electron microscope was employed (Joel Ltd., Tokyo, Japan) at an accelerating voltage of 200kV. Ultrathin sections, 90~100 nm thick, were prepared by cryogenic ultramicrotoming the samples with a glass knife using a Leica EM UC6 cryomicrotome at -80°C. Subsequently, the ultrathin sections were collected on a 600 mesh copper grid. Elemental mapping of the ultrathin sections was performed using energy dispersive X-ray analysis. Elemental maps were acquired using EDAX Genesis software.

Image analysis to determine number of TiO₂ particles and particle sizes in each blend was performed utilizing Microsoft Paint. The number of nanometers per pixel was calculated from the TEM images by determining the number of pixels in the scale bar and dividing this into the number of nanometers represented by the scale bar. One 1300 nm by 1300 nm sample image was randomly cut from each of the larger TEM images for each TiO₂ blend. Particle size was recorded by counting particle width (X) and height (Y) in pixels. The values were converted to length in nanometers using the above mentioned method and averages calculated.

Optical Characterization

A BYK Gardner color-guide apparatus was used to perform color (LAB) (ASTM - E308), opacity (ASTM - D2805) and yellowness index (ASTM - E-313-98), according to the ASTM methods indicated. A BYK Gardner haze-gloss instrument was utilized to perform haze and gloss readings, following ASTM - D4039 and ASTM - D523 test methods respectively.

Thermal and Melt Flow Characterization

Melt flow index (MFI) was obtained on a Dynisco LMI D4004 at 230 °C / 2.16 kg in accordance with ASTM D1238. Thermal gravimetric analysis (TGA) evaluations were conducted on a TA Instruments Q500 at a heating rate of 20 °C/min under a nitrogen atmosphere.

Results and Discussion

In order to evaluate the effect of POSS on dispersion of nano-TiO₂ in a polymer matrix, untreated nano-TiO₂ (with no organic surface treatment) was evaluated as a control. Silanols bind to metal oxide surfaces first by hydrogen bonding followed by covalent bonding if the proper conditions exist.³⁹ The first step involves hydrogen bonding between the silanol and surface hydroxyl groups. Upon elimination of water of reaction, a covalent M-O-Si bond is formed. Assuming a nominal nano-TiO₂ particle size of 21 nm and a POSS surface coverage area of 1.6 nm² per POSS cage derived with molecular simulation, it is calculated that five percent by weight of POSS relative to TiO₂ would be required to provide a monolayer coating that completely covered the nano-TiO₂ particle surface. Thus, to assure an adequate amount of POSS for surface coverage, 10 wt-% TSI-POSS relative to TiO₂ was used in the coating process described in the experimental section.

TGA analysis was performed to verify and quantify the presence of TSI-POSS in the coated nano-TiO₂. (Figure VI-2) Untreated nano-TiO₂, trace 2(a), shows minimal thermal degradation up to a temperature of 800°C. The nano-TiO₂ treated with 10 wt-% TSI-POSS, trace 2(c), exhibits an approximate 10% weight loss above 200°C that is attributed to degradation of the TSI-POSS. This sample (c) was not washed prior to TGA analysis, thus the entire 10 wt-% POSS is observed. Trace 2(b) represents a treated nano-TiO₂ sample that was extensively washed with hexanes and tetrahydrofuran (THF) to remove any non-bound TSI-POSS. For this sample, an approximate three percent weight loss is observed, which is somewhat less than the calculated value of five percent POSS required for monolayer coverage. Most likely there is not a high enough concentration of

hydroxyl groups on the surface of the TiO_2 to obtain complete coverage. The fact that three percent POSS was retained after washing indicates formation of a strong bond, probably covalent, between POSS and TiO_2 .

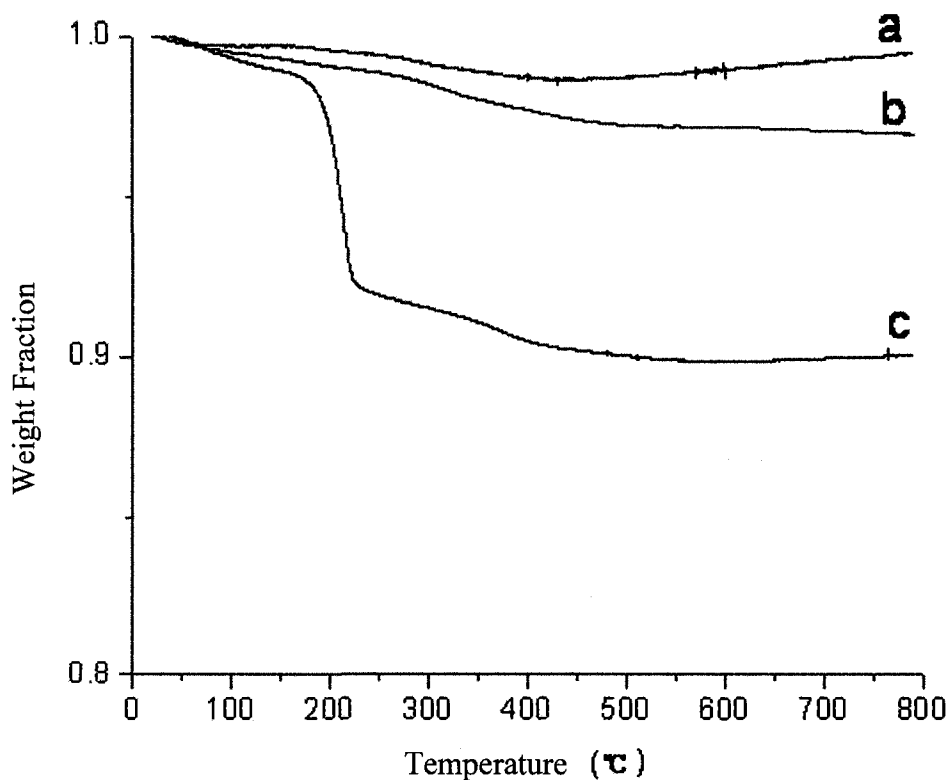


Figure VI-2. TGA analysis of (a) untreated TiO_2 , (b) POSS treated TiO_2 after washing, (c) POSS treated TiO_2 before washing.

Different TiO_2 treatment conditions yield dramatic differences in TiO_2 dispersion in polypropylene as observed by TEM analysis (Figures VI-3 and VI-4). Figure VI-3 shows TEM micrographs of untreated nano- TiO_2 (a), nano- TiO_2 /POSS blend (b) and the POSS chemically treated nano- TiO_2 (c) melt blended in polypropylene. While TiO_2 aggregates of greater than 200 nm diameter are observed for the untreated nano- TiO_2 , smaller, more highly dispersed particles are observed for the nano- TiO_2 /POSS blend, and

even smaller particles are observed for the POSS treated nano-TiO₂ (note that the scale bar for 3c is 100 nm, while it is 200 nm for 3a and 3b).

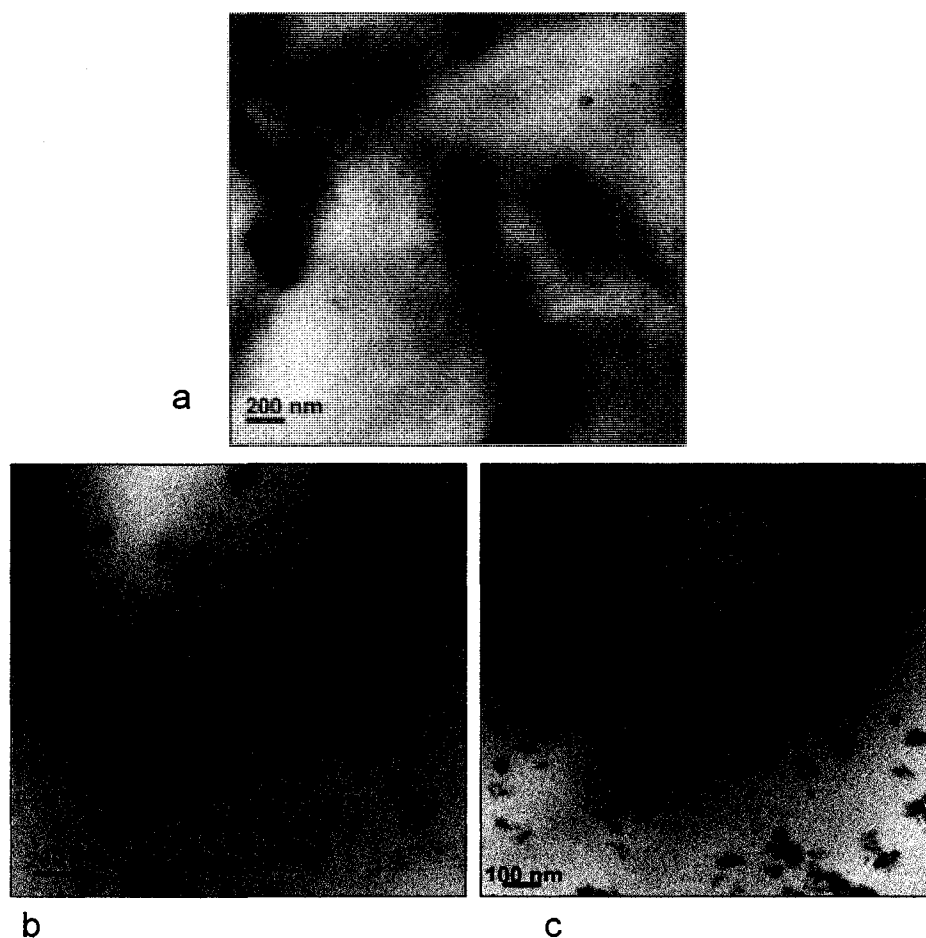


Figure VI-3. TEM images of polypropylene/nano-TiO₂ blends with different TiO₂ treatments a) untreated nano-TiO₂ b) POSS/nano-TiO₂ blend c) nano-TiO₂ chemically treated with POSS. Scale bars are indicated on each figure.

Image analysis indicates that both the average particle size and the particle size distribution decreases with POSS surface treatment, in the order untreated nano-TiO₂ > nano-TiO₂/POSS blend > POSS chemically treated nano-TiO₂ (Table VI-1), with the POSS chemically treated particles showing roughly half the size and polydispersity of the untreated particles. We hypothesize that POSS aids in the dispersion of the TiO₂ by its interaction with both the TiO₂ and the PP matrix. Previous studies have shown a high

level of isobutyl-POSS dispersion in a PP matrix, attributed to POSS's isobutyl R group matched to the polarity and chemical structure of PP.³⁷ In this case, a POSS structure with silanol groups on one corner can bind to the polar TiO₂ particles, while the non-polar isobutyl R group of the POSS interacts *via* Van der Waals forces with polypropylene. The TEM data indicates that POSS added in the melt aids in TiO₂ dispersion. Pre-mixing TiO₂ with POSS in solution provides greater opportunity for chemical reaction between the molecules and results in smaller, more highly dispersed nano-TiO₂ particles in the melt.

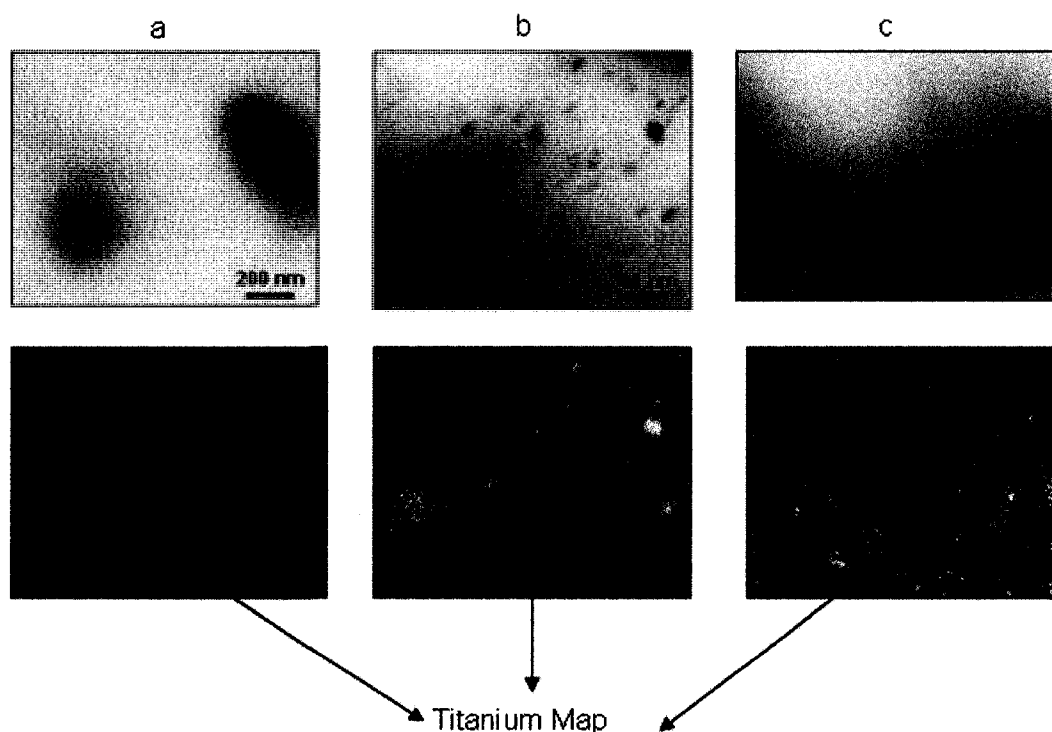


Figure VI-4. TEM-EDAX images of polypropylene/nano-TiO₂ blends with different TiO₂ treatments a) untreated nano-TiO₂ b) POSS/nano-TiO₂ blend c) nano-TiO₂ chemically treated with POSS. Scale bars represent 200 nm. Brightly colored areas indicate titanium.

Table VI-1. Average Particle Diameter for Nano-TiO₂ with Different Surface Treatments after Dispersion in PP Matrix.

| Sample | Untreated TiO ₂ | POSS/TiO ₂ Blend | Chemically Treated POSS/TiO ₂ |
|--------------------------------|----------------------------|-----------------------------|---|
| Average Particle Diameter (nm) | 70.4 | 50.1 | 33.2 |
| Standard Deviation | 31.9 | 21.4 | 11.6 |

Further evidence of the effect of POSS on nano-TiO₂ dispersion is observed by analyzing color, yellowness index, and haze of films prepared from the blends (Table VI-2).

Table VI-2. Optical Properties of Blends with Different TiO₂ Treatment.

| Sample | Untreated TiO ₂ | POSS/TiO ₂ Blend | Chemically Treated POSS/TiO ₂ |
|-------------------------------------|----------------------------|-----------------------------|---|
| Test Method | | | |
| Color, (LAB) (ASTM E308) | | | |
| Axis | Background | | |
| L | 91.8 | 90.2 | 89.7 |
| A | -1.16 | -1.54 | -1.11 |
| B | 5.95 | 7.64 | 6.83 |
| Yellowness Index (ASTM E-313-98) | 14 | 12 | 9 |
| Haze (ASTM D4039) | 164 | 130 | 119 |
| Standard Deviation | 32 | 22 | 11 |
| Opacity, (%) (ASTM D2805) | 38 | 44 | 37 |
| Gloss (ASTM D523) | | | |
| 20° | 2.5 | 2.0 | 1.7 |
| 60° | 23.0 | 18.0 | 15.0 |
| 85° | 43.0 | 39.0 | 36.0 |

Films produced from blends containing POSS are visibly whiter and less yellow than those prepared from the neat TiO₂, quantified by the Yellowness Index and LAB values, with yellowness measurement in decreasing order: untreated nano-TiO₂ > nano-

TiO₂/POSS blend > POSS chemically treated nano-TiO₂. Haze and gloss exhibit the same trend, decreasing in value with the POSS treatment. Opacity measurements show no apparent trend. The decrease in haze can be explained by the decrease in particle size of TiO₂ aggregates observed in TEM studies. Reduction in yellowness is explained by the fact that POSS coats the surface of the TiO₂ particles, making them less reactive to the PP matrix, resulting in reduced discoloration.⁴⁰

Table VI-3. Melt Flow Index of Blends with Different TiO₂ Treatment

| Sample | MFI (gm/10 min) | Std. Dev. |
|---|-----------------|-----------|
| Neat PP | 18.8 | 0.2 |
| PP with 1% uncoated TiO ₂ | 31.4 | 0.2 |
| PP with 5% POSS | 24.5 | 0.4 |
| PP with 1% TiO ₂ , 5% POSS blend | 25.7 | 0.2 |
| PP with 1% POSS-coated TiO ₂ | 20.9 | 0.4 |

The protective coating effect of POSS is further exhibited in melt flow studies (Table VI-3). While the blend of uncoated TiO₂ showed a 70% increase in MFI (from 18.8 for neat PP to 31.4 for the uncoated TiO₂ blend), POSS-treated TiO₂ showed only a minor increase in MFI (from 18.8 to 20.9). The large increase in MFI for the uncoated TiO₂ blend indicates acceleration of thermal oxidative degradation of the PP matrix in the presence of the uncoated TiO₂,³⁸ which was further evidenced by the increase in yellowness index of this blend. Treatment of TiO₂ with POSS in solution largely eliminates this effect. Blends of POSS with TiO₂ in the melt exhibit intermediate behavior.

Conclusions

POSS silanols have successfully been utilized as dispersing agents for nano-titanium dioxide particles in polypropylene. Chemically treating TiO_2 with POSS in a solvent solution was more effective than adding untreated TiO_2 and POSS directly into a melt compounder. POSS treatment reduced the TiO_2 agglomerate size in PP from 70 nm to 33 nm by functioning as a compatibilizing agent, in which the silanol groups of the POSS cage bind to the TiO_2 particle and surround it with a high-surface-area structure of non-polar isobutyl groups.

The effects of POSS observed in this study are believed to be generic for metal oxide surfaces and can be utilized in many other applications. Because of its nanostructured topography, POSS has a distinct advantage over traditional silane coupling agents by dramatically increasing the surface area of the treated particle. A direct comparison between POSS and traditional dispersants is currently being studied.

Acknowledgements

The authors thank the STTR program of the National Science Foundation (Award Number OII-0539295) for supporting this work. This work was also supported by the major research instrumentation program of the National Science Foundation under Award Numbers MRI0421406, DMR0421403.

References

-
- ¹ Calvert, P. Potential Applications of Carbon Nanotubes. *Carbon Nanotubes: Preparation and Properties*; CRC Press: Boca Raton, USA, 1997, p 277.
 - ² Okamoto, M. Rapra Review Report 2003, 14(7) , report 163
http://www.rapra.net/products_and_services/Books/Materials/Composites/PolymerLayered_Silicate_Nanocomposites.asp. Accessed on July 26, 2007.
 - ³ Alexandre, M.; Dubois, P. *Mater Sci Eng R: Reports* **2000**, 28, 1.
 - ⁴ Chow, W. S.; Ishak, Z. A. Mohd, K.; Kocsis, J. *J Polym Sci Part B: Polym Phys* **2005**, 43, 1198.
 - ⁵ Hadal, R.; Nathani, H.; Tanniru, M.; Misra, R. D. K. *Annual Technical Conference-Society of Plastics Engineers* **2005**, 63, 1444.
 - ⁶ Kojima, Y.; Usuki, A.; Kawasumi, M.; Okada, A.; Kurauchi, T.; Kamigaito, O. *J Polym Sci Part A: Polym Chem* **1993**, 31, 983.
 - ⁷ Okada, A.; Usuki, A. *Mater Sci Eng ,C: Biomim Mater Sensors Syst* **1995**, C3, 109.
 - ⁸ Usuki, A.; Kojima, Y.; Kawasumi, M.; Okada, A.; Fukushima, T.; Kurauchi, T.; Kamigaito, O. *J Mater Res* **1993**, 8, 1179.
 - ⁹ Yano, K.; Usuki, A.; Okada, A.; Kurauchi, T.; Kamigaito, O. *J Polym Sci Part A: Polym Chem* **1993**, 31, 2493.
 - ¹⁰ Lan, T.; Pinnavaia, T. *J Chem. Mater* **1994**, 6, 2216.
 - ¹¹ Wang, Z.; Pinnavaia, T. *J Chem. Mater* **1998**, 10, 1820.
 - ¹² Favier, V.; Canova, G.R.; Shrivastava, S.C.; Cavaille, J.Y. *Polym Eng Sci.* **1997**, 37, 1732.

-
- ¹³ Chazeau, L.; Cavaille, J.Y.; Canova, G.; Dendievel, R.; Bouterin, B. *J Appl Polym Sci* **1999**, *71*, 1797.
- ¹⁴ Scott, D.W. *J Am Chem Soc* **1946**, *68*, 356.
- ¹⁵ Phillips, S.H.; Haddad, T.S.; Tomczak, S.J. *Current Opinion in Solid State and Materials Science* **2004**, *8*, 21.
- ¹⁶ Mabry, J. M.; Vij, A.; Iacono, S.T.; Grabow, W.W. *ACS Polymer Preprints* **2005**, *46*, 630.
- ¹⁷ <http://www.hybridplastics.com> (accessed July 20, 2007).
- ¹⁸ Lichtenhan, J. D. *Comments Inorg Chem.* **1995**, *17*, 115.
- ¹⁹ Shockey, E. G.; Bolf, A. G.; Jones, P. F.; Schwab, J. J.; Chaffee, K. P.; Haddad, T. S.; Lichtenhan, J. D. *Appl. Organomet. Chem.* **1999**, *13*, 311.
- ²⁰ Lee, A.; Lichtenhan, J. D. *J Appl Polym Sci* **1999**, *73*, 1993.
- ²¹ Lichtenhan, J. D.; Vu, N. Q.; Carter, J. A.; Gilman, J. W.; Feher, F. J. *Macromolecules* **1993**, *26*, 2141.
- ²² Mantz, R. A.; Jones, P. F.; Chaffee, K. P.; Lichtenhan, J. D.; Gilman, J. W.; Ismail, I. M. K.; Burmeister, J. *Chem Mater* **1996**, *8*, 1250.
- ²³ Mather, P. T.; Jeon, H. G.; Romo-Urbe, A.; Haddad, T. S.; Lichtenhan, J. D. *Macromolecules* **1999**, *32*, 1194.
- ²⁴ Turri, S.; Levi, M. *Macromolecules* **2005**, *38*, 5569.
- ²⁵ Turri, S.; Levi, M. *Macromolecular Rapid Communications* **2005**, *26*, 1233.
- ²⁶ Patel, R. R.; Mohanraj, R.; Pittman, C. U. *J Polym Sci Part B: Polym Phys* **2005**, *44*, 234.

-
- ²⁷ Lichtenhan, J. D.; Otonari, Y. A.; Carr, M. J. *Macromolecules* **1995**, *28*, 8435.
- ²⁸ Lee, A.; Lichtenhan, J. D. *Macromolecules* **1998**, *31*, 4970.
- ²⁹ Romo-Urbe, A.; Mather, P.T.; Haddad, T.S.; Lichtenhan, J.D. *J Polym Sci Part B: Polym Phys* **1998**, *36*, 1857.
- ³⁰ Haddad, T.S.; Lichtenhan, J.D. *Macromolecules* **1996**, *29*, 7302.
- ³¹ Zheng, L.; Farris, R.J. Coughlin EB. *Macromolecules* **2001**, *34*, 8034.
- ³² Fu, B.X.; Hsiao, B.S.; Pagola, S.; Stephens, P.; White, H.; Rafailovich, M.; Sokolov, J.; Mather, P.T.,; Jeon, H.G.; Phillips, S.; Lichtenhan, J.; Schwab, J. *Polymer* **2001**, *42*, 599.
- ³³ Zhao, Y.; Schiraldi, D. A. *Polymer* **2005**, *46*, 11640.
- ³⁴ Fina, A.; Tabuani, D.; Frache, A.; Camino, G. *Polymer* **2005**, *46*, 7855.
- ³⁵ Kopesky, E. T.; McKinley, G. H.; Cohen, R. E. *Polymer* **2006**, *47*, 299.
- ³⁶ Joshi, M.; Butola, B. S.; Simon, G.; Kukaleva, N. *Macromolecules* **2006**, *39*, 1839.
- ³⁷ Misra, R.; Fu, B.; Morgan, S. E. *J Polym Sci Part B: Polym Phys* **2007**, *45*, 2441.
- ³⁸ DeArmitt, C.; Rothon, R. *Plastics, Additives, and Compounding* **2002**, *4*, 12.
- ³⁹ Arkles, B. *Chemtech* **1977**, *7*, 766.
- ⁴⁰ *Plastics Additives Handbook*, Gachter, R.; Muller, H. 4thEd.; Hanser/Gardner: Cincinnati, 1993, Chap. 1,11.

CHAPTER VII

NON-WETTING, NON-ROLLING, STAIN RESISTANT POLYHEDRAL
OLIGOMERIC SILSESQUIOXANE COATED TEXTILES

Abstract

Cotton/polyester fabric surfaces were modified using nanostructured organic-inorganic polyhedral oligomeric silsesquioxane (POSS) molecules *via* solution dip coating. Surface wetting characteristics of coatings prepared from two chemically and structurally different POSS molecules, a closed cage fluorinated dodecafluoropropyl POSS (FL-POSS) and an open cage non-fluorinated trisilanolphenyl POSS (Tsp-POSS), were evaluated with time and compared with Teflon. Surface analysis, including AFM, SEM/EDAX, and NMR revealed the presence of POSS aggregates on the fabric surface leading to a spiky topography, high roughness and hysteresis. POSS coated fabrics showed complete reversal of surface wetting characteristics with contact angles higher than the benchmark Teflon surface. Water contact angle measured as a function of time showed equivalent or better performance for POSS-coated surfaces in comparison to Teflon. Furthermore, FL-POSS coated fabric exhibited exceptional stain and acid resistance along with a 33% reduction in relative surface friction. Additionally, “non-sliding” and high surface adhesion behavior of water droplets on the FL-POSS coated fabric are reported.

Introduction

Advancements in nanostructured materials and coatings have sparked the development of new, multi-functional textiles. A major challenge is to develop stable, nanostructured coatings that impart desired functionality and can be applied using simple coating techniques. Non-wetting fabrics have potential utility in industrial and biomedical applications, for example to provide reduced surface friction, or resistance to staining, harsh chemicals or bacterial activity.^{1,2} Generally, preparation of fabric coatings that impart a high degree of hydrophobicity involves elaborate synthetic routes with stringent reaction conditions along with the use of harsh and/or expensive chemicals.^{3,4} Recently, Cheung et al.⁵ reported titanium dioxide coated self-cleaning cotton surfaces prepared *via* sol-gel processes. These surfaces exhibit bactericidal activity and degradation of red wine and coffee stains under UV irradiation. Similarly, Kiwi and coworkers^{6,7,8} have explored the photocatalytic activity of TiO₂/SiO₂ coated cotton, polyesters, and wool-polyamide. The majority of the research efforts reported to date are focused on utilizing inorganic nanoparticles (TiO₂ and SiO₂) through sol-gel chemistries. However, the high temperature required to achieve a thin layer of sol-gel based TiO₂ coating limits its applicability for many fabrics. There is a need to develop and expand the range of materials for coating fabric surfaces to impart multi-functionality *via* simple coating routes.

Polyhedral oligomeric silsesquioxane (POSS) nanostructured chemicals provide an alternate route to tailor fabric surface characteristics. POSS organic-inorganic hybrid molecules have a silicon-oxygen inorganic core surrounded by a corona of organic groups attached to corner silicon atoms. Organic groups attached to POSS cages can be

readily modified to tailor the compatibility with the substrate. The inorganic cage, with structure $(\text{SiO}_{1.5})_n$ where $n=8, 10$ or 12 , may be a fully condensed “closed” or “open” structure. The diameter of these monodisperse molecules ranges from 1-3 nanometers depending on the composition of the cage.⁹ Additionally, POSS is environmentally benign, non-toxic, and biocompatible, and has been approved by FDA for use in dental composite applications.^{10,11,12} POSS has been widely studied in copolymers^{9,13,14,15,16,17} and blends,^{18,19,20} but few reports have appeared on POSS modified fabric surfaces. Polyurethane/POSS coatings have been reported to improve flame retardant characteristics of textiles.²¹ Recently, Mabry and coworkers^{22,23} reported superhydrophobic and superoleophobic poly(methyl methacrylate) and fabric surfaces using highly hydrophobic long chain fluorodecyl and fluoroctyl POSS. Superoleophobicity was attributed to the interplay of POSS chemical composition, nano/micro-roughened surface texture, and re-entrant surface curvature. Although significant improvement in the hydrophobicity was reported, the researchers utilized long fluorinated chains, which are the subject of potential environmental concerns. Literature reports suggest that due to the strong C-F bond (bond dissociation energy 115 kcal/mol)²⁴ C-F chains with chain length of C8 or higher persist in the environment, bioaccumulate, and have potential toxicity. Fluorocarbon chains with four or fewer carbon atoms are reported to not exhibit bioaccumulation.²⁵ Thus, further studies of short chain fluorinated POSS and non-fluorinated POSS coated fabrics are of interest.

An important characteristic of highly hydrophobic surfaces is the rolling of water droplets across the surface without wetting or adhesion, enabling self-cleaning properties. However, this also leads to poor adhesion and dyeability, limiting the utility of the fabric.

For many applications, it is equally important to maintain low surface friction. Recently, we have demonstrated significantly improved surface hydrophobicity and frictional characteristics of melt blended POSS/polymer composites.^{26,27} In the current work, short chain fluorinated and non-fluorinated POSS nanostructured chemicals are employed to manipulate surface wetting characteristics of fabrics *via* simple solution dip coating. An attempt is made to understand and evaluate the effect of POSS coating on fabric surface friction, hydrophobicity, and resistance to stain and acid. In addition, a non-sliding and high surface adhesion behavior at different tilt angles is discussed.

Experimental

Materials

A laboratory grade polyester/cotton blend (65:35 by wt. ratio) fabric was purchased from Landau Uniforms Inc., (Memphis, TN). A closed cage fluorinated dodecatrifluoropropyl POSS (FL-POSS) and an open cage nonfluorinated trisilanolphenyl POSS (Tsp-POSS) were provided by Hybrid Plastics Inc. (Hattiesburg, MS). POSS samples (Figure VII-1) were received as crystalline white powders at room temperature and used as received. Polytetrafluoroethylene (Teflon) film was provided by DuPont (Circleville, OH).

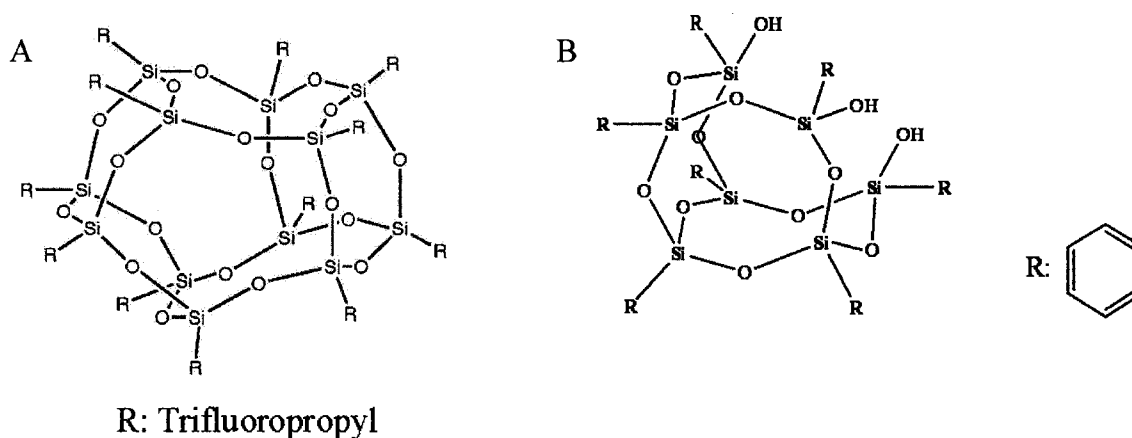


Figure VII-1. Molecular structure of (A) FL-POSS (B) Tsp-POSS.

Sample Preparation

To remove any external contaminants, fabric was washed with soap (mixture of ammonium and sodium lauryl sulfate) followed by thorough rinsing with water and drying in air. Cleaned and dried fabric was dipped in 10 wt.% solution of POSS in tetrahydrofuran (THF) for 12 hrs followed by drying under hood for 4-5 hrs. For surface

characterization, a small piece of fabric was cut and attached to a glass slide using a double sided tape.

Atomic Force Microscopy (AFM) Surface Topography

Surface topography studies were conducted on a MultiModeTM scanning probe microscope from Veeco Instruments, Inc. (Santa Barbara, CA). Probes for surface studies were purchased from Veeco Probes, (Santa Barbara, CA). A silicon probe with a 125 μm long silicon cantilever, nominal force constant of 40 N/m, and resonance frequency of 275 kHz was used for tapping mode surface topography studies. AFM studies were conducted under ambient conditions in a temperature (27°C) and humidity controlled (40-45%) room. All samples were stored in a humidity controlled chamber, and measurements were conducted in the same day to minimize environmental effects. Surface topography was studied on a 2 μm x 2 μm scan area with an image resolution of 512 x 512 pixels at a scan rate of 1Hz. Multiple areas were imaged, and figures show representative morphology. Surface roughness analysis was performed using Nanoscope version 5.30 r2 image analysis software.

Scanning Electron Microscopy-Energy Dispersive X-Ray (SEM-EDAX)

Morphology of the fabric samples was investigated using FEI Quanta 200 Scanning Electron Microscope (SEM) in high voltage mode, equipped with a Thermo-Noran Vantage light element energy dispersive x-ray detector. Prior to imaging, samples were sputter-coated with gold (5nm thickness) to avoid damage to the fabric surface. Characterization of all the elements except hydrogen was obtained by x-ray spectroscopy under electron flux at a voltage of 25 kV and 1 torr pressure.

Proton (^1H) NMR Studies

A Varian 200 MHz NMR equipped with a standard 5 mm $^1\text{H}/^{13}\text{C}$ probe was utilized to identify the presence of POSS on the fabric. FL-POSS coated fabric was dipped in deuterated chloroform (CDCl_3) solution for 10-15 min to extract POSS deposited on the fabric surface. For reference purposes, ^1H NMR spectra of FL-POSS and neat fabric were also taken following a similar procedure. ^1H NMR spectra of all the samples were obtained from 256 scans with a relaxation delay of 1 second.

Surface Hydrophobicity and Hysteresis Evaluation

Surface wetting characteristics of fluorinated and non-fluorinated POSS coated fabrics were evaluated by measuring static contact angle on the fabric surface. Measurements were conducted using the sessile drop technique by a ramè-hart goniometer coupled with DROPimage[®] data analysis software. Ten μl of water was dropped onto a flat fabric surface and contact angle was measured after every 5 minutes over a period of 30 minutes. For comparison purposes, a similar test was performed on the Teflon film surface. Five measurements were taken across the surface, and an average value is reported. Adhesion of water droplets onto POSS coated fabric was observed by capturing an image of the water drop on the fabric surface at different tilt angles. Hysteresis was measured via dynamic contact angle measurements. Advancing and receding contact angles were measured, and their difference reported.

Stain and Acid-resistance

To evaluate the stain-resistance of FL-POSS coated fabric, a few drops (10-12 μl each) of coffee were placed on the fabric surface through a micro-syringe. Spreading of fluids was monitored visually by capturing the pictures through a digital camera at the

beginning and after 10 minutes. The stain area was observed visually by sucking back the fluid drops by a micro-syringe. Similarly, acid-resistance was evaluated by putting drops of concentrated sulfuric acid on the FL-POSS coated fabric. Spreading of acid drops, their permeation beneath the fabric surface, and stain area were also monitored visually by capturing digital pictures at the beginning and after 20 sec time. For comparison purposes, similar tests were also conducted on neat fabric.

Friction Evaluation

Dynamic coefficient of friction (COF) measurements were performed according to ASTM G 99, using a pin-on-disk tribometer (Micro Photonics Inc., PA). Two sets of readings were taken for each sample (1" x 1") inside a controlled humidity chamber (40% relative humidity) at 27°C. FL-POSS coated fabric samples were mounted firmly on a flat metal disc, which was rotated (path radius 3 mm) against a steel ball (3 mm diameter, Small Parts Inc., Miami Lakes, FL) at 20 rpm for 20 min. Relative surface friction measurements were conducted at an external load of 4N.

Thermogravimetric Analysis (TGA)

Chemical composition (polyester to cotton ratio) and thermal stability of neat and FL-POSS coated fabric samples were evaluated by thermogravimetric analysis utilizing a TA series Q500 instrument. Approximately 10-15 mg of fabric sample was used for analysis. Percentage weight loss of each sample was recorded on a platinum pan as a function of temperature from a starting temperature of 35°C up to 700°C, at a rate of 10 °C per minute under 60 ml/min nitrogen purge rate.

Results and Discussion

Tapping mode AFM phase images and 3-D surface topography of neat and POSS coated fabric are shown in Figure VII-2 and VII-3, respectively. Incorporation of POSS significantly alters the fabric surface topography with the appearance of large, raised features (150-200 nm in diameter, up to 100 nm in height) on the surface. These features were identified as POSS aggregates through multiple tools, including surface roughness, NMR, SEM-EDAX, and contact angle measurements as discussed in later sections.

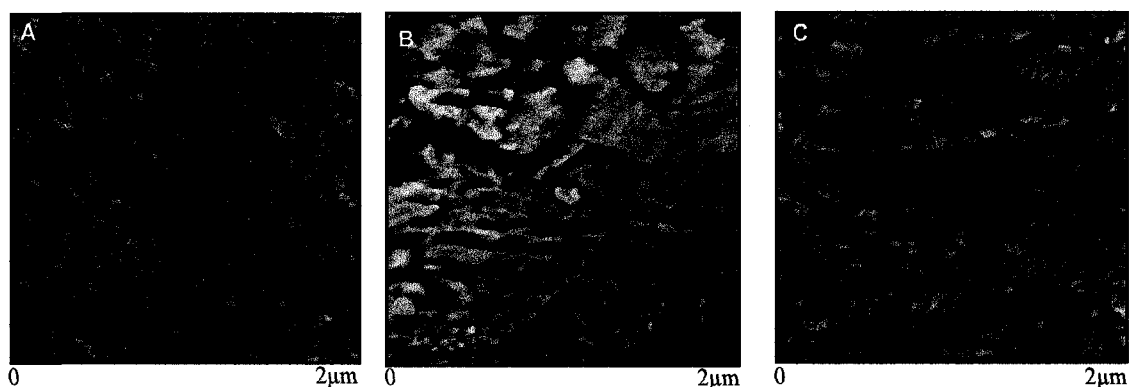


Figure VII-2. AFM Phase image of (A) neat fabric (Z scale:10°) (B) Tsp-POSS coated fabric (Z scale:100°) (C) FL-POSS coated fabric (Z scale:100°)

Table VII-1 shows the influence of POSS coating on the surface roughness profile. Neat fabric appears relatively smooth (root mean square roughness, RMS, of 0.6 nm), whereas Tsp-POSS and FL-POSS coated fabrics exhibit twelve and twenty-fold increase in surface roughness, respectively.

Table VII-1. AFM Roughness Analysis on Neat and POSS Coated Fabrics

| Sample | Mean Roughness (nm) | RMS Roughness (nm) | Max. Height (nm) |
|------------------------|---------------------|--------------------|------------------|
| Neat Fabric | 0.5 | 0.6 | 4.8 |
| Tsp-POSS coated fabric | 5.4 | 7.3 | 55.6 |
| FL-POSS coated fabric | 10.5 | 13.9 | 114 |

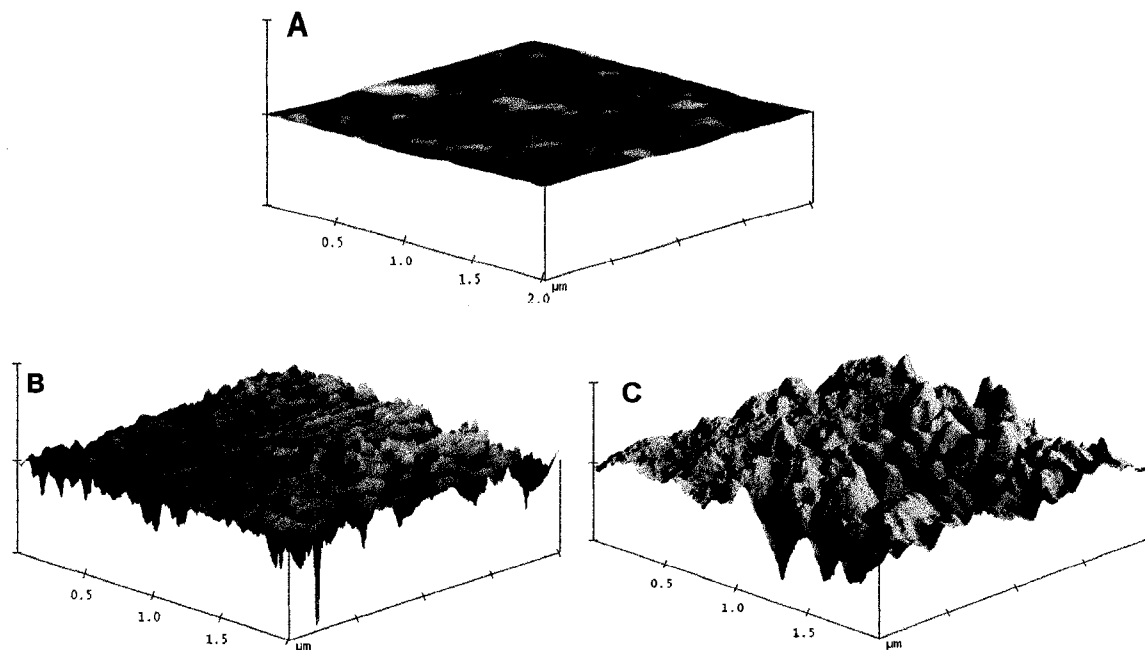


Figure VII-3. Three dimensional surface topography of (A) neat fabric (B) Tsp-POSS coated fabric (C) FL-POSS coated fabric (Z scale: 100 nm)

SEM micrographs and corresponding EDAX elemental analysis of neat and FL-POSS-coated fabrics are shown in Figure VII-4 (A)-(B). Uniform spherical surface features (100-150 nm) are observed on the POSS coated fabric. EDAX elemental analysis identifies these features as POSS aggregates, due to the appearance of the signature peak of silicon atom at 1.7 KeV. Additional peaks at 0.7 and 2.2 KeV are attributed to fluorine (from the trifluoropropyl substituents on FL-POSS) and gold (from the gold sputtering) respectively. Recognizing the fact that SEM/EDAX probes the surface a few microns deep (3-4 μm), proton (^1H) NMR studies were conducted to evaluate the chemical nature of the surface features by extracting them from the fabric surface in CDCl_3 solvent. Figure VII-5 shows the NMR spectra of the FL-POSS, solvent, and neat and FL-POSS coated fabrics. ^1H NMR spectra of neat fabric shows a singlet

due to the presence of moisture in the solvent, whereas neat POSS exhibits two triplets at 2.3 and 1.1 ppm which are attributed to: (a) the protons in proximity to the fluorine atoms and (b) two protons which are close to the silicon atoms. The presence of these two characteristic triplet peaks in the spectra of the coated fabric indicates the presence of POSS on the fabric surface.

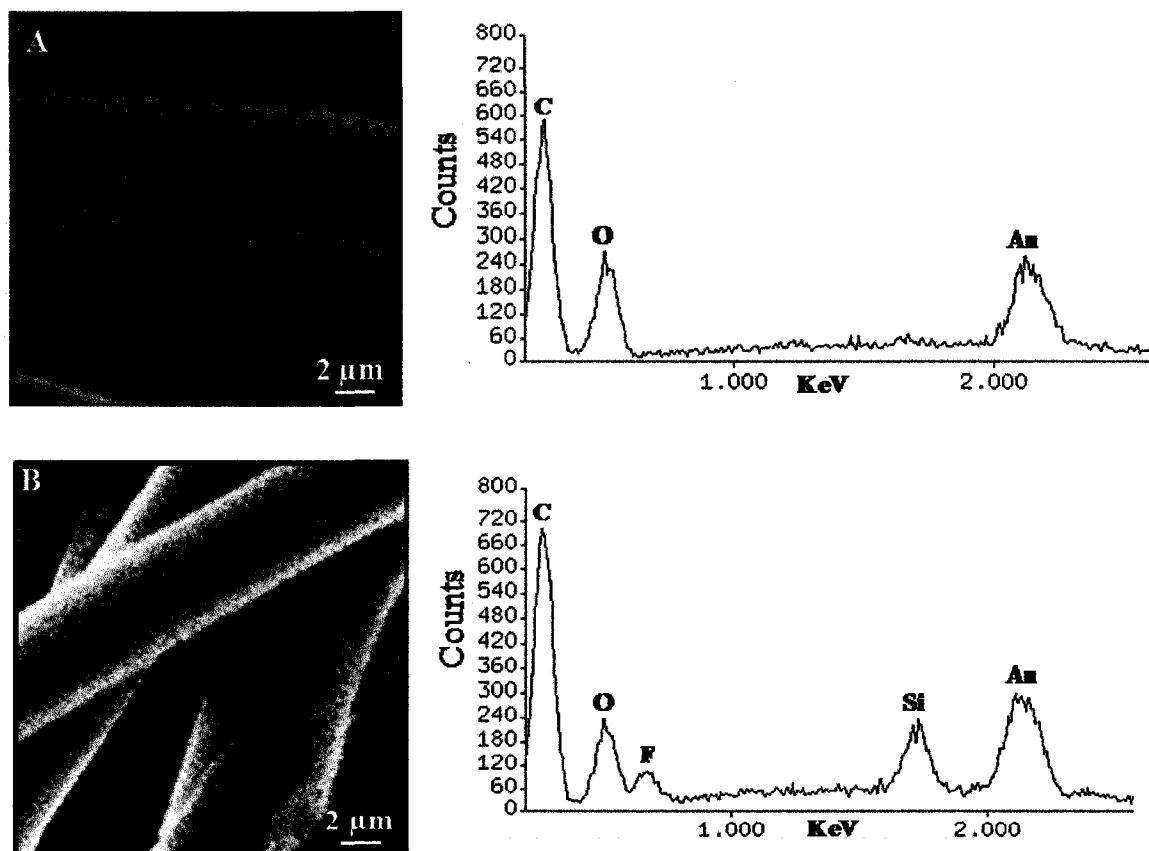


Figure VII-4. SEM micrograph and corresponding EDAX map of (A) neat fabric (B) FL-POSS coated fabric.

Conventionally, fluorinated additives and coatings are employed to impart hydrophobicity to surfaces, so it is of interest to evaluate the wetting characteristics of non-fluorinated POSS coated fabrics as well. Instant spreading of a water droplet on the

uncoated fabric indicates its highly hydrophilic nature. Incorporation of POSS in the fabric results in a dramatic increase in the surface hydrophobicity.

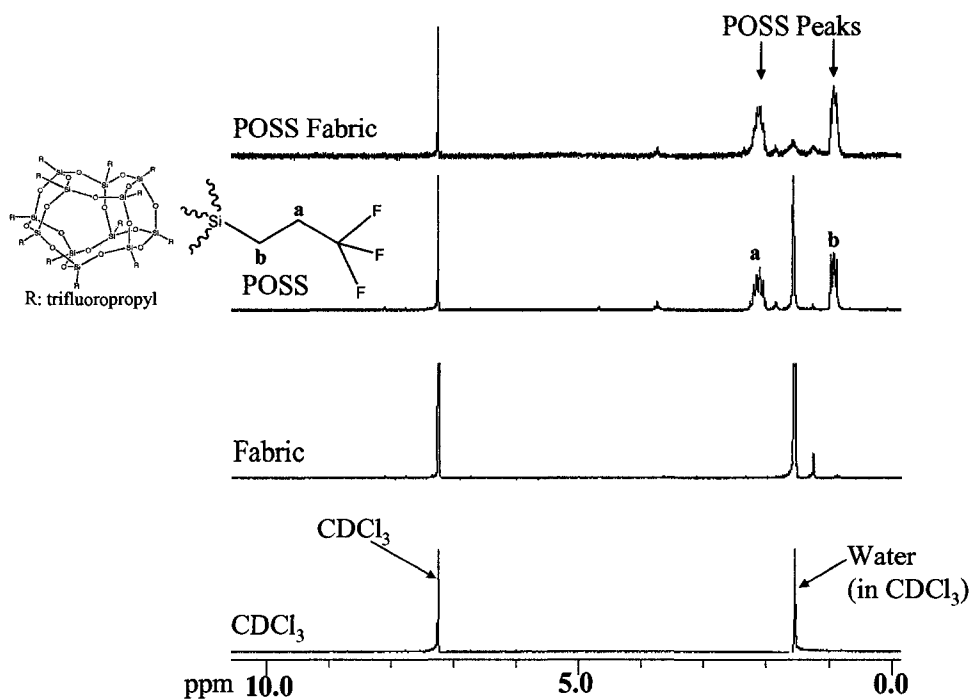


Figure VII-5. Proton NMR showing the presence of POSS on FL-POSS coated fabric.

Table VII-2 shows the water contact angle analysis with time for fluorinated and non-fluorinated POSS coated fabrics in comparison to behavior for a Teflon film surface.

Table VII-2. Comparative Static Water Contact Angle Analysis for POSS Coated Fabrics and Teflon.

| Time (min) | FL-POSS (°) | Tsp-POSS (°) | Teflon (°) |
|------------|-------------|--------------|------------|
| 0 | 137 | 119 | 112 |
| 1 | 136 | 118 | 111 |
| 2 | 136 | 117 | 109 |
| 5 | 136 | 116 | 103 |
| 10 | 134 | 113 | 98 |
| 15 | 134 | 110 | 95 |
| 20 | 133 | 100 | 91 |
| 25 | 132 | 86 | 80 |

The POSS-coated fabric surfaces exhibit contact angles of 120° to 137° , indicating reversal of surface wetting character. Interestingly, POSS coated fabrics exhibited higher hydrophobicity than the benchmark hydrophobic Teflon surface. The FL-POSS coated fabric exhibits a contact angle of 137° , approaching superhydrophobic behavior. Multiple factors, including high surface roughness, spiky morphology caused by the presence of POSS aggregates coupled with the hydrophobic fluorinated organic groups of FL-POSS contribute to the high hydrophobicity. This behavior is in agreement with the recent findings reported by Mabry and coworkers^{22,23} on the superoleophobic and superhydrophobic fabric surfaces using highly hydrophobic long chain fluorodecyl and fluorooctyl POSS.

Contact angle measurements as a function of time provide an indication of the stability of the surface hydrophobicity. All surfaces exhibited some extent of reduction in contact angles with time. Among the two POSS molecules evaluated, FL-POSS exhibited the most stable non-wetting characteristics over the evaluated time period (9% drop in contact angle for FL-POSS vs 50% drop for Tsp-POSS). The Teflon film surface exhibited a 30% drop in contact angle over the same time period. It is important to note that the overall reduction in water contact angle over time is a combined effect of evaporation and spreading of the water droplet. Spreading is mainly characterized by reduction in the height of the water droplet with simultaneous increase in its width. Evaporation, on the other hand, is characterized by reduction in both height and width of the water droplet. Figure VII-6 shows the simultaneous reduction in the height and width of a water droplet on a Teflon surface over time. POSS coated fabric surfaces exhibited contact angle reduction caused primarily by the evaporation over 30 minutes, similar to

the behavior exhibited by Teflon film. More importantly, all surfaces exhibited original levels of high hydrophobicity after drying.

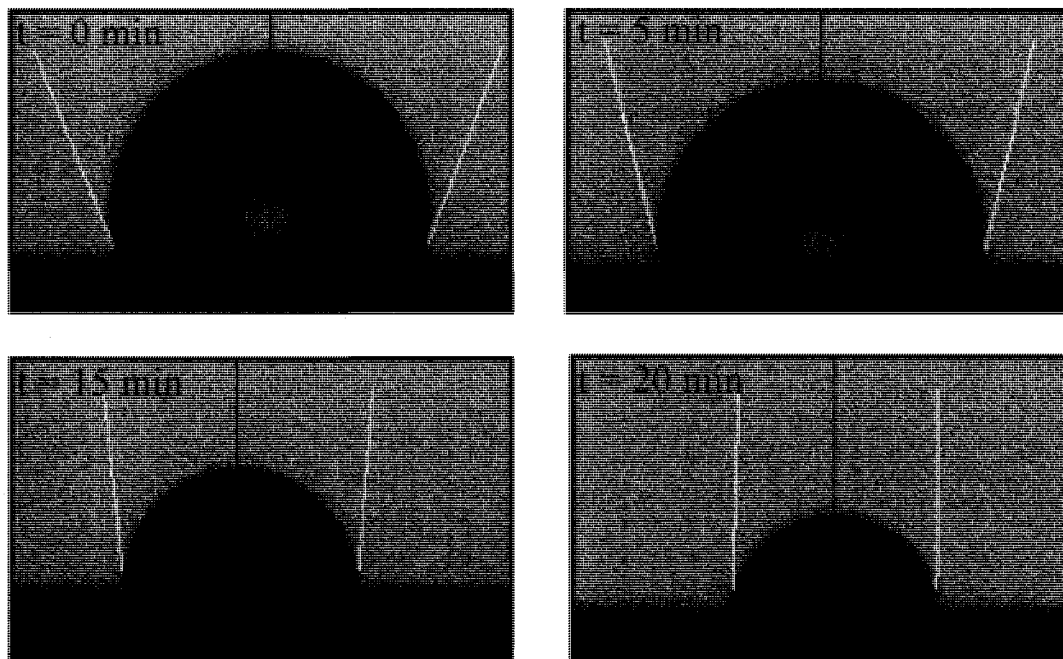


Figure VII-6. Variation in the size of water droplet with time on Teflon film surface.

Commonly, highly hydrophobic surfaces exhibit rolling of a water droplet due to poor adhesion between the solid-liquid interface and limited hysteresis.²² In our samples, an unusual non-sliding behavior of water droplets on POSS coated fabric was observed even after tilting the surface by 180°. Figure VII-7 shows the pinning of a water droplet onto the FL-POSS coated fabric surface at different tilt angles, indicating high adhesion at the fabric-water interface. Hysteresis measurements (Table VII-3) exhibit a large difference between the advancing and receding contact angles, indicating a chemically heterogeneous and highly rough surface. POSS coated fabric exhibited high hysteresis, which, in part, explains the stable non-sliding behavior of the water droplet at different tilt angles. Recently Xu et al.²⁸ reported a similar ultra-hydrophobic and non-sliding

behavior of poly (methyl methacrylate) and amphiphilic polyurethane (hydrophilic polyethylene glycol and hydrophobic fluorinated isocyanate blocks) blend surfaces. While high hydrophobicity is attributed to the increased surface roughness and the presence of low surface energy, hydrophobic POSS domains on the surface, sticking of water droplets is linked to the interaction between the hydrophilic fabric domains and water.

Table VII-3. Contact Angle Hysteresis for POSS Coated Fabrics

| Sample | Advancing (θ_a) ($^\circ$) | Receding (θ_r) ($^\circ$) | Hysteresis ($^\circ$) |
|------------------------|--|---|----------------------------|
| FL-POSS coated fabric | 147 | 120 | 27 |
| Tsp-POSS coated fabric | 128 | 110 | 18 |

Furthermore, stain resistance of the FL-POSS coated fabric, as tested with a coffee droplet, shows significant improvement. Figure VII-8 (A) and (B) clearly show that the coffee droplet spreads instantly on the uncoated fabric leading to a large stain area, whereas minimal spreading is observed for the POSS-coated fabric even after 10 minutes. After removing the coffee droplet from the coated fabric surface, significant reduction in the stain area is observed (Fig.VII-8 (C)).

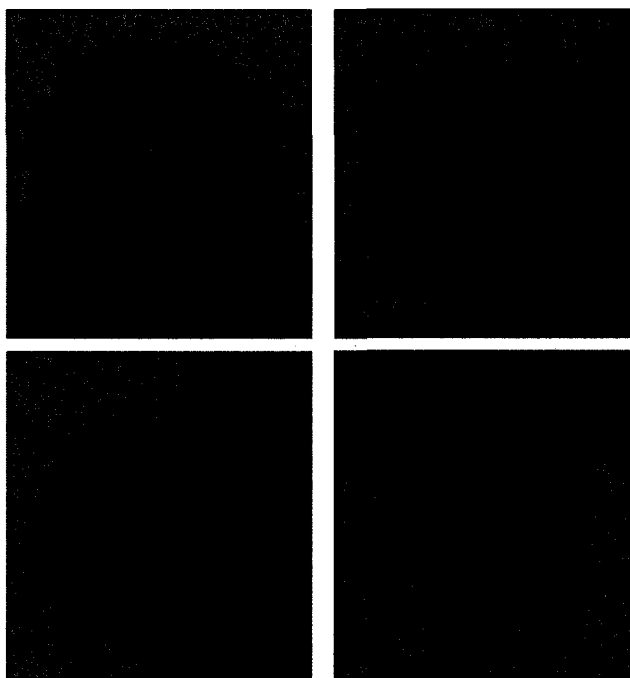


Figure VII-7. Adhesion of water droplet onto FL-POSS coated fabric at varying tilt angles.

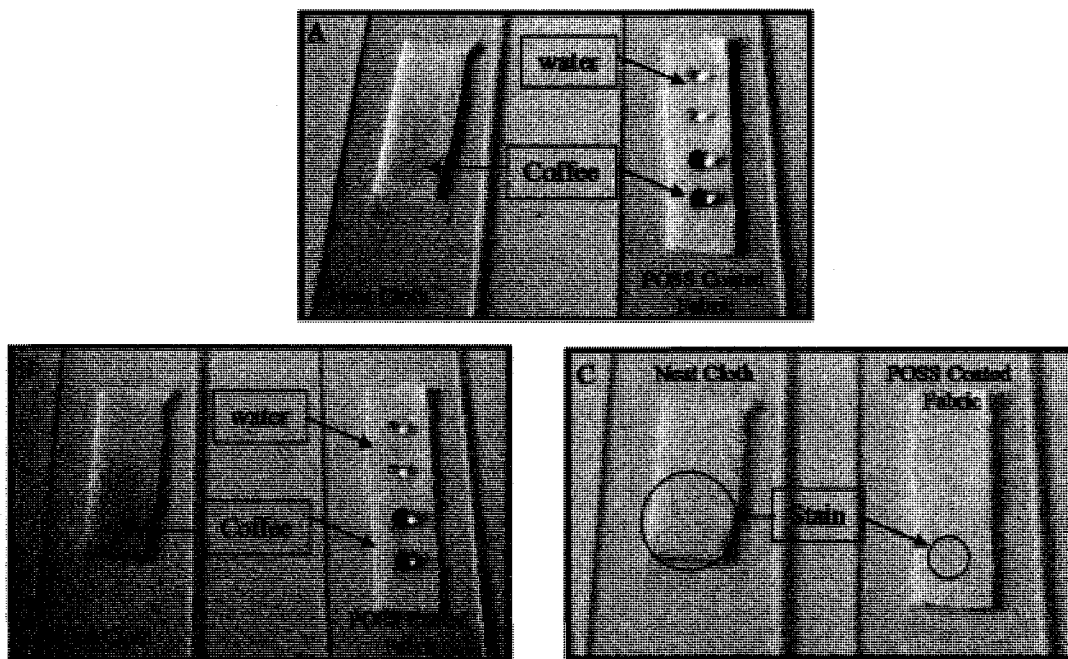


Figure VII-8. Effect of water and coffee droplet on neat and FL-POSS coated fabric (A) time $t=0$ (B) $t=10$ min (C) comparison of stain area after removal of coffee droplets.

Similarly, a dramatic change in the acid resistance is observed for the FL-POSS coated fabric, evaluated with a drop of concentrated sulfuric acid (Figure VII-9 (A)-(B)). In the case of acid spillage, exposure time is critical and a quick response (within a few seconds) is required to minimize the damage to the exposed area. While neat fabric showed instant spreading and permeation of acid to the surface beneath it, POSS-coated fabric offered significant resistance to spreading as well as permeation. Figure VII-9 (B) shows that a relatively small amount of acid permeates to the reverse side of the fabric after 20 seconds, significantly reducing the exposure to the surface beneath it. Enhanced stain and acid resistance is attributed, in part, to the enhanced surface roughness and presence of chemically robust POSS cages on the surface.

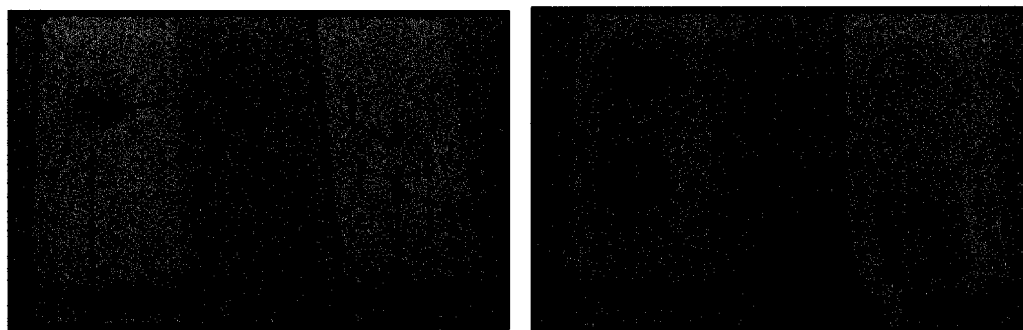


Figure VII-9. Acid resistance of neat and FL-POSS coated fabric at (A) time $t=0$ (B) $t=20$ sec.

Relative surface friction, an important surface characteristic, exhibits a significant reduction on fabrics coated with FL-POSS. Figure VII-10 shows the relative surface friction for neat and FL-POSS treated samples. FL-POSS coated fabric exhibits a surface friction of 0.08 in comparison to 0.13 for neat fabric, a 33% reduction in surface friction. Reduction in relative surface friction is attributed to the presence of POSS aggregates on the surface, as has been observed in previous studies of POSS/polymer

blends.^{26,27} Additionally, increased surface roughness, which reduces the true area of contact between the sliding surfaces, contributes to reduction in measured surface friction. Additionally, increased surface roughness, which reduces the true area of contact between the sliding surfaces, contributes to reduction in measured surface friction.

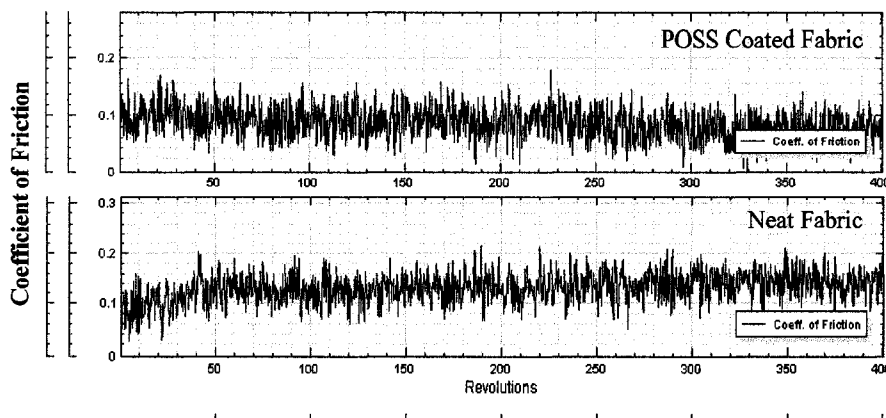


Figure VII-10. Macroscale relative surface friction of neat and FL- POSS coated fabric.

Finally, to understand the influence of POSS coating on the thermal stability and decomposition behavior of fabric, thermogravimetric analysis was performed. Figure VII-11 shows the percentage weight loss with respect to temperature for neat and FL-POSS coated fabrics. Both fabrics exhibit a stepwise decomposition behavior with the cotton component decomposing first at lower temperatures (peak degradation temperature, $T_p = 409^\circ\text{C}$) followed by the decomposition of the polyester component at higher temperatures ($T_p = 478^\circ\text{C}$). Percentage weight loss at the step change is linked to the composition of the fabric, with 35% weight loss at the first degradation peak indicating 35% cotton and 65% polyester, equivalent to the composition reported by the supplier. Furthermore, TGA thermograms show no affect of the POSS coating on the

thermal stability of the fabric over the entire temperature range.

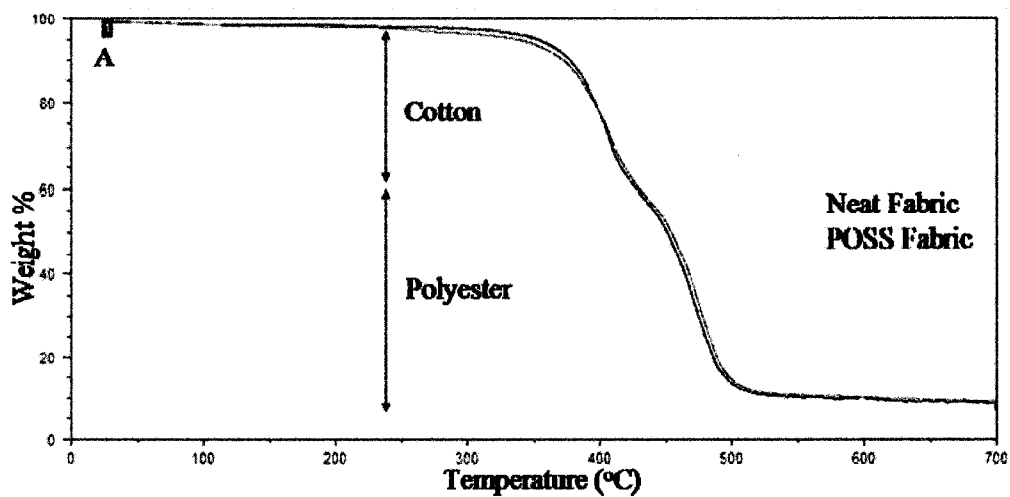


Figure VII-11. TGA analysis of neat and FL-POSS coated fabric.

Conclusions

This study demonstrates the reversal of the surface wetting characteristics of a hydrophilic fabric *via* nanostructured coating of organic-inorganic POSS molecules. The presence of POSS aggregates on the coated fabric surface, confirmed *via* AFM, NMR, and SEM/EDAX, leads to a spiky topography with twelve to twenty fold increases in surface roughness. Short chain FL-POSS molecules exhibited highly stable, non-wetting characteristics, approaching superhydrophobic behavior on a hydrophilic fabric surface. Interestingly, non-fluorinated Tsp-POSS coated fabric showed non-wetting behavior at a level that is typically exhibited by fluorinated materials. Stability of the POSS-induced hydrophobicity as a function of exposure to water over time was similar to that observed for Teflon. More importantly, drying of the POSS-coated surfaces after exposure to water resulted in a return to initial levels of hydrophobicity. Further studies of the effects of washing cycles on hydrophobicity are a subject of ongoing research efforts in our laboratory. The chemical composition of the POSS molecules coupled with their surface morphology and roughness profiles explain their hydrophobic effects.

Typically, water droplets roll on highly hydrophobic surfaces, due to limited hysteresis and adhesion. However, in our studies, POSS coated surfaces exhibited high hydrophobicity coupled with high hysteresis and non-sliding behavior of water droplets even after tilting the surface by 180°. This behavior is attributed to the non-homogeneous, nano-roughened surface, that allows “sticking” of the water droplets to the hydrophilic fabric substrate while the coating of low surface energy, hydrophobic POSS domains on the surface simultaneously promotes hydrophobicity

Additionally, FL-POSS coated fabric exhibited exceptional stain and acid resistance along with a significant reduction in relative surface friction. Current study indicates potential to develop environmentally friendly and cost effective non-fluorinated POSS-based coatings through effective control of surface morphology and POSS chemistry.

Acknowledgements

This work was supported by the STTR Program of the National Science Foundation under Award Number OII-0539295 and the RET Program of the National Science Foundation under EEC-0602032. The authors also gratefully acknowledge Hybrid Plastics Inc., (Hattiesburg, MS) for providing POSS materials.

References

-
- ¹ Nakajima, A.; Hashimoto, K.; Watanabe, T. *Monatsh. Chem.* **2001**, *132*, 31.
- ² Coulson, S.R.; Woodward, I.; Badyal, J.P.S.; Brewer, S.A.; Willis, C. *J. Phys. Chem. B* **2004**, *104*, 8836.
- ³ Lau, K. K. S.; Bico, J.; Teo, K. B. K.; Chhowalla, M.; Amaratunga, G. A. J.; Milne, W. I.; McKinley, G. H.; Gleason, K. K. *Nano Lett.* **2003**, *3*, 1701.
- ⁴ Erbil, Y.H.; Demirel, L.A.; Avci, Y.; Mert, O. *Science* **2003**, *299*, 1377.
- ⁵ Qi, K.; Walid A. D.; Xin, J. H.; Mak, C. L.; Tang, W.; Cheung, W.P. *J. Mater. Chem.* **2006**, *16*, 4567.
- ⁶ Yuranova, T.; Mosteo, R.; Bandara, J.; Laub, D.; Kiwi, J. *Journal of Molecular Catalysis A: Chemical* **2006**, *244*, 160.
- ⁷ Meilert, K.T.; Laub, D.; Kiwi, J. *Journal of Molecular Catalysis A: Chemical* **2005**, *237*, 101.
- ⁸ Bozzi, A.; Yuranova, T.; Kiwi, J. *J. Photochem. Photobiol., A: Chem.* **2005**, *172*, 27.
- ⁹ Lichtenhan, J. D. *Comments Inorg. Chem.* **1995**, *17*, 115.
- ¹⁰ Fong, H.; Dickens, S.H.; Flaim, G. M., *Dental Materials* **2005**, *21*, 520.
- ¹¹ Dodiuk-Kenig, H.; Maoz, Y.; Lizenboim, K.; Eppelbaum, I.; Zalsman, B.; Kenig, S., *J. Adhesion Science and Technology* **2006**, *20*, 1401.
- ¹² Klapdohr, S.; Moszner, N. *Chemical Monthly* **2005**, *136*, 21.
- ¹³ Shockey, E. G.; Bolf, A. G.; Jones, P. F.; Schwab, J. J.; Chaffee, K. P.; Haddad, T. S.; Lichtenhan, J. D. *Appl. Organomet. Chem.* **1999**, *13*, 311.
- ¹⁴ Lee, A.; Lichtenhan, J. D. *J. Appl. Polym. Sci.* **1999**, *73*, 1993.
- ¹⁵ Romo-Urbe, A.; Mather, P. T.; Haddad, T. S.; Lichtenhan, J. D. *J. Polym. Sci., Part B:*

-
- Polym. Phys.* **1998**, *36*, 1857.
- ¹⁶ Patel, R. R.; Mohanraj, R.; Pittman, C. U. *J Polym Sci Part B: Polym Phys* **2006**, *44*, 234.
- ¹⁷ Lee, A.; Lichtenhan, J. D. *Macromolecules* **1998**, *31*, 4970.
- ¹⁸ Ning, H.; Martin, B.; Andreas, S. *Macromolecules* **2007**, *40*, 9672.
- ¹⁹ Fu, B. X.; Hsiao, B. S.; Pagola, S.; Stephens, P.; White, H.; Rafailovich, M.; Sokolov, J.; Mather, P. T.; Jeon, H. G.; Phillips, S.; Lichtenhan, J. D.; Schwab, J. *Polymer* **2001**, *42*, 599.
- ²⁰ Zhao, Y.; Schiraldi, D.A. *Polymer* **2005**, *46*, 11640.
- ²¹ Eric, D.; Maryline; R.; Serge, B. *Fire and Materials* **2002**, *26*, 149.
- ²² Tuteja, A.; Choi, W.; Ma, M.; Mabry, J.; Mazzella, S.; Rutledge, G.; Mckinley, G.; Cohen, R. E. *Science* **2007**, *318*, 1618.
- ²³ Mabry, J. M.; Yandek, G. R.; Haddad, T. S.; Moore, B. M.; McGrath, L. M.; Ruth, P. N. *ACS Polymer Preprints* **2008**, *49*, 872.
- ²⁴ Blanksby, S. J.; Ellison, G. B. *Acc. Chem. Res.* **2003**, *36*, 255.
- ²⁵ http://pubs.acs.org/subscribe/journals/esthag-w/2005/nov/tech/rr_reformulating.html
- ²⁶ Misra, R.; Fu, B. X.; Morgan, S. E. *J. Polym. Sci. Part B: Polym. Phys.* **2007**, *45*, 2441.
- ²⁷ Misra, R.; Fu, B. X.; Morgan, S. E. Manuscript submitted.
- ²⁸ Zhao, N.; Xie, Q.; Kuang, X.; Wang, S.; Li, Y.; Lu, X.; Tan, S.; Shen, J.; Zhang, X.; Zhang, Y.; Xu, J.; Han, C. *Adv. Funct. Mater.* **2007**, *17*, 2739.

CHAPTER VIII

NANOSCALE REDUCTION IN SURFACE FRICTION OF POLYMER SURFACES
MODIFIED WITH SC3 HYDROPHOBIN FROM SCHIZOPHYLLUM COMMUNE

Abstract

Hydrophobins are amphipathic self-assembling proteins secreted by filamentous fungi that exhibit remarkable ability to modify synthetic surfaces. Thin coatings of Sc3 hydrophobin isolated from the wood rotting fungus *Schizophyllum commune* were prepared via spin coating and adsorption techniques onto polymeric surfaces. Surface morphology and nanotribological characteristics of the films were evaluated using lateral force microscopy and nanoindentation techniques. This paper reports the first observation of reduction in nanoscale relative surface friction of Sc3 hydrophobin protein modified polymeric surfaces. Relative friction coefficients were dramatically reduced and hydrophilicity increased for polymer surfaces modified with Sc3 hydrophobin thin films. Morphology of the protein films as well as degree of surface modification was observed to be a function of film formation technique and composition of the substrate.

Introduction

Hydrophobins are small proteins (~100 amino acids) secreted by fungi that can self-assemble into a polymeric amphipathic membrane at interfaces and effect the reversal of the surface polarity. Hydrophobins play multiple roles in the development and reproduction of fungi, including fungal attachment to surfaces, stabilization and aid in emergence of fruiting bodies and aerial hyphae, and protective coatings for fungal structures.^{1,2,3} Isolated hydrophobin proteins self-assemble from aqueous solution onto hydrophobic or hydrophilic surfaces, and form a tightly bound membrane that is highly resistant to removal by solvents, denaturing agents, or changes in temperature or pressure. For example, a Teflon surface can be rendered hydrophilic by introduction into an aqueous solution of a Class I hydrophobin (water contact angle decreases from 120° to ~30°),^{4,5} and the resultant thin protein film is removed from the surface only by treatment with trifluoroacetic acid.^{6,7}

The mechanism of hydrophobin self-assembly has been the subject of considerable research effort. The hydrophobin protein Sc3 from the wood rooting fungus *Schizophyllum commune* has been the most widely studied hydrophobin, and is the subject of the present study. It has been shown that isolated Sc3 dissolved in aqueous solution associates via two distinct mechanisms.⁸ When air bubbles are introduced into hydrophobin solution, spontaneous self-assembly of hydrophobin occurs at the air-water interface, resulting in the formation of hydrophobin-stabilized dispersed microscopic air bubbles. These dispersions are highly stable and the membranes can be disrupted only by treatment with TFA. In undisturbed hydrophobin solutions, on the other hand, less tightly associated aggregates form in a time-dependent manner. These loose aggregates

can be converted to self-assembled membranes via vortexing. The assembled structures, however, do not disassemble over time to produce the loose aggregates. Thus the method of preparation and handling of hydrophobin solutions is extremely important, and it is critical to employ freshly-prepared solutions of known handling history for study of assembly and surface modification.

Hydrophobins are divided into two classes with different assembly behavior.^{1,9,10} Class I proteins, such as Sc3, form assembled membranes that are extremely stable and can be disrupted only with trifluoroacetic acid.¹¹ Class II hydrophobin assemblies; on the other hand, are responsive to a variety of stimuli, including denaturing agents, surfactants, and organic solvents.¹² The three dimensional structure of a Class II hydrophobin, HFBII from *Trichoderma reesei*, has recently been determined.^{13,14} The authors propose that the molecular assembly process creates a “hydrophobic patch” on the outside of the assembly that is directed towards the hydrophobic surface and facilitates attachment to the surface. They suggest that a similar mechanism occurs for Class I proteins. The extreme stability of Class I assemblies in combination with their dramatic propensity to assemble, however, make them more difficult to analyze and characterize by conventional techniques. Recent studies of surface modification by HFBII and SC3 indicate that the class I Sc3 hydrophobin generally yields higher changes in surface character, as measured by water contact angle.¹⁵

Because of their remarkable assembly and surface modification behavior, hydrophobins have been suggested for a wide range of biomedical, technical and personal care applications,^{16,17,18} for example to provide hydrophilic, improved biocompatibility, low friction surfaces for biomedical devices. Due to the difficulties in isolating these

proteins and their currently limited production, the greatest potential for initial application is in the area of high value biomedical or personal care applications.¹³

Recent studies indicate that hydrophobin has low cytotoxicity, and genetic engineering provides hydrophobin derivatives with improved biocompatibility.^{19,20,21} Corvis et al.²² demonstrated the utility of Sc3 hydrophobin for enzyme immobilization. Other potential high value applications of hydrophobins were recently reviewed,²³ and include use as antifouling or antibacterial coatings, and emulsion stabilization aids for personal care products.

Low friction surfaces are required in various biomedical applications including catheters, guide-wires and other medical tools used in surgical procedures. Low friction not only helps to reduce chances of injury to tissues and membranes in contact with these devices, thereby facilitating smooth surgical procedures, but it also enhances long term use of the devices. Conventionally, low friction surfaces for biomedical devices are achieved either by using fluoropolymers for constructing these devices or by coating the surface with lubricants such as silicone oil, glycerin or jelly type materials. Although these lubricants render low friction to the surface initially, due to their weak adhesive properties they migrate to the surface and are unable to maintain their lubricious performance for longer duration. Once migrated to the surface these materials may be potential contaminants. Teflon fluoropolymer provides low friction, however it exhibits poor biocompatibility, which is required for temporary or permanent implant devices.^{20,21} This research work is an effort to address these problems by achieving stable, low friction, lubricious coatings with greater adhesion to the substrate using naturally derived hydrophobin. Although the biological function of hydrophobin proteins has been

extensively studied and the morphology of the assembled films has been reported, the mechanical and tribological performance of these self-assembled thin films has not been studied. A thorough understanding of hydrophobin thin film tribomechanical performance is critical for their eventual use in biotechnology applications.

In the present study, thin films of the hydrophobin Sc3 isolated from the wood-rotting fungus *Schizophyllum commune* were prepared from aqueous solution using adsorption and spin-coating techniques. The two film preparation techniques represent an equilibrium process (adsorption) and a more energy-intensive process (spin-coating) in which solvent is evaporated at a rapid rate to form an evenly distributed film.²⁴ Films were deposited onto two hydrophobic polymeric surfaces, polystyrene and a copolymer of benzoyl-1,4 phenylene and 1,3-phenylene (PBP), with the goal of achieving improved hydrophilicity and reduced friction. Polystyrene (PS) was chosen as the reference amorphous polymer material, as PS is a common amorphous thermoplastic used widely in biomedical and biotechnology applications, whose friction and hydrophobicity behavior at macroscale are well understood. The nanotribological and nanomechanical performance of PS have recently been evaluated using nanoprobe techniques.^{24,25} Newly commercialized PBP copolymers exhibit ultra-high modulus and strength to weight ratios.²⁶ These high performance polymers are under investigation for a wide range of applications, including biomedical applications such as magnetic resonance imaging (MRI)-transparent implants or dental composites. Recent studies of the macro and nanotribological properties of PBP in our laboratories demonstrated ultra-low friction properties for this materials.³⁵ It is of further interest to explore the surface modification behavior of hydrophobin, specifically the friction reduction capabilities of hydrophobin

thin films, as a function of substrate type and film preparation technique. The morphology, adhesion and friction characteristics of hydrophobin thin films assembled onto these surfaces were evaluated via nanoprobe techniques.

Experimental

Materials

The hydrophobin protein Sc3 was isolated from the wood rooting fungus *Schizophyllum commune* and purified according to previously published procedures.^{27,28,29} Briefly, the fungus *Schizophyllum commune* was grown as a 1 L standing culture in minimal medium.³⁰ Purification of the Sc3 hydrophobin that was secreted into the liquid media begins by separating the fungal material from the culture media by centrifugation. Crystalline ammonium sulfate and sodium phosphate are added to clear fungal culture supernatant. Purification of the hydrophobin is performed by hydrophobic interaction chromatography with ammonium sulfate solutions of progressively lower concentration buffered by sodium phosphate at pH 8.0. The collected fractions are dialyzed extensively against water. The obtained solution is then agitated thoroughly. The solution is then centrifuged resulting in small pellet of Sc3 and the supernatant is discarded. The pellet is dissolved in trifluoroacetic acid (TFA) and then dried under nitrogen and lyophilized for 12 h. After redissolving in phosphate buffer, the protein content is analyzed by the bicinchoninic acid assay³¹ (Pierce Chemical) using bovine serum albumin as a standard according to the manufacturer's recommendations. Because Sc3 is prone to self-assemble in response to even the slightest agitation of the solution, prior to the experiment, Sc3 is treated with 100% TFA and then lyophilized, which is reported to disassemble any Sc3 complex.¹¹ The resultant lyophilized Sc3 was then dissolved in 20 mM sodium phosphate buffer (20mM, NaH₂PO₄, pH 7.0) to yield a final protein concentration of 30 µg/mL.

Polystyrene (PS) of weight average molecular weight 280,000 g/mol was purchased from Aldrich. Polyphenylene copolymer (PBP), PARMAX[®] 1200, was supplied by Mississippi Polymer Technologies, Bay St. Louis, MS. Mica discs (9.9 mm diameter, Ted Pella, Inc.) were used as the substrate for PS and PBP films.

Sample Preparation

Spin coating of PBP and PS solutions was performed using a KW-4A (CHEMAT Technology) spin coater onto freshly cleaved mica substrates. PBP was dissolved in benzyl chloride at two weight percent, and PS was dissolved in tetrahydrofuran (THF) at a concentration of 20 mg/mL. 10 μ L of polymer solution was deposited on the mica disc. Spin coating was performed in two successive stages, an initial stage at 500 RPM for 15 seconds followed by a second stage at 3000 RPM for 45 seconds. Samples were dried for 3 hrs in ambient air followed by drying in a vacuum oven for 12 hrs at 70°C.

Hydrophobin film coatings were prepared onto spin coated PS and PBP substrates via two methods: spin coating and adsorption. Spin coating was performed by depositing 10 μ L of Sc3 hydrophobin aqueous solution (30 μ g/mL) onto PS and PBP substrates and spinning at 750 RPM for 20 seconds. Samples were washed with deionized (DI) water and dried in air. The adsorption method involved complete coverage of substrate polymer film surface with hydrophobin solution (30 μ g/mL) for 12 hrs followed by (DI) water washing and drying in ambient air. Freshly prepared Sc3 solutions were employed for the studies in order to minimize time-dependent loose aggregate formation.³⁹

Water Contact Angle Measurement

Surface advancing water contact angle measurements were conducted using sessile drop technique by a First Ten Angstroms (FTA, Portsmouth, VA) contact angle goniometer coupled with FTA 200 data analysis software.

AFM Surface Topography and Section Analysis

AFM evaluations were performed using a Dimension 3000 scanning probe microscope (Digital Instruments, Santa Barbara, CA). Probes for surface topography and friction measurements were purchased from Veeco probes, CA. Surface topography and roughness were obtained in tapping mode using an etched silicon probe, 125 μm long with a resonant frequency of 275 kHz, nominal force constant of 40 N/m and a nominal tip radius of 10 nm. Height and phase images were collected simultaneously on 1 μm x 1 μm scan size with an image resolution of 256 x 256 pixels at a scan rate of 1 Hz. Surface roughness and section analysis was performed on 1 μm x 1 μm scan area for all the samples using Nanoscope version 5.30 r2 image analysis software.

Surface Friction Evaluation

Friction measurements were obtained by operating the AFM in lateral force microscopy (LFM) mode using a triangular silicon nitride probe with a nominal spring constant of 0.58 N/m. Force–distance curves and friction signals were recorded at various setpoint voltages on a scan area of 5 μm x 5 μm and scan frequency of 1 Hz. The normal applied force was calculated from force-distance curves by the product of normal deflection of the cantilever and spring constant of the cantilever. Deflection of the cantilever is due to intermolecular forces between the tip and surface, which may be attractive and/or repulsive in nature.^{30,31} In LFM, friction force is experienced in the

direction opposite to the scan direction, while the normal force acts in the direction perpendicular to both the scan direction and the friction force direction. The cantilever experiences a torque imposed by the tip, which is recorded as a voltage signal. Voltage (mV) signal is then converted to friction force (nN) based on a calibration constant from a silicon wafer, which was determined to be 0.144 nN/mV using a reported friction coefficient of 0.06 for neat silicon wafer.³⁰ Trace and retrace images (Figure VIII- 1(A), (B)) are obtained in LFM while the tip moves over the stationary sample at a scan direction of 90°. The frictional force for a given normal load is calculated as the mean value of the separation distance between the trace and retraces signals.^{30,31,32}

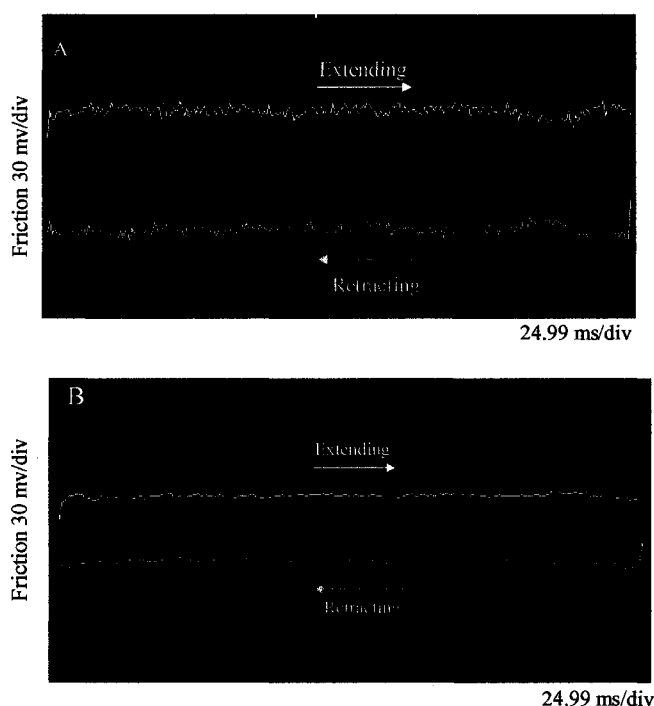


Figure VIII-1. Friction loops for (A) Neat PS (B) Sc3 hydrophobin coated PS.

Triboindenter Film Thickness Measurements

Nanoindentation thickness evaluations were performed on a Hysitron TriboIndenter[®] with a three sided diamond pyramid (Berkovich Type) tip using Triboscan[®] 6.0 image analysis software. Tip calibration was performed using fused silica

as the reference material. Normal force was applied to the surface at a loading and unloading rate of $10 \mu\text{N}/\text{sec}$ with a two second hold period in between loading and unloading cycle. Nanoindentation was performed under closed loop with load control using compliance method in which force-displacements curves are obtained during loading and unloading cycles. As the indenter presses into the surface the displacement is recorded as a function of the applied load.

Results and Discussion

Surface Morphology

Freshly cleaved mica and spin-coated PS and PBP films surfaces imaged by AFM are smooth and featureless, as expected.³⁵ A clear change in surface morphology is observed when Sc3 hydrophobin protein is deposited onto the spin-coated polymer films, with the appearance of spherical raised features (Figures VIII-2 (A), (B) and VIII-3 (A), (B)). The features appear in all films, whether prepared by adsorption or spin-coating on PS or PBP, but their dimensions and distribution vary with film preparation technique, nature and composition of the substrate.

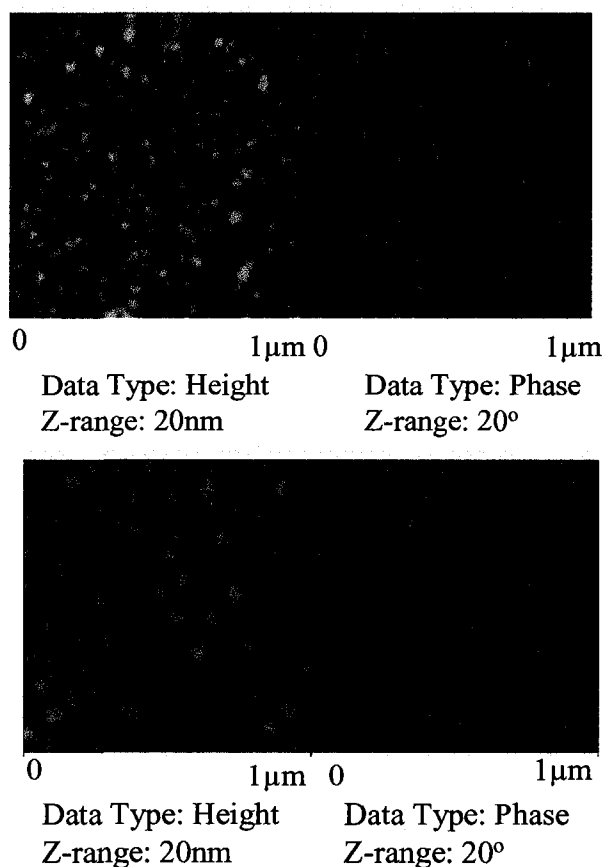


Figure VIII-2. Height and phase image of Sc3 hydrophobin on PS (A) Adsorbed (B) Spin coated.

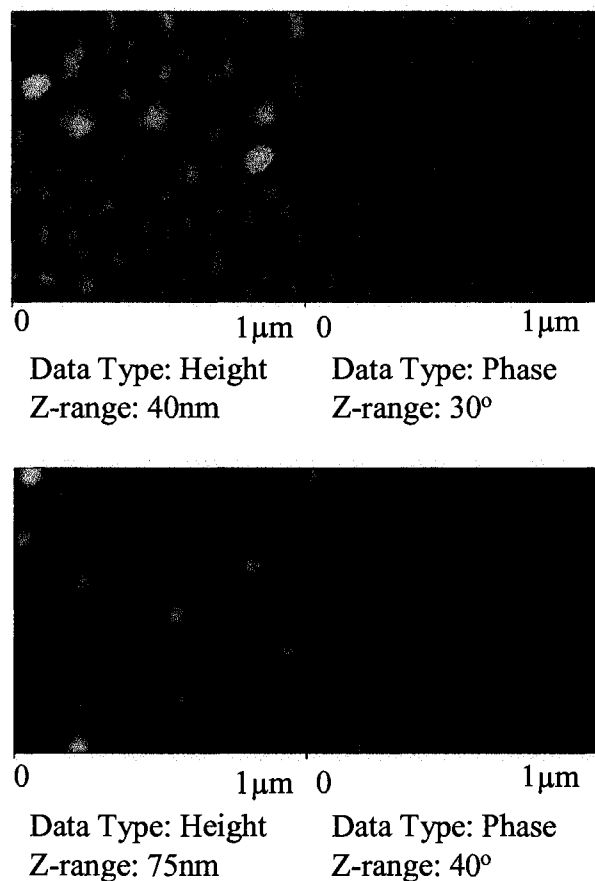


Figure VIII-3. Height and phase image of Sc3 hydrophobin on PBP (A) Adsorbed (B) Spin coated.

The density of these surface features appears to be greater for Sc3 films prepared by adsorption, presumably because the overnight adsorption technique allows adequate time for protein assembly to occur in an equilibrium-type process. Protein films prepared via spin coating exhibit features of more regular size and size distribution, however they appear to exist as separate aggregates rather than as a continuous coating. Protein assembly may occur in solution during the spin coating process prior to the deposition of the film on the surface, as hydrophobin assembly is readily induced by agitation of solution.³⁹ Similar morphological features are observed on PS and PBP substrates, but

the features are larger and more widely dispersed on the PBP film. There is a clear contrast in morphology development on the hydrophobic polymer film surfaces in comparison to hydrophobin assembled onto a hydrophilic glass surface, as shown in the tapping mode image of Sc3 deposited onto a glass slide (Figure VIII-4). On the hydrophilic glass surface, Sc3 hydrophobin self assembles into rodlets approximately 5–12 nm wide by 20 nm length, a typical pattern that has also been observed on fungal spore surfaces.^{1, 6, 11, 32}

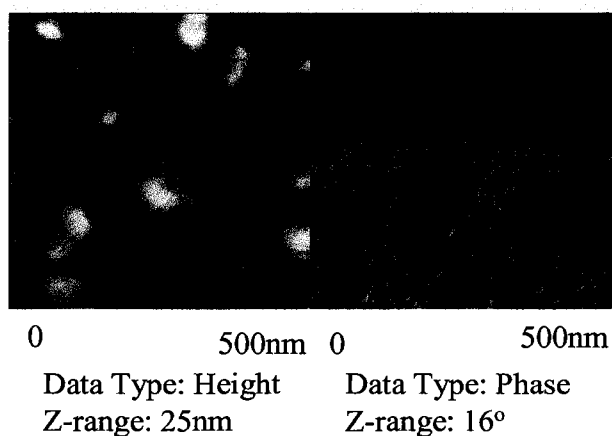


Figure VIII-4. Height and phase image of Sc3 hydrophobin rodlet pattern on glass substrate.

Surface roughness analysis for the samples is summarized in Table VIII-1. Root mean square (RMS) roughness for the neat PS and PBP films is approximately 0.3 nm, indicating a smooth surface that is only slightly rougher than the freshly cleaved mica surface (RMS ~ 0.2 nm). RMS roughness is three to six times greater for polymer films modified with Sc3 hydrophobin, indicating the presence of the protein coating. Adsorbed Sc3 coatings produce rougher surfaces than spin coated films, as would be predicted from the more irregular surface features observed in the tapping mode images of the adsorbed coatings. The greatest RMS roughness value, 2.05 nm, was observed for

Sc3 adsorbed onto the PBP surface, compared to an RMS of 0.99 nm for Sc3 adsorbed onto the PS surface. The observed differences in the morphologies of the adsorbed protein films may be the result of differences in surface interactions and/or adhesion of the proteins to the polymer substrates, which in turn affect the protein self-assembly process and morphology of the resultant film.

Table VIII-1. AFM roughness analysis for neat and Sc3 hydrophobin coated polymer substrates

| Sample | Max. Height (nm) | Mean Roughness (nm) | RMS Roughness (nm) |
|------------------------|---------------------|------------------------|-----------------------|
| Freshly cleaved Mica | 1.35 | 0.11 | 0.15 |
| PS on Mica | 2.61 | 0.21 | 0.26 |
| Sc3 spin coated on PS | 7.55 | 0.57 | 0.76 |
| Sc3 adsorbed on PS | 19.1 | 0.66 | 0.99 |
| PBP on Mica | 10.0 | 0.23 | 0.30 |
| Sc3 spin coated on PBP | 17.2 | 0.49 | 0.91 |
| Sc3 adsorbed on PBP | 33.3 | 1.50 | 2.05 |

Section analysis of the tapping mode images provides quantitative measurement of height and width of observed features, and provides further indication of differences in Sc3 protein interaction with different substrates. Multiple cross sections of the 1 μm x 1 μm tapping mode images were evaluated. Representative sections are shown in Figures VIII-5 (A), (B) and VIII-6 (A), (B). Hydrophobin protein films formed on PS surfaces yielded raised features of 2–3 nm in height, with diameters varying from 60 to 100 nm.

Larger diameter features in greater density were observed for adsorbed coatings in comparison to spin-coated hydrophobin films. As the diameter of the globular Sc3 protein is estimated at approximately 3 nm,²⁰ these raised features would correspond to a single molecule thickness, with the large diameter arising from multiple molecule aggregates. Section analysis of Sc3 protein film on the PBP surface indicates raised features approximately 9 nm in height with diameters varying from 90 to 140 nm. These larger features correspond to multiple protein (or extended molecule) thickness, with a greater number of molecules involved to form the larger horizontal aggregates.

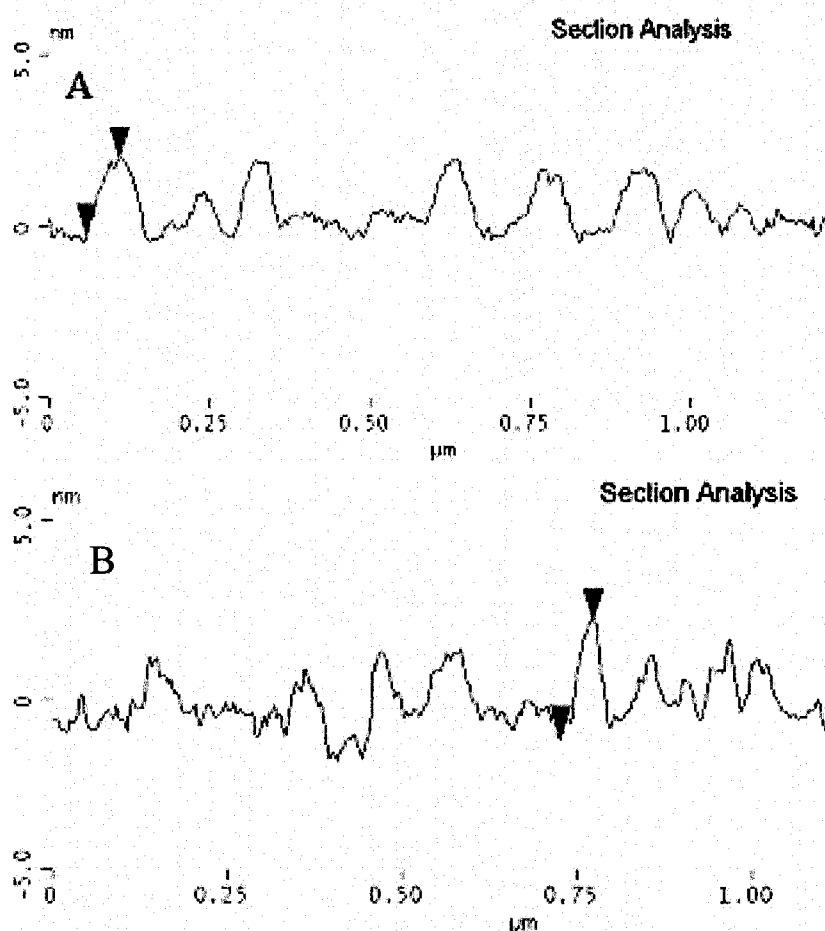


Figure VIII-5. Section analysis of Sc3 hydrophobin on PS (A) Spin coated (B) Adsorbed.

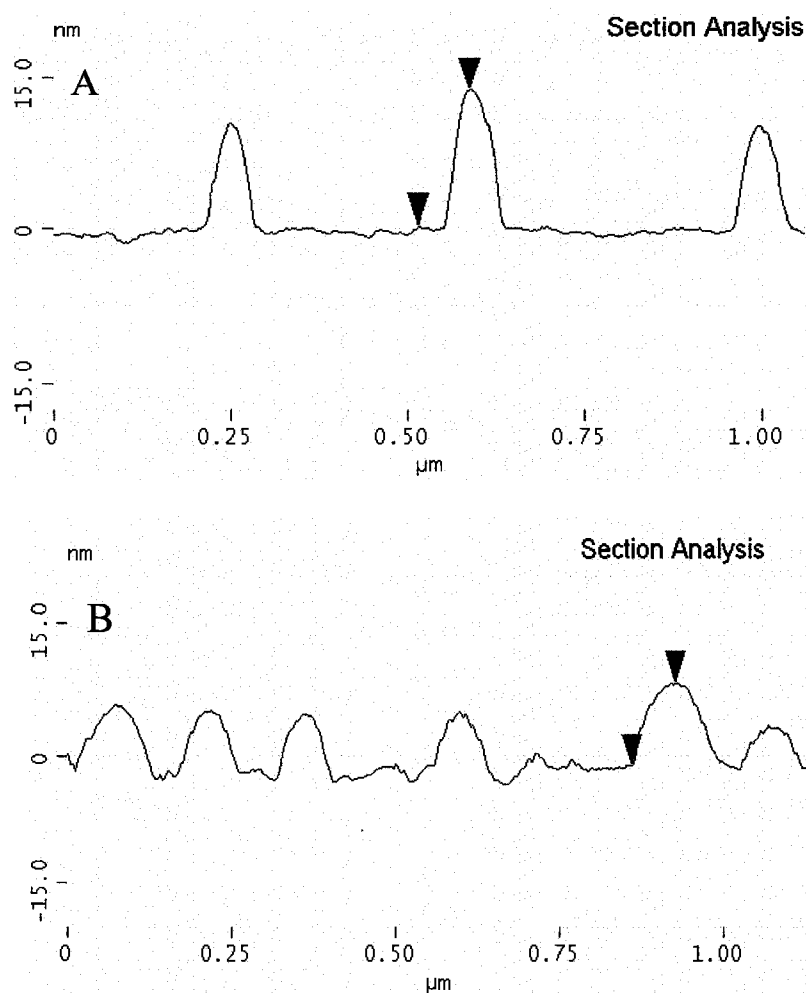


Figure VIII-6. Section analysis of Sc3 hydrophobin on PBP (A) spin coated (B) adsorbed.

Nanoscale Friction Analysis

Measured friction force as a function of applied load yields linear plots for all samples (Figures VIII-7 and VIII-8). Relative coefficient of friction (COF) is obtained from the slopes of the lines, and is summarized in Table VIII-2. The hydrophobin-coated surfaces demonstrate very low friction, with reductions in COF of up to 80% in comparison to neat PS. Although the neat PBP substrate demonstrates a COF

approximately half that of neat PS, all hydrophobin coated surfaces yield similar relative COF, with values ranging from 0.01 to 0.02, indicating similar coating effectiveness for all samples. Friction coefficients were measured repeatedly over a period of several weeks with consistent results obtained in all measurements indicating stable attachment of Sc3 hydrophobin coating onto polymer surfaces.

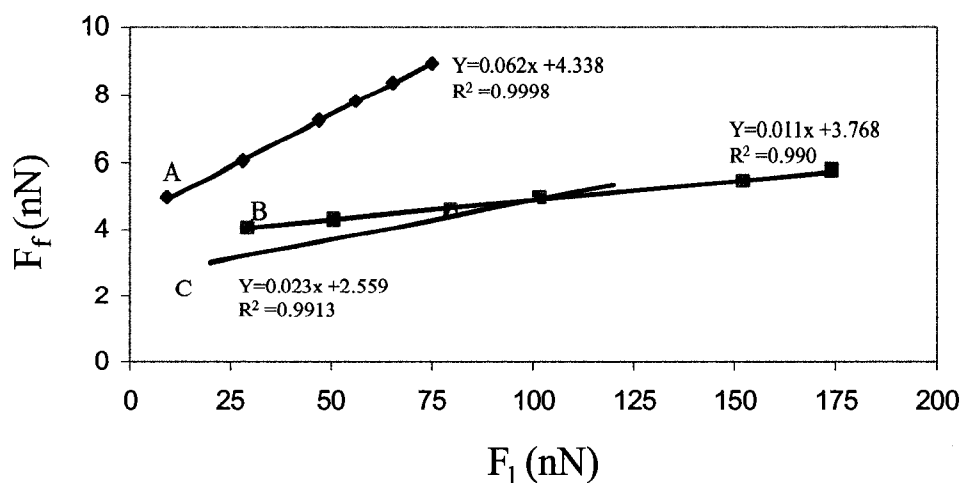


Figure VIII-7. Friction force Vs Normal force plot for (A) Neat PS (B) Sc3 hydrophobin spin coated on PS (C) Sc3 hydrophobin Adsorbed on PS.

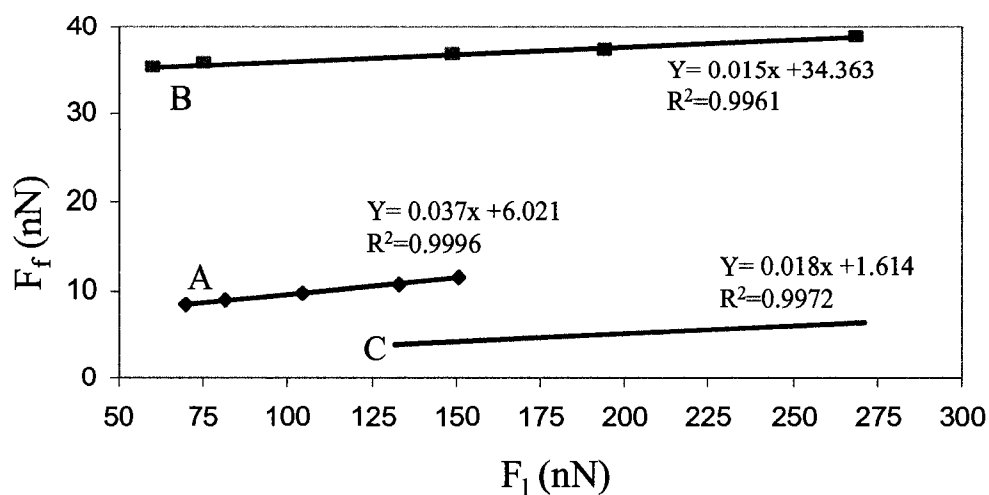


Figure VIII-8. Friction force Vs Normal force plot for (A) Neat PBP (B) Sc3 hydrophobin spin coated on PBP (C) Sc3 hydrophobin Adsorbed on PBP.

Representative friction loops for the neat PS and Sc3 hydrophobin coated PS films are shown in Figure VIII-1 (A), (B). The gap between the trace and retrace friction curves is reduced for the hydrophobin-coated surface, indicating reduction in friction. The adhesive force (F_a) between the AFM tip and the substrate was estimated from force curves and from the intercept of the friction force vs. applied load plots, and is summarized in Table VIII-2. Fairly good agreement is observed for adhesive force values obtained via the two methods. For PS samples, the adhesive force increases in the order neat PS < adsorbed coating Sc3 << spin coated Sc3, with the spin coated sample showing dramatically higher adhesion. For PBP samples, the adhesive force increases in the order of adsorbed coating Sc3 < neat PBP << spin coated Sc3.

Table VIII-2. Relative value of COF and adhesive force for neat and Sc3 hydrophobin coated PS and PBP films.

| Sample | COF | Adhesive Force (nN) from force curve | Adhesive Force (nN) from friction plot |
|------------------------|-------|---|---|
| PS on Mica | 0.062 | 60.8 | 70.0 |
| Sc3 spin coated on PS | 0.011 | 326 | 342 |
| Sc3 adsorbed on PS | 0.023 | 96.1 | 111 |
| PBP on Mica | 0.037 | 116 | 163 |
| Sc3 spin coated on PBP | 0.015 | 925 | 2290 |
| Sc3 adsorbed on PBP | 0.018 | 82.2 | 89.7 |

Typical force curves for neat and Sc3 coated PBP substrates are shown in Figure VIII-9, illustrating the dramatic increase in adhesive force for spin-coated hydrophobin surfaces. It would be expected that the greatest adhesive force would be exhibited for the

most hydrophilic surface, due to interaction between the hydrophilic silicon nitride probe tip and the surface. However, the adhesive force trends do not match the trends obtained by macroscale water contact analysis (Table VIII-3).

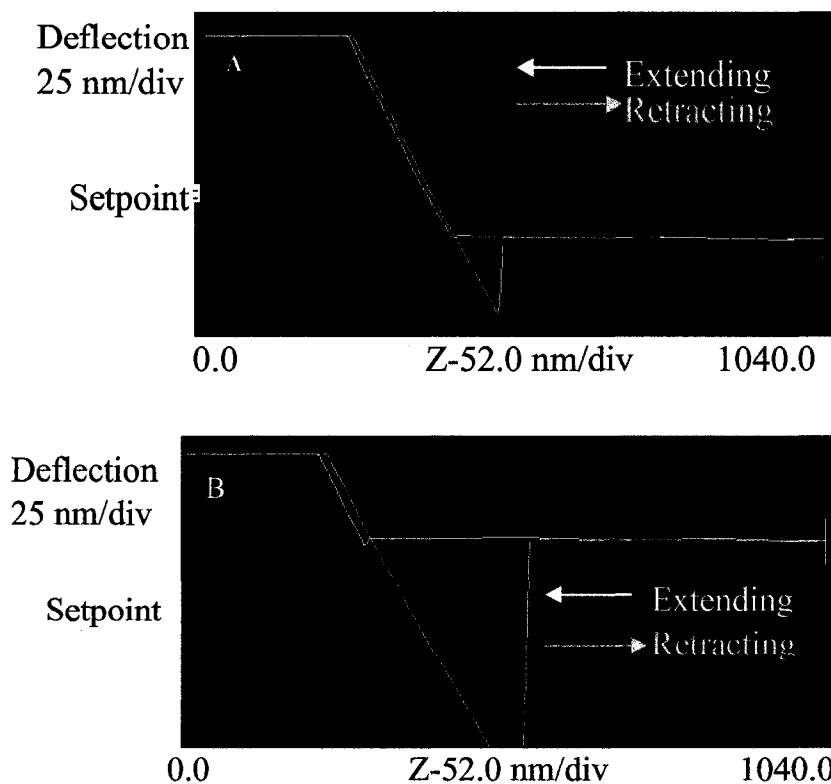


Figure VIII-9. Force curves for (A) Neat PS (B) Sc3 hydrophobin coated PS.

Water contact angle studies further illustrate the reversal of surface polarity provided by the assembled hydrophobin coating. Unmodified PS and PBP surfaces are hydrophobic, yielding contact angle values greater than 80 degrees. Coating with Sc3 hydrophobin yielded dramatically reduced water contact angles. For the adsorbed protein coatings, contact angle is 30 to 40 degrees, as has been previously reported for Sc3 coatings on hydrophobic polymer substrates.⁵ For the spin coated protein coatings, contact angle is approximately 60 degrees, indicating only partial coverage of the polymer surfaces or a difference in protein assembly during the spin coating process.

The difference in observed trends for nanoprobe adhesive force measurements and water contact angle measurements could be due to several factors. First, the water contact angle measurement is a bulk measurement, where a surface area of several mm² is analyzed, while the nanoprobe force curve measurements analyze nanoscale areas. Secondly, differences in surface roughness may partially explain the differences. It has been shown that differences in surface roughness can affect water contact angle measured values^{33,34,35} and may also be a factor in nanomechanical measurements.³⁶ Thirdly, it has been reported that a second layer of hydrophobin may assemble on top of an assembled hydrophobin layer, causing a second reversal of the surface polarity³⁷ (i.e. hydrophobic → hydrophilic → hydrophobic). Thus, differences in surface roughness, related to differences in height of the raised features observed, may result from a distribution of multilayer assemblies, with different surface properties.

Table VIII-3. Water contact angle for unmodified and Sc3 hydrophobin coated PS and PBP film surface.

| Sample | Contact Angle (°) |
|------------------------|-------------------|
| PS on Mica | 88 |
| Sc3 spin coated on PS | 62 |
| Sc3 adsorbed on PS | 28 |
| PBP on Mica | 82 |
| Sc3 spin coated on PBP | 65 |
| Sc3 adsorbed on PBP | 40 |

Film Thickness Analysis

Thickness measurements via triboindenter are summarized in Table VIII-4. Thickness of the polymer spin-coated film substrates, which is indicated by the change in slope in the force-distance curve, is similar for both films, estimated as approximately 55 nm for neat PBP and 50 nm for neat PS.

Table VIII-4. Triboindenter thickness data for unmodified and Sc3 hydrophobin spin coated PS and PBP film surface.

| Sample | Thickness (nm) |
|------------------------|----------------|
| PS on Mica | 50 |
| Sc3 spin coated on PS | 20 |
| PBP on Mica | 55 |
| Sc3 spin coated on PBP | 12 |

Representative force distance curves for neat PBP, neat PS, Sc3 spin coated onto the PBP and PS substrate are shown in Figures VIII-10 (A), (B) and VIII-11(A), (B) respectively. Analysis of these curves indicates a protein layer thickness of approximately 12 nm on PBP whereas Sc3 coating on the PS substrate was estimated to be almost double this thickness, at 20 nm. Note that these measurements represent the thickness of the entire Sc3 film, while the section analysis measurements discussed earlier represent only the height of the raised features on the surface of the film. Thus, Sc3 coatings on PBP have average thickness of 12 nm, with RMS roughness of 0.91 nm; while Sc3 coating on PS has average thickness of 20 nm, with RMS roughness of 0.76

nm. The differences in observed protein layer thickness, morphology and roughness of the Sc3 coating on the two polymer substrates most likely explain the differences in measured water contact angle for the different coatings. Interestingly, however, the measured surface friction does not vary for the different coating types, with very low friction coefficients obtained for all Sc3 coated surfaces. This indicates that only a very thin Sc3 film is required for dramatic friction reduction on the polymer surface.

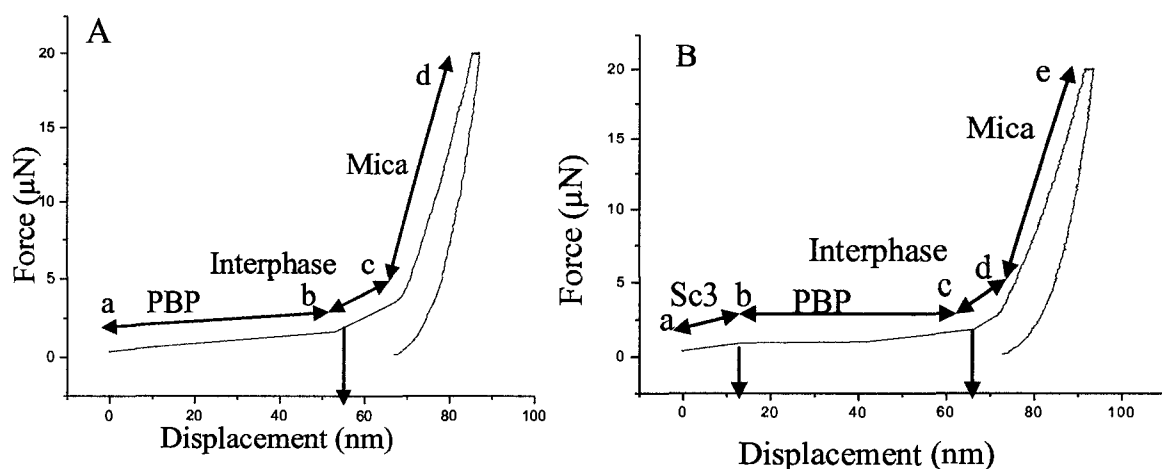


Figure VIII-10. Triboindenter film thickness for (A) Neat PBP (B) Sc3 hydrophobin coated PBP

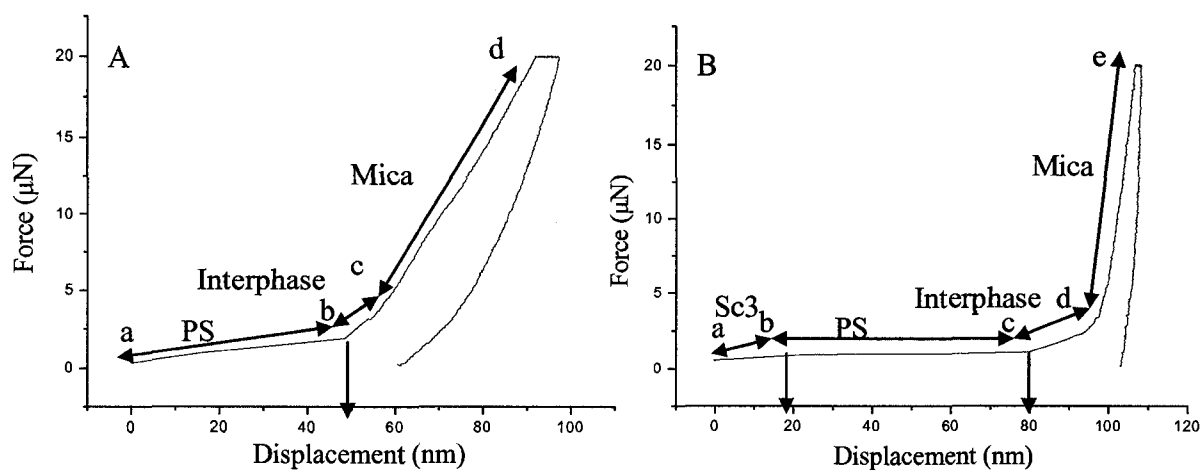


Figure VIII- 11. Triboindenter film thickness for (A) Neat PS (B) Sc3 hydrophobin coated PS.

Conclusions

Thin and stable coatings of Sc3 hydrophobin, in the range of 10–20 nm, were prepared via spin coating and adsorption techniques from aqueous solution onto polymeric substrates. Polymeric surfaces with enhanced lubricity and reduced surface friction were obtained *via* Sc3 hydrophobin surface modification. Nanotribological analysis using lateral force microscopy indicates ultra low relative friction coefficients for all hydrophobin-coated surfaces, in the range of 0.01 to 0.02 for measured relative friction coefficient. This represents a 70-80% reduction in friction coefficient in comparison to neat polystyrene, and a 50-60% reduction in comparison to neat PBP, as the neat PBP has an initial friction coefficient that is substantially lower than that of PS. Friction measurements are reproducible and the coatings provide stable friction reduction over a period of several weeks.

Hydrophilicity of the hydrophobin coated polymer surfaces is significantly increased. Films prepared via the adsorption technique yielded more dense morphology, with more complete coverage of the polymer substrate, and greater hydrophilicity as measured via water contact angle. Nanoscale force of adhesion measurements, however, yielded different trends, with the spin-coated samples showing higher adhesion between the hydrophilic silicon nitride tip and the Sc3 coated surface. These differences may in part be explained by surface roughness effects and differences in the surface area measured in the different techniques. Morphology, thickness and surface polarity of the Sc3 coatings can be altered by varying the substrate composition and coating conditions. The results indicate potential utility of hydrophobin coatings for personal care or

biomedical applications requiring lubricious, low friction surfaces and further studies of these potential applications are underway.

Acknowledgements

This work was supported primarily by the MRSEC Program of the National Science Foundation under Award Number DMR 0213883. Additionally, acknowledgement is made to the donors of the American Chemical Society Petroleum Research Fund for partial support of this research and NSF MRI award number DMR-0421403. The authors thank Dr. Sergei Magonov (VEECO Industries, CA) for valuable discussions and inputs during this study.

References

-
- ¹ Wosten, H. A. B. *Annu. Rev. Microbiol.* **2001**, *55*, 625.
- ² Wessels, J. G. H. *Proceedings of the National Science Council, ROC, Part B: Life Sciences* **1992**, *16*, 134.
- ³ Wessels, J. G. H.; deVries, O. M. H.; Asgeirsdottir, S. A.; Schuren, F.H.J. *Plant Cell* **1991**, *3*, 793.
- ⁴ Hong, C., K.; Benson, S. D.; Cannon, G. C.; McCormick, C. L., Morgan, S. E., ANTEC Proceedings **2004**.
- ⁵ Wosten, H. A. B.; deVocht, M. L. *Biochimica et Biophysica Acta* **2000**, *1469*, 79.
- ⁶ Wosten, H. A. B.; Schuren, F. H. J; Wessels, J. G. H. *The EMBO Journal* **1994**, *13*, 5848.
- ⁷ DeVocht, M. L. Ph.D. Dissertation, University of Groningen, **2001**.
- ⁸ Stroud, P.A.; Goodwin, J. S.; Butko, P.; Cannon, G.C.; McCormick, C. L., *Biomacromolecules* **2003**, *4*, 956.
- ⁹ Wessels, J. G. H. *Annu. Rev. Phytopathol.* **1994**, *32*, 413.
- ¹⁰ Wessels, J. G.H. *Adv. Microb. Physiol.* **1997**, *38*, 1.
- ¹¹ Wosten, H. A. B.; de Vries, O.; Wessels, J. G. H. *The Plant Cell* **1993**, *5*, 1567.
- ¹² Russo, P. S.; Blum, F. D.; Ipsen, J. D.; Yusuf, J. A.; Miller, W. G. *Can. J. Botany* **1982**, *60*, 1414.
- ¹³ Linder, M.B.; Szilvay,G.R.; Setala, T.N.;Penttila,M.B. *FEMS Microbiology Reviews* **2005**, *29*, 877.
- ¹⁴ Hakanpa , J.; Paananen, A.; Askolin, S.; Nakari-Seta la , T.; Parkkinen, T.; Penttila, M.; Linder, M.B.; Rouvinen, J. *J. Biol. Chem.* **2004**, *279*, 534.

-
- ¹⁵ Lumsdon, S.O.; Grenn, J.; Stieglitz, B. *Colloids and Surfaces B: Biointerfaces* **2005**, *44*, 172.
- ¹⁶ Scholtmeijer, K.; Wessels, J. G. H.; Wosten, H. A. B. *Appl Microbiol Biotechnol* **2001**, *56*, 1.
- ¹⁷ FR2833490 Assigned to L'Oreal, France.
- ¹⁸ Scholtmeijer, K.; Wessels, J. G. H.; Wosten, H. A. B. *Appl Microbiol Biotechnol* **2001**, *56*, 1.
- ¹⁹ Scholtmeijer, K.; Janssen, M.I.; Van Leeuwen, M.B.M.; Van Kooten, T.G.; Hektor, H.; Wösten, H.A.B. *Bio-Medical Materials and Engineering* **2004**, *14*, 447.
- ²⁰ Scholtmeijer, K.; Janssen, M.I.; Gerssen, B.; De Vocht, M.L.; Van Leeuwen, M.B.M.; Van Kooten, T.G.; Wösten, H.A.B.; Wessels, J.G.H. *Appl. Environ. Microbiol.* **2002**, *68*, 1367.
- ²¹ Janssen, M.I.; Van Leeuwen, M.B.M.; Scholtmeijer, K.; Van Kooten, T. G.; Dijkhuizen, L.; Wösten, H.A.B. *Biomaterials* **2002** *23*, 4848.
- ²² Corvis, Y.; Walcarius, A.; Rink, R.; Mrabet, N.T.; Rogalska, E. *Anal. Chem* **2005**, *77*, 1622.
- ²³ Hektor, H. J.; Scholtmeijer, K. *Current Opinion in Biotechnology* **2005**, *16*, 434.
- ²⁴ Weill, A.; Dechenaux, E. *Polym. Eng. Sci.* **1988**, *28*, 945.
- ²⁵ Morgan, S. E.; Misra, R.; Jones, P. J. *Polymer* **2006**, *47*, 2865.
- ²⁶ MPT Polymers <http://www.mptpolymers.com/>, accessed 10/01/05
- ²⁷ Martin, G. G.; Cannon, G. C.; McCormick, C. L. *Biopolymers* **1999**, *49*, 621.
- ²⁸ Martin, G. G.; Cannon, G. C.; McCormick, C. L. *Biomacromolecules* **2000**, *1*, 49.

-
- ²⁹ Stroud, P.A.; Goodwin, J. S.; Butko, P.; Cannon, G.C.; McCormick, C. L. *Biomacromolecules* **2003**, *4*, 956.
- ³⁰ Dons, J. J. M.; de Vries, O. M. H.; Wessels, J. G. H. *Biochem. Biophys. Acta* **1979**, *563*, 100.
- ³¹ Smith, P. K.; Krohn, R. I.; Hermanson, G. T.; Mallia, A. K.; Gartner, F. H.; Provenzano, M. D.; Fujimoto, E. K.; Goeke, N. M.; Olson, B. J.; Klenk, D. C. *Anal. Biochem.* **1985**, *150*, 76.
- ³² DeVocht, M.; Scholtmeijer, K.; vander Vegte, E.; de Vries, O.; Sonveaux, N.; Wosten, H.; Ruyschaert, J.; Hadziioannou, G.; Wessels, J.; Robillard, G. *Biophysical Journal* **1998**, *74*, 2059.
- ³³ Lin, C. T.; Lin, K. L. *Applied Surface Science* **2003**, *214*, 243.
- ³⁴ Miller, J.D.; Veeramasuneni, S.; Drelich, J.; Valamanchill, M. R. *Polymer Engineering and Science* **1996**, *36*, 1849.
- ³⁵ Taniguchi, M.; Pieracci, J. P.; Belfort, G. *Langmuir* **2001**, *17*, 4312.
- ³⁶ <http://physicsweb.org/articles/world/18/2/9>
- ³⁷ Vander, V. W.; Vander, M. H. C.; Woosten, H. A.; Wessels, J. G.; Busscher, H. J. *Biophys. Chem.* **1996**, *57*, 253.

CONCLUSIONS

Hybrid polymer nanocomposites based on nanostructured POSS chemicals were prepared successfully *via* melt and solution blending. Two structurally and chemically different POSS molecules, a closed cage, non-polar octaisobutyl POSS (Oib-POSS) and an open cage, polar trisilanolphenyl POSS (Tsp-POSS) with differing predicted solubility parameters were evaluated in a variety of polymer matrices ranging from semi-crystalline polypropylene (PP) and nylon 6 to amorphous polystyrene (PS). Selection criteria for these materials were based on their expected compatibility, crystalline and amorphous nature of the polymer matrices, the nature of the POSS cage and substituents, solubility in common solvents, and melt processability. Parallel microscopic and spectroscopic analysis exhibited significant differences in POSS dispersion and aggregation states in selected POSS/polymer combinations. This study successfully demonstrate that POSS solubility and dispersion in a polymer matrix can be tailored by varying the substituent organic groups and that calculated solubility parameters provide a good indication of ultimate dispersion in films. For example, Oib-POSS with large difference in solubility parameter with PS ($\Delta\delta_{\text{Oib-POSS/PS}} = 1.4 \text{ (cal/cm}^3)^{1/2}$) exhibited preferential surface migration with large POSS domains (50-100 nm). Tsp-POSS, on the other hand, with its solubility close to PS ($\Delta\delta_{\text{Tsp-POSS/PS}} = 0.6 \text{ (cal/cm}^3)^{1/2}$) showed nano-level dispersion throughout the bulk PS with smaller POSS domains of 5-10 nm. Interestingly, the same Tsp-POSS molecules when blended with nylon 6 showed preferential surface migration due to their differences in solubility parameter ($\Delta\delta_{\text{Tsp-POSS/nylon 6}} = 1.2 \text{ (cal/cm}^3)^{1/2}$). Morphology, molecular miscibility, and solution and solid-state chain dynamics were

explained on the basis of classical thermodynamic principles (Gibbs free energy equation) taking into account various enthalpic and entropic factors.

In addition, these HPNC's exhibited exceptional improvements in the surface properties, especially tribomechanical and wetting characteristics, with minimal changes in the bulk thermo-mechanical properties. For example, incorporation of 10% Oib-POSS in polypropylene yielded a 60% reduction in relative coefficient of friction, significantly improved nanoscale scratch and wear resistance, and a two-fold increment in hardness and modulus measured by nanoindentation. Similarly, surface wetting characteristics were altered significantly on incorporation of POSS, with measured water contact angles approaching that of Teflon for 10% POSS filled nylon blends. The ultra-low nanoscale friction demonstrated by the POSS nanocomposites is related to the structural features of POSS molecules and the surface nanomechanical properties. The low friction is attributed to the interplay of a number of factors, with the enhanced surface hardness and modulus reducing surface friction by providing resistance to plastic deformation, surface damage, and production of wear particles. Further, the increased surface roughness, resulting in reduced contact area between the AFM probe and the surface, in combination with the demonstrated high hydrophobicity and reduced adhesion, contribute significantly towards reducing surface friction. More importantly, enhancements in the surface properties were achieved from non-fluorinated POSS and polymer combinations.

Findings and insights from the above research were utilized to expand the application domain of POSS from friction modifiers to novel dispersing aids for other nanoparticles (chapter 6) as well as surface modifiers for fabrics to impart hydrophobicity

and stain/acid resistance (chapter 7). Driven by the overall research interest of the Morgan research group to understand the molecular level lubricity and nanotribology of modified surface, the behavior of hydrophobin protein-modified surfaces (chapter 8) was also explored. Thin and stable coatings of hydrophobin, in the range of 10–20 nm, were prepared *via* spin coating and adsorption techniques from aqueous solution onto polymeric substrates. Polymeric surfaces with enhanced lubricity and significantly reduced surface friction were obtained *via* hydrophobin surface modification.

In summary, this dissertation reports the fundamental factors that control the dispersion and segregation states of nanostructured POSS chemicals in a polymer matrix. Precise control of surface properties is demonstrated through optimization of POSS structure and POSS/polymer interactions. To the best of our knowledge this research is a first comprehensive work on the friction characteristics of POSS/polymer HPNC's relating both material (structure, functionalities, stratification, and aggregation) and mechanical (roughness, hardness, and modulus) characteristics. These studies suggest possibilities of developing cost-effective non-fluorinated POSS/polymer HPNC's with tailored surface and bulk properties through control of morphology and POSS chemistry. Finally, these studies contribute to the field of structure-property-performance relationships for physically blended POSS/polymer HPNC's, surface science, and tribology.

RECOMMENDED FUTURE WORK

This research successfully demonstrated the control of dispersion states of POSS nanostructured chemicals by varying the substituent organic groups of POSS in relation to the polymer matrix. Qualitative and quantitative differences in the surface vs. bulk dispersion of POSS are reported. However, in order to have an absolute quantitative concentration profile of POSS, selected composite samples should be evaluated *via* XPS. Macro- and nanoscale tribomechanical properties and surface wetting characteristics were explored in detail however; theoretical simulation studies of surface friction and wetting behavior of POSS-polymer nanocomposites will be helpful in developing further mechanistic understanding. In this study we have measured relative surface friction using a similar probe for all the samples to maintain consistency. However, variation of surface friction with contact area can further be explored by varying the AFM probe geometry and dimensions. In addition, to obtain an absolute value of surface friction, it is recommended that individually calibrated AFM probes should be used. For commercialization interest, long term aging studies of these nanocomposites to evaluate any changes in the surface morphology, friction and wetting characteristics is also recommended. Studies of segregation as a function of annealing time and temperature are also suggested.

In our studies we have demonstrated preferential surface segregation of POSS in selected POSS/polymer combination. It will be of further interest to attach antifouling agents and/or stimuli responsive polymers to POSS molecules. This may have potential application for naval ship coatings which needs antifouling characteristics along with low friction and a high degree of hydrophobicity.

We have conducted initial studies on the flow behavior of POSS/Hyaluronic acid blends and friction behavior of hyaluronic acid modified surfaces. This area needs further investigation by physically as well as chemically attaching suitable POSS moieties with hyaluronic acid and evaluating rheological and surface frictional characteristics. In addition, biocompatibility studies of selected POSS systems will open new avenues for these blends in low friction biomedical devices.